Analysing human aquaporin-4 purified from *P. pastoris* in the context of neuromyelitis optica spectrum disorder

Caolan Browne

Doctor of Philosophy

Aston University

September 2025

Thesis Abstract

Analysing human aquaporin-4 purified from *P. pastoris* in the context of neuromyelitis optica spectrum disorder

Caolan Browne
Doctor of Philosophy

Aston University
September 2025

Aquaporin-4 (AQP4) is the predominant water channel in the central nervous system (CNS), controlling water homeostasis in the brain, spinal cord, and optic nerve. Neuromyelitis optica spectrum disorder (NMOSD) is an autoimmune disease in which antibodies attack the optic nerves and spinal cord. In the majority of cases, NMOSD is associated with anti-AQP4 autoantibodies (NMO-IgGs). NMO-IgGs bind preferentially to higher order oligomers of AQP4 tetramers, known as orthogonal arrays of particles (OAPs).

Solubilisation and purification of membrane proteins (MPs) is challenging due to their large hydrophobic domains that lie within biological membranes. The styrene-maleic acid (SMA) co-polymer can form nanodisc-like lipid particles (SMALPs) from biological membranes, and can encapsulate MPs within a native annulus of lipid. Recently, mass photometry has been developed as an analytical technique for label-free measurement of the mass of single particles in solution. Mass photometry requires samples of low concentration (~10 nM) and low heterogeneity, making it applicable to the analysis of purified MP-SMALPs.

This thesis presents recombinant expression of human AQP4 in *Pichia pastoris*, solubilisation of AQP4 with SMA, and purification of the AQP4-SMALPs for analysis with mass photometry amongst other biophysical characterisation techniques. This work showed that AQP4-SMALPs exist as a distribution of different nanodisc sizes after SMA solubilisation. These SMALPs of increasing size were hypothesised to contain different tetrameric assemblies of AQP4. When analysed by dot blotting, NMO-IgGs preferentially targeted purified AQP4-SMALPs predicted to contain large arrays of AQP4. Blue-native PAGE identified that hAQP4 was able to form higher-order oligomers in *P. pastoris* and, using a biochemical assay, hAQP4 was found to be palmitoylated by *P. pastoris*. This may represent a possible mechanism of OAP regulation in this host.

These results suggest that AQP4 tetramers and OAPs can be captured and characterised in SMALPs from the *P. pastoris* membrane. *P. pastoris* can replicate features of hAQP4 that are observed in mammalian expression systems. Therefore, this could be the basis for a future model in understanding AQP4 oligomerisation in the context of NMOSD.

Acknowledgements

Firstly, I'd like to thank my supervisor, Professor Roslyn Bill, for the opportunity to undertake this project, but more so for the constant motivation, support, and guidance. Roslyn, you have a natural gift for bringing researchers together and a never-ending supply of wisdom to share with your community. You have taught me so much about the world of academic research and the importance of collaboration. Thank you for making this experience so enjoyable. I'd like to give special thanks to the exceptional talents of Dr. Philip Kitchen. You have been a key mentor for me from the very beginning, and you have taught me the majority of the technical abilities that I know. Thank you for your patience, your keen interest in my project, and for always being there when things went wrong. I'd also like to thank my co-supervisors, Dr Alice Rothnie and Professor Alan Goddard, for their expertise and advice throughout my project. Thank you for all of your guidance in the complex problems and your enthusiasm for new ideas and suggestions.

I'd like to give thanks to my research colleagues. Thank you, Lucas, Zaid, Manish, Grant, Ophelie, Amandeep, and Mina. I am forever grateful for all of your support in and around the lab. It is an utter delight to work with you as a team. I'd also like to extend my thanks to everyone in the wider AQP research group that joins us for our weekly catch-up. Thank you to all of my other AIME and Aston colleagues, for being such a great community to work with. A special thanks to Calum, Miguel, and Anthony, who reminded me to have a good laugh every now and then.

Thank you to my parents, my two brothers, and my extended family and friends, for all of your support over the last few years, and the many years before. Thank you for all of your inspiration and encouragement.

Finally, I'd like to thank my partner, Sophie, without whom this journey wouldn't be possible. You have always been there to support me through the highs and lows, and you have always reminded me to keep going.

Table of Contents

List of Abbreviations

1T – one tetramer
2T – two tetramer(s)
3T – three tetramer(s)
aa – amino acid(s)
$A_{2A}R$ – adenosine A_{2A} receptor
Ab(s) – antibody (antibodies)
ABE – acyl-biotinyl exchange
ADH – alcohol dehydrogenase
AMP – AquireMP
AQP – aquaporin
AQP4 – aquaporin-4
AQP4-SMALP(s) – aquaporin-4 styrene-maleic acid lipid particle(s)
(m)AU – (milli-) absorbance units
AUC – area under the curve
βME – beta-mercaptoethanol
BMGY – buffered glycerol-complex medium
BMMY – buffered methanol-complex medium
BSA – bovine serum albumin
CBA – cell-based assay
CD – circular dichroism
CDC – complement-dependent cytotoxicity
CHIP – channel-forming integral protein
CHO – Chinese hamster ovary
CMC – critical micelle concentration
CNS – central nervous system
Cryo-EM – cryogenic electron microscopy
CSF – cerebrospinal fluid
DAPC – dystrophin-associated protein complex
DDM – *n*-dodecyl-*β*-D-maltoside
DIBMA – diisobutylene maleic acid
DLS – dynamic light scattering
DMP – DiscoverMP
DMSO – dimethyl sulfoxide
DNA – deoxyribonucleic acid
DO – dissolved oxygen
EM – electron microscopy
ER – endoplasmic reticulum
EtOH – ethanol
FIDA – flow-induced dispersion analysis
GFP – green fluorescent protein
HA – hydroxylamine
HPDP-biotin – pyridyldithiol-biotin
HRP – horseradish peroxidase
IgG – immunoglobulin G
IMAC – immobilised metal affinity chromatography
LB – lysogeny broth

LILBID-MS – laser induced liquid bead ion desorption mass spectrometry
MD – molecular dynamics
MDCK – Madin-Darby canine kidney
MeOH – methanol
MP(s) – membrane protein(s)
MP-SMALP(s) – membrane protein styrene-maleic acid lipid particle
mRNA – messenger ribonucleic acid
MS – mass spectrometry
MSP(s) – membrane scaffold protein(s)
MW – molecular weight
NEM – N-ethylmaleimide
Ni-NTA – nickel nitrilotriacetic acid
NMO – neuromyelitis optica
NMOSD – neuromyelitis optica spectrum disorder
NS-TEM – negative stain transmission electron microscopy
OAPs – orthogonal arrays of particles
OD – optical density
PAGE – polyacrylamide gel electrophoresis
PBS – phosphate buffered saline
PDB – Protein Data Bank
PTM(s) – post-translational modification(s)
PVDF – polyvinylidene fluoride
RNA – ribonucleic acid
RT – room temperature
SAXS – small-angle X-ray scattering
SD – standard deviation
SDS – sodium dodecyl-sulphate
SDS-PAGE – sodium dodecyl-sulphate polyacrylamide gel electrophoresis
SEC – size-exclusion chromatography
SMA – styrene-maleic acid
SMALP(s) – styrene-maleic acid lipid particle(s)
SMA-PAGE – styrene-maleic acid polyacrylamide gel electrophoresis
SV-AUC – sedimentation velocity analytical ultracentrifugation
TCM – chloroform
TEM – transmission electron microscopy
UV – ultraviolet
YPD – yeast extract peptone dextrose (agar)

List of Figures

List of Tables

1. Introduction

1.1. Membrane proteins

Determination of the structure and function of a protein is a key process in understanding its role in biological systems. Membrane proteins (MPs) are of particular interest because they make up a significant part of the cell membrane, a gateway to processes that take place inside cells. They perform essential cell functions such as molecule transport, signal transduction, enzymatic reactions, and contributing to cellular structure. Approximately 20–30% of the human proteome is thought to encode for MPs (Krogh *et al.*, 2001; Almén *et al.*, 2009; Fagerberg *et al.*, 2010). By comparison, it is estimated that that over 60% of therapeutic drug targets are membrane proteins (Overington, Al-Lazikani and Hopkins, 2006; Yin and Flynn, 2016), a disproportionate quantity compared to their genome representation, thus highlighting their importance in cellular function.

MPs have previously been underrepresented in the Protein Data Bank (PDB) (Berman *et al.*, 2000), largely due to the difficulty of MP extraction from lipid bilayers in a native form (Li and Buck, 2021). MPs are stabilised by the natural hydrophobic core of the cell membrane because of their large hydrophobic domains. Various components of the natural lipid bilayer act to stabilise these structures (Lee, 2003). Expression and extraction into hydrophilic solvent for purification can be difficult without denaturation of the native MP structure. With advances in experimental design and analysis techniques, the number of MP entries in resources such as the PDB are increasing rapidly (Newport, Sansom and Stansfeld, 2019; Bittrich *et al.*, 2022). However, resolving membrane protein structures in complex with surrounding lipids, their native and functional environment, remains an enduring challenge (Hong, Choi and Yoon, 2022; Urner, 2022; Ansell *et al.*, 2023).

1.2. Aquaporins

Water is essential for all biological processes. It acts as a natural solvent for molecules, is a key component in most chemical reactions, and is an excellent thermal regulator due to its high specific heat capacity. Efficient transport of water for organisms is therefore essential. Water is able to diffuse across cell membranes, but the polar charge of water molecules makes this process too slow to accommodate for physiological process that require fluxes of large volumes of water (Johansson *et al.*, 2000).

Aquaporins (AQPs) are integral membrane proteins that serve as water channels to allow transport of water across biological membranes in response to osmotic gradients or hydrostatic pressure. AQPs are found abundantly in eukaryotes for water homeostasis, though they are also present in prokaryotic organisms, thought to give protection against osmotic shock (Kruse, Uehlein and Kaldenhoff, 2006; Tanghe, Van Dijck and Thevelein, 2006). Some AQPs are exclusively selective for water, whilst others (also known as aquaglyceroporins) are also permeable to uncharged solutes such as glycerol (Zeuthen and Klaerke, 1999; Gomes *et al.*, 2009). AQPs were first discovered in red blood cell membranes. AQP1 (then identified as channel-forming integral protein 28; CHIP28) was co-purified with another erythrocyte membrane protein. It was functionally identified as a water channel by injecting *Xenopus laevis* (frog) oocytes with RNA encoding for CHIP28. The oocytes, which are normally impermeable to water, demonstrated increased osmotic water permeability after CHIP28 RNA injection, suggesting oocytes had been transiently transfected with a water channel protein (Preston *et al.*, 1992; Agre *et al.*, 2002).

AQP monomers have a conserved structure of six transmembrane α-helices, with five connecting loops (identified as A–E), with both amino- (N-) and carboxyl- (C-) termini located on the cytosolic side of the membrane (Figure 1.1.A, B and C). Two of the connecting loops (B and E) form short hydrophobic α-helices that insert into the membrane from either side to form a connected segment that appears as a seventh transmembrane helix. These helices bundle together to form a tertiary hydrophilic channel structure for water molecule transport (Verkman, 2013; Kreida and Törnroth-Horsefield, 2015). AQPs have conserved NPA (asparagine-proline-alanine) motifs on each of the B and E loop short helical domains. AQPs also have a partially conserved ar/R (aromatic/arginine) region on the extracellular side of the channel pore. Along with overall pore size, these motifs are important for water-selective transport, determining permeability to glycerol (and other uncharged solutes), and exclusion of protons (Fu and Lu, 2007; Kitchen *et al.*, 2019). High resolution structural studies have demonstrated how water molecules move in a single-file through the narrowest part of the AQP monomer channel (Murata *et al.*, 2000; Sui *et al.*, 2001).

The AQP family monomers are ~30 kilodaltons (kDa) in size, though sizes can vary between homologues (Verkman and Mitra, 2000). The quaternary structure of AQP monomers in the lipid bilayer is a tetramer. This tetrameric formation is a highly conserved trait in the AQP family (Ozu *et al.*, 2018). However, each AQP monomer appears to function independently as a water channel (Jung, Preston, *et al.*, 1994; Hub, Grubmüller and de Groot, 2009), so the

necessity of this tetrameric formation is not exactly clear. In the example of AQP4, one study has shown that tetrameric assembly is not essential for endoplasmic reticulum (ER) to Golgi apparatus trafficking or water channel function, but could be important for cell membrane re-localisation and regulation (Kitchen *et al.*, 2016). The tetramer creates an additional hydrophobic central pore between monomers. It has been suggested that this acts as a transporter for ions and carbon dioxide (Yu *et al.*, 2006; Kaldenhoff, Kai and Uehlein, 2014), though its exact function (if any) is still uncertain. Molecular dynamics (MD) simulations have confirmed that this central pore is not expected to be involved in water transport (Cui and Bastien, 2011).

Thirteen AQPs have been identified in humans (hAQP0–12). These AQPs provide systemic water homeostasis and function in a variety of tissues, playing roles in solute transport, fluid secretions, cell migration, immunity and inflammation, signal transduction, and glymphatic system clearance, just to name a few (Verkman, 2005; Wagner *et al.*, 2022). As such, disorders of, or those associated with, AQPs results in a wide variety of pathophysiological consequences, including neurological disorders, cancer, cardiovascular disease, renal dysfunction, and obesity (Agre *et al.*, 2002; Verkman, 2012; Azad *et al.*, 2021).

1.2.1. Aquaporin-4

Aquaporin-4 (AQP4) was originally identified and cloned form rat lung and brain, later being identified in other species (Hasegawa *et al.*, 1994; Jung, Bhat, *et al.*, 1994). AQP4 is the predominant AQP in the central nervous system (CNS) out of the three that have been identified there (AQP1, 4, and 9). It controls water homeostasis in the brain, spinal cord, and optic nerve (Nagelhus and Ottersen, 2013; Mader and Brimberg, 2019). It is most abundantly expressed at the end-feet of astrocytes surrounding blood vessels, synaptic junctions, the brain ventricle lining, and those forming the glia limitans connecting to the pia mater of the innermost meninges (Papadopoulos and Verkman, 2013; Salman *et al.*, 2022). Studies of transgenic mice models lacking AQP4 have demonstrated its importance for cerebral water homeostasis, neuronal signal transduction, and astrocyte migration (Verkman *et al.*, 2006). AQP4 has been proposed as a key component of the glymphatic system for clearance of waste solutes, using an influx of the cerebrospinal fluid (CSF) to flush the brain interstitial fluid (Iliff *et al.*, 2012, 2013; Rasmussen, Mestre and Nedergaard, 2018).

Multiple studies have implicated the importance of glymphatic clearance in relation to neurodegenerative diseases, such as Alzheimer's disease (Kress *et al.*, 2014; Peng *et al.*, 2016; Nedergaard and Goldman, 2020). Therefore, due to its role in the glymphatic system,

the function and regulation of AQP4 has been proposed as a key factor in the development of these diseases (Burfeind *et al.*, 2017; Zeppenfeld *et al.*, 2017; Chandra *et al.*, 2021). CNS oedema (swelling of the brain and spinal cord), as a result of factors such as CNS trauma or stroke, is facilitated by AQP4 due to its abundance in this region (Halsey *et al.*, 2018). Inhibition of AQP4 function has previously been proposed (Verkman *et al.*, 2017), and targeting AQP4 re-localisation to the cell membrane has been investigated as viable preventative measure for the acute phase of CNS oedema (Kitchen *et al.*, 2020). AQP4 is also strongly associated with the autoimmune condition, neuromyelitis optica spectrum disorder (NMOSD), in which the majority of cases involve detectable autoantibodies targeting AQP4 (known as AQP4 IgGs or NMO IgGs) (Wingerchuk *et al.*, 1999; Lennon *et al.*, 2005).

Electron microscopy (EM) and x-ray crystallography have been used to determine the structure of rat and human AQP4 (rAQP4 / hAQP4) (Hiroaki *et al.*, 2006; Ho *et al.*, 2009; Tani *et al.*, 2009). However, the N- and C-termini have been difficult to resolve, due to their disordered flexibility. For example, the first structure of hAQP4 determined by x-ray crystallography used trypsinisation for improved resolution. The 1.8 Å resolution structure did not include the 19 amino acids (aa) of the N-terminus or 64 aa of the C-terminus (Glu-20 to Lys-259) of the full-length hAQP4 sequence (Figure 1.1.D and E). Full-length AQP4 crystals reportedly diffracted to ~8 Å (Ho *et al.*, 2009). The same group very recently determined the cryogenic-EM (cryo-EM) structure of full-length tetrameric hAQP4 in lipid nanodiscs (specifically, membrane scaffold protein (MSP) nanodiscs) to a resolution of 2.1 Å. They reported that a similar number of the terminal aa residues (1 to 31 and 254 to 323) were not visible in the EM structure due to the flexibility of these regions, consistent with that reported for the x-ray crystallography structure previously (Gupta *et al.*, 2025).

AQP4 exists as two isoforms, M1 and M23, where M1 is the longer (full-length) isoform with translation initiation at Met-1, and M23 is the shorter isoform with translation initiation at Met-23 (Jung, Bhat, *et al.*, 1994; Lu *et al.*, 1996). Both alternative splicing (Yang, Ma and Verkman, 1995), and “leaky scanning” (Rossi *et al.*, 2010), have been proposed as mechanisms to derive the M23 isoform. The “leaky scanning” mechanism suggests that the M23 isoform can be translated from the full-length M1 AQP4 mRNA sequence, whereby ribosomal skipping of the Met-1 initiation site allows for translation initiation from Met-23. M1 and M23 AQP4 monomers can combine to form heterotetramers in the membrane (Neely *et al.*, 1999).

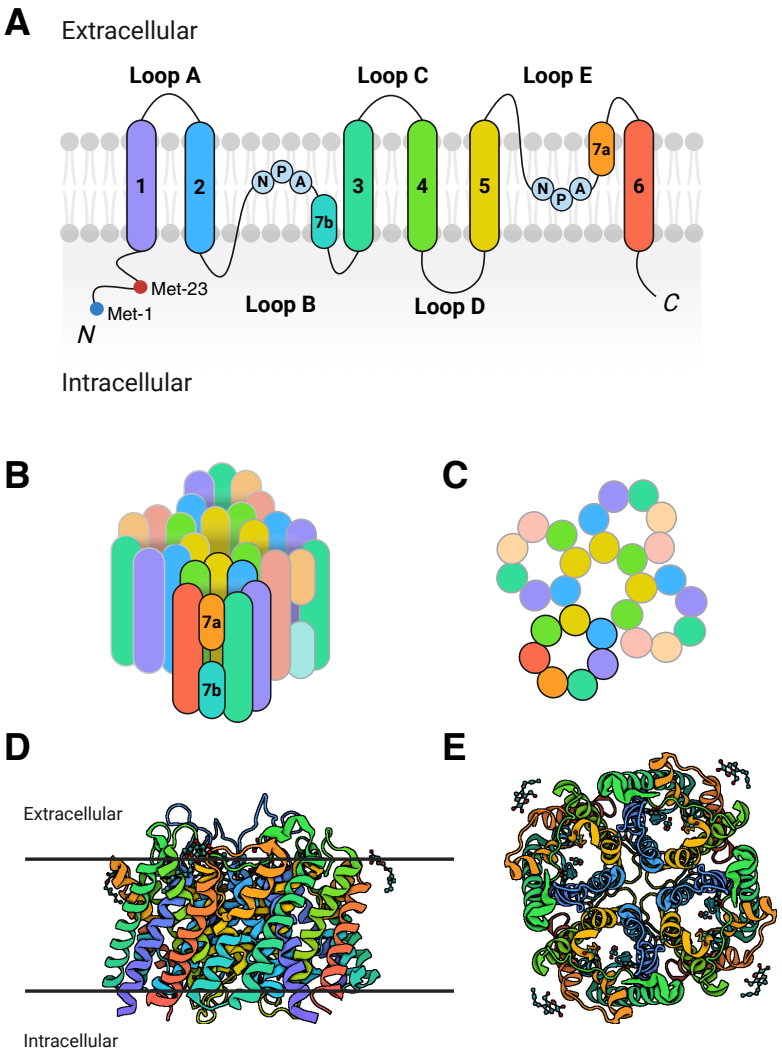

Figure 1.1. Aquaporin-4 topology and quaternary structure.
AQP4 tetramers form four hydrophilic water channels and a fifth hydrophobic pore in the centre. **A)** AQP4 monomer topology indicating transmembrane α-helices 1 to 6 and connecting loops A to E. Loop B and E contain the conserved NPA motifs and short helical domains (7b and 7a, respectively) that form a connected transmembrane segment. Met-1 (blue) and Met-23 (red) translation initiation sites are indicated. **B, C)** AQP4 tetramer constructed of monomer topology shown in **A**, with side view (**B**) and top view (**C**). **D,E)** AQP4 tetramer crystal structure with colour-coding of helices corresponding to **A**, with side view (**D**) and top view (**E**). Figure created in BioRender.com. **A**, **B**, and **C** are adapted from a template by Moëlo, C., BioRender (Moëlo, 2025b). **D** and **E** show the PDB 3GD8 AQP4 crystal structure (Ho *et al.*, 2009).

1.2.2. AQP4 orthogonal arrays of particles

AQP4 is one of two AQPs (including AQP0) with a unique ability to form large organised square arrays in the cell membrane, called, orthogonal arrays of particles (OAPs) (Roche and Törnroth-Horsefield, 2017). OAPs have long been observed in cell membranes of the brain and other tissues (Landis and Reese, 1974; Wolburg, 1995). Stable transfection of Chinese hamster ovary (CHO) cells with rAQP4 resulted in the presence of OAPs (Yang, Brown and Verkman, 1996). The role of AQP4 in OAP formation was further supported with the absence of OAPs in AQP4 knockout mice (Verbavatz *et al.*, 1997). Immunogold labelling and EM of AQP4 in cell membranes of the rat brain and spinal cord confirmed that AQP4 was contained within these OAPs (Rash *et al.*, 1998, 2004).

M23 AQP4 preferentially forms OAPs, whereas M1 AQP4 is unable to form these multi-tetrameric assemblies. This has been shown by a number of studies that expressed these isoforms individually (Furman *et al.*, 2003; Silberstein *et al.*, 2004; Crane and Verkman, 2009). It has also been demonstrated that M1 AQP4 diffuses freely in the membrane, whereas M23 AQP4 OAPs are mostly immobile (Crane, Tajima and Verkman, 2010). OAPs can be constructed of M1 and M23 AQP4 units, in part due to the formation of AQP4 heterotetramers (Tajima, Crane and Verkman, 2010). Studies that co-expressed M1 and M23 AQP4 demonstrated that OAP size could be modulated by adjusting the ratio of M1:M23 expression (Figure 1.2). With higher proportion of M23, OAPs were larger, and with higher proportion of M1, OAPs were smaller. With M1 alone, OAPs were typically absent (Crane, Bennett and Verkman, 2009; Jin, Rossi and Verkman, 2011). The relative expression of M1 AQP4 in the native membrane is therefore believed to be the determinant and regulator of AQP4 OAP size. Using super-resolution imaging of cells co-expressing M1 and M23 isoforms, one study demonstrated that the M1 isoform forms a boundary around the edge of OAPs (Rossi, Moritz, *et al.*, 2012).

Previous EM crystallographic structures have utilised the rAQP4 M23 isoform as this features the truncated N-terminus. Ordered 2D-crystals for M23 AQP4 were reportedly achievable, but these studies reported difficulty in producing these crystalline arrays for M1 AQP4, suggesting that this is consistent with it not being able to form OAPs (Hiroaki *et al.*, 2006; Tani *et al.*, 2009). Arg-108 and Tyr-250 are two AQP4 residues on the cytoplasmic side that are not conserved in other AQPs. Based on interaction of these residues between M23 tetramers in the 2D crystals, these residues were proposed as a mechanism of stabilisation between tetramers in AQP4 OAPs. For M1 APQ4, it was suggested that interaction of Tyr-250 with Arg-9 in the N-terminus prevents this interaction (Hiroaki *et al.*, 2006). Alternatively, it was

suggested that residues just downstream of Met-23 were key in OAP formation. Mutation of Val-24, Ala-25 and Phe-26, resulted in disappearance of M23 AQP4 OAPs (Crane and Verkman, 2009).

Due to the differing ability of the AQP4 isoforms to form OAPs, the OAP preventative mechanism has been attributed to the M1 isoform N-terminus (that the M23 isoform lacks). Suzuki *et al.* proposed that *S*-palmitoylation of the M1 AQP4 N-terminal residues, Cys13 and Cys17, were responsible for prevention of OAP formation by the M1 isoform. They examined rAQP4 expressed in CHO cells, finding that mutagenic substitution of both Cys13 and Cys17, to alanine, resulted in M1 AQP4 OAP formation. With single mutations of either of these cysteines individually, OAPs were either very small or non-existent. They were also able to experimentally determine that both cysteines were palmitoylated. This study suggested that the presence of only one cysteine (and probable palmitoylation) was significant enough to disrupt OAPs (Suzuki *et al.*, 2008). This influence of palmitoylation on OAP prevention has also been supported by other studies (Crane, Bennett and Verkman, 2009; Strand *et al.*, 2009). A very recent study reconstituted purified M1 AQP4 into supported lipid bilayers for temperature-dependent single-particle tracking, using time-lapse single-molecule fluorescence microscopy. They were able to demonstrate that, when palmitoylated, M1 AQP4 can form a dimer of tetramers, but when de-palmitoylated, could further associate into a trimer of tetramers. They also demonstrated that palmitoylated M1 AQP4 showed a higher mobility in the membrane when compared to de-palmitoylated M1 AQP4 (Carder *et al.*, 2024).

Others have proposed that at least seven residues upstream of Met-23 in the M1 isoform N-terminus are required for OAP prevention. They demonstrated that single residue mutations in the M1 N-terminus were not sufficient to cause OAP assembly of the M1 isoform (Crane and Verkman, 2009). It has been suggested that OAPs are regulated by multiple factors, including palmitoylation, relative expression of M1 and M23 isoforms, and calcium- or phosphorylation- mediated signalling (Crane, Bennett and Verkman, 2009). The exact structure of the AQP4 N-terminal region still remains elusive, likely due to innate functional flexibility. Thus, the exact mechanism of OAP prevention by this region is still not fully understood.

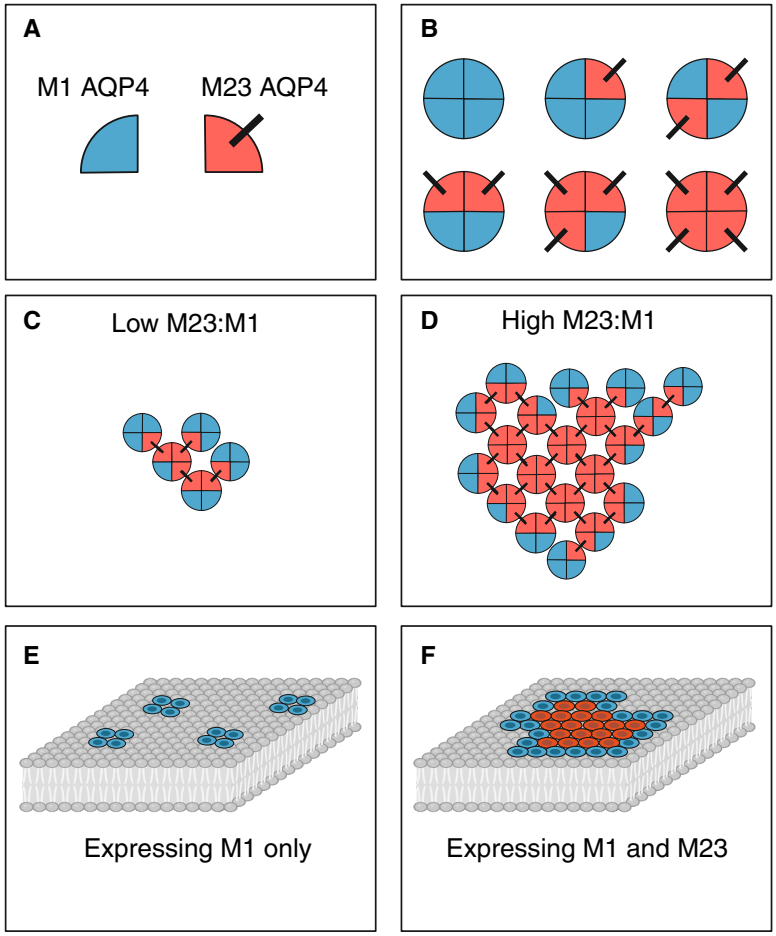

Figure 1.2. Schematic of AQP4 OAP assembly.
Proposed model for AQP4 OAP formation by Jin, Rossi and Verkman, 2011, assuming formation of AQP4 M1 and M23 isoform heterotetramers. **A)** AQP4 M1 (blue) and M23 (red) monomers. M23 isoform projection (black) indicates tetramer interaction site. **B)** Possible AQP4 heterotetramer conformations. **C)** A low M23 : M1 ratio creates small OAPs in the membrane. **D)** A high M23 : M1 ratio creates large OAPs in the membrane. **E)** Association of AQP4 monomers in the cell membrane of cells only expressing M1 AQP4. **F)** Association of AQP4 monomers in the cell membrane of cells expressing M1 and M23 isoforms of AQP4. Figure created in BioRender.com, adapted from template by Moëlo, C., BioRender (Moëlo, 2025a).

1.2.3. AQP4 OAP involvement in physiology and pathophysiology

AQP4 OAPs have previously been proposed to enhance water permeability compared to individual M1 isoform tetramers alone (Silberstein *et al.*, 2004). It has also been demonstrated that AQP4 could play a role in cell adhesion, with speculation that the formation of OAPs could enhance this adhesive ability (Hiroaki *et al.*, 2006). Another study has proposed that AQP4 OAP disaggregation may increase the invasive potential of glioma cells, whereas OAP assembly may activate apoptosis (Simone *et al.*, 2019).

Polarisation of AQP4 to cell membrane regions, such as the astrocyte end-feet, has been linked to OAP formation, with suggestions that regulation of M1 and M23 isoform expression may influence localisation as a result of differential OAP formation (Smith *et al.*, 2014). Localisation of AQP4 is known to be associated with the dystrophin-associated protein complex (DAPC), anchoring AQP4 to the cell cytoskeleton (Amiry-Moghaddam, Frydenlund and Ottersen, 2004; Nicchia *et al.*, 2004). Deletion of key DAPC protein genes in mice resulted in impaired membrane localisation of AQP4 (Amiry-Moghaddam *et al.*, 2003; Belmaati Cherkaoui *et al.*, 2021). Studies have therefore proposed a link between OAP immobilisation and DAPC, but questions still remain, such as the extent to which the DAPC could interact with the localisation of AQP4 isoforms to mediate OAP formation (Yang *et al.*, 2024).

Recent studies of OAP-null mouse models have found varying results in AQP4 expression and localisation. One study generated a mouse model with an AQP4 Met-23 mutation to isoleucine for expression of only of the M1 isoform. This resulted in a reduction in overall AQP4 expression levels, suggesting that formation of OAPs are necessary for normal levels of AQP4 expression (de Bellis *et al.*, 2021; Pisani *et al.*, 2021). Another study generated an OAP “depolymerisation” mouse model by AQP4 Ala-25 mutation to glutamine, finding that reduced abundance of OAP structures were associated with a reduction in polarised localisation at astrocyte end-feet (Crane and Verkman, 2009; Zhu *et al.*, 2022).

Studies have demonstrated that OAPs are physiologically and pathologically relevant. However, there is still a general agreement that there is some uncertainty around their exact physiological function, and the importance of their role in the membrane (Nagelhus and Ottersen, 2013; Verkman *et al.*, 2013; Roche and Törnroth-Horsefield, 2017; Salman *et al.*, 2022).

1.2.4. Neuromyelitis optica spectrum disorder

Neuromyelitis optica spectrum disorder (NMOSD), previously known simply as NMO or Devic's disease, is a rare autoimmune disease of the CNS. It is characterised by acute inflammation of the spinal cord and optic nerves, known as myelitis and optic neuritis, respectively. It is also associated with attacks on the brainstem, although less frequently, causing brainstem encephalitis. Some of the main symptoms of the resultant myelitis and optic neuritis are muscle weakness or paralysis, muscle spasms, loss of sensation, loss of bowel and bladder control, erectile dysfunction, pain with eye movement, blurred vision, and headaches. Symptoms can easily be mistaken for multiple sclerosis and NMOSD was historically considered a variant of multiple sclerosis (Jarius *et al.*, 2023; Kümpfel *et al.*, 2024).

In 2004, pathogenic immunoglobulin G (IgG) antibodies (Abs) to AQP4 (AQP4-IgGs; abbreviated here as NMO Abs) were discovered in relation to NMOSD (Lennon *et al.*, 2004), and it has now been established that the majority (≥ 80%) of NMOSD cases are associated with the presence of NMO Abs in patient serum targeting AQP4 (Paul *et al.*, 2007; Jarius *et al.*, 2020). The discovery of AQP4 specific IgGs was a key clinical distinction of NMOSD from multiple sclerosis (Lennon *et al.*, 2004, 2005). Along with identification of symptoms and neuroimaging (using magnetic resonance imaging) to identify characteristic lesions, identification of NMO Abs is used as one of the principle criteria for diagnosis of NMOSD. For diagnosis, these Abs are typically identified in patient sera using live cell based assays (CBAs) with cells expressing recombinant AQP4 (Wingerchuk *et al.*, 2015; Jarius *et al.*, 2023). Early diagnosis to discriminate from multiple sclerosis is important, as some studies have demonstrated that treatments intended for multiple sclerosis may increase the occurrence NMOSD relapses (Palace *et al.*, 2010).

Binding of NMO Abs to AQP4 has been demonstrated to induce pathogenesis by activating complement-dependent cytotoxicity (CDC), causing damage and loss of astrocytes (Hinson *et al.*, 2007; Sabater *et al.*, 2009; Nishiyama *et al.*, 2016). However, studies have demonstrated that binding of NMO Abs to AQP4 is unlikely to directly inhibit water permeability or cause AQP4 internalisation (Nicchia *et al.*, 2009; Rossi, Ratelade, *et al.*, 2012).

NMO Abs have been reported to bind to both M1 and M23 isoforms of AQP4 (Hinson *et al.*, 2007; Bennett *et al.*, 2009; Crane, Bennett and Verkman, 2009; Verkman *et al.*, 2011). However, multiple studies have shown a higher binding affinity of NMO Abs to the M23 isoform (Nicchia *et al.*, 2009; Mader *et al.*, 2010; Crane *et al.*, 2011; Pisani *et al.*, 2011, 2013; Soltys *et al.*, 2019). For example, Crane *et al.* used dual-colour quantitative fluorescence ratio

imagining of astrocyte-derived cells transfected with AQP4. Cells were stained with NMO Abs targeting the extracellular region of AQP4 and commercial anti-AQP4 Abs targeting the AQP4 C-terminus. Cells were probed with NMOSD patient serum and recombinant NMO monoclonal Abs (mAbs) derived from NMOSD patient CSF. They found a consistently greater affinity of NMO Abs to the M23 isoform (Crane *et al.*, 2011). This higher affinity of NMO Abs to M23 AQP4 is thought to be facilitated by OAP structures, rather than a difference between AQP4 isoforms alone. OAP disrupting mutations in M23 AQP4 has been shown to result in reduced binding of NMO Abs (Crane *et al.*, 2011; Pisani *et al.*, 2011; Papadopoulos and Verkman, 2012). It has also been suggested that OAPs could aid CDC activation due to clustered binding of NMO Abs to AQP4 arrays (Phuan *et al.*, 2012; Soltys *et al.*, 2019).

It is believed that complex combinations of the AQP4 extracellular loops created by OAP formation provide favourable binding epitopes for NMO IgGs (Pisani *et al.*, 2011; Abe and Yasui, 2022; Gupta *et al.*, 2025). Studies that have introduced residue mutations into AQP4 extracellular loops A, C, and E, present on each AQP4 monomer, demonstrated reduced binding of NMO Abs (Pisani *et al.*, 2011; Owens *et al.*, 2015). One study also demonstrated that patient-derived NMO Abs do not recognise linear peptide forms of these epitopes, showing that 3D conformational epitopes created by AQP4 tetramers and OAPs are required for binding (Owens *et al.*, 2015). NMO Abs in individual patient serum are polyclonal in nature, with multiple different binding epitopes within AQP4 extracellular loops identified. Broadly speaking, two binding patterns have previously been identified; binding of one group of NMO Abs is dependent on extracellular loop A, while binding of the other group is independent of extracellular loop A (Tuller *et al.*, 2016).

In cell-based assays, patient-derived NMO Ab Fab fragments have previously demonstrated similar binding affinities to AQP4 when compared with whole divalent NMO IgGs. This further suggested that epitope structural features created by OAP assemblies allowed for increased binding affinity, as opposed to bivalent binding of the NMO IgG molecule (Crane *et al.*, 2011). A very recent study was able to structurally determine the binding of patient-derived NMO Ab Fab fragments to AQP4. AQP4 was recombinantly expressed, solubilised with detergent, and reconstituted in to MSP nanodiscs. After confirming the binding affinity of Fab fragments for tetrameric AQP4 using bio-layer interferometry, structures were determined using cryo-EM (Gupta *et al.*, 2025).

Questions still remain surrounding the exact dynamics of AQP4 OAPs upon NMO Ab binding (Verkman *et al.*, 2013; Salman *et al.*, 2022). Studies have suggested different outcomes for OAP dynamics and size changes upon NMO IgG interaction (Hinson *et al.*, 2012; Rossi,

Ratelade, *et al.*, 2012; Ciappelloni *et al.*, 2019), highlighting that certain aspects of pathogenesis still need to be explored.

1.3. Palmitoylation

Post-translational modifications (PTMs) are changes made to proteins via covalent attachments after protein synthesis. PTMs have a variety of functions, such as regulating activity, protein stability, subcellular localisation, and cellular signalling. PTMs can be attached to protein N- and C- termini, or onto aa side chains. Common PTMs include phosphorylation (attachment of phosphate groups), glycosylation (attachment of carbohydrate molecules), lipidation (attachment of lipid molecules), and proteolytic cleavage (Ramazi and Zahiri, 2021; Bobalova, Strouhalova and Bobal, 2023).

Palmitoylation is a type of lipidation, in which palmitic acid (a 16-carbon saturated fatty acid) is covalently linked to a protein. The three main types of palmitoylation are *S*-palmitoylation, *N*-palmitoylation, and *O*-palmitoylation. *S*-palmitoylation (or *S*-acylation) is the most common of these types, in which palmitic acid is covalently bound to a cysteine residue on the sulfhydryl (or thiol) functional group (-SH) by forming a thioester linkage (Shang, Ding and Zhou, 2025).

S-palmitoylation is facilitated by a group of enzymes called palmitoyl acyltransferases (PATs), which were first identified in yeast in 1999 (Bartels *et al.*, 1999; Lobo *et al.*, 2002). PATs of the zDHHC family are defined by a zinc finger and conserved DHHC (Asp-His-His-Cys) motif in their catalytic domain, which is found in many eukaryotic PATs (Roth *et al.*, 2002; Mitchell *et al.*, 2006; Rana, Lee and Banerjee, 2018). PATs use palmitoyl-CoA as a lipid substrate to transfer palmitic acid to protein Cys residues. The covalent attachment is reversible and palmitic acid can be removed by acyl-protein thioesterases (Tabaczar *et al.*, 2017).

Palmitoylation increases the hydrophobicity of proteins, or certain protein domains, and can anchor proteins to lipid membranes. As *S*-palmitoylation is reversible, the effect it has on proteins can be modulated. It plays a critical role in subcellular localisation and the traffic of proteins between the cell membrane and different membrane bound organelles (Van Itallie *et al.*, 2005; Greaves and Chamberlain, 2007). Palmitoylation is also important for influencing protein-protein interactions, such as those involved in signal transduction (Smotrys and Linder, 2004; Guan and Fierke, 2011).

S-palmitoylation occurs on both soluble and transmembrane proteins. Palmitoylation of soluble proteins regulates their interaction with different lipid membranes. However, the exact purpose of palmitoylation for MPs, that are already associated to the lipid membrane, can appear more trivial and enigmatic (Blaskovic, Blanc and van der Goot, 2013). Studies have suggested various functional outcomes for the palmitoylation of MPs, including: conformational changes, such as transmembrane domain tilting demonstrated with a synthetic peptide (Joseph and Nagaraj, 1995); association to sphingolipid- and cholesterol-rich lipid rafts, such as for the transmembrane linker for activation of T cells (Levental *et al.*, 2010); and influence on protein-protein interactions, such as with tetraspanin-enriched microdomains (Yang *et al.*, 2004; Delandre *et al.*, 2009). In the case of AQP4, *S*-palmitoylation appears to be crucial in the preventative mechanism for higher-order oligomerisation (Suzuki *et al.*, 2008; Carder *et al.*, 2024).

1.4. Heterologous expression

Heterologous expression is the process of expressing a gene in a host organism or cell type that is different to the origin of its natural expression. Typically, molecular cloning is performed to create recombinant DNA. Recombinant DNA vectors can then be introduced into the host organism via transfection (or transformation) for expression. Transient transfection involves introduction of recombinant DNA, whereby the gene of interest is not integrated into the host genome, typically resulting in transient expression. Stable transfection involves integration of recombinant DNA into the host genome, to create organism clones that permanently contain the inserted gene for expression.

Heterologous expression is very important for protein research and production in biology, biotechnology, and medicine. It can be used for studying gene and protein function, large-scale protein production, compound production using biosynthetic pathways, disease modelling and drug screening, and improvement of crops for agriculture. For the study of proteins, recombinant expression in a simple host system can provide a controlled environment for expression, away from the complexity of the native environment.

Common host expression systems for production of recombinant proteins include bacteria, such as *Escherichia coli*, and yeasts, such *Saccharomyces cerevisiae* and *Pichia pastoris*. These examples can be cultured to a high density very quickly and typically at a low material cost. The use of strong inducible promoters in recombinant DNA vectors allows for over-

expression of the desired protein. For example, recombinant protein production in *E. coli* often utilises the Lac operon that can be induced with IPTG (isopropyl β-D-1-thiogalactopyranoside). For studies requiring a high quantity of purified protein, such as for structural analyses, recombinant protein expression is therefore essential. A common approach is to design recombinant DNA constructs of the desired protein gene with attached tags, such as a poly-histidine tag (His-tag). Proteins with an attached poly-His tag can be purified using immobilised-metal affinity chromatography (IMAC) using nickel nitrilotriacetic acid (Ni-NTA) agarose resins.

1.4.1. *Pichia pastoris*

P. pastoris (also known by its reclassification, *Komagataella phaffii*) is one of two yeast species (the other being *S. cerevisiae*) most commonly used for expression of recombinant proteins (Darby *et al.*, 2012). Cregg *et al.* were the first to develop this yeast species as a DNA transformation host (Cregg *et al.*, 1985; Cereghino *et al.*, 2002). *P. pastoris* has since become a popular choice for production of eukaryotic membrane proteins (Brooks, Morrison and Joanne Lemieux, 2013; Bill, 2014; Ayub *et al.*, 2022). It is often favoured over other expression hosts for its ease-of-use, efficient protein production, ability to culture to high cell densities, higher-eukaryotic protein folding, PTM ability, and lipid composition (Kesidis *et al.*, 2020; Zha *et al.*, 2023).

One study directly compared expression of the same recombinant human soluble proteins in *P. pastoris* and *E. coli*, finding that *P. pastoris* was much more successful at expressing these proteins in a soluble and purifiable form (Lueking *et al.*, 2000). Similar observations have been reported for a number of other proteins from different species (Daly and Hearn, 2005). The first recombinant mammalian membrane protein crystal structures were determined from recombinant proteins produced in yeast, including one produced in *P. pastoris* (Long, Campbell and Mackinnon, 2005). It has since been used to solve a number of high-resolution membrane protein structures (Byrne, 2015).

P. pastoris is a methylotrophic yeast, which allows it to use methanol (MeOH) as a sole carbon source. This is particularly important for its inducible mechanism for recombinant protein expression, the MeOH-inducible alcohol oxidase (*AOX*) promoter, which is commonly used in recombinant DNA constructs (Byrne, 2015). Transformation of *P. pastoris* typically involves linearisation of the recombinant DNA vectors (plasmids), uptake by competent cells, and integration of the recombinant DNA into the host cell genome by homologous recombination (stable transfection). Plasmid vectors typically feature the *AOX1* promoter, allowing

recombination crossover with the *AOX1* promoter in the yeast genome (Karbalaei, Rezaee and Farsiani, 2020). This recombination event can result in multiple copy numbers of the recombinant DNA being integrated.

Some have suggested that an increase in copy number after homologous recombination can result in increased expression of the desired construct, without negative impact on cell growth (Athmaram *et al.*, 2012; Betancur *et al.*, 2017). Studies have demonstrated that, following transformation, these high-expressing clones can be identified by their level of resistance to antibiotics for selective pressure, which is facilitated by genes incorporated into the recombinant DNA vectors. They found that increased resistance to antibiotics was associated with a higher recombinant construct copy number (Scorer *et al.*, 1994; Kumar, Mannil and Mutturi, 2020). However, it is important to note that others have suggested that the correlation between plasmid copy number and recombinant protein expression is not always linear (Aw and Polizzi, 2013).

1.4.2. AQP expression in *P. pastoris*

The first AQP structures were solved using proteins purified from their native expression source. For native sources that were difficult to culture or produced low levels of expression for the desired protein, recombinant protein production has been required. *P. pastoris* has since become the most common choice for recombinant production of AQPs, especially those of eukaryotic origin (Bill and Hedfalk, 2021; Al-Jubair *et al.*, 2022).

The first crystal structure of hAQP4 was determined using protein recombinantly expressed in *P. pastoris* (Ho *et al.*, 2009). The same group recently used *P. pastoris* again for production of hAQP4 for structural determination using cryo-EM. They solubilised AQP4 from *P. pastoris* membranes using detergent for purification, before reconstituting the AQP4 tetramers into MSPs (Gupta *et al.*, 2025). Other studies have also utilised *P. pastoris* for production of AQP4 (Öberg *et al.*, 2011; Kitchen *et al.*, 2020), demonstrating not only a preference of *P. pastoris* as an expression host for human AQPs, but also specifically for human AQP4.

1.5. Extraction and analysis of membrane proteins

In order to purify membrane proteins (MPs) for downstream analysis, they need to be solubilised from the lipid bilayer. This poses a challenge, as it involves extracting them from

their native hydrophobic environment into a hydrophilic solvent. MPs have large hydrophobic domains for stability in the lipid bilayer. Improper extraction of MPs typically results in deformation, degradation, and aggregation, as these proteins are not stable in aqueous solution. Generally, approaches to MP solubilisation consist of using amphipathic molecules that can displace the cell membrane to interact with MPs. The hydrophobic moieties of the amphipathic molecules interact with the MP hydrophobic domains, and the hydrophilic moieties of the amphipathic molecules interact with the hydrophilic solvent. This allows the MPs to become soluble particles for purification and further downstream analysis (Bowie, 2001).

Detergents have traditionally been used for solubilisation of MPs and are still used to a large extent in modern MP research (Seddon, Curnow and Booth, 2004; Lee *et al.*, 2022). These are typically small amphipathic molecules that act to disrupt the cell membrane and form micelles around hydrophobic domains of MPs, forming MP-detergent micelles. Common conventional detergents include *n*-dodecyl-*β*-D-maltoside (DDM), *n*-octyl-*β*-D-glucoside (OG), and *n*-undecyl-*β*-D-maltoside (UDM) (Stetsenko and Guskov, 2017). Many MP extractions and analyses have been performed using a diverse selection of detergents, with DDM being the most commonly used. Detergents have been, and still are, essential for extracting MPs for structural determination with methods such as X-ray crystallography (Choy *et al.*, 2021).

However, detergent solubilisations present with a few issues. Crucially, detergents need to be used above the critical micelle concentration (CMC) in order to form and retain micelles. The CMC needs to be maintained throughout solubilisation and purification to ensure that micelles are maintained around MPs. This is costly in terms of materials, as all buffers required for these processes require a maintained detergent concentration. Detergent-only micelles, a result of maintaining the CMC, can also present issues in downstream analyses. For each MP, detergent type and concentration often needs to be optimised to provide efficient extraction but also prevent MP denaturation. For MPs, detergent solubilisation often means disruption or complete loss of the associated native lipids. For functional and structural analyses this can be detrimental, as the lipid bilayer is often crucial for the function and stability of MPs (van den Brink-van der Laan *et al.*, 2004; Dawaliby *et al.*, 2016; Zoghbi, Cooper and Altenberg, 2016).

Alternative MP stabilisation methods have been developed to mimic the native environment for MPs after detergent solubilisation. Amphiphilic polymers (amphipols) can be introduced after detergent solubilisation to form a wrapping effect around MP hydrophobic regions in place of detergents. These molecules have demonstrated improved stability of MPs over detergent-only solubilisations (Zoonens and Popot, 2014). However, this approach still lacks

an actual lipid environment surrounding the MP. To mimic the native lipid bilayer, MPs can be extracted with detergents, followed by mixing with a selective composition of lipids to form discoidal lipid-MP structures supported by detergents or amphipols (Zhou and Cross, 2013). This principle has been further utilised by the development of membrane scaffold proteins (MSPs). MSPs are amphipathic helical peptides that can be used to encircle a lipid bilayer around MPs after detergent solubilisation. MSP MP-nanodiscs have demonstrated improved stability over detergent-stabilised membrane mimetic methods. They also offer the advantage of tuneability for size and composition (Bayburt, Grinkova and Sligar, 2002; Denisov and Sligar, 2016).

A disadvantage of all of these methods is that they still require detergent solubilisation to remove MPs from their native environment of the cell membrane before any further stabilisation. Stripping the native lipid bilayer has been suggested as a primary cause for the denaturing of native structure and loss of natural activity (Popot, 2010; Zhou and Cross, 2013). The use of MSPs can also prevent the effective use of techniques such as circular dichroism (CD) and nuclear magnetic resonance (NMR) spectroscopy due to interference from the stabilising protein (Jamshad, Grimard, *et al.*, 2015).

1.5.1. Styrene-maleic acid

In 2009, the styrene-maleic acid (SMA) co-polymer (Figure 1.3) was introduced as an effective alternative to detergents for solubilisation of MPs (Knowles *et al.*, 2009). SMA is an amphipathic co-polymer that is able to solubilise MPs directly from their native environment. SMA spontaneously forms SMA-lipid-particles (SMALPs) in the presence of biological membranes. Upon formation of SMALPs, SMA is able to encapsulate MPs with an annulus of native lipid around the protein (MP-SMALPs). Unlike detergents, SMA does not require maintenance of a constant concentration (i.e. detergent CMC) for efficient encapsulation and MP stability after solubilisation. MPs can be solubilised with SMA and easily purified within the MP-SMALP complex, removing the excess SMA required for solubilisation during purification (Lee *et al.*, 2016). SMA is reported as being relatively unselective for lipid type or membrane composition (Juan J. Dominguez Pardo *et al.*, 2017). This makes it applicable for use with a variety of different expression systems (Unger *et al.*, 2021). As the lipid is taken directly from parent membrane, SMALPs can retain features of the membrane environment that are important for native MP stabilisation.

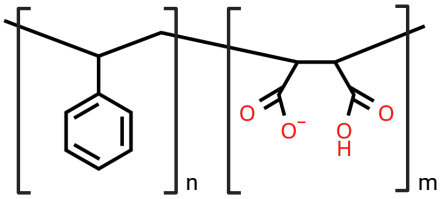

Figure 1.3. Chemical structure of the styrene-maleic acid co-polymer.
SMA of ratio n:m, where the n represents the styrene subunit and m represents the maleic acid subunit. Created using moldraw.com and BioRender.com.

Upon interaction with the lipid membrane, it is believed that the styrene moieties drive insertion of SMA into the lipid bilayer core, consequently resulting in bilayer destabilisation via water filled pores created by the hydrophilic maleic acid moieties. Further membrane disruption results in the formation of nanodiscs stabilised by a belt of SMA around the hydrophobic lipid bilayer core (Figure 1.4). SMA polymers stabilise the lipid bilayer disc via interactions of styrene moieties with the hydrophobic lipid tails. The hydrophilic maleic acid moieties interact with the solvent or lipid head groups via their carboxyl groups to maintain solubility (Jamshad, Grimard, *et al.*, 2015; Scheidelaar *et al.*, 2015; Xue *et al.*, 2018).

Studies have demonstrated that the styrene to maleic acid ratio can influence the solubilisation process and capability to extract membrane proteins, suggesting that SMA co-polymer properties could be optimised for different MPs. SMA 2000 (2:1 styrene : maleic acid) is the most commonly used and most effective SMA ratio for solubilisation (Swainsbury *et al.*, 2014a; Morrison *et al.*, 2016; Scheidelaar *et al.*, 2016; Grethen *et al.*, 2017; Hall *et al.*, 2018). Other commonly used ratio variants exist, such as the more hydrophobic SMA 3000 (3:1 styrene : maleic acid) and SMA 1440 (~1.5:1 styrene : maleic acid). Phase transition behaviour of lipids within 2:1 SMA SMALPs is reportedly more similar to that of the natural membrane when compared to lipids within 3:1 SMA SMALPs (Orwick et al., 2012; Jamshad, Grimard, et al., 2015). This would suggest that 2:1 SMA more accurately represents a native environment for MPs.

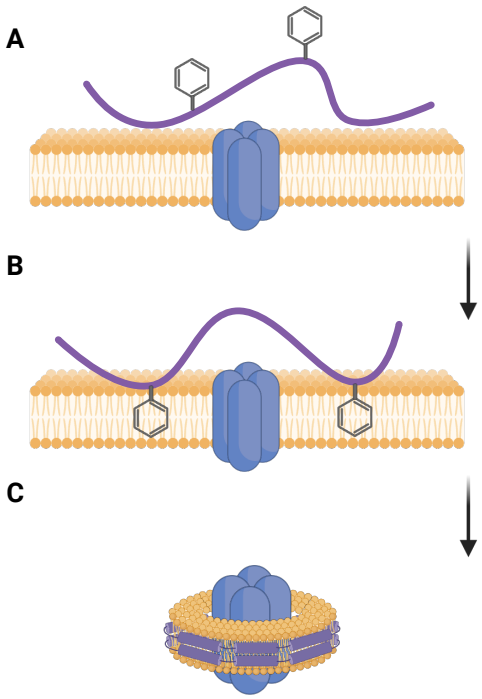

Figure 1.4. Schematic representing the proposed mechanism of MP solubilisation by SMA. **A)** Interaction of SMA polymers with the lipid membrane. **B)** Styrene moieties drive insertion of the polymer into the lipid bilayer core, resulting in membrane destabilisation. **C)** Formation of MP-SMALP nanodiscs. The lipid bilayer is stabilised via interactions of SMA styrene moieties with the lipid tails. The maleic acid moieties maintain hydrophilic solubility. Figure created in BioRender.com.

Lipid-only SMALPs have been reported to be ~10 nm in diameter (Jamshad, Grimard, *et al.*, 2015; Scheidelaar *et al.*, 2015). However, with an MP embedded, it appears that SMA can accommodate larger sizes in order to encapsulate large MPs (Orwick-Rydmark *et al.*, 2012; Long *et al.*, 2013; Swainsbury *et al.*, 2014a; Dörr *et al.*, 2016). SMALPs encapsulating the ~1.2 MDa trimeric photosystem I from *Thermosynechococcus elongatus* (PSI-SMALPs) are reportedly ~35 nm in diameter (Brady *et al.*, 2019, 2021, 2022). This protein was extracted using SMA 1440, demonstrating that tuning the SMA type (composition) used for solubilisation can aid in encapsulating larger MP complexes.

MPs encapsulated in SMALPs have demonstrated increased thermal stability over other solubilisation methods (Jamshad, Charlton, *et al.*, 2015; Gulamhussein *et al.*, 2019). SMALPs have also demonstrated the retention of functional stability for a variety of different MPs, where detergent solubilisations were often inferior (Dörr *et al.*, 2014; Jamshad, Charlton, *et al.*, 2015; Li *et al.*, 2015; Logez *et al.*, 2016; Smirnova *et al.*, 2016; Rehan, Paavilainen and Jaakola,

2017). Through lipidomic analysis, MP-SMALP complexes have also revealed the preference of MPs for certain lipids, due to the retention of native lipids (Dörr *et al.*, 2014; Smirnova *et al.*, 2016; Teo *et al.*, 2019).

The use of SMA is not without its limitations. SMA is generally insoluble below pH 7 and is sensitive to divalent cations. Most commercially available SMA co-polymers (such as SMA2000) have high polydispersity and sequence variation, meaning that there are polymer chains of variable length and with a non-ordered ratio of styrene : maleic acid (Pollock *et al.*, 2018; Gulamhussein *et al.*, 2019). Alternative amphipathic co-polymers have been explored to address these issues. DIBMA (diisobutylene-maleic acid) has a higher tolerance to cations, causes less interference with UV spectroscopy (due to the lack of a styrene moiety), and can form larger lipid nanodiscs, potentially making it more suitable for solubilisation of larger MP complexes (Oluwole *et al.*, 2017; Gulamhussein *et al.*, 2020; Grime *et al.*, 2021). Reversible addition–fragmentation chain transfer (RAFT) polymerisation has also been investigated as a way of producing strictly alternating styrene : maleic acid polymer variants for MP solubilisation (Craig *et al.*, 2016; Akram *et al.*, 2025).

1.5.2. Biophysical characterisation of MP-SMALPs

SMA has been used extensively as a vehicle to analyse MPs using a variety of biophysical techniques, beyond initial characterisation by techniques such as sodium dodecyl-sulphate polyacrylamide gel electrophoresis (SDS-PAGE) and size-exclusion chromatography (SEC). Purified MP-SMALPs can been analysed by native-PAGE (or SMA-PAGE). The establishment of this technique demonstrated that the high negative charge density of SMA could be utilised for electrophoresis (Pollock *et al.*, 2019). Dynamic light scattering (DLS) is often used to analyse MP-SMALPs to give an indication of particle hydrodynamic size and sample heterogeneity. For example, it has been used to compare different co-polymer types for solubilisation of MPs (Hawkins *et al.*, 2021). Sedimentation velocity analytical ultracentrifugation (SV-AUC) can also give an indication of hydrodynamic size, sample heterogeneity, and estimation of MP-SMALP mass. It is often used to assess homogeneity of prepared MP-SMALP samples (Lee *et al.*, 2016, 2019; Cioccolo *et al.*, 2024).

Small-angle X-ray scattering (SAXS) have been used previously to characterise MP-SMALPs (Brady, Qian and Bruce, 2019; Lee *et al.*, 2019; Pollock *et al.*, 2022). SAXS can provide information on particle size and shape, protein flexibility, morphological dispersity and low-resolution structural data. CD can provide detail on protein backbone conformation, such as quantitative data on the presence of α-helices and β-sheets. CD shows good compatibility with

MP-SMALPs, as demonstrated by data on secondary structures of MPs within SMALPs (Knowles *et al.*, 2009; Dörr *et al.*, 2014; Jamshad, Charlton, *et al.*, 2015).

Cryo-EM of has been very successful for analysis of MP-SMALPs. Multiple studies have demonstrated the applicability of this techniques to determine high-resolution protein structures in the 3-4 Å range (Qiu *et al.*, 2018; Sun *et al.*, 2018; Tascón *et al.*, 2020; Yoder and Gouaux, 2020; Yu *et al.*, 2021). One structure for an SMA extracted MP has, thus far, been solved by X-ray crystallography. This involved extraction and purification with SMA, and transfer into the lipid cubic phase for crystallisation. They were able to resolve a 2 Å structure of bacterial rhodopsin that was comparable to that determined from detergent solubilisation (Broecker, Eger and Ernst, 2017). However, this is the only current example of an X-ray crystal structure for a SMALP purified protein, and doesn't necessarily demonstrate the structure of an MP within a SMALP.

Native mass spectrometry (native-MS) (specifically, laser induced liquid bead ion desorption MS; LILBID-MS) has been used to analyse SMALPs for determination of mass (Hellwig *et al.*, 2018; Cioccolo *et al.*, 2024). For example, a rhomboid protease SMALP (GlpG-SMALP) was analysed by LILBID-MS to find a broad peak corresponding to ~72 kDa. Increasing the LILBID laser power disrupted the SMALPs and released the monomeric GlpG, revealing a molecular weight (MW) peak of 34.5 kDa. This group performed similar analyses on KtrB (a subunit of the bacterial potassium channel, KtrAB) -SMALPs and AcrB (part of the bacterial AcrAB-TolC efflux pump) -SMALPs (Hellwig *et al.*, 2018).

Despite the success of the techniques discussed, MP-SMALPs can still be difficult to characterise biophysically, especially in terms of estimating an accurate mass. This is mainly because MP-SMALPs have an inherent heterogeneity of different molecules, as they contain protein, lipids, and the SMA co-polymer.

1.5.3. Mass photometry

Mass photometry is a novel technique for mass measurement of biomolecules (or bioparticles) based on interferometric scattering microscopy (iSCAT) (Ginsberg *et al.*, 2025). It allows mass measurement of unlabelled single molecules in solution (Young *et al.*, 2018; Sonn-Segev *et al.*, 2020). Mass photometry has been used to estimate molecule mass of various biomolecule types (Asor and Kukura, 2022), assess sample heterogeneity (Sonn-Segev *et al.*, 2020), investigate sample oligomerisation (Balakrishnan *et al.*, 2024), and quantify biomolecule interactions (Soltermann *et al.*, 2020; Wu and Piszczek, 2020).

In basic principle, a laser directs light through a binding surface (glass slide) at a sample in solution. Light is reflected by the glass slide and scattered by molecules binding to the glass surface (Figure 1.5.A). This scattering happens due to these molecules displacing water at the binding interface, changing the local refractive index. The interference signal between reflected light and scattered light is measured and quantified as a contrast value (interferometric contrast). Molecules of different sizes cause a different degree of light scattering, and thus, different measured contrast values. Ratiometric imaging over time is used to determine contrast measurements for individual binding events over the static scattering background (Figure 1.5.B). This involves calculating a moving average and dividing current imaging frames by previous frame averages, removing the background noise. A histogram of binding events over the recorded time can be plotted against the measured contrast for each binding event (Figure 1.5.C). The mass of a protein molecule scales linearly with its measured interferometric contrast, regardless of its structural shape (Young *et al.*, 2018). Therefore, by calibrating to contrast values of standards of known masses, the mass of unknown samples can be estimated (Figure 1.5.D).

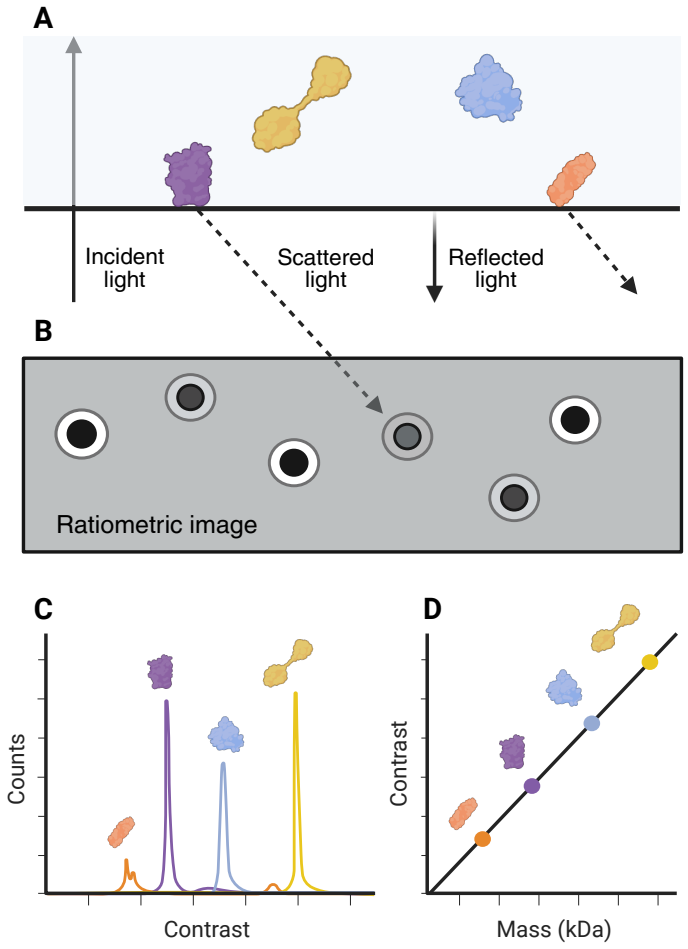

Figure 1.5. Principle of mass photometry.
A) A laser (incident light) directs light through a binding surface (glass slide) at a sample in solution. Light is reflected by the glass slide and scattered by binding molecules. **B)** The interference between reflected and scattered light is measured and visualised via ratiometric imaging as contrast “spots" (indicated by blank dots with a white outline). **C)** Interferometric contrast is quantified and plotted as histograms against the number of counts (binding events). **D)** The mass of a protein molecule scales linearly with its measured interferometric contrast. Figure created in BioRender.com.

Mass photometry has a limited mass range, from ~30 kDa to ~5 MDa, which makes it unsuitable for the study of small molecules or small molecule interactions. Another key limitation of mass photometry is that it relies on samples of low concentration and low heterogeneity. A high concentration or high heterogeneity will create a saturation of overlapping binding events, lowering the resolution of measured contrast. Therefore, mass photometry is generally not applicable for studying low affinity interactions or samples of poor purity (Kratochvíl *et al.*, 2024; Asor *et al.*, 2025).

For mass photometry analysis of MPs, this presents an advantage of using SMA over detergents. Detergent samples typically have a high concentration of micelles, due to the necessity of maintaining detergent concentrations above the CMC. This can create imaging over-saturation, making it very difficult to detect binding events for the protein of interest. MPs solubilised in detergent can be diluted away from detergent for analysis, but this can result in immediate deformation and aggregation. By comparison, SMA solubilisation creates individually stable particles, with excess SMA typically being removed during MP-SMALP purification. Mass photometry has previously shown promise with analysis of MPs, estimating mass and determining heterogeneity of MPs in various membrane mimetic complexes, including MP-SMALPs (Olerinyova *et al.*, 2021; Young *et al.*, 2024). For example, Olerinyova *et al.* used SMA to solubilise and purify the KcsA potassium channel tetramer expressed in *E. coli*. Mass photometry analysis revealed that the predominant KcsA-SMALP size observed was likely to contain a dimer of KcsA homo-tetramers, based on estimated protein-to-lipid ratios. Mass photometry has also been used for tracking membrane associated proteins on supported lipid bilayers (Foley *et al.*, 2021).

For mass photometry analysis of MP-SMALPs and other membrane mimetic complexes, it is important to consider that calibration would most likely be performed with soluble protein standards. Soluble protein calibrants don't represent the heterogenous complexity of particles such as MP-SMALPs, that contain a combination of protein, lipids, and SMA. The light scattering properties of MP-SMALP complexes could vary from that of soluble proteins, which could result in inaccurate mass estimates for the whole particle.

1.6. Project aim and objectives

Although AQP4 structure has been well characterised after detergent solubilisation (Ho *et al.*, 2009; Gupta *et al.*, 2025), it has not been investigated in a purified form with a native annulus of lipid. The loss of these associated lipids with detergent solubilisation may have an impact on the observed structure. Palmitoylation state of M1 AQP4 appears to play a key role in OAP prevention (Suzuki *et al.*, 2008; Carder *et al.*, 2024). The native lipid may have an influence on association of the M1 isoform N-terminus to the lipid membrane, preventing tetramer association. An expression system and purification strategy that allows purification of AQP4 tetramers and higher-order oligomers, within a native annulus of lipid, could be crucial for investigating these molecular interactions.

Many questions also remain about the exact physiological roles of AQP4 OAPs and the influence of NMO Ab binding on their dynamics (Nagelhus and Ottersen, 2013; Verkman *et al.*, 2013; Salman *et al.*, 2022). A model system with accessible manipulation strategies would be incredibly valuable for investigating AQP4 tetramers and OAPs in the context of NMOSD.

Therefore, the aim of this project was to determine if AQP4 tetramers and higher-order oligomers (OAPs) could be captured and characterised in SMALPs from the *P. pastoris* membrane. This could be the basis for a future model in understanding AQP4 oligomerisation in the context of NMOSD.

This project therefore had four main objectives:

- Express and purify comparable yields of M1 and M23 AQP4 isoforms from *P. pastoris*.
- Characterise the AQP4-SMALPs using mass photometry amongst other biophysical techniques, whilst assessing the ability of these various techniques to estimate AQP4-SMALP mass.
- Probe purified AQP4-SMALPs with NMO Abs to determine if key binding epitopes are retained.
- Determine if *P. pastoris* allows formation of OAPs in the *P. pastoris* membrane, similar to mammalian expression systems, and investigate whether OAP regulation in *P. pastoris* is governed by palmitoylation.

2. Methods and Materials

2.1. Antibodies

Table 2.1. Antibodies (Abs) used for this project.
Table shows Abs used for immunoblotting and mass photometry assays.

Antibody	Supplier
Rabbit mAb anti-AQP4 IgG	Abcam (ab128906)
Rabbit mAb anti-AQP4 IgG	Cell Signalling Technology (CST; #59678)
Rabbit pAb anti-GFP IgG	Abcam (ab6556)
Mouse mAb anti-6×His IgG	Takara Bio (631212)
Mouse mAb anti-6×His IgG	Invitrogen (MA1-21315)
Human NMO Ab F3	University of Oxford
Human NMO Ab D3	University of Oxford
Human NMO Ab F2	University of Oxford
HRP-linked Ab anti-rabbit IgG	Cell Signalling Technology (CST; #7074)
HRP-linked Ab anti-mouse IgG	Cell Signalling Technology (CST; #7076)
HRP-linked Ab anti-human IgG	Cell Signalling Technology (CST; #32935)

NMO Abs were kindly provided by Professor Sarosh R Irani's research group, Nuffield Department of Clinical Neurosciences, University of Oxford. They were prepared as described by Damato *et al.*, 2022, and Sun *et al.*, 2025. The Abs are identified as F3, D3, and F2, referring to well numbers in which cells were cultured and identified for production of AQP4 (NMO) IgGs.

2.2. Plasmid constructs and *P. pastoris* clones

Genes encoding hAQP4 isoforms M1 and M23 had been previously cloned into pPICZ plasmid vectors by our research group. The resultant protein constructs included a recombinant 6× His-tag on the AQP4 C-terminus. Both plasmid constructs had been transfected into the *E. coli* DH10B strain and stored as glycerol stocks (-80 °C). The M1 AQP4 plasmid construct had been transformed into the GS115 strain of *P. pastoris* and established for expression and purification of M1 AQP4 by Drs Phil Kitchen and Lucas Unger of our research group. The M23 AQP4 plasmid construct had been transformed into the X33 strain of *P. pastoris*, but this clone had not yet been characterised. An adenosine A_{2A} receptor ($A_{2A}R$) *P. pastoris* clone was also available in our library. This clone was optimised for expression and purification of $A_{2A}R$ by Dr Zharain Bawa (Bawa, 2014).

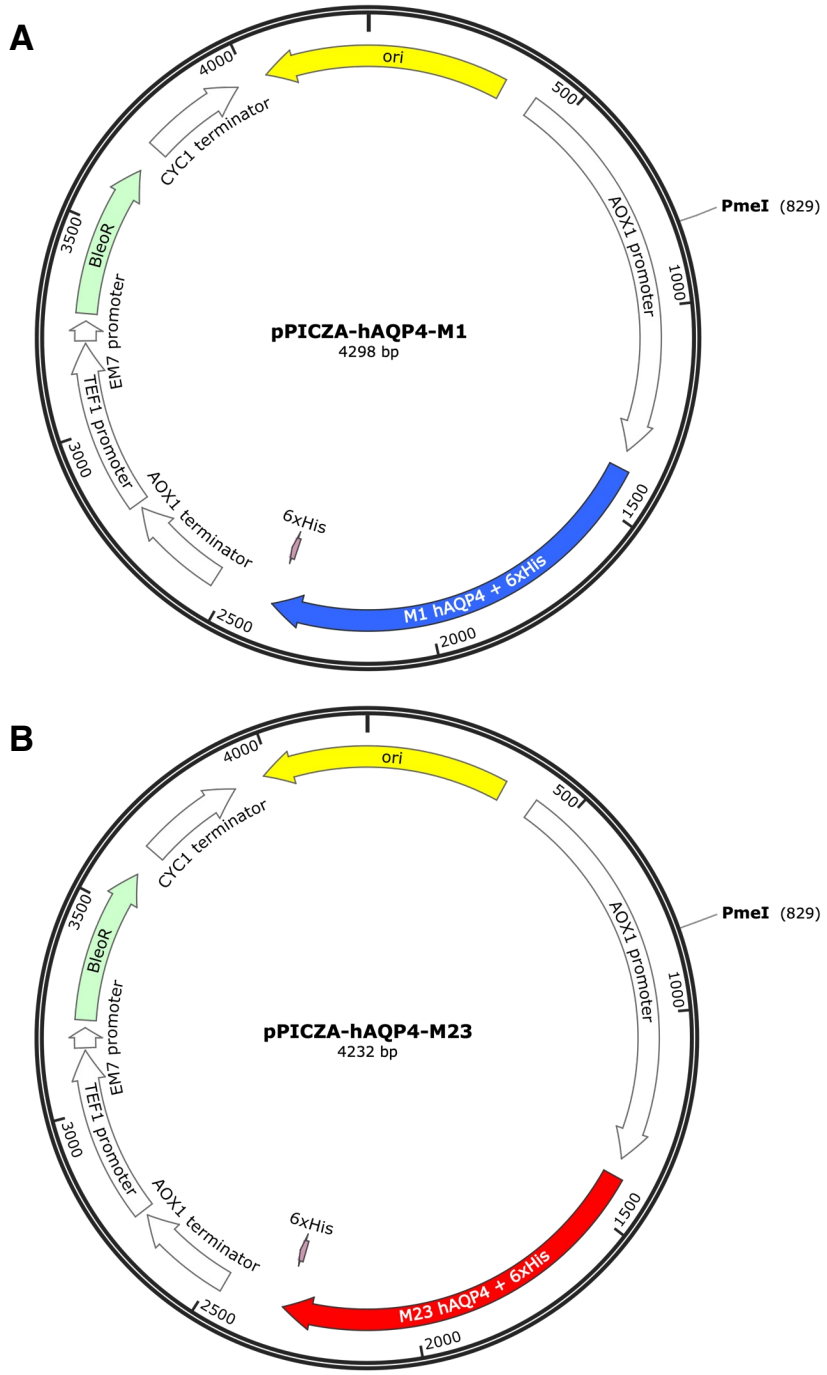

Figure 2.1. pPICZ plasmid expression vectors for recombinant expression of hAQP4.
Plasmid construct maps of M1 (**A**) and M23 (**B**) hAQP4 isoforms cloned into pPICZA plasmids for recombinant expression of hAQP4 in *P. pastoris*. Features clockwise from the plasmid origin: origin of replication, MeOH inducible *AOX1* promotor, human M1/M23 *AQP4* genes cloned into the plasmid multiple cloning site also containing the sequence encoding a recombinant 6× His-tag, *AOX1* terminator region, the *TEF1* and *EM7* promoter regions, the Sh *ble (BleoR)* gene for zeocin resistance, and the *CYC1* terminator region. The restriction site for the PmeI restriction enzyme is also shown. Both the M1 and M23 AQP4 plasmid constructs were sequenced by PlasmidsNG (Birmingham, UK). Plasmid maps were generated in SnapGene software (www.snapgene.com).

2.3. Plasmid preparation and *P. pastoris* transformation

2.3.1. Plasmid amplification and purification

Glycerol stocks of *E. coli* DH10B transfected with the recombinant pPICZ-hAQP4-M23 plasmid were streaked onto plates of lysogeny broth (LB) agar (20 g/L LB low salt powder (Sigma-Aldrich), 15 g/L agar) supplemented with 100 µg/mL zeocin (Gibco, Thermo Fisher Scientific). Plates were incubated for 24 h at 37 °C. Single colonies were picked and used to inoculate starter cultures of 5 mL LB medium (20 g/L LB low salt powder (Sigma-Aldrich)) supplemented with 100 µg/mL zeocin in 50 mL conical centrifuge tubes. Starter cultures were grown for 6 h (37 °C, 220 rpm). The 5 mL starter culture was then used to inoculate 200 mL of fresh LB medium supplemented with 100 µg/mL zeocin in a 2L round-bottom flask, and this culture was incubated overnight (37 °C, 220 rpm). Cells were harvested by centrifugation (4,000 × g, 10 min, RT).

Plasmids were purified using a plasmid maxiprep kit (PureLink HiPure, Invitrogen). HiPure Maxi columns were equilibrated with 30 mL equilibration buffer. *E. coli* cell pellets from 200 mL of culture were resuspended in 10 mL resuspension buffer with RNase A. 10 mL lysis buffer was added and incubated for 5 min at RT. 10 mL precipitation buffer was added and the mixture was centrifuged (4,000 × g, 10 min, RT). The supernatant was loaded onto the equilibrated HiPure Maxi column, and the column was washed with 60 mL wash buffer. Plasmid DNA was then eluted with 15 mL elution buffer. To precipitate the DNA, 10.5 mL 100% isopropanol was added to the elution and the mixture was centrifuged (4,000 × g, 30 min, 4 °C). The DNA pellet was resuspended in 5 mL 70% EtOH and centrifuged (4,000 × g, 10 min, 4 °C). The DNA pellet was then air-dried (~15 min) and resuspended in 250 µL TE Buffer. DNA concentration was estimated using a NanoDrop 2000c Spectrophotometer (Thermo Scientific) and the plasmid was stored at -20 °C.

2.3.2. Chemical transformation of *P. pastoris*

Chemical transformation of *P. pastoris* with LiCl was performed using an adapted protocol from Kumar, Mannil and Mutturi, 2020 (Kumar, Mannil and Mutturi, 2020).

2.3.2.1. Plasmid linearisation

Purified plasmid DNA was linearised using PmeI with rCutSmart buffer (R0560, New England Biolabs) targeting the plasmid *Pme*I restriction site. Per 10 µg of plasmid, 50 units of PmeI were used for the linearisation reaction. A non-linearisation control reaction was also performed without PmeI (plasmid DNA and rCutSmart buffer only). Linearisation reactions were done in a thermal cycler (MultiGene OptiMax, Labnet) – linearisation reaction (1 h, 37 °C), followed by inactivation (20 min, 65 °C). Linearised plasmid DNA was stored at 4 °C until use for the transformation procedure.

For further purification of linearised plasmid DNA, an adapted protocol for a gel-extraction kit was used (QIAquick Gel Extraction Kit, Qiagen). 150 µL Buffer QG (pH ≤ 7.5) was added to 50 µL of linearised plasmid DNA (equal to 10 µg). 50 µL of 100% isopropanol was then added to the sample and mixed. Samples were added to QIAquick spin columns and centrifuged for 1 min (18,000 × g, 4 °C). The column was washed with 750 µL of Buffer PE and further centrifugation (1 min, 18,000 × g, 4 °C). Bound DNA was eluted with 50 µL of Buffer EB (10 mM Tris-HCl, pH 8.5) by incubating the spin column for 1 min, followed by centrifugation (1 min, 18,000 × g, 4 °C). The linearised and purified plasmid DNA was stored at 4 °C until use for the transformation procedure.

2.3.2.2. LiCl transformation of *P. pastoris*

Wild-type (WT) *P. pastoris* (GS115 strain) was streaked from glycerol stocks onto YPD agar plates (no antibiotic) and incubated to develop single colonies (Section 2.4.1). Single colonies were used to inoculate 5 mL YPD medium (20 g/L peptone, 10g g/L yeast extract, 20 g/L dextrose) in 50 mL conical centrifuge tubes and this was incubated overnight (30 °C, 200 rpm). The overnight cultures were resuspended to optical density (OD_{600}) = 0.1 in 50 mL fresh YPD medium in 500 mL shake flasks. This culture was incubated (30 °C, 200 rpm) and grown to OD_{600} in the range of 0.8 – 1.0 (approx. 5 – 7 h). The cell pellet was harvested by centrifugation (1,500 × g, 10 min, RT) and washed 3 times with sterile dH_2O by resuspension and further centrifugation. Cell pellets were then washed and resuspended in 1 mL 1 M LiCl and incubated for 1h (30 °C, gentle mixing) to generate competent cells. Cells were then centrifuged (1,500 × g, 10 min, RT) and resuspended in 400 µL of 1 M LiCl. 50 µL of this resuspension were used per transformation condition. Per 50 µL resuspension, cells were pelleted (1,500 × g, 10 min, RT), and the following was added to the obtained pellets: 240 µL of 50% w/v polyethylene glycol (MW 3015-3685); 36 µL of 1 M LiCl; 25 µL of 2 mg/mL boiled salmon-sperm DNA; and

50 µL (equal to 10 µg) of plasmid DNA. The mixture was vortexed and incubated for 30 min (30 °C, gentle mixing). After incubation, the transformation cultures were heat shocked (30 min, 42 °C). Cells were pelleted (4000 × g, 10 min, RT) and resuspended in 1 mL YPD medium. YPD transformation cultures were then incubated for 2 – 4 h (30 °C, 200 rpm). 100 µL of the YPD cultures were spread onto YPD agar plates supplemented with 100 µg/mL zeocin (Gibco, Thermo Fisher Scientific). Cultures were also streaked onto control YPD agar plates containing no antibiotic to confirm cell survival. Plates were incubated for ~4 days at 30 °C to develop colonies. Colonies from plates with zeocin selective pressure were picked at random and made into glycerol stocks (Section 2.4.2). Prior to freezing, glycerol stocks were streaked onto YPD agar plates supplemented with 500 µg/mL zeocin for initial expression screening of the recombinant plasmid.

2.4. *P. pastoris* cell culture

2.4.1. Growth of *P. pastoris* on YPD agar plates

YPD agar (20 g/L peptone, 10g g/L yeast extract, 20 g/L dextrose, 15 g/L agar) plates were streaked with *P. pastoris* glycerol stocks of the desired clone. Plates were typically incubated for ~3 days at 30 °C to develop single colonies.

For growth of *P. pastoris* clones transformed with recombinant plasmids carrying the *BeoR* gene, YPD agar was supplemented with 100 µg/mL of zeocin (Gibco, Thermo Fisher Scientific), unless stated otherwise.

2.4.1.1. Plate colony counting

YPD agar plate colonies were counted using ImageJ (Fiji). Image area was cropped to the plate (excluding the plate edges). The threshold was adjusted to highlight the colonies and watershed was applied. Analyse Particles was used to provide a colony count. Circularity was adjusted to avoid background objects and particle size was adjusted to fit the smallest colonies without introducing background noise.

2.4.2. *P. pastoris* glycerol stock preparation

Glycerol stocks were prepared for long-term storage of *P. pastoris* clones transformed with recombinant pPICZ plasmids carrying the *BleoR* gene for zeocin resistance.

Single *P. pastoris* colonies were picked from YPD agar plates and grown in 5 mL YPD medium (20 g/L peptone, 10 g/L yeast extract, 20 g/L dextrose) supplemented with 100 µg/mL zeocin. Cultures were incubated overnight (~16 h, 30 °C, 200 rpm). 500 µL of the overnight YPD cultures was mixed with 500 µL of 30% v/v sterile glycerol in cryovials. Glycerol stocks were stored at -80 °C.

2.4.3. Small-scale growth and induction of *P. pastoris*

Starter cultures were prepared in 50 mL conical centrifuge tubes containing 5 mL buffered glycerol-complex medium (BMGY; 20 g/L peptone, 10 g/L yeast extract, 100 mM potassium phosphate buffer pH 6, 6.7 g/L yeast nitrogen base, 0.4 mg/L biotin, 0.5% v/v glycerol) supplemented with 100 µg/mL zeocin (Gibco, Thermo Fisher Scientific). For each starter culture, the medium was inoculated with a single colony of the desired *P. pastoris* clone picked from a YPD agar plate. Starter cultures were incubated for 24 h (30 °C, 200 rpm), followed by resuspension at OD_{600} = 1 in 5 mL buffered methanol-complex medium (BMMY; 20 g/L peptone, 10 g/L yeast extract, 100 mM potassium phosphate buffer pH 6, 6.7 g/L yeast nitrogen base, 0.4 mg/L biotin, 0.5% v/v MeOH) in 50 mL conical centrifuge tubes. BMMY cultures were incubated for 48 h (30 °C, 200 rpm) with supplementation of 1% v/v MeOH at the midpoint (after 24 h). Cells were harvested by centrifugation (4,000 × g, 10 min). Cell pellets were either stored at -80 °C or resuspended and broken immediately.

Small-scale cultures were also prepared as 25 mL cultures. In this case, starter cultures were prepared as described, followed by resuspension at OD_{600} = 1 in 25 mL BMMY medium in 250 mL baffled shake flasks. Other culture conditions and cell harvesting remained the same.

2.4.4. Large-scale growth and induction of *P. pastoris* in shake flasks

Starter cultures were prepared in 500 mL baffled shake flasks containing 50 mL BMGY medium (20 g/L peptone, 10 g/L yeast extract, 100 mM potassium phosphate buffer pH 6, 6.7 g/L yeast nitrogen base, 0.4 mg/L biotin, 0.5% v/v glycerol) supplemented with 100 µg/mL zeocin (Gibco, Thermo Fisher Scientific). For each starter culture, the medium was inoculated with a single colony of the desired *P. pastoris* clone picked from a YPD agar plate. Starter cultures were incubated for 24 h (30 °C, 200 rpm). 5 mL of the starter culture was then used to inoculate 250 mL BMGY medium in a 2.5 L shake-flask and this was incubated for 24 h (30 °C, 200 rpm). This culture was then resuspended at OD_{600} = 1 in 250 mL BMMY medium (20

g/L peptone, 10 g/L yeast extract, 100 mM potassium phosphate buffer pH 6, 6.7 g/L yeast nitrogen base, 0.4 mg/L biotin, 0.5% v/v MeOH) in 2.5 L baffled shake flasks. At this stage, cultures were scaled up to the volume required by using multiple flasks of 250 mL BMMY medium. BMMY cultures were incubated for 48 h (30 °C, 200 rpm) with supplementation of 1% v/v MeOH at the midpoint (after 24 h). Cells were harvested by centrifugation (4,000 × g, 20 min). Cell pellets were either stored at -80 °C or resuspended and broken immediately.

2.4.5. Large-scale growth and induction of *P. pastoris* in bioreactors

2 L bioreactor vessels (Applikon) were used for *P. pastoris* cultures. The Applikon ez-Control controller was used to automatically monitor and adjust culture conditions. Temperature was measured using the controller thermometer probe. pH was measured using an AppliSens pH probe. Dissolved oxygen (DO) was measured using an Applisens dO_2 probe. Off-gasses were measured using a GasX GXA gas analyser. OD was measured with a Buglab BE 2100 biomass monitor. The Lucullus PIMS (3.7.2) data logger software was used to monitor culture conditions and create bioreactor profiles. Bioreactor profiles were exported from the Lucullus software and additional culture phase annotations were added manually.

2.4.5.1. Bioreactor vessel setup and equilibration

2 L bioreactor vessels were set up with: tubing with a 0.2 µm filter for the gas inlet; an autoclavable pH probe, calibrated prior to setup; an autoclavable DO probe (and polarising unit for autoclaving); a condenser and output tubing with a 0.2 µm filter for the gas analyser; feeding tubes for acid, base, and glycerol / MeOH; and an injection port. A sampling bottle and tubing were also attached to the vessel sampling port. After autoclave sterilisation, 1 L BMGY medium (20 g/L peptone, 10 g/L yeast extract, 100 mM potassium phosphate buffer pH 6, 6.7 g/L yeast nitrogen base, 0.4 mg/L biotin, 0.5% v/v glycerol) was funnelled into the vessel. A temperature probe was inserted into the vessel thermowell, and the controller was set to maintain temperature at 30 °C using a circulating water jacket. Acid (50% phosphoric acid) and base (28% ammonium hydroxide) lines were connected to the vessel through the controller peristaltic pumps. Stirrer speed was set to 700 rpm and gas flow (air) was set to 1.5 L/min. The controller was then set to maintain pH 6. A biomass monitor was attached to the outside of the vessel and OD was set to baseline (OD_{600} = 0). BMGY medium was supplemented with 50 µg/mL chloramphenicol (via the vessel injection port) to prevent contamination prior to inoculation. The vessel was allowed to equilibrate (~ 3 h) before

calibrating the DO sensor to 100%. The controller was set to maintain DO above 30% by adjusting gas flow and stirrer speed.

2.4.5.2. Inoculation, growth and induction

Starter cultures were prepared in 500 mL baffled shake flasks containing 50 mL BMGY medium supplemented with 100 µg/mL zeocin (Gibco, Thermo Fisher Scientific). Medium was inoculated with a single colony of the desired *P. pastoris* clone picked from a YPD agar plate. Starter cultures were incubated for 24 h (30 °C, 200 rpm). 3 mL of the starter culture was then used to inoculate the bioreactor BMGY medium through the injection port. 1 mL of antifoam (Antifoam C emulsion, Sigma-Aldrich) was added to the vessel via the injection port alongside inoculation. After batch phase glycerol from the starting medium had been used up (indicated by a small DO spike), a glycerol fed-batch (50% v/v glycerol, 6.7 g/L yeast nitrogen base) was provided at 14 mL L^{-1} h^{-1} for 4 h via peristaltic pump. Cultures were then grown and starved until all fed-batch phase glycerol had been used up (indicated by a large DO spike). Cultures were then induced by MeOH feed (50% v/v MeOH) provided at 4.8 mL L^{-1} h^{-1} for 48 h via peristaltic pump. During growth and induction, 500 µL injections of antifoam were added if the culture foam level was approaching the top of the vessel. After 48 h induction, cells were harvested by centrifugation (4,000 × g, 20 min, 4 °C). Cell pellets were either stored at -80 °C or resuspended and broken immediately.

For the induction phase of the $A_{2A}R$ *P. pastoris* clone, 2% v/v DMSO was added (via the injection port) and vessel temperature was lowered to 22 °C.

2.4.6. Light microscopy of *P. pastoris* cultures

If required, *P. pastoris* cultures were diluted. 5 µL of live culture was placed onto clean 76 x 26 mm (1 mm thick) glass slides and covered with 22 × 22 mm coverslips (#1.5). Slides were observed by phase contrast light microscopy at 20× magnification using the Invitrogen EVOS M5000 microscope. Coverslips were discarded and slides were cleaned with 70% EtOH and dH_2O.

2.5. Cell disruption and membrane fragment preparation

2.5.1. *P. pastoris* cell disruption by glass bead homogenisation

The Qiagen TissueLyser LT was used for cell disruption of *P. pastoris* cells from small-scale growth methods.

Cell pellets from 5 mL of small-scale cultures (Section 2.4.3) were washed by resuspending in dH_2O and centrifugation (4,000 × g, 10 min, 4 °C) to pellet the cells. Unless specified otherwise in results, cell pellets from 5 mL cultures were resuspended in 5 mL cold dH_2O. Cell resuspensions were mixed 1:1 with 212–300 µm glass beads (Sigma-Aldrich) in 1.5 mL microcentrifuge tubes (typically 100 µL resuspended cells to 100 µL glass beads) with protease inhibitor (cOmplete cocktail tablets, Roche). The TissueLyser sample holder was pre-cooled at -20 °C prior to breaking. Cells were broken with 1 min in the bead mill at 50 Hz, followed by 1 min rest on ice. This was repeated 5 times for a total of 5 minutes of cell breaking. Lysates were centrifuged (18,000 × g, 10 min, 4 °C) to separate glass beads and unbroken material, and the supernatant was collected. Lysates were either analysed immediately or frozen (-20 °C).

For lysates to be immediately analysed by SDS-PAGE and western blot, the lysates were incubated with Laemmli buffer (2% w/v SDS, 5% v/v βME, 50 mM Tris-HCl pH 6.8, 10% v/v glycerol, 0.005% w/v bromophenol blue) for 10 min at RT prior to centrifugation.

2.5.2. *P. pastoris* cell disruption by high-pressure homogenisation

The Avestin EmulsiFlex-C3 was used for cell disruption of *P. pastoris* cells from large-scale growth methods (Section 2.4.4 and 2.4.5)

Cell pellets (defrosted at 4 °C if frozen at -80 °C) were resuspended at 0.33 g/mL in cold breaking buffer (2 mM EDTA, 100 mM NaCl, 50 mM potassium phosphate buffer pH 7.4, 5% v/v glycerol, protease inhibitor (cOmplete cocktail tablets, Roche)) and cell resuspensions were kept on ice. The EmulsiFlex-C3 was cooled via water/ice bath with peristaltic pump and the lysate output chamber wrapped in ice. The system was equilibrated with cold breaking buffer before adding resuspended cells. Cells were pumped through the system for five cycles with 25,000 psi homogenising pressure. Lysates were centrifuged (4,000 × g, 10 min, 4 °C) to remove unbroken cells and debris. The lysate supernatant was collected and stored on ice for

membrane fragment preparation. 100 µL aliquots were incubated with Laemmli buffer (10 min, RT) for SDS-PAGE and western blotting. SDS-PAGE samples were stored at -20 °C.

2.5.3. *P. pastoris* membrane fragment preparation

P. pastoris lysates from high-pressure homogenisation (Section 2.5.2) were used for membrane fragment preparation. Membrane fragments were separated from the lysates by ultracentrifugation (150,000 × g, 90 min, 4 °C). The supernatant was separated, and the pellet (membrane fragment) was resuspended in membrane resuspension buffer (20 mM Tris pH 8.0, 20 mM NaCl, 10% v/v glycerol) at a concentration of 180 mg/mL, without protease inhibitor. Membrane pellets were homogenised using a handheld Fisherband glass vessel and PTFE tissue grinder. The resuspended membranes were stored at -80 °C or used immediately for membrane protein (MP) solubilisation and purification. Smaller aliquots of the resuspended membranes were also collected and stored for solubilisation trials or incubation with Laemmli buffer (10 min, RT) for SDS-PAGE and western blotting. Laemmli buffer samples were stored at -20 °C.

2.6. Membrane protein (MP) solubilisation and purification

2.6.1. SMA preparation

Styrene-maleic acid copolymer (SMA) was synthesised from styrene-maleic anhydride (SMAnh; SMA2000, ca. 2:1 mole ratio styrene:maleic anhydride, Cray Valley) by hydrolysis using the autoclave method, as previously described (Rothnie, 2016; Kopf *et al.*, 2019; Broadbent *et al.*, 2022).

25 g SMAnh powder was dissolved into 250 mL of 1 M NaOH. The solution was autoclaved (15 min, 121 °C) 3 times, being allowed to cool between each autoclave cycle. SMA was precipitated by addition of ~50 mL concentrated HCl. The precipitated SMA was washed 3 times with dH_2O by centrifugation (3000 × g, 10 min, RT) and resuspension. The SMA precipitate was then dissolved in 250 mL 0.6 M NaOH and pH corrected to pH 8. The polymer solution was transferred to round-bottom flasks, frozen (-20 °C), and freeze-dried to form SMA powder.

2.6.2. SMA solubilisation of *P. pastoris* membranes

Unless stated otherwise, 1.8 g membranes were typically used for SMA solubilisation and purification (equal to 10 mL of membranes at 180 mg/mL). SMA was dissolved in purification buffer (300 mM NaCl, 20 mM Tris-HCl pH 8.0) at a concentration of 3.33% w/v to prepare solubilisation buffer. Solubilisation buffer was mixed 3:1 with resuspended *P. pastoris* membranes (Section 2.5.3) at a concentration of 180 mg/mL (defrosted at 4 °C if stored at -80 °C), without protease inhibitor. This gave a final SMA concentration of 2.5% w/v and final membrane concentration of 45 mg/mL. The solubilisation was incubated for 1 h (RT, rolling). The insoluble fraction was separated by ultracentrifugation (100,000 × g, 45 min, 4 °C) and the soluble fraction collected for purification of MP-SMALPs.

For analysis of soluble and insoluble fractions, the insoluble fraction was resuspended in a volume of purification buffer equal to the total solubilisation volume. Insoluble pellets were homogenised using a tissue grinder. Soluble and insoluble fractions were incubated with Laemmli buffer (2% w/v SDS, 5% v/v βME, 50 mM Tris-HCl pH 6.8, 10% v/v glycerol, 0.005% w/v bromophenol blue) for 10 min at RT. Laemmli buffer samples were stored at -20 °C.

2.6.3. IMAC purification of MP-SMALPs

Immobilised metal affinity chromatography (IMAC) purifications of SMA solubilised MPs from *P. pastoris* membranes were performed using Ni-NTA agarose resin (Qiagen) targeting the recombinant MP 6× His-tags.

Ni-NTA agarose resin was washed with dH_2O and equilibrated with purification buffer (300 mM NaCl, 20 mM Tris-HCl pH 8.0) via centrifugation (500 rpm, 10 min, 4 °C) and resuspension. Typically, 1 mL of agarose resin (2 mL of resin slurry) was used per 20 mL of sample to be purified. Equilibrated Ni-NTA resin was mixed with the soluble fraction obtained from SMA solubilisation of *P. pastoris* membranes (Section 2.6.2). This mixture was supplemented with 5 mM imidazole to prevent non-specific binding. Resin was incubated with the SMA-membrane soluble fraction overnight (rolling, 4 °C).

Imidazole buffers for resin washing and elution were all prepared in purification buffer without protease inhibitor. Gravity-flow columns were equilibrated with purification buffer prior to use. The resin/sample mixture was poured through the gravity-flow column, and a sample of the flowthrough (FT) was collected. The resin was washed with 50× resin bed-volumes of a low imidazole concentration buffer, followed by 50× resin bed-volumes of a slightly higher imidazole concentration buffer. Samples of the imidazole washes were collected for the first and second resin bed-volumes. The bound proteins were eluted in 12× resin bed-volumes

using a high imidazole concentration buffer. The elution was collected in 0.5× resin bed-volume fractions (for the first 3 resin bed-volumes) for individual analysis by SDS-PAGE, or as one large fraction. Eluted fractions were concentrated using centrifugal concentrators (Vivaspin, Sartorius) with a specified MW cut-off filter.

For purification of AQP4-SMALPs, the resin was washed with 25 mM imidazole, followed by a wash of 75 mM imidazole. Bound protein was eluted with 300 mM imidazole and elutions were concentrated with a MW cut-off of 100 kDa. For purification of A_{2A}R-SMALPs, the resin was washed with 10 mM imidazole, followed by a wash of 20 mM imidazole. Bound protein was eluted with 300 mM imidazole and elutions were concentrated with a MW cut-off of 50 kDa.

2.7. Electrophoresis and immunoblotting

2.7.1. Agarose gel electrophoresis

Plasmid DNA was analysed by agarose gel electrophoresis using Geneflow electrophoresis equipment. 1% w/v agarose was prepared in TAE electrophoresis buffer (Thermo Scientific) with DNA stain (RedSafe, Chembio) added at 1:20,000 dilution. DNA samples were prepared with purple gel loading dye (New England Biolabs). A DNA ladder mix (GeneRuler, Thermo Scientific) was used for molecular size markers.

For electrophoresis, agarose gels were run in TAE buffer. Samples were loaded onto gels and separated at 100 V for 1 h. Gels were imaged using the G:Box UV transilluminator (Syngene).

2.7.2. SDS-PAGE

All SDS-PAGE polyacrylamide gels were prepared and run using Bio-Rad electrophoresis equipment. SDS-PAGE polyacrylamide gels were hand-cast with separating gels (375 mM Tris-HCl pH 8.8, 0.1% w/v SDS) of 10% or 4–16% gradient acrylamide (acrylamide/bis 30:0.8%; National Diagnostics), and 4% acrylamide stacking gels (125 mM Tris-HCl pH 6.8, 0.1% w/v SDS). Samples were typically incubated with Laemmli buffer (2% w/v SDS, 5% v/v βME, 50 mM Tris-HCl pH 6.8, 10% v/v glycerol, 0.005% w/v bromophenol blue) for 10 min at RT prior to loading into gel wells. A pre-stained protein ladder (PageRuler Plus, Thermo Scientific) was used as a molecular weight (MW) marker (10 kDa to 250 kDa) for all SDS-PAGE and western blot analysis.

For electrophoresis, gels were run in Tris-glycine-SDS buffer (25 mM Tris pH 8.8, 192 mM glycine, 0.1% SDS). Samples were loaded onto gels and separated at 180 V for 50 min, or until the dye front began to run off the bottom of the gel. Gels were stained with Coomassie (InstantBlue, Abcam) and imaged using the Bio-Rad GelDoc Go system.

2.7.3. Western blotting

Western blots were transferred using Bio-Rad wet-transfer equipment. Proteins were transferred from gels onto PVDF membranes (0.2 µm pore size, Thermo Scientific) at 100 V for 1 h in cold Tris-glycine-MeOH buffer (25 mM Tris pH 8.8, 192 mM glycine, 20% v/v MeOH). Membranes were rinsed briefly in PBS-T (PBS, 0.1% w/v Tween 20) before blocking for 1 h at RT in 5% w/v skimmed milk powder in PBS-T. Membranes were washed 3 times for 10 min in PBS-T, followed by primary Ab (dilutions specified in results) incubation overnight at 4 °C in 5% w/v bovine serum albumin (BSA) in PBS-T. Membranes were washed 3 times for 10 min in PBS-T, followed by secondary horseradish peroxidase (HRP) -conjugated Ab (dilutions specified in results) incubation for 1 h at RT in 5% skimmed milk powder in PBS-T. Membranes were washed 3 times for 10 min in PBS-T and incubated with chemiluminescent substrate (SuperSignal West Pico PLUS, Thermo Scientific) for 5 min at RT. Excess substrate was drained off the membrane, and membrane chemiluminescence was imaged using the Bio-Rad ChemiDoc MP imaging system.

2.7.3.1. Ponceau S staining

For blots probed with ponceau stain, Ponceau S was applied after transfer and prior to blocking. 0.1% w/v Ponceau S (Sigma-Aldrich) was dissolved in 5% acetic acid. Western blot membranes were rinsed once in dH_2O after transfer (1 min, rocking). Membranes were incubated in Ponceau S solution for 5 min (rocking, RT). Membranes were destained by rinsing with dH_2O to the desired band intensity and bands were marked with pen. Membranes were washed 2 times for 5 min in dH_2O to completely destain before proceeding to blocking and Ab incubations.

2.7.3.2. Western blot stripping for re-staining

For western blots to be re-probed, blots were stripped immediately after chemiluminescence imaging. Blots were washed 3 times for 10 min in PBS-T, followed by incubation in stripping buffer (1.5% w/v glycine, 0.1% w/v SDS, 1% v/v Tween 20, pH 2.2) 2 times for 10 min at RT.

Blots were then washed 3 times for 5 min in PBS-T, before proceeding to blocking and Ab re-probing as described in 2.7.3.

2.7.4. Densitometry analysis

Densitometry of SDS-PAGE and western blots was performed using ImageJ (Fiji). Unprocessed images were used for quantification. The gel analyser tool was used to select sample lanes and lane intensity was plotted. The area of each peak, corresponding to the sample band intensity, was measured.

2.7.4.1. Densitometry of SDS-PAGE to estimate protein concentration

MP concentrations after SMA solubilisation and purification were estimated by densitometry analysis of SDS-PAGE alongside a BSA concentration gradient. Intensity of the BSA bands was used to make a concentration standard curve. The purified MP samples and BSA serial dilution were always run on the same SDS-PAGE gel to ensure comparative staining for densitometry analysis. Separate standard curves were calculated for each gel analysed. Purified MP concentrations were estimated by using band intensity values to interpolate from the BSA standard curve.

2.7.4.2. Densitometry of western blots to calculate solubilisation efficiency

SMA solubilisation efficiency was determined by western blot analysis of the soluble and insoluble fractions after SMA solubilisation and ultracentrifugation (Section 2.6.2). Intensity of the target MP bands in the soluble and insoluble fractions were determined by densitometry. Solubilisation efficiency (%) was calculated as the proportion of intensity from the soluble fraction out of the total sum of intensities from the soluble and insoluble fractions.

2.7.5. SMA-PAGE

Native PAGE for purified MP-SMALPs (SMA-PAGE) was performed using an adapted protocol from Pollock *et al.* (Pollock *et al.*, 2019).

All SMA-PAGE polyacrylamide gels were prepared and run using Bio-Rad electrophoresis equipment. SMA-PAGE polyacrylamide gels (375 mM Tris-HCl pH 8.8) were hand-cast with acrylamide (acrylamide/bis 30:0.8%; National Diagnostics) concentrations of 10% or 3–20%

gradient. Purified MP-SMALPs were mixed with native sample buffer (25 mM Tris-HCl pH 8.0, 10% v/v glycerol, 0.005% w/v bromophenol blue) for loading onto gels. NativeMark unstained protein ladder (Invitrogen, Thermo Fisher Scientific) and BSA (0.5 mg/mL, mixed with native sample buffer) were used as MW markers (NativeMark, 20 kDa to 1,200 kDa; BSA, ~66 kDa).

For electrophoresis, gels were run in Tris-glycine buffer (25 mM Tris pH 8.8, 192 mM glycine). Samples were loaded onto gels and separated at 150 V for 90 min, or until the dye front began to run off the bottom of the gel. Gels were stained with Coomassie (InstantBlue, Abcam) and imaged using the Bio-Rad GelDoc Go system.

For SMA-PAGE gels to be used for immunoblotting, gels were soaked in SDS (2% w/v) prior to western blot transfer (instead of Coomassie staining). Blots were stained with Ponceau S to identify the NativeMark and BSA (Section 2.7.3.1).

2.7.5.1. Mass estimation by SMA-PAGE

SMA-PAGE was used to estimate mass by calculating the relative migration distances (R_f) of mass standard proteins. R_f = protein band distance / dye-front distance. Mass standard curves were determined using NativeMark. A log transform of the MW (kDa) was calculated to fit a linear regression line. A standard curve was calculated for each individual SMA-PAGE gel analysed for mass estimates. R_f values of sample bands were then interpolated to estimate sample mass.

2.7.6. Dot blotting

Dot blots for purified MP-SMALPs were performed using nitrocellulose membranes (0.45 µm pore size, Protran BA85, Whatman, Cytiva). 1 µL per sample was blotted as specified in results, and allowed to dry on the membrane for 30 min. For preparation of denatured samples, samples were incubated 1:1 with 2× denaturing buffer (4% w/v SDS, 10% v/v βME, 100 mM Tris-HCl pH 6.8) for 10 mins and 2 µL of denatured sample was blotted. Membranes were hydrated briefly in PBS-T (PBS, 0.1% w/v Tween 20) before blocking for 1 h at RT in 5% w/v skimmed milk powder in PBS-T. Membranes were washed 3 times for 10 min in PBS-T, followed by primary Ab (dilutions specified in results) incubation overnight at 4 °C in 5% w/v BSA in PBS-T. Membranes were washed 3 times for 10 min in PBS-T, followed by secondary HRP-conjugated Ab (dilutions specified in results) incubation for 1 h at RT in 5% skimmed milk powder in PBS-T. Membranes were washed 3 times for 10 min in PBS-T and incubated with

chemiluminescent substrate (SuperSignal West Pico PLUS, Thermo Scientific) for 5 min at RT. Excess substrate was drained off the membrane, and membrane chemiluminescence was imaged using Bio-Rad ChemiDoc MP imaging system.

For blots soaked in SDS, blots were hydrated in PBS-T, followed by soaking in 2% w/v SDS for 10 min. Blots were rinsed 2 times in PBS-T before proceeding to blocking and Ab incubations.

2.7.6.1. Dot blot quantification

Quantification of dot blots was done in ImageJ (Fiji) with unprocessed dot blot images. The image background was subtracted using a rolling ball radius of 50 pixels. A circle of fixed area (large enough to enclose the largest sample dot) was used to measure the integrated density of each sample dot. For each blot, sample intensities were normalised to the sum of integrated densities measured for all samples on the blot.

2.7.7. BN-PAGE

Blue native PAGE (BN-PAGE) was performed using an adapted protocol from methods described previously (Crane, Bennett and Verkman, 2009; Kitchen *et al.*, 2016).

2.7.7.1. *P. pastoris* cell lysis

P. pastoris cells were prepared by small-scale growth and induction (Section 2.4.3). *P. pastoris* cell pellets from 5 mL culture were washed in cold dH_2O (resuspension and centrifugation, 4,000 × g, 10 min, 4 °C) and resuspended in cold dH_2O (volume specified in results) for lysis. Cells were disrupted using glass bead homogenisation (Section 2.5.1). Before centrifugation, cell lysates were mixed with an equal volume of cold 2× native lysis buffer (40 mM Bis-Tris, 1 M aminocaproic acid, 40 mM NaCl, 4 mM EDTA, 20% v/v glycerol, 1% v/v Triton X-100, pH 7) and incubated on a spinning wheel (30 min, 10 rpm, 4 °C). Lysates were then centrifuged (18,000 × g, 10 min, 4 °C) to separate the glass beads. The supernatant was kept on ice or at 4 °C until use. For freeze-thaw samples, lysates were stored at -20 °C for 1 h, followed by defrosting at 4 °C.

2.7.7.2. MDCK cell lysis

Madin-Darby canine kidney (MDCK) cells were cultured and kindly provided by Drs Lucas Unger and Phil Kitchen of our research group. The MDCK cells were stably transfected with a construct of either the M1 or M23 isoform of AQP4, with a C-terminally fused green fluorescent protein (GFP).

MDCK cells were washed on ice 3 times with cold PBS. After removing the PBS wash, cells were lysed with 250 µL of cold native lysis buffer (20 mM Bis-Tris, 500 mM aminocaproic acid, 20 mM NaCl, 2 mM EDTA, 10% v/v glycerol, 0.5% v/v Triton X-100, pH 7) and incubated with the lysis buffer on a spinning wheel (45 min, 10 rpm, 4 °C). Lysates were then centrifuged (18,000 × g, 10 min, 4 °C) and the supernatant was kept on ice or at 4 °C until use. For freeze-thaw samples, lysates were stored at -20 °C for 1 h, followed by defrosting at 4 °C.

2.7.7.3. BN-PAGE

Gels were cast and run using Bio-Rad electrophoresis equipment. All running buffers and gels were cooled before use. BN-PAGE polyacrylamide gels (50 mM Bis-Tris, 0.5 M aminocaproic acid, pH 7) were hand-cast with 10% or 4–8% gradient acrylamide (acrylamide/bis 30:0.8%; National Diagnostics) concentrations. NativeMark Unstained Protein Standard (Invitrogen, Thermo Fisher Scientific) and BSA (1% w/v, 10% v/v/ glycerol) were used as MW standards (NativeMark, 20 kDa to 1,200 kDa; BSA, ~66 kDa).

For electrophoresis, gels were run in cooled tanks at 4 °C with a cathode buffer (50 mM Tricine, 15 mM Bis-Tris, 0.02% w/v Coomassie Brilliant Blue G-250, pH 7) in the inner/upper reservoir and anode buffer (50 mM Bis-Tris, pH 7) in the outer/lower reservoir. Samples were loaded onto gels and separated at 100 V for 15 min, followed by 180 V for 1 h 45 min.

Gels were destained 3 times for 10 mins (rocking, RT) in Coomassie destain solution (10% v/v acetic acid, 40% v/v MeOH). Gels were then soaked in SDS (1% w/v SDS, 50 mM Tris-HCl, 150 mM NaCl, pH 7.4) for 30 min (rocking, RT). Gels were transferred by western blot onto PVDF membranes (Section 2.7.3). Approximate band positions for NativeMark and BSA were marked with pen. Membranes were probed with Abs as described in Section 2.7.3 and 6.1.

2.8. Biophysical techniques

2.8.1. SEC

Size-exclusion chromatography (SEC) for further purification after IMAC was performed using the ÄKTA pure (Cytiva) with either the Superdex 200 Increase 10/300 GL or Superose 6 Increase 10/300 GL columns (Cytiva).

SEC columns were flushed with 2× column volumes of dH_2O, followed by equilibration with 2× column volumes of purification buffer (300 mM NaCl, 20 mM Tris-HCl pH 8.0). Affinity purified MP-SMALPs were concentrated to 500 µL after IMAC purification (Section 2.6.3) and inserted into the ÄKTA via the injection valve. Samples were flowed through the column with 28 mL of purification buffer (without protease inhibitor) at 0.5 mL/min. Column output was fractionated as 200 µL fractions into 96 deep-well plates. The UV monitor was set to monitor wavelength at 260 nm and 280 nm for SMA and protein, respectively. Typically, 600 µL samples were collected (from three fractions) for each corresponding identified peak in the SEC UV trace.

2.8.1.1. Mass estimation by SEC

SEC was used to estimate mass by identifying retention volumes of mass standards. A SEC protein standard mix (15 – 600 kDa; Supelco, MilliporeSigma) was run through the Superose 6 column. Retention values were determined by finding the apex of the SEC UV trace peak for the corresponding protein. A function in Excel was used to find the maximum milli-absorbance unit (mAU) value (and corresponding retention volume) in a range of retention values covering the peak of interest. Retention volumes were used to generate a mass standard curve. A log transform of the MW (kDa) was calculated in order to fit a linear regression line. Retention values of samples were then interpolated to estimate sample mass.

2.8.2. Mass photometry

Mass photometry analysis was performed using the TwoMP instrument (Refeyn). AquireMP (AMP; Refeyn) software was used for instrument control, sample measurement, and measurement recordings. Sample recording data was analysed using DiscoverMP (DMP; Refeyn). Mass calibrations were performed using either NativeMark (Invitrogen, Thermo Fisher Scientific) or MS1000. MS1000 (Dyn1-deltaPRD) was expressed and purified by Dr Manish S. Kushwah, Aston University, using the protocol described by Foley *et al.*, 2021 (Foley

et al., 2021). Mass calibrants were generally recorded and analysed prior to sample measurements. Mass calibrations were routinely performed before each data acquisition session. Purification buffer (300 mM NaCl, 20 mM Tris-HCl pH 8.0) was used as a diluent for all samples. Sample pre-dilutions were usually prepared in RT purification buffer to equilibrate sample temperature. For Ab incubation samples, Abs were incubated with the target protein for 10 min at RT prior to mass photometry analysis. Incubation concentrations are detailed in results.

2.8.2.1. Slide and sample cassette preparation

24 × 50 mm cover glasses (#1.5H, Marienfeld Superior) were used as sample carrier slides. Slides were cleaned by washing in 100% isopropanol followed by dH_2O. This was followed by a second wash in fresh solutions of the same. Slides were dried under a stream of air through a 0.2 µm filter and stored in a dust-free environment. Slides were discarded after use. 6-well sample cassettes (Refeyn) were either used fresh or cleaned as described for the slides and re-used.

2.8.2.2. Sample measurements

The TwoMP instrument was turned on ~1 h prior to use for thermal equilibration of the laser. Cassettes were applied to sample-carrier slides using the MP alignment tool (Refeyn). Immersion oil was placed on the instrument objective and slides were positioned onto the instrument stage, held in place using the supplied magnets. For normal measurement procedure, droplets (≥ 15 µL) of purification buffer were pipetted into cassette wells, the objective focus was found automatically by AMP software, and samples were droplet-diluted into the purification buffer in the cassette well to give a final volume of 20 µL. Volume and dilution for each measurement varied depending on the desired final concentration. Optimal sample concentrations and dilutions were determined so that there were not too many or too few detected events (counts). AMP was used to measure samples over the regular field of view. Binding events (counts) and contrast were recorded for 1 min. Recordings were captured with native and ratiometric imaging.

2.8.2.3. Data analysis

DMP was used to analyse sample data and produce histograms. Histograms of event counts (from ratiometric images) were plotted against measured contrast automatically. For

calibrants, histogram peaks were identified and selected for automatic Gaussian distribution fitting by the DMP software. Pre-defined calibrant masses were assigned to the identified peaks corresponding to each mass. Mass standard curves and curve-fit accuracy values were then calculated automatically by the DMP software. The mass calibration was then applied to the desired samples. Sample histogram peaks were identified and selected for automatic Gaussian distribution fitting. A bin width of 5.5 kDa was used as default for mass histograms. Gaussian distribution means were interpreted as mass estimates. For histograms with normalised counts, normalisation was calculated automatically by the software – the number of counts in each histogram bin are divided by the total number of counts (events) recorded for the sample. Gaussian distributions were not typically fitted to far-left peaks below 30 kDa, as this is below the mass photometry detection limit and represented low MW noise.

2.8.3. Flow-induced dispersion analysis (FIDA)

Flow-induced dispersion analysis (FIDA) was performed on the FIDA 1 instrument (Fidabio) using a standard uncoated capillary of 75 µm inner diameter and total length of 1 m. Samples and purification buffer (300 mM NaCl, 20 mM Tris-HCl pH 8.0) were loaded in vials into the autosampler and kept at 4 °C. The capillary was washed with dH_2O (1,500 mbar, 180 s) and then equilibrated with purification buffer (1,500 mbar, 180 s). The samples were injected into the capillary at 50 mbar for 10 s and then run through the capillary with purification buffer at 400 mbar for 3 min at RT. Fluorescence was monitored at 280 nm. The capillary was washed with 1 M NaOH followed by dH_2O (1,500 mbar, 300 s) at the end of each run. Samples were typically run as three technical replicates. The data was analysed on the Fidabio data analysis software to estimate hydrodynamic radius (R_h) and polydispersity index (PDI).

2.9. Biochemical assays

2.9.1. CPM thermal shift assay

Thiol reactive coumarin dye (CPM; 7-diethylamino-3-(4'-maleimidylphenyl)-4-methylcoumarin; Invitrogen) was used for the protein thermal shift assay. The CPM assay protocol described here was based on similar CPM assays described previously (Alexandrov *et al.*, 2008; Sampson *et al.*, 2021).

2.9.1.1. CPM assay and fluorescence measurements

CPM (from a stock solution of 5 mg/mL in DMSO, stored at -80 °C) was prepared in purification buffer (300 mM NaCl, 20 mM Tris-HCl pH 8.0) at a concentration of 36 µg/mL. 225 µL purified protein (50 µg/mL) was mixed with 25 µL of the CPM solution (to give final CPM concentration of 3.6 µg/mL) and mixed thoroughly by vortex. Replicates of 50 µL per reaction were transferred into qPCR plates (BrightWhite, Primerdesign) and plates were covered with an optical adhesive seal. Assay fluorescence with increasing temperature was measured with the LightCycler 480 (Roche) instrument. Plates were equilibrated to 20 °C in the LightCycler instrument, followed by temperature increase to 99 °C at a rate of 3.6 °C/min. Fluorescence was monitored during the temperature increase using the SYBR Green filter (Ex 465 nm / Em 510 nm).

2.9.1.2. Data processing

Fluorescence values for three replicates per sample were first processed in Microsoft Excel. The mean fluorescence for a CPM only (no protein) control was used as a baseline subtraction to calculate corrected fluorescence values for the purified protein samples. Fluorescence was normalised by using the average of values from 20.06 °C to 20.97 °C as the minimum (0), and the average of values from 97.84 °C to 98.76 °C as the maximum (1). Prism (ver. 10, GraphPad) was used for further data processing. The first derivative of the normalised data was calculated with 2nd order smoothing (30 neighbours). A Lorentzian curve was fitted to the first derivatives (up to x = 97.5 °C), with the curve centre being used to determine the melting point (T_m).

2.9.2. Bradford assay for protein concentration

Bradford assays to estimate protein concentration were performed using Bradford Plus Protein Assay Reagent (Pierce, Thermo Scientific). BSA was used as a concentration standard in serial dilution. Three replicates of each BSA concentration and sample were used per assay. Per 10 µL of buffer blank, BSA, or sample, 300 µL of Bradford reagent was added, mixed, and allowed to incubate for 10 min at RT. Absorbance was measured at 595 nm with the FLUOstar Omega plate reader (BMG Labtech). The average blank measurement was subtracted from averages of all other samples and the BSA measurements were used to make a concentration standard curve. Sample concentrations were estimated by interpolating from the BSA standard curve.

2.9.3. Acyl-biotinyl exchange (ABE) assay

The acyl-biotinyl exchange (ABE) assay described here was adapted from the protocol described by Lei *et al.* (Lei *et al.*, 2021).

2.9.3.1. *P. pastoris* cell lysis

P. pastoris cells were prepared by small-scale growth and induction (Section 2.4.3). *P. pastoris* cell pellets from 5 mL of culture were washed in cold dH_2O (resuspension and centrifugation, 4,000 × g, 10 min, 4 °C). Washed pellets were resuspended in 1 mL cold lysis buffer (5 mM EDTA, PBS, protease inhibitor (cOmplete cocktail tablets, Roche)). Resuspended cells were broken by glass bead homogenisation (Section 2.5.1). Lysates were centrifuged (5,000 × g, 5 min, 4 °C) and the supernatant collected. A Bradford assay (Section 2.9.2) was used to determine lysate protein concentration. Lysate equal to 1 mg of protein was diluted to 600 µL in lysis buffer with the addition of 1% v/v Triton X-100 and 25 mM N-ethylmaleimide (NEM). Samples were incubated on a spinning wheel (30 min, 10 rpm, 4 °C) and then diluted to 1 mL in buffer B1 (150 mM NaCl, 50 mM Tris-HCl pH 7.4, 5 mM EDTA) containing protease inhibitor.

2.9.3.2. Precipitation and thiol blocking

Protein was precipitated by chloroform-methanol (TCM-MeOH) precipitation. TCM-MeOH precipitations were performed as follows: 4 mL of MeOH was added the samples and vortexed, 1.5 mL TCM was added to the samples and vortexed, 3 mL of dH_2O was added to the samples and vortexed. Samples were centrifuged (4,000 × g, 15 min, 4 °C) to separate the phases and form the protein precipitate interphase. The top phase (dH_2O and MeOH) was discarded. 3 mL MeOH was added and vortexed. Samples were centrifuged (4,000 × g, 15 min, 4 °C) to pellet the protein precipitate. The supernatant (MeOH and TCM) was discarded and the pellet was allowed to air dry (~ 10 min).

The protein precipitate was dissolved (37 °C, 10 min) in 200 µL buffer B2 (4% SDS, 50 mM Tris-HCl pH 7.4, 5 mM EDTA), followed by dilution to 1 mL with buffer B1 containing protease inhibitor, and addition of 10 mM NEM. Samples were incubated (16 h, 4 °C), followed by four repeats of TCM-MeOH precipitation to remove excess NEM. The protein precipitate was air dried (~10 min) and dissolved (37 °C, 10 min) in 450 µL buffer B2.

2.9.3.3. Cleavage of palmitoylation and biotinylation

50 µL of sample was retained as an assay input. The remaining was split into – and + hydroxylamine (HA) conditions. 200 µL was incubated (2 h, RT, gentle mixing) with 800 µL +HA-buffer (0.7 M HA-HCl pH 7, 1 mM HPDP-biotin (EZ-Link, Thermo Scientific), 0.2% v/v Triton X-100, PBS, protease inhibitor) and the other 200 µL was incubated (2 h, RT, gentle mixing) with -HA-buffer (1 mM HPDP-biotin (EZ-Link, Thermo Scientific), 0.2% v/v Triton X-100, PBS, 50 mM Tris-HCl pH 7.4, protease inhibitor). Four repeats of TCM-MeOH precipitation were then used to remove excess HPDP-biotin. The protein precipitate was air dried (~10 min), dissolved (37 °C, 10 min) in 100 µL buffer B3 (2% SDS, 50 mM Tris-HCl pH 7.4, 5 mM EDTA), and diluted to 1 mL with buffer B1.

2.9.3.4. Streptavidin binding

Samples were incubated (2 h, RT, gentle mixing) with 50 µL (100 µL slurry) of high-capacity streptavidin agarose resin (Pierce, Thermo Scientific). Resin was pelleted by centrifugation (2,500 × g, 2 min) and the unbound fraction (FT) collected. The resin was washed 5 times by resuspension in wash buffer (150 mM NaCl, 50 mM Tris-HCl pH 7.4, 0.1% Triton X-100, 5 mM EDTA) and centrifugation (2,500 × g, 2 min). Bound proteins were eluted by incubation (15 min, RT) in elution buffer (150 mM NaCl, 50 mM Tris-HCl pH 7.4, 5 mM EDTA, Laemmli buffer (2% w/v SDS, 5% v/v βME, 50 mM Tris-HCl pH 6.8, 10% v/v glycerol, 0.005% w/v bromophenol blue)), separated from the resin by centrifugation (2,500 × g, 2 min), and supernatant collected. Samples were stored at -20 °C before analysis by 4–16% gradient SDS-PAGE and western blotting.

2.10. Statistical analysis

All statistical analysis was performed in Prism (ver. 10, GraphPad). The number of replicates (n = replicate number) is indicated in the figure legend for the relevant analyses. The chosen statistical test is also indicated with a p-value legend (ns – $p > 0.05$ (not significant), *$p \leq 0.05$; **$p \leq 0.01$; ***$p \leq 0.001$; ****$p \leq 0.0001$).

Where statistical tests have been performed, parametric statistical tests were chosen for all data sets. Normality was assumed as data was not clearly skewed (non-normal). The lower statistical power of non-parametric tests at low values of *n* was also considered.

3. Expression and purification of M1 and M23 AQP4 isoforms using *Pichia pastoris* as a recombinant expression host

Differences between the AQP4 M1 and M23 isoforms are well understood, and their behaviour has been characterised in whole cells. The ability to purify MPs with solubilisation tools such as SMA offers a different perspective. Characterising proteins in a purified form allows investigation away from other *in vivo* components and offers a deeper understanding of structural roles independent of the whole cell.

Before purification and characterisation, it is first necessary to express proteins to a reasonable level using a suitable recombinant expression system that allows purification to a sufficient yield. As previously discussed, *P. pastoris* is an excellent expression system for the production of recombinant human proteins. AQP4 has previously been successfully expressed in *P. pastoris* (Ho *et al.*, 2009). As *P. pastoris* is a eukaryotic organism, using it as a recombinant expression system can increase the likelihood of replicating protein folding and post-translational modifications similar to mammalian expression systems (Daly and Hearn, 2005; Karbalaei, Rezaee and Farsiani, 2020). This is desirable for this project, as a key functional difference between the M1 and M23 AQP4 isoforms is a post-translational modification (PTM). The M1 AQP4 isoform typically features S-palmitoylation of cysteine residues in the N-terminal region that the M23 isoform lacks (Suzuki *et al.*, 2008).

This chapter describes how *P. pastoris* clones were established and selected for high yields of recombinant hAQP4, in forms representing both the M1 and M23 isoforms of AQP4. Following selection of high expressing clones, AQP4 was solubilised from *P. pastoris* membrane fragments using SMA, followed by Ni-NTA IMAC targeting the AQP4 recombinant 6× His-tag to purify the resultant AQP4-SMALPs. Methods of protein production and yields of the IMAC purified AQP4 isoforms were compared.

3.1. Expression and purification of AQP4 from existing M1 and M23 *P. pastoris* clones

At the start of this project, two separate *P. pastoris* clones expressing either the M1 or M23 isoform of AQP4 were already available in our research group library. The respective AQP4 isoform plasmid constructs, as described in Section 2.2, had previously been transfected into

E. coli DH10B for amplification. The M1 AQP4 construct had been transformed into the GS115 strain of *P. pastoris* and established for high yields of purified AQP4 by Drs Phil Kitchen and Lucas Unger of our research group. The M23 AQP4 construct had been transformed into the X33 strain of *P. pastoris*, but this clone had not yet been investigated for expression and pure protein yield. The established M1 AQP4 clone was used as a benchmark to investigate the available M23 AQP4 clone for expression and purification yield.

The predicted monomer weights for the M1 and M23 AQP4 isoforms expressed by these *P. pastoris* clones were ~35.6 kDa and ~33.1 kDa, respectively. This was based on the full hAQP4 sequence of each isoform, plus the weight of the recombinant 6× His-tag (~0.8 kDa) (see appendix Figure A.1).

3.1.1. Comparing AQP4 expression between the M1 and original M23 *P. pastoris* clones

With *P. pastoris* clones for M1 and M23 AQP4 already available, the first step was to compare the relative levels of AQP4 expression between the clones to assess whether the original M23 AQP4 clone could provide levels of expression comparable to the M1 AQP4 clone. Ultimately, levels of protein expression will have an influence on the yield of purified protein.

Glycerol stocks of *P. pastoris* clones for the M1 and original M23 AQP4 isoforms were streaked on to YPD agar plates containing 100 μg/mL zeocin and the plates were incubated (72 h, 30 °C). Both M1 and M23 AQP4 pPICZ plasmid constructs featured the Sh *ble* (*BleoR*) gene from *Streptoalloteichus hindustanus* that encodes for bleomycin resistance protein. This allowed for antibiotic selective pressure using zeocin antibiotic. Single colonies of the M1 and M23 AQP4 isoform clones were picked and grown according to the small-scale growth and expression protocol (Section 2.4.3). Briefly, 5 mL BMGY was inoculated per selected colony and cultured for 24 h (30 °C, 200 rpm). Cells were collected by centrifugation and washed with BMMY, before resuspension at OD_{600} = 1, in 5 mL BMMY. This helped to ensure expression comparison from relatively even culture densities. Cultures were induced for 48 h (30 °C, 200 rpm), with addition of MeOH (1% v/v) at the 24 h midpoint. Both M1 and M23 plasmid constructs utilise the *AOX1* MeOH-inducible promoter for recombinant gene expression. After induction, cells were collected (4,000 × g, 4 °C, 10 min), washed and resuspended in 5 mL cold dH_2O, and immediately broken by glass bead homogenisation (Section 2.5.1). Whole cell lysates were incubated with Laemmli buffer (10 min, room temperature (RT)), separated by 4–16% gradient SDS-PAGE, followed by western blotting (Section 2.7.3). AQP4 in the

samples was probed with a rabbit anti-AQP4 Ab (1:5,000, 16 h, 4 °C), followed by a secondary anti-rabbit-HRP Ab (1:2,500, 1 h, RT), and visualised by chemiluminescence.

The resulting western blot of whole cell lysates is shown in Figure 3.1. Bands for the AQP4 monomer (~35.6 kDa for M1 AQP4, ~33.1 kDa for M23 AQP4) and dimer are clearly present for both isoform clones, with the M1 clone also showing bands at molecular masses for trimers and tetramers of AQP4. MW differences between the two isoforms are clear, with this being particularly apparent at the dimer band. The M23 AQP4 clone showed relatively low expression compared to the established M1 isoform clone. Analysis of the AQP4 band intensities by densitometry (Section 2.7.4) revealed that this original M23 AQP4 clone showed ~10% relative intensity to the established M1 AQP4 isoform clone. An AQP4 degradation band is also visible between 10–15 kDa for the M1 clone.

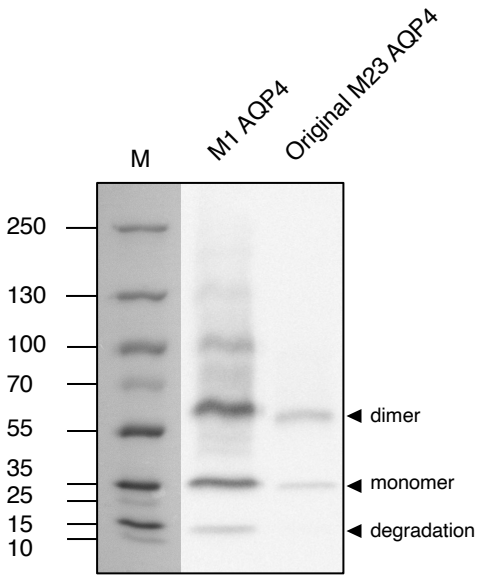

Figure 3.1. Western blot targeting AQP4 of whole cell lysates from M1 and original M23 AQP4 *P. pastoris* clones.
5 mL cultures of *P. pastoris* clones expressing either the M1 or original M23 isoforms of AQP4 were grown, induced, and broken by glass bead homogenisation. Cell lysates were separated by 4–16% gradient SDS-PAGE, followed by western blotting. AQP4 was probed with a rabbit anti-AQP4 Ab (1:5,000). An anti-rabbit-HRP Ab was used as secondary (1:2,500) and the blot was imaged using chemiluminescence. The blot lanes are labelled according to clone name, where; 'M1 AQP4' is the established M1 AQP4 clone, and 'Original M23 AQP4' is the original M23 AQP4 clone. Positions of monomer, dimer and degradation bands of AQP4 are labelled with arrows. MW markers are shown under 'M' with mass labels in kDa shown on the left of the blot.

3.1.2. Purification of AQP4 from the M1 and original M23 *P. pastoris* clone membranes

Having assessed the comparative expression of the AQP4 isoforms from small-scale cell culture of the two *P. pastoris* clones, an IMAC purification of AQP4 from both clones was used to assess pure AQP4 yield. This was to investigate whether M23 AQP4 could be purified from *P. pastoris* but also confirm that low expression of AQP4 from this clone was likely to have a negative impact on purified M23 AQP4-SMALP yield. The M1 AQP4 clone had already been established as providing a high yield of purified AQP4 after SMA solubilisation, so provided a good comparative benchmark.

Single colonies of the M1 and M23 AQP4 isoform clones were picked from YPD agar plates and grown according to the large-scale growth and expression protocol (Section 2.4.4). Briefly, colonies were grown as starter cultures for 24 h in BMGY (30 °C, 200 rpm), before inoculating into larger shake flask cultures of 250 mL BMGY (30 °C, 200 rpm). Cultures were spun down and washed with BMMY, before resuspending in BMMY at OD_{600} = 1. Cultures were induced for 48 h (30 °C, 200 rpm), with addition of 1% MeOH (final concentration) at the 24 h midpoint. After induction, cells were spun down (4,000 × g, 4 °C, 20 min) and frozen at - 80 °C. Cells were defrosted and broken using high pressure homogenisation (Section 2.5.2). Cell debris and unbroken cells were removed by centrifugation (4,000 × g, 4 °C, 10 min), and cell lysate was spun via ultracentrifugation (150,000 × g, 4 °C, 90 min) to pellet the cell membrane. Membrane pellets were homogenised and resuspended, before freezing in aliquots at -80 °C.

SMA solubilisation and purification conditions had been optimised for M1 AQP4 by Drs Philip Kitchen and Lucas Unger. As such, these optimised conditions were used for M23 AQP4 to create comparable preparations of purified AQP4-SMALPs.

Resuspended membranes were defrosted and solubilised with 2.5% w/v SMA (1 h, RT) followed by ultracentrifugation (100,000 × g, 4 °C, 45 min) to remove the insoluble fraction (Section 2.6.2). From the M1 AQP4 clone, 1.8 g membranes were solubilised, whereas 6.1 g membranes were solubilised for the M23 AQP4 clone. A high quantity of M23 AQP4 clone membranes was used to account for the expected low purification yield. Compared to standard methods, SMA solubilisation was performed at a higher membrane concentration of 90 mg/mL to reduce solubilisation volume.

Soluble AQP4-SMALPs were purified by Ni-NTA IMAC targeting the AQP4 recombinant 6× His-tag (Section 2.6.3). After washing the Ni-NTA agarose resin with 50× resin bed-volumes of both 20 mM and 75 mM imidazole, AQP4-SMALPs were eluted in fractions of ½ resin bed-

volumes of 300 mM imidazole. Fractions were incubated with Laemmli buffer (10 min, RT) before separation by 4–16% gradient SDS-PAGE and staining with Coomassie. Figure 3.2A and B show the elution fractions from this IMAC purification of M1 and M23 AQP4. M1 AQP4 shows a higher band intensity per fraction from a lower quantity of membranes. Bands for the monomer to tetramer forms of AQP4 appear to be visible.

A separate purification was used to quantify the protein yield per weight of membranes (Figure 3.2C). This purification was performed as described for Figure 3.2A and B, with 0.4 g and 1.8 g of membranes solubilised for the M1 and M23 AQP4 clones, respectively. Elutions were pooled and concentrated to 1 mL with a MW cut-off of 100 kDa. Samples were separated by SDS-PAGE and stained with Coomassie as already described. AQP4 concentration was estimated, using densitometry analysis (Section 2.7.4), against a serial dilution of a BSA. The purified AQP4 samples and BSA serial dilution were run on the same gel to ensure comparative staining for densitometry analysis. The total protein yield was ~0.11 mg of M1 AQP4 and ~0.02 mg of M23 AQP4. This equates to ~0.28 mg protein per g of membranes from the M1 AQP4 clone, and ~0.01 mg protein per g of membranes from the M23 AQP4 clone.

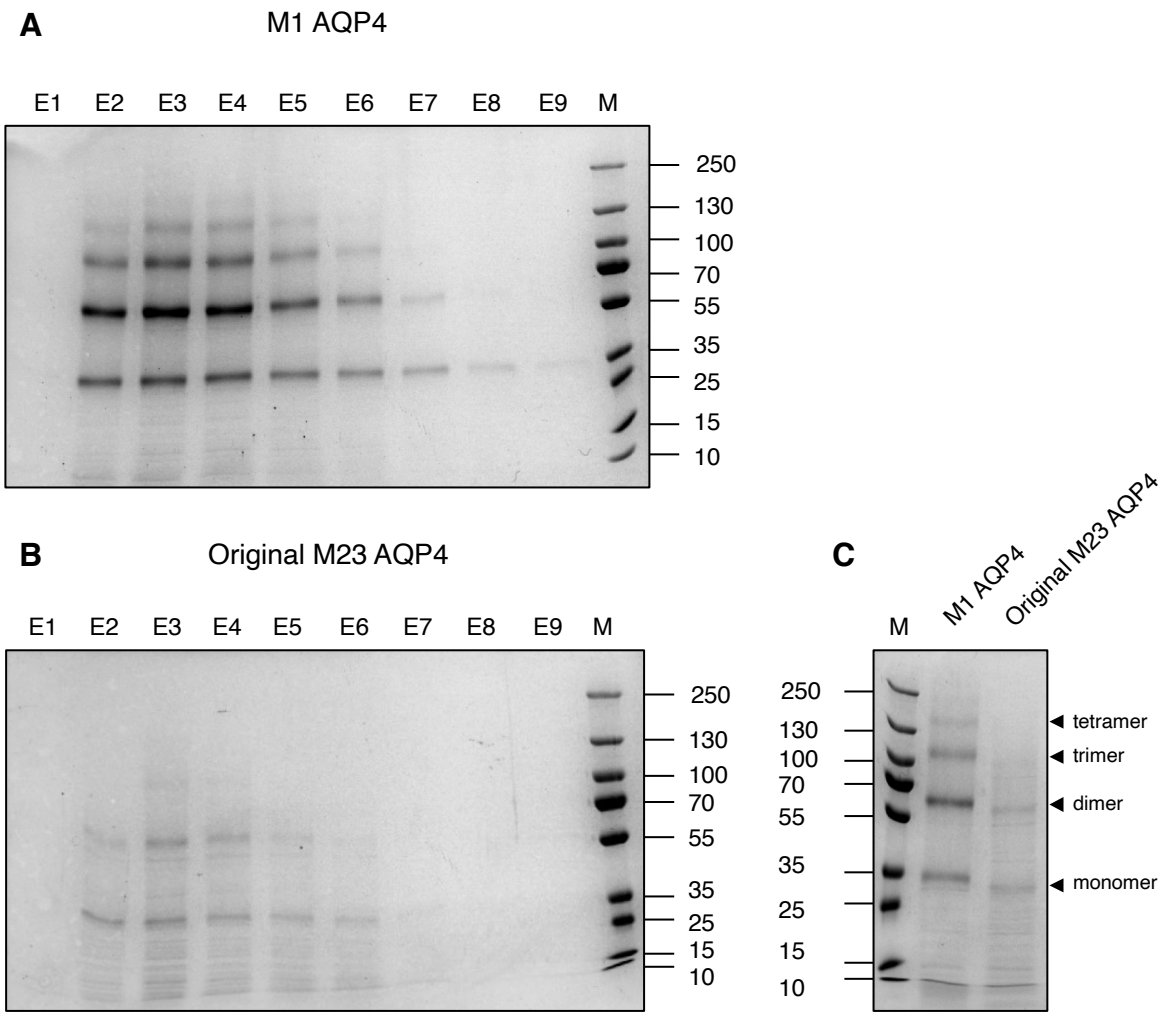

Figure 3.2. SDS-PAGE of purified M1 and M23 AQP4 isoforms from *P. pastoris* clones.
Resuspended membranes of the M1 and original M23 AQP4 isoform clones were solubilised at 90 mg/mL with 2.5% w/v SMA. Soluble fractions were separated by ultracentrifugation (100,000 × g, 45 min, 4 °C) and AQP4-SMALPs were purified by Ni-NTA IMAC. Ni-NTA agarose resin was washed with 20 mM and 75 mM imidazole before elutions at 300 mM imidazole. Samples were separated by 4–16% gradient SDS-PAGE and stained with Coomassie blue. **A, B)** elution fractions from IMAC purification of M1 AQP4 **(A)** purified from 1.8 g membranes and M23 AQP4 **(B)** purified from 6.1 g membranes. For both **A** and **B**, E1–6 represents consecutive elutions of ½ resin bed-volumes, and E7–9 represents consecutive elutions of 2 × resin bed-volumes. **C)** 1 mL concentrates of M1 and M23 AQP4 IMAC purifications from 0.4 g and 1.8 g membranes, respectively. Positions of monomer, dimer, trimer and tetramer bands of AQP4 are labelled with arrows. For all gels, MW markers are shown under 'M', with mass labels in kDa shown on the right of gel **A** and **B**, and left of gel **C**.

3.2. Transformation to generate a new M23 AQP4 *P. pastoris* clone

The whole cell lysate and purification yield of the original M23 AQP4 *P. pastoris* clone showed a significantly lower AQP4 yield compared to the M1 clone. A large quantity of membrane material was required to provide a small fraction of protein relative to what the M1 AQP4 *P. pastoris* clone could produce. Producing this amount of membrane fragment required a high quantity of cell culture, which is undesirable in terms of time and cost of materials. This provided justification for transformation of *P. pastoris* to generate a new M23 AQP4 clone with improved levels of expression, comparable with that of the M1 AQP4 *P. pastoris* clone.

3.2.1. Plasmid amplification, maxi-prep, and linearisation

The M23 AQP4 pPICZ plasmid construct had previously been transfected into *E. coli* DH10B for amplification. Before transformation, this plasmid construct had to be amplified and purified. LB agar plates with 100 µg/mL zeocin were streaked with a glycerol stock of *E. coli* DH10B transfected with the M23 plasmid construct, and incubated (24 h, 37 °C). A random colony was picked and grown in a starter culture of 5 mL LB medium (6 h, 37 °C, 220 rpm), which was used to inoculate 200 mL LB medium for an overnight culture (~16 h, 37 °C, 220 rpm). The cells were harvested by centrifugation (4,000 × g, 10 min, RT) and the M23 AQP4 pPICZ plasmid construct was purified using a maxiprep kit (Section 2.3.1). Plasmid concentration after maxiprep was estimated using a NanoDrop spectrophotometer (Figure 3.3A). DNA concentration was measured as 3.4 µg/mL, and the A260 / A280 and A260 / A230 ratios were measured as 1.89 and 2.32, respectively.

The purified plasmid was linearised using the PmeI restriction enzyme, targeting the plasmid PmeI restriction site to create a single digestion in the *AOX1* promoter region (Section 2.3.2.1). Some of the purified whole plasmid was also used for a non-linearisation control reaction (linearisation conditions without PmeI). After linearisation, half of the linearised plasmid was further purified using a gel-extraction kit (Section 2.3.2.1). Figure 3.3B shows the three plasmid conditions analysed using 1% agarose DNA-gel electrophoresis (Section 2.7.1). The pPICZ-AQP4 plasmid construct is ~4200 bp, thus, the lowest band in the agarose gel most likely represented the plasmid construct in its linear form. There was a downward shift in plasmid weight for the linearised plasmid that had been further purified using the gel-extraction kit compared to the plasmid that had only been linearised.

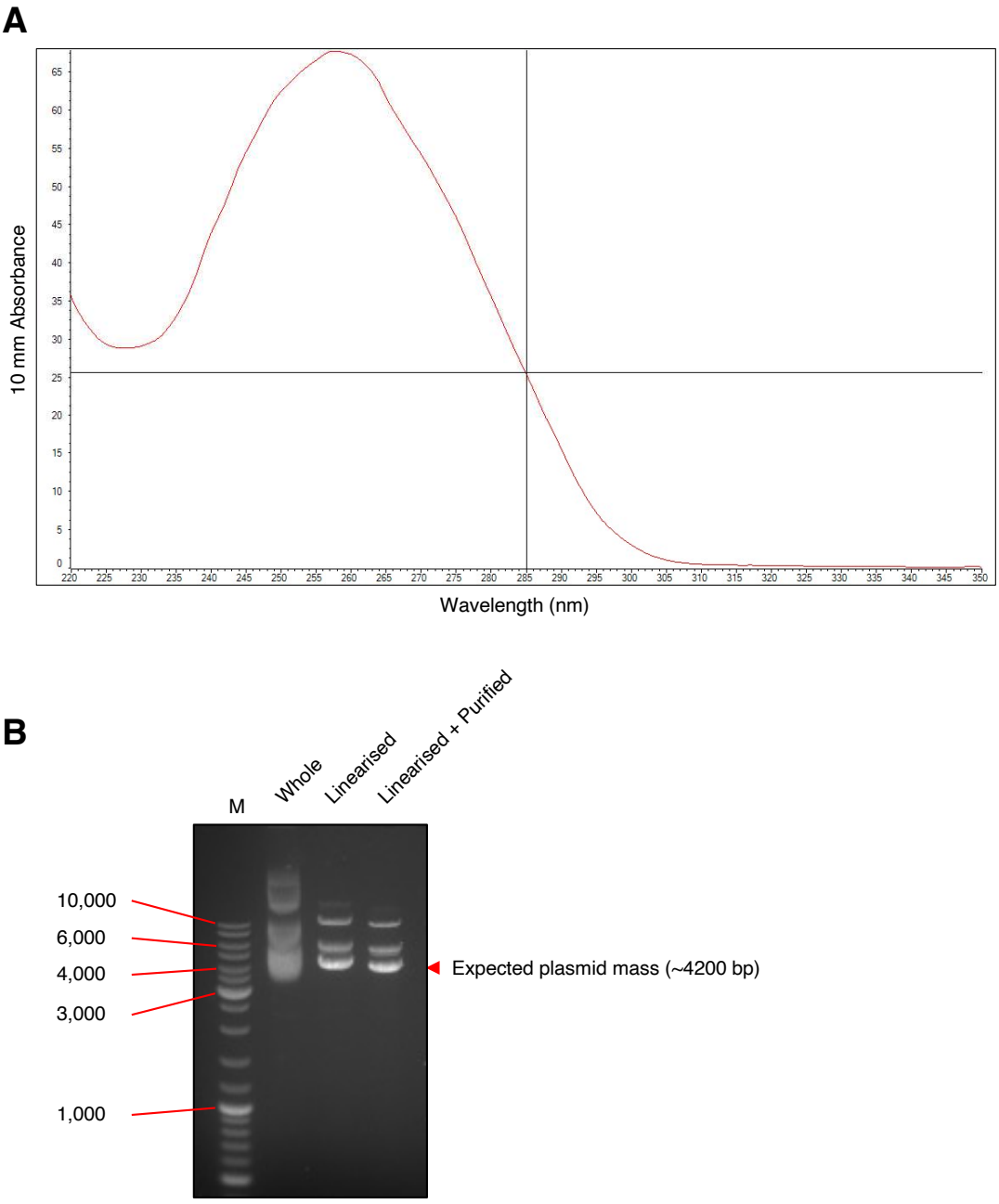

Figure 3.3. Maxi-prep of M23 hAQP4 pPICZ plasmid DNA construct.
Plasmids were isolated from *E. coli* transfected with a pPICZ plasmid construct expressing the M23 isoform of hAQP4. **A)** NanoDrop spectrophotometer absorbance trace of the maxi-prepped M23 AQP4 pPICZ plasmid DNA, showing 10 mm absorbance against wavelength (nm). DNA concentration was measured as 3.37 mg/mL. **B)** Agarose gel of the M23 pPICZ plasmid. Samples were mixed with purple loading dye (NEB) and visualised with a UV illuminator. Lane 'M' shows the DNA ladder with bands labelled with corresponding size in base pairs (bp). The 'Whole' lane shows the purified plasmid from the non-linearisation control reaction (whole plasmid). The 'Linearised' lane shows plasmid that has been linearised at the plasmid restriction site using PmeI. The 'Linearised + Purified' lane shows plasmid that has been linearised and further purified using a gel extraction kit. A red arrow is used to indicate the expected plasmid mass (bp).

3.2.2. Transformation of *P. pastoris* with the M23 AQP4 plasmid construct

YPD agar plates were streaked with the *P. pastoris* GS115 wild type strain and incubated (72 h, 30 °C). A chemical method of generating competent *P. pastoris* cells and transforming them with plasmid DNA was performed following an adapted protocol from Kumar, Mannil and Mutturi, 2020 (Section 2.3.2.2). Four different plasmid conditions were used for transformation: A) plasmid that had been linearised and further purified with a gel extraction (DNA clean-up) kit, B) plasmid that had only been linearised, C) circular plasmid (from the non-linearisation control reaction), and D) no plasmid (negative control). All other conditions for the transformation cultures remained the same. Transformation cultures were spread and incubated (72 h, 30 °C) on YPD agar plates containing 100 µg/mL zeocin, allowing for selective pressure of plasmid expression (Figure 3.4). Colony numbers were counted (Section 2.4.1.1) and are reported in Table 3.1. Control YPD agar plates with no zeocin were used to confirm cell survival after transformation. The transformation condition using the plasmid additionally purified after linearisation (condition A) showed a much higher number of colonies than the linearised-only condition (Figure 3.4 and Table 3.1).

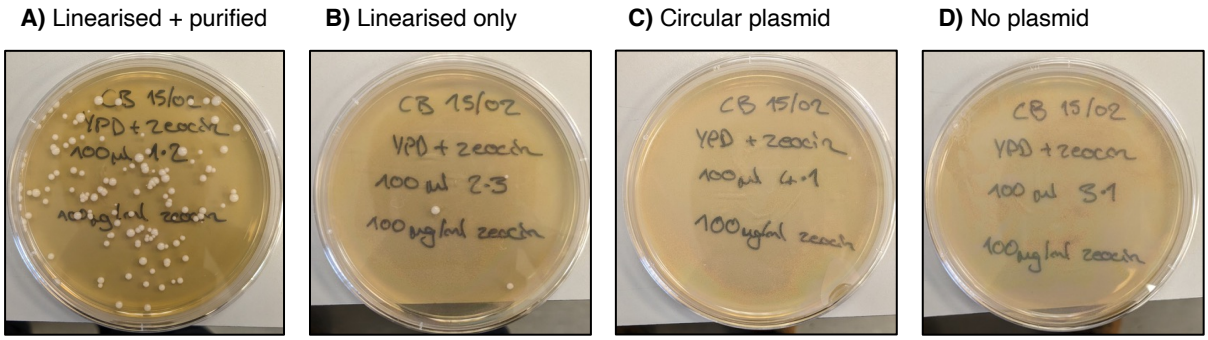

Figure 3.4. Example YPD agar plates spread with transformation colonies with different plasmid conditions.
LiCl transformation of *P. pastoris* wild type cells incubated with hAQP4 M23 pPICZ plasmid construct containing the *BleoR* gene, with different conditions of plasmid preparation. Transformation cultures were spread onto YPD agar plates containing 100 µg/mL zeocin. **A)** plasmid that had been linearised and further purified using a DNA clean-up kit, **B)** plasmid that had only been linearised, **C)** circular plasmid that had not been linearised (from the non-linearisation control reaction), and **D)** no plasmid (negative control). All other transformation conditions were the same for each condition.

Table 3.1. Colony numbers from YPD agar plates spread with transformation colonies with different plasmid conditions.
LiCl transformation of *P. pastoris* wild type cells incubated with a hAQP4 M23 pPICZ plasmid construct containing the *BleoR* gene, with different conditions of plasmid preparation. Transformation cultures were spread onto YPD agar plates containing 100 µg/mL zeocin. **A)** plasmid that had been linearised and further purified using a DNA clean-up kit, **B)** plasmid that had only been linearised, **C)** circular plasmid that had not been linearised (linearisation control), and **D)** no plasmid. Condition **A** and **B** are rounded means over 3 plates spread from one transformation culture per condition. Results for condition **C** and **D** are taken from one plate per condition. Colonies were counted by analysing particles after thresholding in ImageJ.

Condition	Average number of colonies (from n plates)
A) Linearised + purified	96 (n=3)
B) Linearised only	2 (n=3)
C) Circular plasmid	1 (n=1)
D) No plasmid	0 (n=1)

3.2.3. Screening transformation clones for antibiotic resistance

After successful transformation of *P. pastoris* GS115 strain with the M23 AQP4-pPICZ construct to generate zeocin resistance, colonies were selected at random to screen for high resistance to zeocin. As mentioned, the M23 AQP4 plasmid construct contains the *BleoR* gene, allowing for selective pressure using zeocin. Kumar *et al.* and others have described how increased resistance to selective pressure can indicate integration of multiple copy numbers of the recombinant plasmid by homologous recombination (Scorer *et al.*, 1994; Kumar, Mannil and Mutturi, 2020). A high plasmid copy number has been reported to result in increased expression of the recombinant protein (Scorer *et al.*, 1994; Athmaram *et al.*, 2012). This method of expression screening was used, assuming that clones expressing the highest resistance to zeocin were also highly expressing the M23 AQP4 isoform.

15 colonies were randomly selected from the ‘condition A’ YPD agar plates, and 5 colonies from the ‘condition B’ YPD agar plates. These colonies were made into YPD glycerol stocks (Section 2.4.2), streaked onto YPD agar plates containing 500 µg/mL zeocin (5× normal concentration used for selective pressure on YPD agar plates), and incubated for 72 h at 30 °C. Clones that grew to a high density on 500 µg/mL zeocin agar were presumed to have high

copy numbers of the M23 AQP4-plasmid construct. Figure 3.5 shows the 500 µg/mL zeocin colony screening, where T1 are the 15 clones selected from plasmid condition A (T1 C1–15), and T2 are the 5 clones selected from plasmid condition B (T2 C1–5). From this screen, the following clones were selected as those with highest resistance to zeocin; T1C2, T1C3, T1C6, T1C7, T1C8, T1C12, and T1C14. These clones were selected for AQP4 expression screening via western blot.

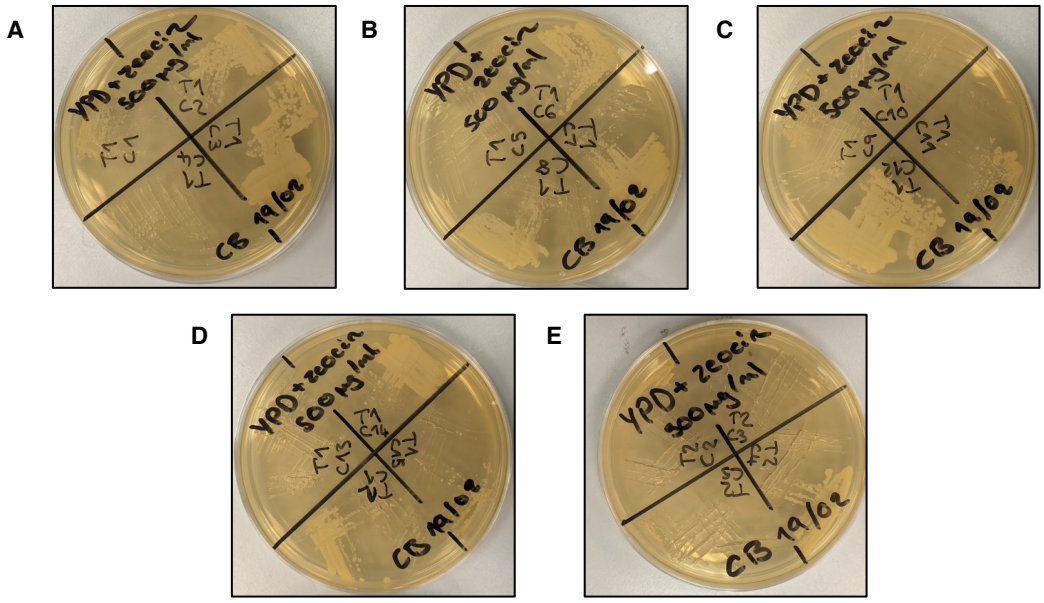

Figure 3.5. Increasing selective pressure to screen for *P. pastoris* transformation clones with highest resistance to zeocin.
LiCl transformation of *P. pastoris* wild type cells incubated with an hAQP4 M23 pPICZ plasmid construct containing the *BleoR* gene. Transformation colonies were selected at random and made into glycerol stocks. Glycerol stocks were used for streaking onto YPD agar plates containing 500 µg/mL zeocin. T1 C1–15 **(A – D)** are colonies transformed with plasmid that had been linearised and further purified using a DNA clean-up kit. T2 C1–5 **(D – E)** are colonies transformed with a plasmid that had only been linearised.

3.2.4. Screening transformation clones for AQP4 expression

The selected clones from the high zeocin resistance screen were streaked from their glycerol stocks and incubated (72 h, 30 °C) on YPD agar plates containing 100 µg/mL zeocin. The M1 AQP4 clone and original M23 AQP4 clone were also streaked onto YPD agar plates so that the new transformants could be compared for their relative expression. Single colonies for each clone were picked for small-scale cell growth and expression as described in Section

2.4.3. After resuspension of cultures in 5 mL dH_2O for cell breaking, OD_{600} was measured to check for similar cell density across the different clones. All cultures were within 10% variation of optical density. Cells were broken by glass bead homogenisation as described in Section 2.5.1. SDS-PAGE separation of cell lysates and western blotting were performed as described in Section 2.7.2 and 2.7.3. Figure 3.6A shows the resulting western blot, where the M1 AQP4 clone and original M23 clone were compared to the new M23 AQP4 transformants. The T1C3 clone appeared to be the best performing new clone for AQP4 expression. Densitometry analysis (Section 2.7.4) for band intensity revealed that this clone had 83% band intensity relative to the M1 clone (Figure 3.6B). This was calculated using the band intensity of the monomer and dimer AQP4 bands. This meant that T1C3 was the preferred new clone for adaptation to large-scale production of M23 AQP4.

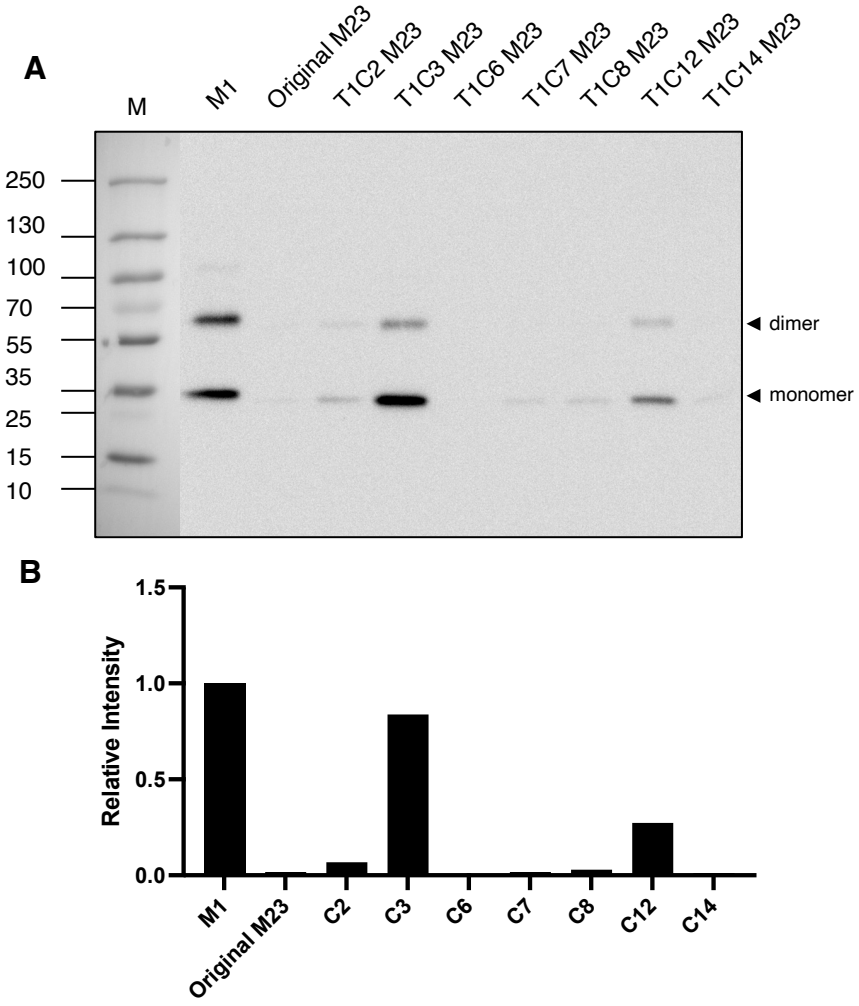

Figure 3.6. Screening the newly transformed *P. pastoris* clones for AQP4 expression.
New M23 AQP4 isoform *P. pastoris* clones were generated using LiCl transformation with a hAQP4 M23 pPICZ plasmid construct containing the *BleoR* gene. Clones were selected based on a high resistance to zeocin. 5 mL cultures of the M1 AQP4 clone, the original M23 AQP4 clone, and the new M23 AQP4 transformants, were grown, induced, and broken by glass bead homogenisation. Cell lysates were separated by 4–16% gradient SDS-PAGE, followed by western blotting. **A)** Western blot of cell lysates probing AQP4 with a rabbit anti-APQ4 Ab (1:5,000). An anti-rabbit-HRP Ab was used as secondary (1:2,500) and the blot was imaged using chemiluminescence. The blot lanes are labelled according to clone name, where; 'M1' is the established M1 AQP4 clone, 'Original M23' is the original M23 AQP4 clone, and the remaining labels are new M23 AQP4 transformants. Positions of monomer and dimer bands of AQP4 are labelled with arrows. MW markers are shown under 'M' with mass labels in kDa shown on the left of the blot. **B)** Bar chart quantifying AQP4 band intensity from the western blot in **A**, relative to the M1 clone. Intensity was calculated as the sum of intensity from both AQP4 monomer and dimer bands present for each clone. Bands were quantified using densitometry analysis.

With the T1C3 M23 AQP4 transformant established as the favourable clone for high expression, it was directly compared to the established M1 AQP4 clone in a separate small-scale growth and expression. This was done to perform a second repeat of growth and expression for the M1 and T1C3 M23 clones alongside each other. This meant that comparable AQP4 expression levels could be confirmed with the inclusion of non-induction controls for both of these clones. This was also used as an opportunity to test two different acrylamide concentrations for SDS-PAGE separation of AQP4.

The small-scale growth and expression (Section 2.4.3) were repeated as described for the M1 AQP4 clone and T1C3 M23 AQP4 clone. The non-induction control cultures were prepared using BMGY media throughout the entire growth process (no MeOH added at any stage). Cells were mechanically disrupted (Section 2.5.1), with lysates separated by SDS-PAGE and analysed by western blot probing AQP4 (Section 2.7.2 and 2.7.3).

Figure 3.7 shows the resulting western blots of the M1 and T1C3 M23 clone lysates alongside the non-induction controls. The non-induction controls do not give a signal, confirming that the signal is coming from MeOH induced production of AQP4 in both clones. M1 and M23 induced clones were loaded in adjacent lanes on the right for close comparison of the differences in MW between the AQP4 isoforms. Figure 3.7A and B represent 4–16% gradient and 8% acrylamide SDS-PAGE, respectively. 4–16% gradient SDS-PAGE was confirmed as the preferred choice of acrylamide concentration as it best demonstrated the mass difference between the M1 and M23 isoform (~35.6 vs ~33.1 kDa, respectively) and allowed even separation of AQP4 quaternary structures whilst still being able to visualise breakdown products below 30 kDa. As seen previously with the M1 clone, an AQP4 degradation band is now visible for both clones between 10 and15 kDa (Figure 3.7A).

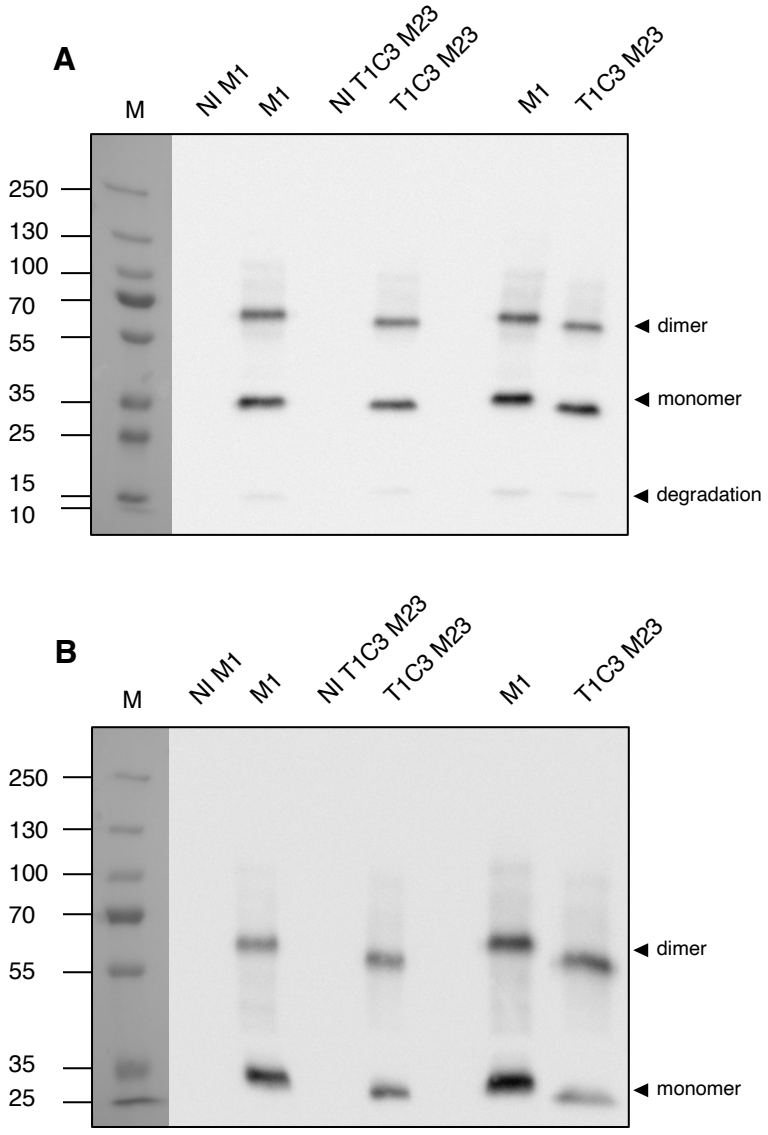

Figure 3.7. Screening the T1C3 M23 AQP4 clone against the M1 AQP4 clone.
A new M23 AQP4 isoform *P. pastoris* clone (T1C3) was generated using LiCl transformation with a hAQP4 M23 pPICZ plasmid construct and selected for highest expression of AQP4. 5 mL cultures of the M1 AQP4 clone and the new T1C3 M23 AQP4 clone were grown and split into induced and non-induced (NI) control conditions, and broken by glass bead homogenisation. Cell lysates were separated by SDS-PAGE, followed by western blotting. **A)** 4–16% acrylamide SDS-PAGE western blot targeting AQP4 of *P. pastoris* lysates from the M1 AQP4 clone and the T1C3 M23 AQP4 clone. NI represents lysates from non-induced control cultures that have not been induced for AQP4 expression with MeOH. **B)** 8% acrylamide SDS-PAGE western blot of samples specified in **A**. For both blots, AQP4 was probed with a rabbit anti-APQ4 Ab (1:5,000). An anti-rabbit-HRP Ab was used as secondary (1:2,500) and the blot was imaged using chemiluminescence. Positions of monomer, dimer and degradation bands of AQP4 are labelled with arrows. MW markers are shown under 'M' with mass labels in kDa shown on the left of each blot.

3.2.4. Light microscopy of the *P. pastoris* AQP4 clones

Throughout the growth and expression protocols, cell cultures were routinely examined by light microscopy to check for density at different growth stages and signs of contamination. The M1 and T1C3 M23 AQP4 *P. pastoris* clones were compared to each other after 48 h induction, to check that expression of AQP4 was not abnormally affecting cell morphology or cell survival (Figure 3.7). No apparent morphological differences between the M1 and M23 isoform *P. pastoris* clones was observed after AQP4 induction.

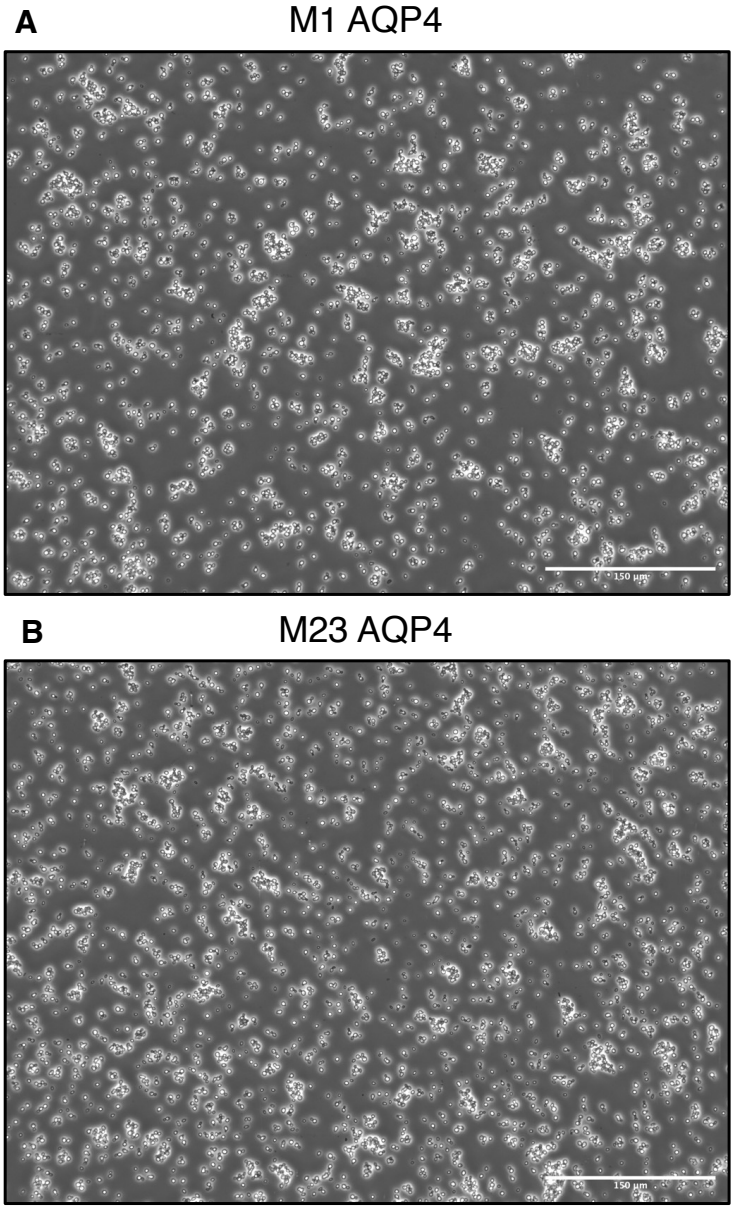

Figure 3.8. Light microscopy of *P. pastoris* M1 and T1C3 M23 AQP4 clones after induction. Images are of cultures after 48 h of induction in BMMY, with MeOH added to cultures at 1% final concentration at 24 h. Phase contrast images were captured at 20× magnification using an Invitrogen EVOS M5000 microscope. Scale bars represent 150 µm. Images of the cultures are labelled according to the *P. pastoris* clone – M1 AQP4 **(A)** and M23 AQP4 (T1C3) **(B)**.

3.3. Purification of AQP4 from the M1 and T1C3 M23 *P. pastoris* clones

Having confirmed that the newly transformed M23 AQP4 *P. pastoris* clone, T1C3, had an improved level expression compared to the original, the next step was to assess whether this clone would provide an improvement in purified AQP4 yield. As previously stated, the M1 AQP4 clone was already established as giving a high yield of pure protein and provided a good benchmark. The M1 AQP4 clone and T1C3 M23 AQP4 clone were cultured in shake-flasks for large-scale growth and expression, and cells were broken by high-pressure homogenisation for membrane fragment preparation (Section 2.4.4, 2.5.2, and 2.5.3).

3.3.1. Solubilisation efficiency of M1 and M23 AQP4 with SMA

Before purification of the M1 and M23 AQP4 isoforms, both were assessed for solubilisation efficiency at 2.5% w/v SMA. As previously mentioned, this concentration of SMA was optimised for purification of M1 AQP4 by Drs Philip Kitchen and Lucas Unger, and was used for solubilisation of M23 AQP4 to create comparable preparations of purified AQP4-SMALPs in downstream analyses.

Aliquots of resuspended membranes were defrosted and solubilised at 45 mg/mL with 2.5% w/v SMA for 1 h at RT followed by ultracentrifugation (100,000 × g, 4 °C, 45 min) to remove the insoluble fraction (Section 2.6.2). After separation of the soluble fraction, the insoluble fraction was resuspended in a volume of buffer equal to the total solubilisation volume. The soluble and insoluble fractions were incubated with Laemmli buffer (10 min, RT), before separation by 4–16% SDS-PAGE and western blotting. AQP4 in the samples was probed with a rabbit anti-AQP4 Ab (1:5,000, 16 h, 4 °C), followed by a secondary anti-rabbit-HRP linked Ab (1:2,500, 1 h, RT), and visualised by chemiluminescence.

Figure 3.9A shows a resulting western blot from an SMA solubilisation trial, with Figure 3.9B showing the results from four trial repeats analysed by densitometry (Section 2.7.4). Comparison of the isoform solubilisations by eye would suggest that M23 AQP4 appeared to show a lower solubilisation efficiency. M1 AQP4 demonstrated a solubilisation efficiency of 50.6 ± 4.0%, whereas M23 AQP4 demonstrated a solubilisation efficiency of 44.7 ± 4.7%. However, a Welch's unpaired t-test found no significant difference ($p = 0.107$) in solubilisation efficiency between M1 and M23 AQP4. This provided confidence to proceed to large-scale purification with 2.5% w/v SMA for both AQP4 isoforms. It is important to note the variability in

solubilisation efficiency, which may have resulted from insufficient re-homogenisation of the insoluble membrane fraction after ultracentrifugation of the SMA solubilised membranes.

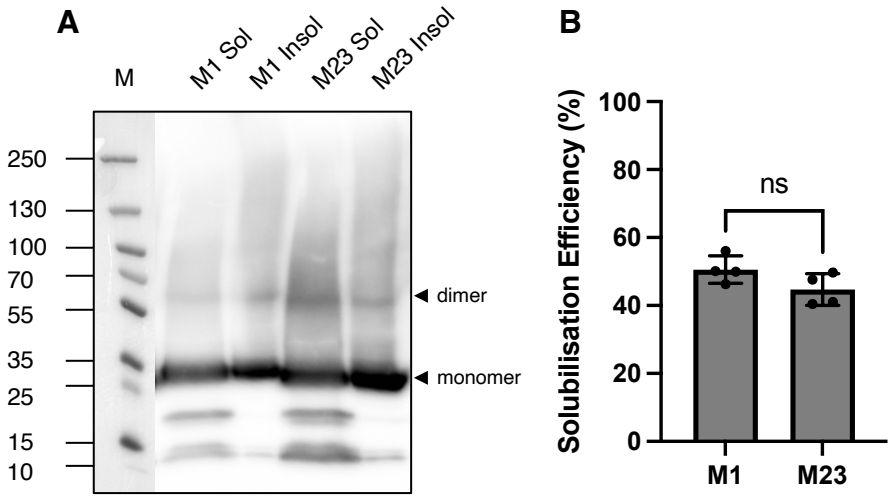

Figure 3.9. Solubilisation efficiency of M1 and M23 AQP4 with 2.5% w/v SMA.
Resuspended membranes of the M1 or T1C3 M23 AQP4 isoform *P. pastoris* clones were solubilised at 45 mg/mL with 2.5% w/v SMA. The soluble and insoluble fractions were separated by ultracentrifugation (100,000 × g, 45 min, 4 °C), with the insoluble fraction resuspended in a volume of buffer equal to the solubilisation volume after separation. Soluble and insoluble samples were separated by SDS-PAGE (4–16% gradient), followed by western blotting. **A)** Representative western blot of soluble and insoluble fractions for M1 and M23 AQP4 *P. pastoris* membranes after SMA solubilisation, where 'S' and 'I' represent soluble and insoluble fractions, respectively. AQP4 was probed with a rabbit anti-APQ4 Ab (1:5,000). An anti-rabbit-HRP Ab was used as secondary (1:2,500) and the blot was imaged using chemiluminescence. Positions of monomer and dimer bands of AQP4 are labelled with arrows. MW markers are shown under 'M' with mass labels in kDa shown on the left of the blot. **B)** Bar chart of solubilisation efficiency for M1 and M23 AQP4 at 2.5% SMA. Densitometry analysis of western blots (such as **A**) was used to calculate solubilisation efficiency (Soluble Intensity / Soluble + Insoluble Intensity). Data are shown as mean ± SD (n = 4 per AQP4 isoform clone). Statistical analysis was performed with a Welch's unpaired t-test (ns – $p > 0.05$ (not significant)).

3.3.2. Purification of M1 and M23 AQP4 from *P. pastoris* membranes for improved M23 AQP4 yield

Purification of AQP4 from the M1 and T1C3 M23 *P. pastoris* clones was performed similar to the that described in Section 3.1.2. Resuspended membranes were defrosted and solubilised with 2.5% w/v SMA followed by ultracentrifugation (100,000 × g, 4 °C, 45 min) to remove the insoluble fraction. 1.8 g membranes were solubilised for each clone. Membranes were solubilised at 45 mg/mL as stated in Section 2.6.2. Soluble AQP4-SMALPs were purified by Ni-NTA IMAC and separated by SDS-PAGE as previously described (Section 2.6.3 and 2.7.2).

Figure 3.10A and C show purification stages and elution fractions from IMAC purification of M1 AQP4, and Figure 3.10B and D show the same for M23 AQP4. A small amount of AQP4 appears to be lost during the 75 mM imidazole wash (collected from the second resin bed-volume), but the majority of the protein was eluted during the 300 mM imidazole elution. Monomer to tetramer quaternary structures are visible for both AQP4 isoforms. A contaminant band is present at ~40 kDa for the purified samples of both M1 and M23 AQP4.

As before, a separate purification was used to quantify the purified protein yield (Figure 3.10E). This purification was performed using 1.8 g membranes for both M1 and M23 AQP4 isoforms. Elution fractions were pooled and concentrated to 1 mL using a centrifugal concentrator with MW cut-off of 100 kDa. Samples were separated by SDS-PAGE and stained with Coomassie as already described. AQP4 concentration was estimated using densitometry analysis (Section 2.7.4.1), with a serial dilution of BSA to be used as a densitometry standard curve (as shown in Figure 3.10E). The total protein yield was ~1.15 mg M1 AQP4 and ~0.7 mg M23 AQP4. This equates to approximately ~0.64 mg protein per g of membranes from the M1 AQP4 clone, and ~0.39 mg protein per g of membranes from the M23 AQP4 clone.

Improved expression of M23 AQP4 from the new T1C3 *P. pastoris* clone appeared to have greatly improved the yield of purified M23 AQP4-SMALPs. Measuring by mg of purified protein per gram of membrane, the original M23 AQP4 clone provided less than $\frac{1}{25}$ of pure protein compared to the M1 AQP4 clone. By comparison, the T1C3 M23 AQP4 clone gave $\sim\frac{3}{5}$ of pure protein relative to the M1 AQP4 clone. There was also an improvement on the previous M1 AQP4 purification yield.

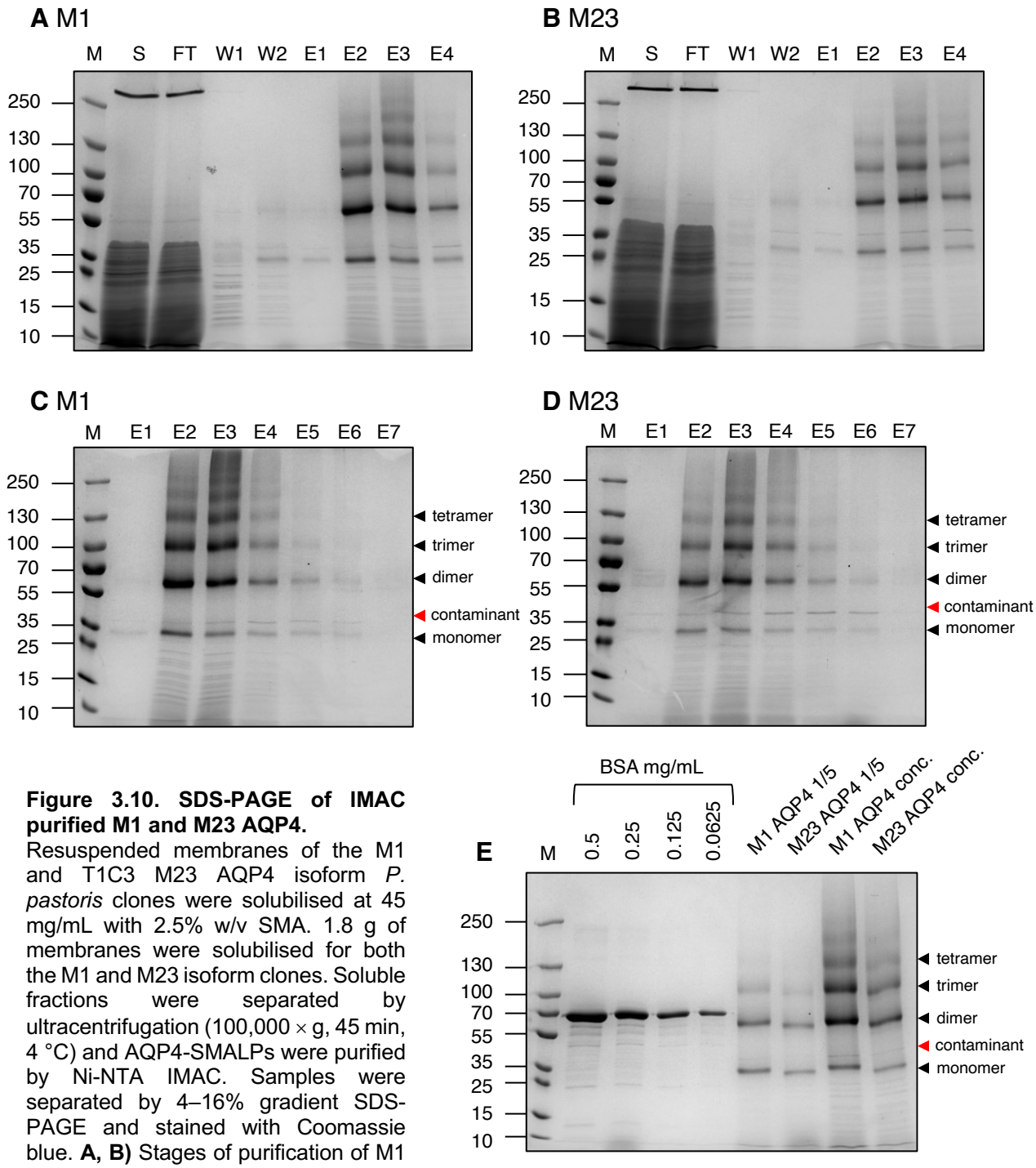

Figure 3.10. SDS-PAGE of IMAC purified M1 and M23 AQP4. Resuspended membranes of the M1 and T1C3 M23 AQP4 isoform *P. pastoris* clones were solubilised at 45 mg/mL with 2.5% w/v SMA. 1.8 g of membranes were solubilised for both the M1 and M23 isoform clones. Soluble fractions were separated by ultracentrifugation (100,000 × g, 45 min, 4 °C) and AQP4-SMALPs were purified by Ni-NTA IMAC. Samples were separated by 4–16% gradient SDS-PAGE and stained with Coomassie blue. **A, B)** Stages of purification of M1 **(A)** and M23 **(B)** AQP4, where 'S' is the soluble fraction after SMA solubilisation, 'FT' is the flowthrough from the affinity chromatography column (unbound protein), 'W1' is the second resin bed-volume of the imidazole wash at 20 mM, 'W2' is the second resin bed-volume of the imidazole wash at 75 mM, and E1–4 are consecutive elutions of ½ resin bed-volumes at 300 mM imidazole. **C, D)** 300 mM imidazole elution fractions from the same IMAC purification shown in **A** and **B**, where E1–6 represent consecutive elutions of ½ resin bed-volumes, and E7 represents the remaining elution of 9× resin bed-volumes. **E)** SDS-PAGE for protein concentration estimation where BSA was used as a standard in serial dilution. BSA concentrations are labelled for each lane. Samples labelled as 'conc.'are IMAC purified AQP4-SMALPs concentrated to 1 mL with 100 kDa MW cut-off, where samples labelled '1/5' are 5-fold dilutions of these concentrates. For gels **C**, **D** and **E**, positions of monomer, dimer, trimer and tetramer bands of AQP4 are labelled with black arrows. A contaminant band is labelled with a red arrow. For all gels, MW markers are shown under 'M' with mass labels in kDa shown on the left of each gel.

3.3.3. Comparing protein stability between IMAC elution and centrifugal concentration

During initial purification optimisation, a lower-than-expected band intensity was frequently observed for M1 AQP4 IMAC purifications that were left for 24 h at 4 °C overnight before centrifugal concentration using MW cut-off filters. This was unexpected, as AQP4-SMALPs appeared stable based on SDS-PAGE run immediately after IMAC purification. SMALPs are also reported to retain functional stability at 4 °C for multiple weeks (Jamshad, Charlton, *et al.*, 2015).

In order to assess whether protein degradation was taking place after IMAC purification, the two separate purifications of M1 and M23 AQP4 discussed above (Section 3.3.2. and Figure 3.10) were compared as they had been concentrated and preserved in Laemmli buffer at two different time points. The AQP4 IMAC purifications shown in Figure 3.10E were concentrated to 1 mL immediately after Ni-NTA IMAC elution, whereas the AQP4 IMAC elutions shown in Figure 3.10C and D were pooled and concentrated to 1 mL after 24 h at 4 °C. In both cases, the purified protein samples were incubated with Laemmli buffer (10 min, RT) and frozen immediately after concentration. All of the purified protein samples were prepared following the same SMA solubilisation and IMAC purification protocol (Section 2.6.2 and 2.6.3). The M1 and M23 *P. pastoris* membranes used for these two separate purifications were from the same cell batch preparations and the same quantity of membranes had been used for each solubilisation.

Figure 3.11 shows the resulting 4–16% SDS-PAGE of these samples. The M1 AQP4 band intensity was much lower after 24 h when compared to the M1 AQP4 concentrated immediately after Ni-NTA IMAC elution. By comparison, the M23 AQP4 showed increased intensity at high MW after 24 h when compared to M23 AQP4 concentrated immediately after Ni-NTA IMAC elution. After 24 h, the purified M23 AQP4 sample also appeared to have increased intensity of the contaminant band. Some AQP4 is present in the MW cut-off flowthrough for the M1 and M23 AQP4 samples concentrated immediately after Ni-NTA IMAC elution.

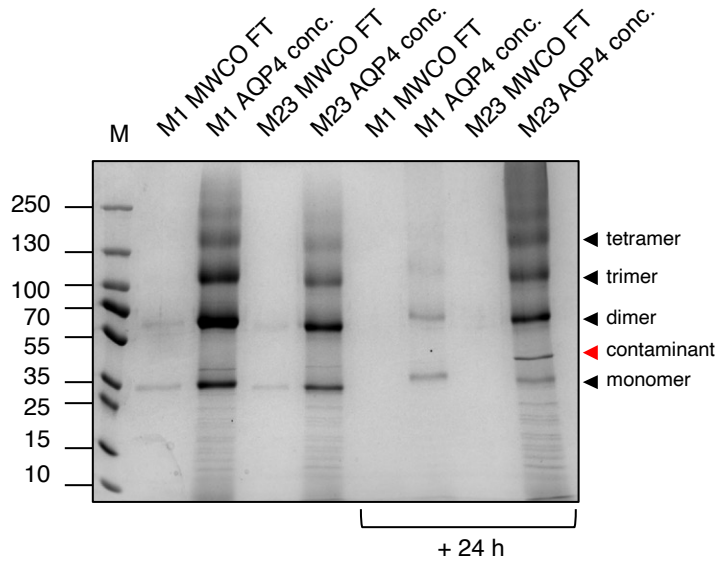

Figure 3.11. SDS-PAGE of IMAC purified and concentrated M1 and M23 AQP4.
Resuspended membranes of the M1 or M23 AQP4 isoform *P. pastoris* clones were solubilised at 45 mg/mL with 2.5% w/v SMA. 1.8 g membranes were solubilised for both the M1 and M23 isoforms. Soluble fractions were separated by ultracentrifugation (100,000 × g, 45 min, 4 °C) and AQP4-SMALPs were purified by Ni-NTA IMAC. Purified AQP4 isoforms were concentrated to 1 mL with 100 kDa MW cut-off, separated by 4–16% gradient SDS-PAGE, and stained with Coomassie blue. Samples labelled 'conc.' are the AQP4 concentrates, where 'MWCO FT' represents the flowthrough from centrifugal concentrators. Samples labelled '+ 24 h' were concentrated 24 h after elution from the Ni-NTA agarose resin. Positions of monomer, dimer, trimer and tetramer bands of AQP4 are labelled with black arrows. A contaminant band is labelled with a red arrow. MW markers are shown under 'M' with mass labels in kDa shown on the left of each gel.

3.4. Increasing protein production using bioreactors

Up to this point, large-scale cell growth and membrane preparation had been done in 2.5 L baffled shake flasks. For adequate aeration and optimal growth of *P. pastoris* cultures, the volume of media used was 10% of the flask volume (i.e. 250 mL BMGY in 2.5 L flasks). This was maintained for all shake-flask growth protocols used in this project. For multiple litres of culture, this required multiple flasks and extra preparation time.

Cell culture in bioreactors allows for continuous monitoring of culture conditions in a closed system. This means that automatic adjustments can be made for conditions such as pH, temperature, and dissolved oxygen concentration (DO; by adjusting stirrer speed or gas flow). This maintains suitable conditions for cell cultures to grow quickly and to a high density. By comparison, cell culture in shake flasks can be difficult to monitor at frequent time-steps,

resulting in lower sensitivity to culture changes and adequate adjustments. In additions to this, shake flasks are not normally considered a closed system – frequent opening and closing of flasks to add required materials such as MeOH increases the risk of culture contamination.

3.4.1. Growth of M1 and M23 AQP4 *P. pastoris* clones in bioreactors

To make production of *P. pastoris* membranes easier and more efficient, bioreactor vessels were used for growth of M1 and M23 AQP4 *P. pastoris* clones (Section 2.4.5). The bioreactor growth profiles for these clones are shown in Figure 3.12 and Figure 3.13. Briefly, starter cultures for M1 or M23 AQP4 *P. pastoris* clones were used to inoculate BMGY in equilibrated bioreactor vessels with added chloramphenicol to prevent contamination. Vessels were set-up to monitor temperature (maintained at 30 °C), pH (maintained at pH 6), DO (maintained above 30%), and off-gases. After batch phase glycerol from the starting BMGY media had been used up (indicated by DO spike 1 in Figure 3.12 and 3.13), a glycerol fed-batch phase at a rate of 14 mL L^{-1} h^{-1} of 50% v/v glycerol was provided for 4 h. Cultures were then grown and starved until another DO spike (DO spike 2 in Figure 3.12 and 3.13). This was used an indicator to begin MeOH induction. A DO spike in the culture medium indicates decreased oxygen demand by the culture as a result of decreased aerobic metabolism due to the primary carbon source (glycerol) being depleted. It is important to ensure that glycerol in the medium has been used up, as it represses the *AOX1* promoter (Inan and Meagher, 2001; Ahmad *et al.*, 2014). After 48 h induction with MeOH at a rate of 4.8 mL L^{-1} h^{-1} 50% v/v MeOH, cultures were harvested by centrifugation (4,000 × g, 20 min, 4 °C) to pellet the cells. Cell pellets were frozen at -80 °C.

Due to sensitivity issues with the DO sensor in the later stages of this project, it became difficult to distinguish DO spikes in culture bioreactor profiles. Figure 3.11 was provided by Dr Philip Kitchen for this thesis in order to demonstrate a desirable culture trace for the M1 AQP4 *P. pastoris* clone. Despite issues with DO sensor sensitivity, cultures were still grown according to approximate time stages for batch and glycerol depletion (starvation) phases. The duration of these phases was based on DO spike time points in previous successful cultures – the glycerol fed-batch phase was started approximately 20 h after vessel inoculation, with MeOH induction started approximately 44 h after inoculation (~20 h after the end of the 4 h glycerol feed). These cultures produced comparable levels of AQP4 expression to previous cell batches relying on the DO sensor (refer to measured expression from bioreactor culture repeats shown in Figure 3.16B).

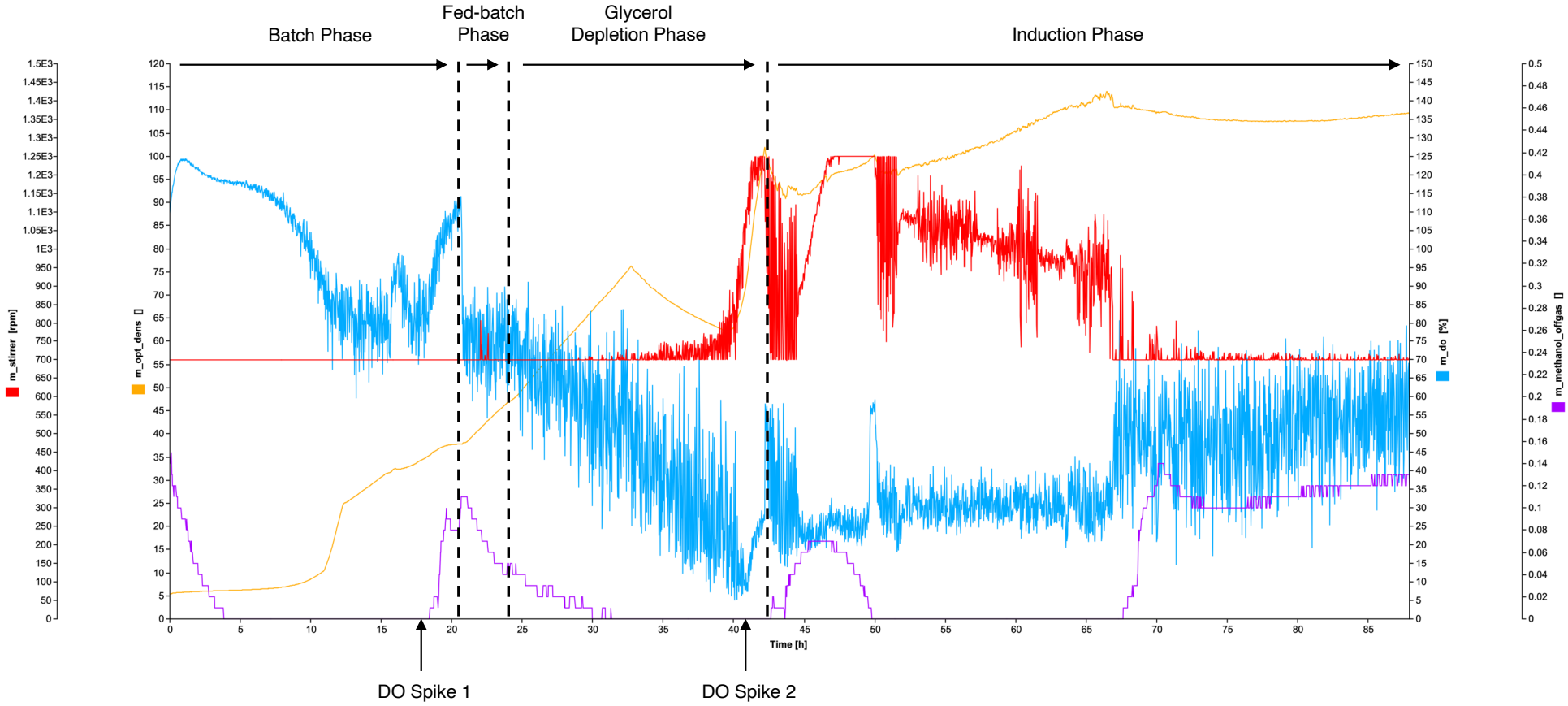

Figure 3.12. Bioreactor growth profile of the *P. pastoris* M1 AQP4 clone.
Blue: dissolved oxygen (%). Purple: MeOH off-gas (%). Yellow: Optical density of culture (AU). Red: Stirrer speed (rpm). Phases of culture feeding conditions are separated by dotted lines. Batch phase indicates the growth phase relying on the glycerol in the growth medium only. Fed-batch phase indicates the glycerol fed-batch stage with a feed rate of 14 mL L^{-1} h^{-1} of 50% v/v glycerol. Glycerol depletion phase indicates the growth and starvation phase (no feeding). Induction phase indicates MeOH induction with a feed rate of 4.8 mL L^{-1} h^{-1} 50% v/v MeOH. Time points of DO spikes used to determine the start of the fed-batch and induction phases are indicated by DO spike arrows 1 and 2, respectively. Data collected by Dr Philip Kitchen.

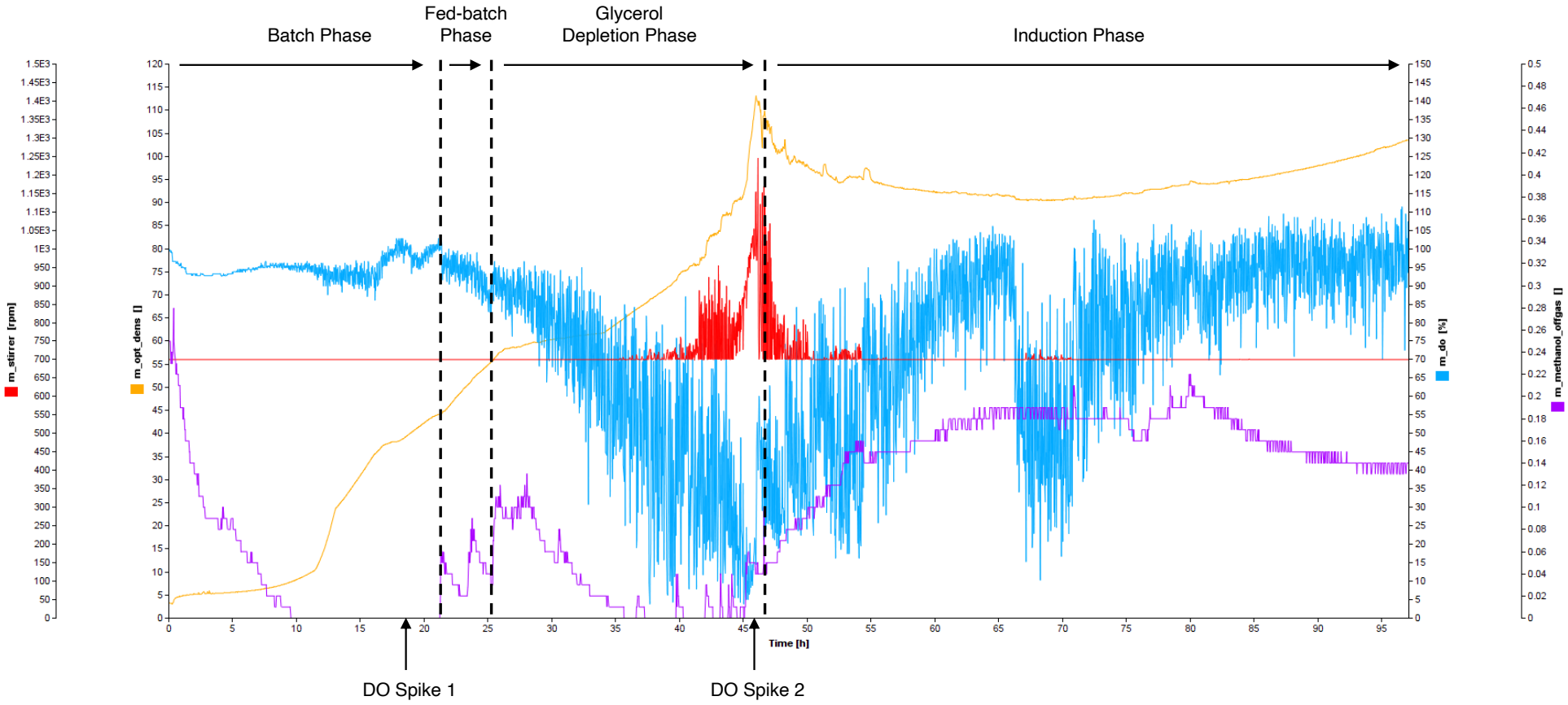

Figure 3.13. Bioreactor growth profile of the T1C3 M23 AQP4 *P. pastoris* clone.
Blue: dissolved oxygen (%). Purple: MeOH off-gas (%). Yellow: Optical density of culture (AU). Red: Stirrer speed (rpm). Phases of culture feeding conditions are separated by dotted lines. Batch phase indicates the growth phase relying on the glycerol in the growth medium only. Fed-batch phase indicates the glycerol fed-batch stage with a feed rate of 14 mL L^{-1} h^{-1} of 50% v/v glycerol. Glycerol depletion phase indicates the growth and starvation phase (no feeding). Induction phase indicates MeOH induction with a feed rate of 4.8 mL L^{-1} h^{-1} 50% v/v MeOH. Time points of DO spikes used to determine the start of the fed-batch and induction phases are indicated by DO spike arrows 1 and 2, respectively.

3.4.2. Expression of AQP4 in *P. pastoris* membranes produced in bioreactors

As with the large-scale shake flask preparations, cells from bioreactor cultures were defrosted and broken using high pressure homogenisation (Section 2.5.2). Cell debris and unbroken cells were removed by centrifugation (4,000 × g, 4 °C, 10 min), and cell lysate was spun via ultracentrifugation (150,000 × g, 4 °C, 90 min) to pellet the cell membrane. Membrane pellets were homogenised and resuspended (Section 2.5.3), before freezing in aliquots at - 80 °C.

Firstly, it was important to check that AQP4 had been adequately expressed using bioreactors as a growth and induction method and confirm that the M1 and T1C3 M23 AQP4 *P. pastoris* clones were showing comparable AQP4 expression. Defrosted membrane fragments were incubated with Laemmli buffer (10 min, RT), separated by 4–16% gradient SDS-PAGE at a concentration of 36 mg/mL, before analysis by western blot (Section 2.7.3). AQP4 in the samples was probed with a mouse anti-His Ab (1:2,500, 16 h, 4 °C), followed by a secondary anti-rabbit-HRP linked Ab (1:2,500, 1 h, RT), and visualised by chemiluminescence.

Figure 3.14 shows the resulting western blot. Probing with an anti-His Ab showed that AQP4 could be targeted using the recombinant 6× His-tag. Expression between the two AQP4 isoform clones appears comparable and at a reasonably high level, as observed with small-scale preparations. The previously seen AQP4 degradation band at 10–15 kDa is visible for both clones. As the 6× His-tag is on the AQP4 C-terminus, this degradation product must be part of the C-terminal end of the AQP4 sequence.

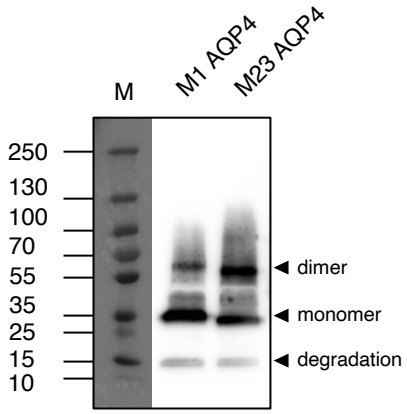

Figure 3.14. Western blot targeting expression of AQP4 in membrane fragments isolated from *P. pastoris* clones cultured in bioreactors.
Cultures of the M1 AQP4 clone and the T1C3 M23 AQP4 clone were grown and induced in bioreactors, followed by high pressure cell homogenisation. Membrane fragments were separated from cell lysates by ultracentrifugation (150,000 × g, 90 min, 4 °C). Resuspended membrane fragments were separated by 4–16% gradient SDS-PAGE at a concentration of 36 mg/mL, followed by western blotting. AQP4 was probed with a mouse anti-His Ab (1:2,500). An anti-mouse-HRP Ab was used as secondary (1:2,500) and the blot was imaged using chemiluminescence. Lanes are labelled according to the membranes loaded. Positions of monomer, dimer and degradation bands of AQP4 are labelled with arrows. MW markers are shown under 'M' with mass labels in kDa shown on the left of the blot.

3.5. Comparing culture production in shake flasks and bioreactors

To establish bioreactors as a production method for M1 and M23 AQP4, it was important to compare them to shake flasks for their efficiency in cell production for membrane fragment extraction, and AQP4 expression for purification yield.

3.5.1. Comparison of cell pellet yield from shake flasks and bioreactors

To demonstrate the ability of bioreactor cultures to reach a higher culture density than shake flask cultures, culture yields after growth and induction were compared between shake flask and bioreactor cultures. Wet cell pellet weights were measured after cultures were centrifuged (4,000 × g, 20 min, 4 °C) and the growth medium was discarded. As the M1 and T1C3 M23 AQP4 *P. pastoris* clones grew to comparable culture densities and gave consistent wet cell pellet yields, yield weights for the clones were pooled together per condition (shake flask or bioreactor culture).

Figure 3.15 compares the wet cell pellet yields in g/L of culture. Bioreactor cultures clearly grew to a higher density per litre of culture and, as a result, could provide a higher cell pellet

yield for a given volume of growth medium. A Welch's unpaired t-test found a significant difference between shake flask and bioreactor wet pellet yields (g/L).

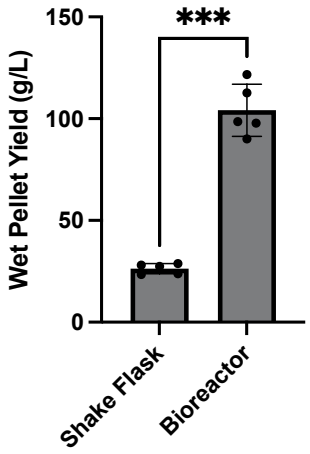

Figure 3.15. *P. pastoris* wet cell pellet yields from cultures grown in baffled shake flasks and bioreactors.
P. pastoris cultures were grown and induced in baffled shake flasks or bioreactors. Bar chart shows wet cell pellet yields (g/L) from each growth method after centrifugation of culture (4,000 × g, 20 min, 4 °C). Wet cell pellet yields from M1 and M23 AQP4 *P. pastoris* clones were used together as replicates for each condition (shake flask or bioreactor). Data are shown as mean ± SD (n = 5 per culture method). Statistical analysis was performed with a Welch's unpaired t-test (***p ≤ 0.001).

3.5.2. Comparison of AQP4 expression in membranes produced in shake flasks or bioreactors

Although the culture density and resulting cell pellet yield were significantly higher from bioreactor cultures, it was important to ascertain whether AQP4 expression in the extracted membrane fragments could match that observed for shake flask cultures. This would confirm whether bioreactors were going to provide a more efficient production system for membranes from which to purify the AQP4 isoforms.

Membrane fragments from shake flask and bioreactor cultures were prepared as discussed previously (Section 2.5.2 and 2.5.3) and were frozen as aliquots at -80 °C. Membrane aliquots for the M1 and M23 AQP4 clones were defrosted and incubated with Laemmli buffer (10 min, RT), separated by 4–16% gradient SDS-PAGE at a concentration of 36 mg/mL, followed by western blotting. AQP4 in the samples was probed with a rabbit anti-AQP4 Ab (1:5,000, 16 h, 4 °C), followed by a secondary anti-rabbit-HRP linked Ab (1:2,500, 1 h, RT), and visualised by chemiluminescence.

Figure 3.16A shows the resulting western blot. There aren't any large visual differences in AQP4 membrane fragment expression between shake flask and bioreactor cultures for either the M1 or T1C3 M23 clones. Similar degradation products are visible for both isoforms for both growth methods. This includes the AQP4 degradation band at 10–15 kDa seen previously. In total, two repeats per culturing method per isoform clone were analysed by western blot (Figure 3.16A shows one representative example). Figure 3.16B shows the AQP4 band intensity calculated from these western blots. Intensity was calculated by densitometry (Section 2.7.4) and reported relative to the mean of the M1 AQP4 bioreactor band intensity. It is clear that membrane expression of AQP4 can vary between batches, but there are no obvious outliers, and there are no clear differences in expression between shake flask and bioreactor cultures.

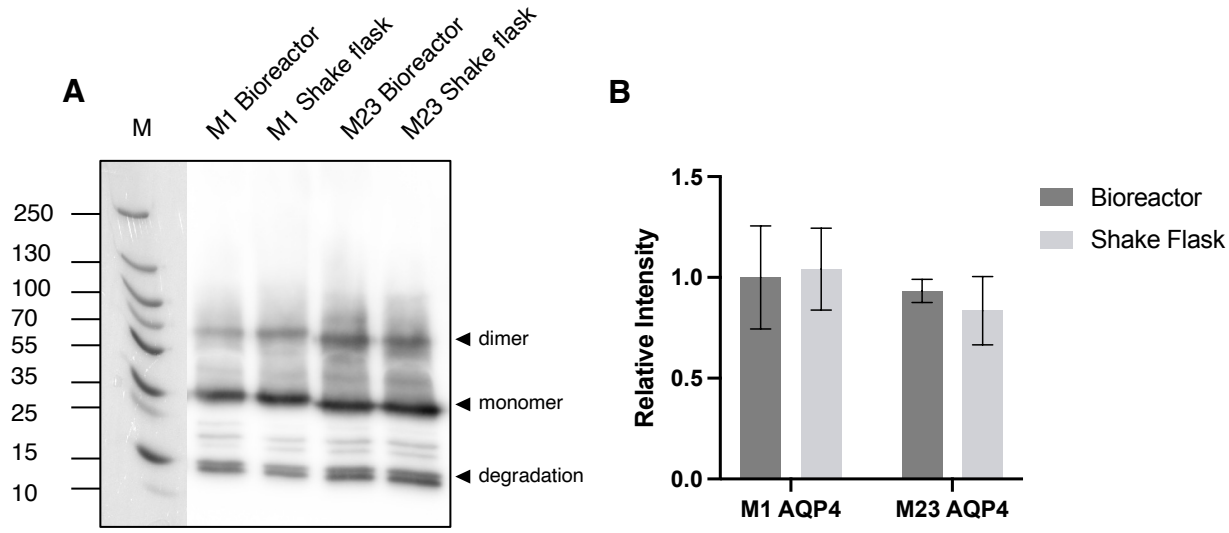

Figure 3.16. Comparing expression of AQP4 in membrane fragments isolated from *P. pastoris* clones cultured in baffled shake flasks or bioreactors.
Cultures of the M1 AQP4 clone and the T1C3 M23 AQP4 clone were grown and induced in baffled shake flasks or bioreactors, followed by high pressure cell homogenisation. Membrane fragments were separated from cell lysates by ultracentrifugation (150,000 × g, 90 min, 4 °C). Resuspended membrane fragments were separated by 4–16% gradient SDS-PAGE at a concentration of 36 mg/mL, followed by western blotting. **A)** Representative western blot of membrane fragments, with lanes labelled according to the AQP4 isoform *P. pastoris* clone and growth method. AQP4 was probed with a rabbit anti-APQ4 Ab (1:5,000). An anti-rabbit-HRP Ab was used as secondary (1:2,500) and the blot was imaged using chemiluminescence. Positions of monomer, dimer and degradation bands of AQP4 are labelled with arrows. MW markers are shown under 'M' with mass labels in kDa shown on the left of the blot. **B)** Bar chart quantifying AQP4 band intensity from western blots such as **A**. Bands were quantified using densitometry analysis. Intensity was calculated as the sum of intensity from both AQP4 monomer and dimer bands present for each condition. Values are relative to the M1 AQP4 Bioreactor mean intensity. Data are shown as the mean with error bars representing the range (n = 2 per condition).

3.6. Chapter Summary

This chapter has described how two existing clones of *P. pastoris* expressing recombinant constructs of either the M1 or M23 isoform of AQP4 were grown and induced to compare their levels of AQP4 expression and protein yield after purification. With the original M23 clone showing comparatively poor levels of expression and pure protein yield compared to the M1 clone, *P. pastoris* was chemically transformed with the recombinant hAQP4-M23-plasmid construct to generate a new clones. A clone, T1C3, showing higher levels of M23 AQP4 expression was selected, and shown to give a pure protein yield comparable to yields from the M1 AQP4 clone. Both AQP4 isoform clones were cultured in bioreactors to establish a more efficient and higher-yielding way of producing membrane fragments for AQP4 purification and downstream analysis.

4. Biophysical characterisation of M1 and M23 AQP4-SMALPs

Having shown that M1 and M23 isoforms of AQP4 can be purified in SMALPs to comparative yields, and cultured in bioreactors to provide a more efficient way of producing membranes for solubilisation, the purified AQP4-SMALPs were next biophysically characterised.

This chapter describes how IMAC purified AQP4-SMALPs were characterised by SMA-PAGE, mass photometry, and SEC. SEC purified AQP4-SMALPs were then further characterised by flow-induced dispersion analysis (FIDA) and a thermal stability assay. Following this, AQP4-SMALPS were probed in solution using an anti-AQP4 Ab to investigate whether AQP4 could be identified within SMALPs using mass photometry. Mass photometry, SEC, and SMA-PAGE were then compared as mass estimation techniques for AQP4-SMALPs.

Apart from initial SMA-PAGE optimisation (Figure 4.1 and 2) and SEC with the Superdex 200 column (Figure 4.6), all analyses in this chapter were performed with M1 and M23 AQP4-SMALPs solubilised from membrane fragments extracted from bioreactor cultures, as described in Section 3.4.2. For Figures 4.1, 4.2, and 4.6, SMALPs were solubilised from membrane fragments extracted from shake flasks (Section 3.3).

4.1. Initial characterisation of IMAC purified AQP4-SMALPs

Having shown with SDS-PAGE analysis that M1 and M23 isoforms of AQP4 could be efficiently purified using SMA solubilisation and Ni-NTA IMAC, the next step was to characterise the IMAC purified SMALP particles using SMA-PAGE and mass photometry, before further purification by SEC.

4.1.1. SMA-PAGE optimisation and visualising AQP4-SMALP degradation

SMA-PAGE was developed as a native PAGE technique for MP-SMALPs by Pollock *et al.*, essentially utilising native PAGE with conditions optimised for separation of SMALPs, such as using loading buffers and running gels at pH ≥ 8. At this pH, SMA is soluble and negatively charged, which is thought to allow it to migrate during PAGE, regardless of charge associated with the encapsulated MP (Pollock *et al.*, 2019).

For this project, SMA-PAGE was intended for analysis and comparison of native AQP4-SMALPs after IMAC purification and after further separation by SEC. At this optimisation stage, a suitable M23 AQP4 *P. pastoris* clone had not been established for M23 AQP4 high-yield purification alongside M1 AQP4. Therefore, results show optimisation of SMA-PAGE using M1 AQP4 alone. For initial optimisation, the technique was first tested using only IMAC purified AQP4-SMALPs. SMA-PAGE was performed using an adapted method from Pollock *et al.*, 2019 (Section 2.7.5).

Resuspended membranes of the M1 AQP4 isoform *P. pastoris* clone were solubilised at 45 mg/mL with 2.5% w/v SMA. The soluble fraction was separated by ultracentrifugation and AQP4-SMALPs were purified by Ni-NTA IMAC (Section 2.6). IMAC purified AQP4-SMALPs were concentrated with 100 kDa MW cut-off, separated by SMA-PAGE, and stained with Coomassie blue (Section 2.7.5). Crucially, non-denaturing and non-reducing loading buffers and running gels were used to preserve AQP4-SMALP complexes. Two concentrations of acrylamide were tested for the SMA-PAGE gels (10% and a 3–20% gradient). AQP4-SMALPs were also loaded onto gels at full and half concentration after MW cut-off concentration to assess a suitable total protein load.

Figure 4.1 shows the resulting SMA-PAGE gels for optimisation. At full concentration, AQP4-SMALPs show better visibility than at half concentration, demonstrating that a high quantity of pure protein is needed to visualise with Coomassie. The predicted position of the AQP4-SMALP band (~300 kDa relative to the MW markers) is indicated on the gels. The 3–20% acrylamide gradient gel provided better separation of the AQP4-SMALPs. This gel presented further bands at higher MWs compared to those visualised by the 10% gel. Therefore, this gel concentration was chosen for future SMA-PAGE analysis. There was also indication of unmigrated protein, suggesting the existence of even larger SMALP particles or potential aggregates.

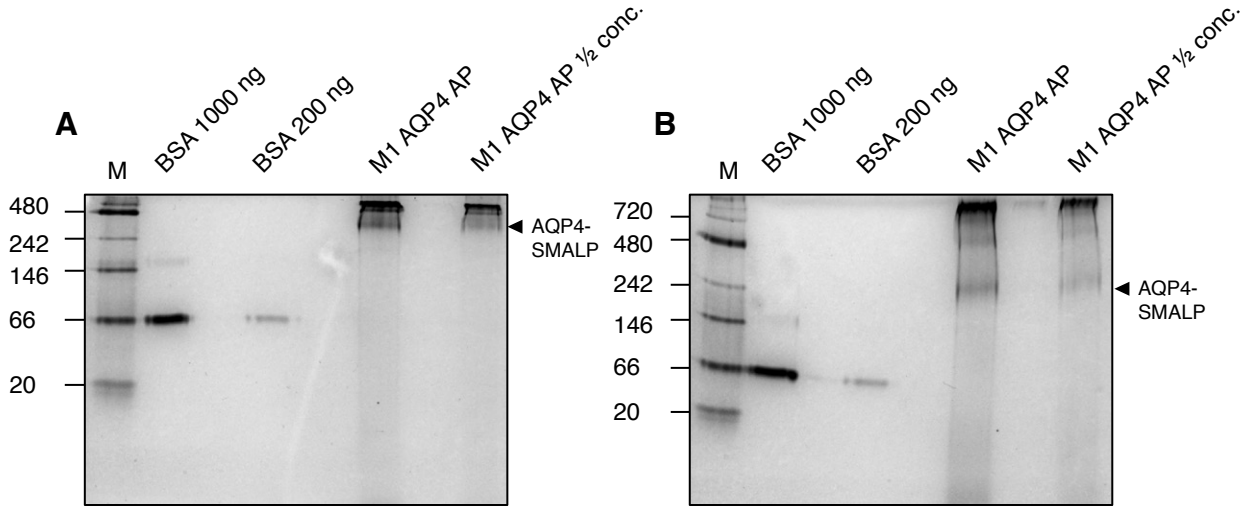

Figure 4.1. Comparing acrylamide concentrations for SMA-PAGE analysis of IMAC purified AQP4-SMALPs.
Resuspended membranes of the M1 AQP4 isoform *P. pastoris* clone were solubilised at 45 mg/mL with 2.5% w/v SMA. The soluble fraction was separated by ultracentrifugation (100,000 × g, 45 min, 4 °C) and AQP4-SMALPs were purified by Ni-NTA IMAC. IMAC purified AQP4-SMALPs were concentrated with 100 kDa MW cut-off, separated by SMA-PAGE (non-denaturing conditions) and stained with Coomassie blue. **A)** 10% acrylamide SMA-PAGE of purified and concentrated M1 AQP4-SMALPs. **B)** 3–20% acrylamide gradient SMA-PAGE of purified and concentrated M1 AQP4-SMALPs. For both gels, 'AP' represents Ni-NTA IMAC purified and concentrated AQP4-SMALPs, with '½ conc.' representing the same sample diluted twofold in purification buffer. An arrow indicates the position of the predicted M1 AQP4-SMALP band. NativeMark and BSA markers are shown under 'M' and 'BSA' (with loaded quantity in ng), respectively, with mass labels in kDa shown on the left.

Two Ni-NTA IMAC purifications of M1 AQP4 were performed ~1.5 months apart, as described for the previous experiment, with both preparations being stored at 4 °C after purification and concentration. This was used as an opportunity to assess SMALP degradation over time. SMALP stability is reported to be very good, with complexes being stable for multiple weeks (Jamshad, Charlton, *et al.*, 2015). However, as seen in Section 3.3.3, AQP4-SMALPs (and M1 AQP4) appear to degrade after IMAC elution. Pollock *et al.* were also able to demonstrate that SMA-PAGE could be followed by immunoblotting (Pollock *et al.*, 2019). This method was used here alongside Coomassie staining to provide a more sensitive detection method for degradation products.

The two preparations of IMAC purified M1 AQP4-SMALPs, one newly purified and another purified and stored for ~1.5 months at 4 °C, were separated by 3–20% SMA-PAGE. One gel was stained with Coomassie, and another was used for western blotting (Section 2.7.3). For the SMA-PAGE western blot, the newly purified AQP4-SMALPs were loaded at a 20-fold dilution, whereas the ~1.5 month old sample was diluted 5-fold. This was to ensure that bands

could be visualised, as degradation was expected to result in a lower band intensity. AQP4 in the samples was probed with a rabbit anti-AQP4 Ab (1:5,000, 16 h, 4 °C), followed by a secondary anti-rabbit-HRP linked Ab (1:2,500, 1 h, RT), and visualised by chemiluminescence.

Figure 4.2 shows the resulting SMA-PAGE stained with Coomassie (Figure 4.2A) and SMA-PAGE western blot (Figure 4.2B). The M1 AQP4-SMALP stored for ~1.5 months after IMAC purification and concentration appeared to show the predicted AQP4-SMALP band at lower MW relative to the newly purified sample. The older sample also appeared to show degradation products below the predicted AQP4-SMALP band (Figure 4.2B).

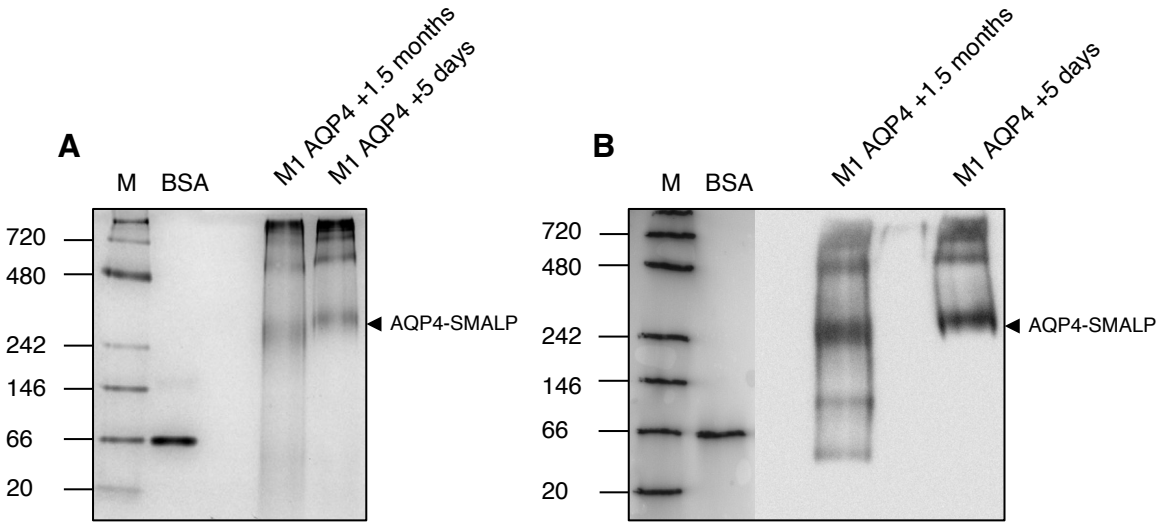

Figure 4.2. Investigating AQP4-SMALP degradation by SMA-PAGE analysis.
Resuspended membranes of the M1 AQP4 isoform *P. pastoris* clone were solubilised at 45 mg/mL with 2.5% w/v SMA. The soluble fraction was separated by ultracentrifugation (100,000 × g, 45 min, 4 °C) and AQP4-SMALPs were purified by Ni-NTA IMAC. IMAC purified AQP4-SMALPs were concentrated with 100 kDa MW cut-off. This was performed for two separate purifications ~1.5 months apart. Purified and concentrated AQP4-SMALPs were kept at 4 °C before separation by 3–20% acrylamide SMA-PAGE (non-denaturing conditions). **A)** SMA-PAGE of purified and concentrated M1 AQP4-SMALPs stained with Coomassie blue. **B)** SMA-PAGE western blot of purified and concentrated M1 AQP4-SMALPs. AQP4 was probed with a rabbit anti-AQP4 Ab (1:5,000). An anti-rabbit-HRP Ab was used as secondary (1:2,500) and the blot was imaged using chemiluminescence. For both **A** and **B**, 'M1 AQP4 +1 month' represents AQP4-SMALPs kept at 4 °C for 1.5 months after purification, and 'M1 AQP4 +5 days' represents AQP4-SMALPs kept at 4 °C for 5 days after purification. An arrow indicates the position of the predicted M1 AQP4-SMALP band. NativeMark and BSA markers are shown under 'M' and 'BSA', respectively, with mass labels in kDa shown on the left. NativeMark and BSA markers for the western blot (**B**) were stained with Ponceau S and marked with pen for imaging.

4.1.2. Mass photometry characterisation of IMAC purified AQP4-SMALPs

As discussed in Section 1, mass photometry has been developed as a label-free method to quantify the mass of biological molecules. Molecules in solution can be detected as binding events to a glass slide. Measured contrast is proportional to molecule mass and the mass of unknown molecules can be estimated by calibrating contrast to masses of known standards (Young *et al.*, 2018; Asor *et al.*, 2025). Mass photometry has already been used for analysis of MP-SMALPs, and was able to characterise these particles after SEC purification (Olerinyova *et al.*, 2021). Mass photometry offers a novel approach to quantify the mass of MP-SMALPs, which can be difficult due to the innate heterogeneity of these complexes containing protein, lipids, and SMA.

As shown in Section 3, M23 AQP4 had been IMAC purified with conditions optimised for M1 AQP4 by Drs Philip Kitchen and Lucas Unger. This allowed preparation of the two AQP4-SMALP isoforms using comparable conditions, with M23 AQP4 showing purification results comparable to that of M1 AQP4 (Section 3.3). Due to the ability of mass photometry to quickly analyse samples of low concentration, it lends itself as a technique for rapid assessment of IMAC purification fractions. Therefore, mass photometry was used to investigate M23 elution fractions at increasing concentrations of imidazole, to confirm that IMAC purification conditions optimised for M1 AQP4-SMALPs were equally applicable to M23 AQP4-SMALPs.

Resuspended membranes (1.8 g) of the M23 AQP4 isoform *P. pastoris* clone were solubilised at 45 mg/mL with 2.5% w/v SMA. The soluble fraction was separated by ultracentrifugation and AQP4-SMALPs were purified by Ni-NTA IMAC (Section 2.6). Instead of elution at 300 mM imidazole as per standard protocol, M23 AQP4-SMALPs were eluted with increasing imidazole concentrations: 100 mM, 150 mM, 200 mM, 250 mM, 300 mM and 600 mM. Two consecutive fractions of 300 mM imidazole were used to ensure protein had been eluted at the standard concentration used for elution. All elution fractions were 2.5× resin bed-volumes, as the majority of M23 AQP4 had eluted by this volume at 300 mM imidazole according to purification results shown in Figure 3.10. Elution fractions were immediately analysed by mass photometry (Section 2.8.2), droplet diluting by half into sample well cassettes.

Figure 4.3 shows the resulting mass photometry analysis of the elution fractions. Counts were normalised to compare relative proportion of sample components in each fraction. Peaks predicted to represent the M23 AQP4-SMALPs were fitted with Gaussian distributions (red). These peaks appear at ~300 kDa, similar to SMA-PAGE mass predictions for M1 AQP4-SMALPs. Wash fractions (20 mM and 75 mM imidazole) show removal of low MW

contaminants, with the first indication of M23 AQP4-SMALPs appearing at the 100 mM imidazole elution (indicated by the fitted Gaussian distribution red line). The highest proportion of M23 AQP4-SMALPs appear in the 200 mM imidazole elution, after which proportions diminish. A small proportion, relative to low MW contaminants, is also evident in the 600 mM imidazole elution.

Ni-NTA IMAC purifications of M1 and M23 AQP4-SMALPs were compared using mass photometry. This was done to characterise the AQP4-SMALP IMAC purifications and assess sample heterogeneity before SEC purification. Resuspended membranes of the M1 and M23 AQP4 isoform *P. pastoris* clones were solubilised at 45 mg/mL with 2.5% w/v SMA. The soluble fractions were separated by ultracentrifugation (100,000 × g, 45 min, 4 °C) and AQP4-SMALPs were purified by Ni-NTA IMAC (Section 2.6). IMAC purified AQP4-SMALPs were concentrated with 100 kDa MW cut-off. The IMAC purified AQP4-SMALPs were analysed by mass photometry (Section 2.8.2) at a final concentration of ~5 µg/mL. This equates to a monomer concentration of ~140 nM and ~151 nM for M1 and M23 AQP4, respectively.

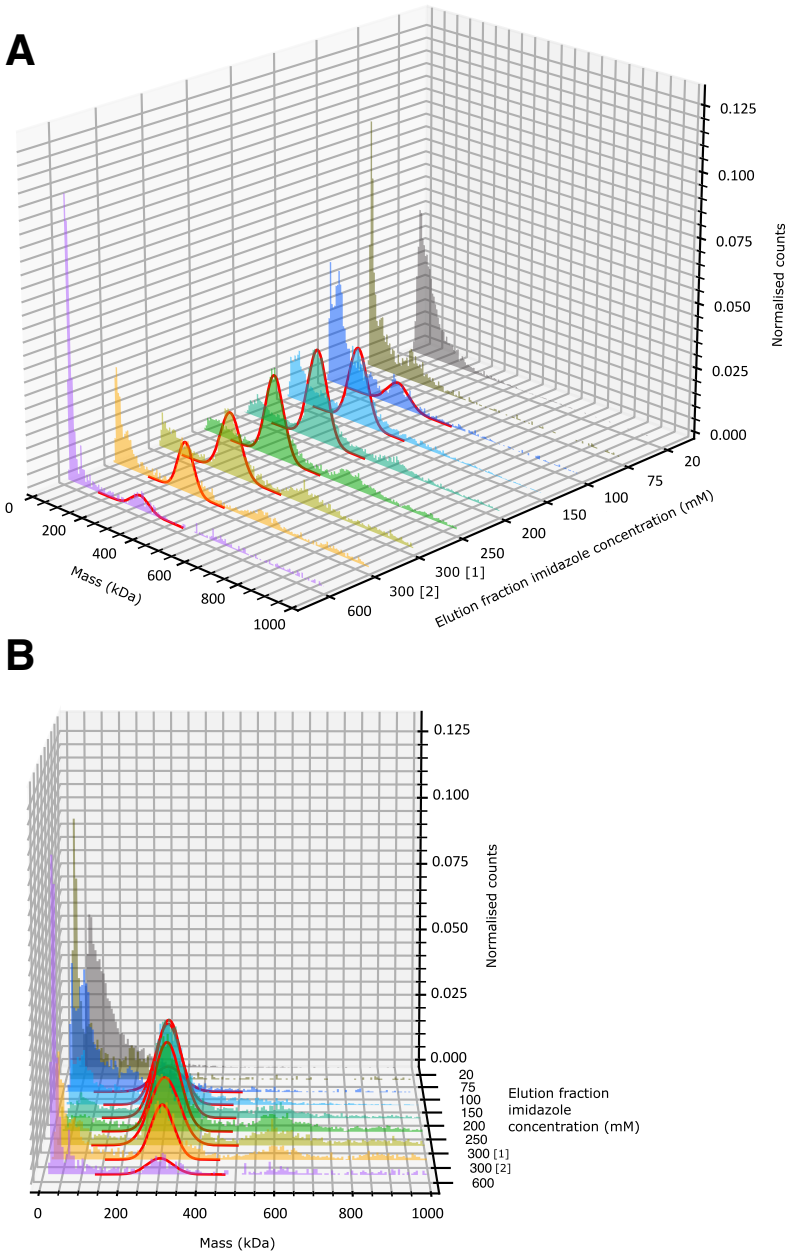

Figure 4.3. Investigating increasing imidazole elution concentration during Ni-NTA IMAC purification of M23 AQP4-SMALPs.
Resuspended membranes of the M23 AQP4 isoform *P. pastoris* clone were solubilised at 45 mg/mL with 2.5% w/v SMA. The soluble fraction was separated by ultracentrifugation (100,000 × g, 45 min, 4 °C) and AQP4-SMALPs were purified by Ni-NTA IMAC. This consisted of 20 mM and 75 mM imidazole wash fractions of 50× resin bed-volumes (the first 2.5× resin bed-volumes were collected as samples for analysis), followed by elution in 2.5× resin bed-volume fractions of increasing imidazole concentration (100 mM, 150 mM, 200 mM, 250 mM, 300 mM and 600 mM). Two consecutive fractions of 300 mM imidazole were used and are indicated as [1] and [2]. Each fraction was analysed by mass photometry (n = 1 per fraction). NativeMark was used for mass calibration. The figure shows a mass photometry 3D histogram of each fraction with normalised sample counts plotted against calibrated mass (kDa). The z-axis shows the imidazole concentration of each elution fraction: 20 mM (grey), 75 mM (brown), 100 mM (blue), 150 mM (cyan), 200 mM (turquoise), 250 mM (green), 300 mM [1] (chartreuse), 300 mM [2] (yellow), and 600 mM (purple). The histogram peak in each sample predicted to represent M23 AQP4-SMALPs is fitted with a Gaussian distribution (red). **A)** 3D histogram side view. **B)** 3D histogram front view.

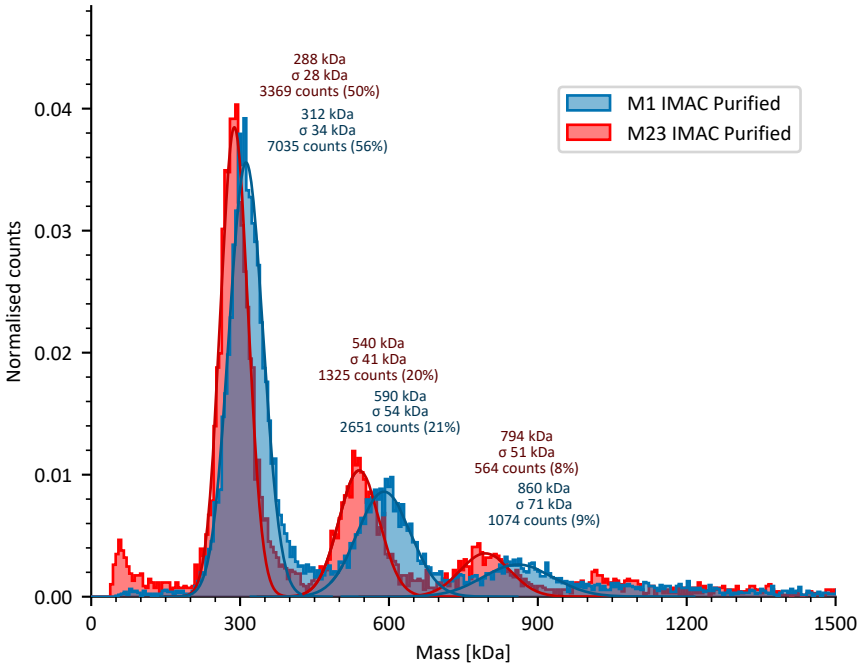

Figure 4.4. Mass photometry of Ni-NTA IMAC purified and concentrated M1 and M23 AQP4-SMALPs.
Resuspended membranes of the M1 and M23 AQP4 isoform *P. pastoris* clones were solubilised at 45 mg/mL with 2.5% w/v SMA. The soluble fractions were separated by ultracentrifugation (100,000 × g, 45 min, 4 °C) and AQP4-SMALPs were purified by Ni-NTA IMAC. IMAC purified AQP4-SMALPs were concentrated with 100 kDa MW cut-off and each purified sample analysed by mass photometry (n = 1 per sample). MS1000 was used for mass calibration. The figure shows overlayed mass photometry histograms of the purified M1 (blue) and M23 (red) AQP4-SMALP samples with normalised counts plotted against calibrated mass (kDa). The histogram peaks in each sample are fitted with Gaussian distributions (M1,blue; M23, red). Gaussian distributions are labelled with the mean, SD, and distribution counts (and percentage of total sample counts).

Figure 4.4 shows overlayed mass photometry histograms for IMAC purified M1 and M23 AQP4-SMALPs. Counts were normalised to show relative proportions of sample components. Three predominant peaks are visible for both AQP4-SMALP samples. These are fitted with Gaussian distributions and masses estimated. The small peak on the far-left of the histogram was not fitted with a Gaussian distribution as this represented either purification contaminant or low MW noise. A difference in mass between M1 and M23 is evident in all peaks, with the M23 AQP4-SMALP peaks estimated to be lower mass than those for M1 AQP4-SMALPs. This multiple peak pattern is consistent with the multiple band pattern observed for SMA-PAGE of M1 AQP4-SMALPs (Figure 4.1 and 2). No significant unbinding peaks were observed for the AQP4-SMALP peaks in the negative kDa region (not shown).

Due to this feature of multiple peaks (mass photometry) and multiple bands (SMA-PAGE) for the IMAC purified AQP4-SMALPs, the IMAC purified samples were analysed by mass photometry for 3 technical replicates, to ascertain whether mass photometry could estimate these peak masses with precision (Figure 4.5A and C). The mass estimates were determined by fitting Gaussians to the peaks as described (Section 2.8.2.3), and mean estimates were calculated from the replicate Gaussian mean values. The mean mass estimates were plotted against the identified peak number in order of increasing size and a linear regression line calculated (Figure 4.5B and D). Both M1 and M23 AQP4-SMALP IMAC purified samples individually demonstrated a strong linear relationship (r^2 = 0.9993 for M1 AQP4-SMALPs, r^2 = 0.9999 for M23 AQP4-SMALPs) between peak number and peak mass (Figure 4.5E).

These observed peaks were assumed to be different AQP4-SMALP sizes after solubilisation and IMAC purification. Assuming an AQP4 tetramer mass of 142.4 kDa and 132.4 kDa (based on monomer mass of 35.6 kDa and 33.1 kDa) for M1 and M23 isoforms, respectively, the incremental mass increase between each of the observed peaks would accommodate for the addition of one (but not greater than one) AQP4 tetramer unit. As AQP4 is known to form OAPs (Yang, Brown and Verkman, 1996; Verbavatz *et al.*, 1997), it was theorised that these particles could be different oligomeric forms of AQP4 tetramers in SMALP complexes, with ‘Peak 1’, ‘Peak 2’, and ‘Peak 3’ representing 1- (1T), 2- (2T), and 3- (3T) tetramer complexes of AQP4 within SMALPs, respectively (Figure 4.5). As such, visualised SMALP complexes (by SEC, SMA-PAGE, and mass photometry) theorised to represent this pattern are labelled in this way from here on in this chapter. Although M1 AQP4 is thought to be unable to form OAPs in the membrane (Furman *et al.*, 2003; Crane, Bennett and Verkman, 2009), it is possible that it is able to do so in *P. pastoris*, unlike in mammalian expression systems. Palmitoylation is thought to play a role in OAP prevention (Suzuki *et al.*, 2008), and lack of this could potentially be a factor here. Others have also found that M1 AQP4 tetramers are able to form small oligomers, with and without the presence of palmitoylation (Carder *et al.*, 2024). It is also possible that SMA forces this AQP4 assembly into particles containing more than one tetramer during AQP4 encapsulation. These possibilities would explain the similarity in the observed relationship between M1 and M23 AQP4 here.

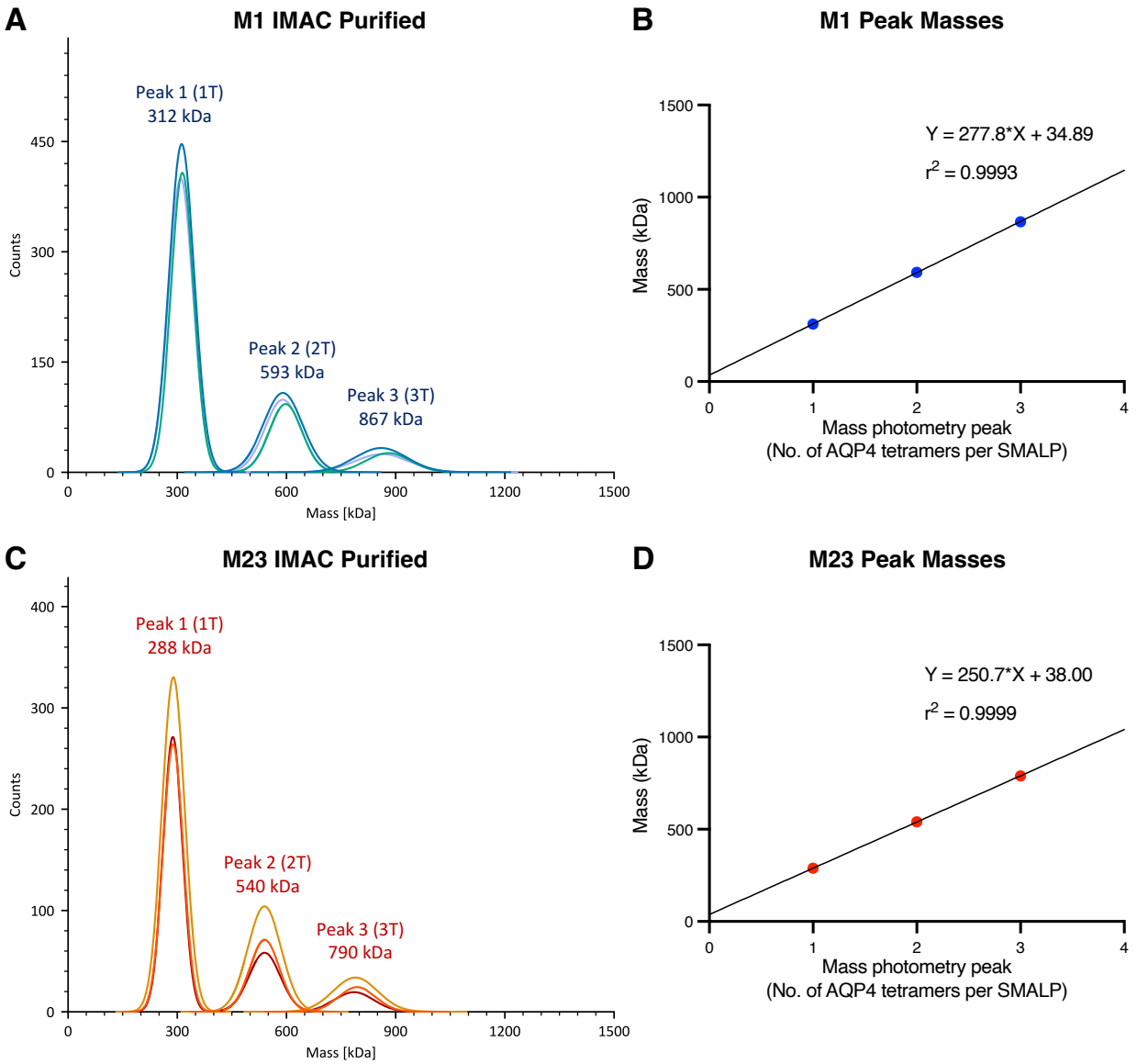

Figure 4.5. Linear correlation of mass photometry identified peaks in IMAC purified AQP4-SMALPs. Further mass photometry analysis of IMAC purified AQP4-SMALPs shown in Figure 4.4. **A, C)** Mass photometry histograms of overlayed technical replicates (n = 3) for M1 AQP4-SMALPs (**A**) and M23 AQP4-SMALPs (**C**), with counts plotted against calibrated mass (kDa). The plots show only Gaussian distribution lines that were fitted to histogram peaks, colour-coded to individual replicates. Gaussian distributions are labelled with the peak number and mean mass estimate (Gaussian mean) across replicates. 1T, 2T, and 3T represent theorised AQP4 tetrameric assembly of 1-, 2-, and 3-tetramers in SMALPs. **B, D)** Plots of mean estimated mass against peak number for M1 AQP4-SMALPs (**B**) and M23 AQP4-SMALPs (**D**), corresponding to mass photometry histograms **A** and **C**, respectively. Plots were fitted with a linear regression line, with lines labelled with the line equation and r^2 value. **E)** Combined plot of **B** and **D**.

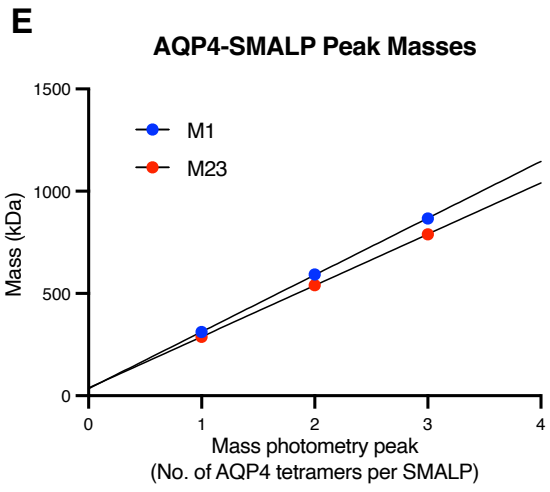

4.2. Further purification of AQP4-SMALPs by SEC

Having observed these different AQP4-SMALP sizes by mass photometry and SMA-PAGE, the next step was to further separate the IMAC purified samples by SEC. This would potentially allow assessment of the different SMALPs individually.

4.2.1. Optimisation of SEC purification

Resuspended membranes of M1 and M23 AQP4 isoform *P. pastoris* clones were solubilised at 45 mg/mL with 2.5% w/v SMA. Soluble fractions were separated by ultracentrifugation (100,000 × g, 45 min, 4 °C) and AQP4-SMALPs were purified by Ni-NTA IMAC (Section 2.6). IMAC purified samples were concentrated to ~500 µL with 100 kDa MW cut-off and separated by SEC using the Superdex 200 column (Section 2.8.1).

Figure 4.6A and B show the resultant 280 nm absorbance (UV) SEC traces for M1 and M23 AQP4-SMALPs. 600 µL fractions corresponding to the labelled peaks were collected and analysed by 3–20% SMA-PAGE alongside samples of the IMAC purified and concentrated AQP4-SMALPs, shown in Figure 4.6C. The SMA-PAGE of the IMAC purified AQP4-SMALPs showed a similar band-laddering pattern for both the M1 and M23 AQP4-SMALPs. The SEC fractions show a clear breakdown of the bands observed in the IMAC purified protein. The 1-tetramer (1T) AQP4-SMALP appeared to show a prominent peak in the SEC UV trace, whereas the 2-tetramer (2T) AQP4-SMALP was mostly present in a shoulder of the void peak. The void fraction showed separation of larger IMAC purified species that could not be resolved by SMA-PAGE. A peak or shoulder corresponding to the 3-tetramer (3T) SMALP could not be identified in the SEC UV trace. The trace shows a large void peak, demonstrating a large proportion of protein in the void fraction. This may represent the 3T AQP4-SMALP (observed by SMA-PAGE and mass photometry), larger AQP4-SMALP complexes, and aggregates of AQP4 or AQP4-SMALPs. The hydrodynamic radii of this fraction determined by flow-induced dispersion analysis (FIDA) is investigated in Section 4.3 (Figure 4.13 and Table 4.2).

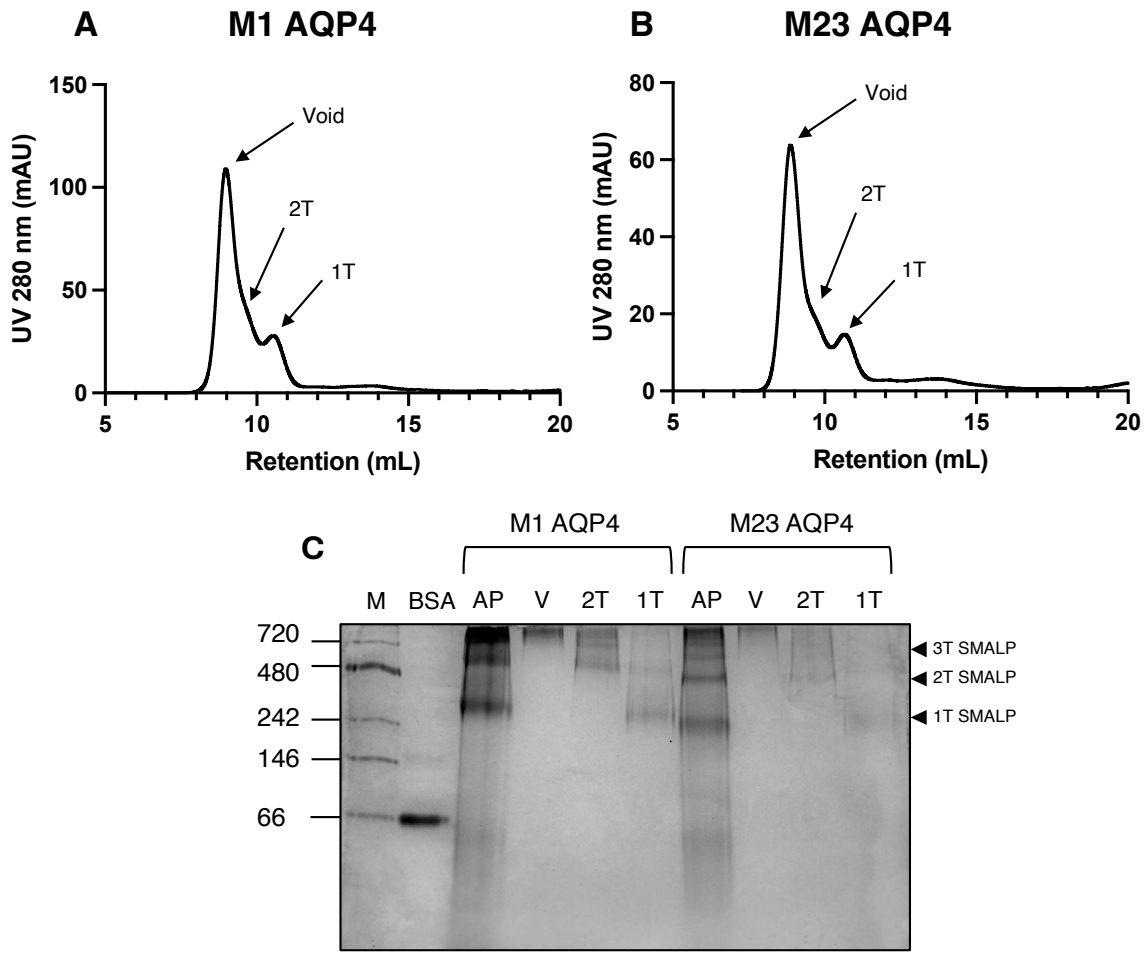

Figure 4.6. SEC of AQP4-SMALPs using the Superdex 200 column and analysis of fractions by SMA-PAGE.

Resuspended membranes of M1 and M23 AQP4 isoform *P. pastoris* clones were solubilised at 45 mg/mL with 2.5% w/v SMA. Soluble fractions were separated by ultracentrifugation (100,000 × g, 45 min, 4 °C) and AQP4-SMALPs were purified by Ni-NTA IMAC. Purified samples were concentrated to ~500 µL and separated by SEC using the Superdex 200 column. **A, B)** SEC profiles of Ni-NTA IMAC purified M1 **(A)** and M23 **(B)** AQP4-SMALPs. Profiles show mAU measured at UV 280 nm against the buffer retention volume (mL). Peaks are labelled according to the predicted fraction contents, where the 'Void' peak represents the SEC void, and the '2T' shoulder and '1T' peak represent 2- and 1-tetramer AQP4-SMALPs. 600 µL fractions were collected at each of these peaks. **C)** 3–20% gradient SMA-PAGE of M1 and M23 AQP4-SMALPs before and after SEC. 'AP' represents Ni-NTA IMAC purified and concentrated protein. The other AQP4 samples are the void (V), 2T, and 1T fractions collected from SEC shown in **A** and **B**. Arrows indicate positions of predicted AQP4-SMALP bands. Positions are labelled with '1T', '2T', and '3T', representing theorised AQP4 tetrameric assembly of 1-, 2-, and 3-tetramers in SMALPs. NativeMark and BSA markers are shown under 'M' and 'BSA', respectively, with mass labels in kDa shown on the left. Gel was stained with Coomassie blue.

SEC was able to separate these differently sized AQP4-SMALPs visualised by SMA-PAGE and mass photometry after IMAC purification. This gave confidence that these SMALP complexes were individual particles of different sizes, as opposed to aggregates of the smallest visualised SMALP at ~300 kDa. Despite good separation of the ~300 kDa SMALP, other SEC trace peaks could not be identified. The larger AQP4-SMALPs appeared to elute very close to the void peak, such as with the 2T AQP4-SMALP shoulder peak. The Cytivia Superose 6 column offers a broader fractionation range than the Superdex 200 column for large molecular sizes. Therefore, it was used to improve separation of the larger AQP4-SMALPs (that could be visualised by SMA-PAGE and mass photometry) from the SEC void peak.

As before, resuspended membranes of M1 and M23 AQP4 isoform *P. pastoris* clones were solubilised at 45 mg/mL with 2.5% w/v SMA. Soluble fractions were separated by ultracentrifugation and AQP4-SMALPs were purified by Ni-NTA IMAC (Section 2.6). For this purification, samples were concentrated to ~500 µL with 100 kDa MW cut-off and separated by SEC using the Superose 6 column (Section 2.8.1).

Figure 4.7 shows the resulting SEC purification by the Superose 6 column. The SEC traces for M1 and M23 AQP4-SMALPs show two prominent peaks after the void peak (Figure 4.7A and B). Analysis of 600 µL fractions collected at these peaks, and at intermediate regions of the SEC fractionation, showed a similar laddering of AQP4-SMALPs as before, when observed by SMA-PAGE (Figure 4.7C and D). The 1T and 2T AQP4-SMALPs were confirmed to show independent prominent peaks in the SEC UV trace. M1 and M23 1T AQP4-SMALP fractions were also directly compared by SMA-PAGE (Figure 4.7E).

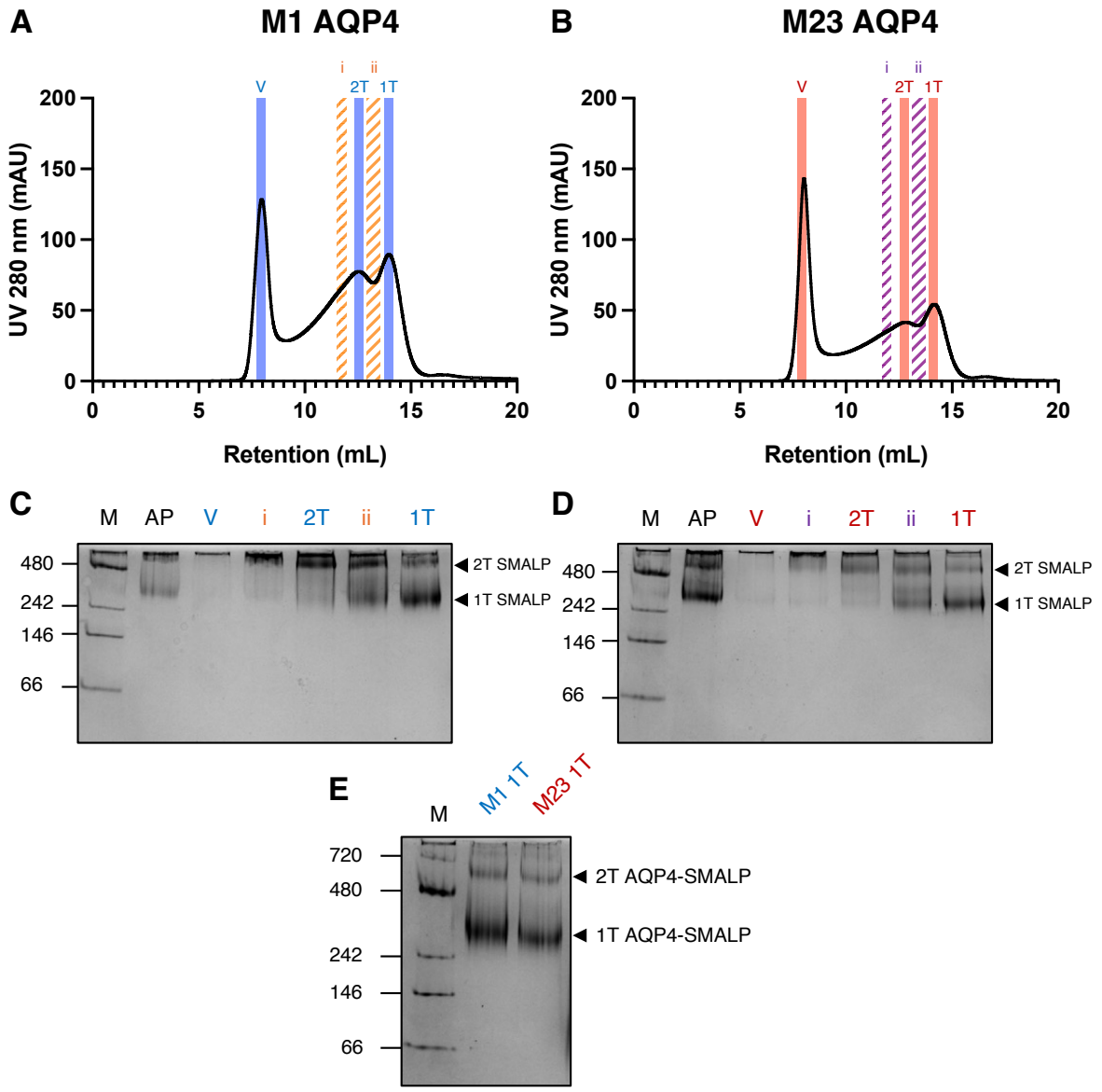

Figure 4.7. Improved SEC separation of AQP4-SMALPs using the Superose 6 column and analysis of fractions by SMA-PAGE.
Resuspended membranes of M1 and M23 AQP4 isoform *P. pastoris* clones were solubilised at 45 mg/mL with 2.5% w/v SMA. Soluble fractions were separated by ultracentrifugation (100,000 × g, 45 min, 4 °C) and AQP4-SMALPs were purified by Ni-NTA IMAC. Purified samples were concentrated to ~500 µL and separated by SEC using the Superose 6 column. **A, B)** SEC profiles of Ni-NTA IMAC purified M1 **(A)** and M23 **(B)** AQP4-SMALPs. Profiles show mAU measured at UV 280 nm against the buffer retention volume (mL). Peaks and corresponding collected fractions are labelled and highlighted. For **A**, 'V' represents the SEC void peak, and the '2T' and '1T' peaks represent 2- and 1-tetramer M1 AQP4-SMALPs (all highlighted blue). 'i' and 'ii' represent first and second peak intermediate fractions (both highlighted dashed orange), respectively. For **B**, 'V' represents the SEC void peak, and the '2T' and '1T' peak represent 2- and 1-tetramer M23 AQP4-SMALPs (all highlighted red). 'i' and 'ii' represent first and second peak intermediate fractions (both highlighted dashed purple), respectively. **C, D)** 3–20% gradient SMA-PAGE of M1 (**C**) and M23 (**D**) AQP4-SMALPs before and after SEC. 'AP' represents Ni-NTA IMAC purified and concentrated protein. The other AQP4 samples are labelled corresponding to fractions collected from SEC peaks identified in **A** and **B**. **E)** 3–20% gradient SMA-PAGE of the M1 and M23 AQP4-SMALP 1T fraction collected from SEC shown in **A** and **B**, respectively. For **C**, **D** and **E**, arrows indicate positions of predicted AQP4-SMALP bands. Positions are labelled with 1T and 2T, representing theorised AQP4 tetrameric assembly of 1- and 2-tetramers in SMALPs. NativeMark markers are shown under 'M', with mass labels in kDa shown on the left. Gels were stained with Coomassie blue.

To directly compare SEC profiles for the M1 and M23 AQP4-SMALPs, two normalisation techniques were used for the SEC traces shown in Figure 4.7A and B. This would allow overlay of the traces and comparison of the relative mAU values at 280 nm for the different peaks observed. SEC traces were normalised by using the total area under the curve (AUC) or by using the maximum mAU value (max.). The resulting SEC profile overlays are shown in Figure 4.8. The SEC profile for M23 AQP4 showed a slight shift to the right when compared to the M1 AQP4 profile (for the 1T and 2T peaks). This was expected, as M23 AQP4-SMALPs had so far shown lower masses compared to the M1 AQP4-SMALPs. Normalisation by AUC gave better relative comparison between all SEC peaks. This made sense, as normalisation by AUC relied on the 280 nm signal from all protein in the sample, as opposed to one specific peak with the highest mAU value (which in this case was the void peak). As such, normalisation by AUC was chosen as the preferred method for future SEC profile comparison.

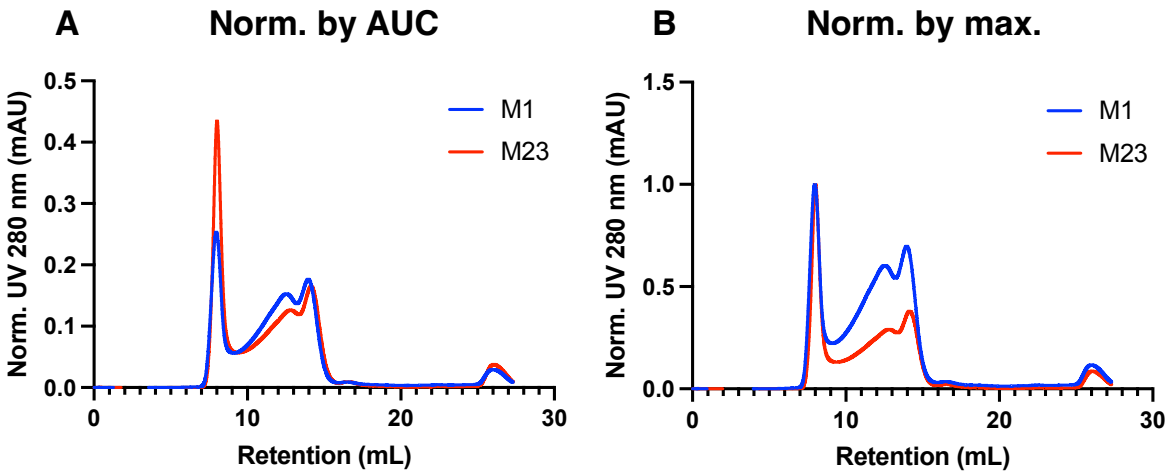

Figure 4.8. Comparing normalisation techniques for comparison of M1 and M23 AQP4-SMALP SEC profiles.
Figures show overlay of M1 (blue) and M23 (red) AQP4-SMALP SEC profiles shown in Figure 4.7A and B. Profiles show normalised mAU measured at UV 280 nm against the buffer retention volume (mL). **A)** Normalisation of mAU by the total area under the curve (AUC) for each profile. **B)** Normalisation of mAU by the maximum mAU value (max.) for each profile.

As observed in Section 3.3.3, degradation of protein appears to take place between IMAC elution and centrifugal concentration of AQP4-SMALPs (Figure 3.11). Therefore, two subsequent SEC purifications of AQP4-SMALPs were compared where the time between IMAC elution and SEC purification was different for each one. As before, resuspended membranes of M1 and M23 AQP4 isoform *P. pastoris* clones were solubilised at 45 mg/mL with 2.5% w/v SMA. Soluble fractions were separated by ultracentrifugation and AQP4-SMALPs were purified by Ni-NTA IMAC (Section 2.6). For one purification, protein was eluted in fractions for analysis before SEC. This meant a brief storage period, before pooling fractions together, centrifugal concentration, and separation by SEC, resulting in ~3 h between IMAC elution and SEC. A new purification method was used in which protein was eluted in one large fraction, immediately concentrated, and separated by SEC, resulting in < 1 h between IMAC elution and SEC. In both cases, IMAC purified protein was concentrated to ~500 µL with 100 kDa MW cut-off before separation with the Superose 6 column. Resuspended membranes for both conditions were taken from the same bioreactor cell culture batch and both solubilisations and purifications were performed using the same protocol (Section 2.6).

Figure 4.9 shows a comparison of these two different purifications for M1 and M23 AQP4-SMALPs. For the SEC purification with reduced time between IMAC elution and SEC separation, M23 AQP4 appears to show an increased proportion of the 1T AQP4-SMALP, with M1 AQP4 showing an increased proportion in the 2T AQP4-SMALP peak and tail. M1 AQP4 shows a significantly decreased proportion in the void. Both profiles also show the appearance of another small peak after the 1T AQP4-SMALP, potentially representing a purification contaminant.

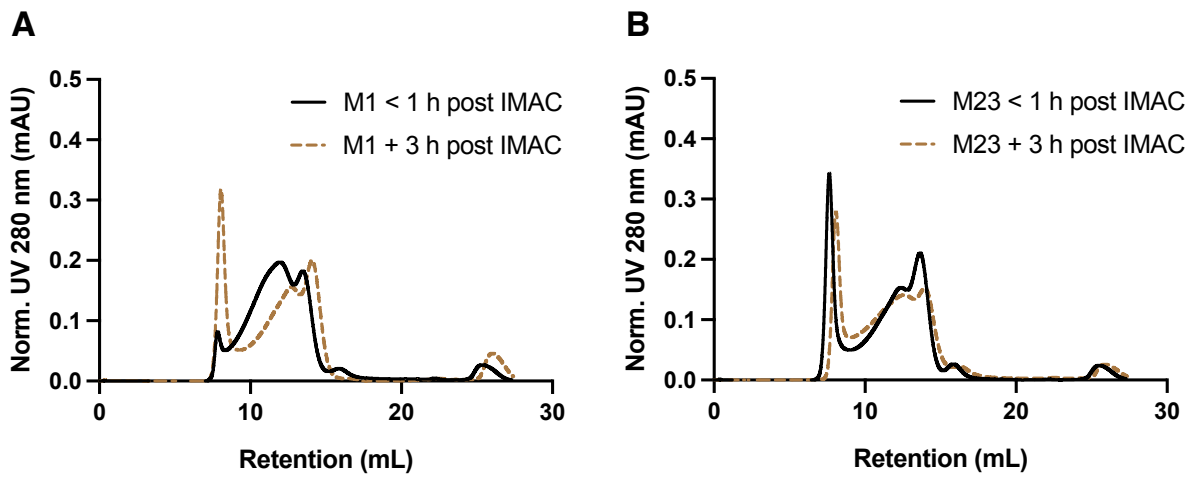

Figure 4.9. Reducing time between Ni-NTA IMAC purification and SEC separation using the Superose 6 column.
Resuspended membranes of M1 and M23 AQP4 isoform *P. pastoris* clones were solubilised at 45 mg/mL with 2.5% w/v SMA. Soluble fractions were separated by ultracentrifugation (100,000 × g, 45 min, 4 °C) and AQP4-SMALPs were purified by Ni-NTA IMAC. In one condition, protein was eluted in fractions, stored, and pooled together before concentration and separation by SEC, resulting in ~3 h between IMAC elution and SEC (brown dotted trace). A new purification method was used in which protein was eluted in one large fraction and immediately concentrated and separated by SEC, resulting in < 1 h between IMAC elution and SEC (solid black trace). Both SEC purifications were performed with the Superose 6 column. For M1 (**A)** and M23 (**B**) AQP4, the figures show an overlay of SEC profiles from this new purification method, with < 1 h between IMAC and SEC (black solid trace), and the SEC profiles of the previous purification method (dotted brown trace), resulting in + 3 h between IMAC and SEC. Profiles show normalised mAU measured at UV 280 nm against the buffer retention volume (mL).

Figure 4.10 shows an overlay of M1 and M23 AQP4 SEC profiles for the new purification method described with reduced time between IMAC elution and SEC (Figure 4.9, solid black trace). Fractions of the identified peaks were collected and analysed by SDS-PAGE (Section 2.7.2). Monomer, dimer and trimer AQP4 bands were present in the 2T and 1T SEC fractions, at expected MW for M1 (~35.6 kDa) and M23 (~33.1 kDa). The monomer and dimer AQP4 bands were also faintly present in the void peak for both M1 and M23 AQP4. The small peak identified after the 1T AQP4-SMALP gave a band matching the purification contaminant seen in IMAC purified AQP4 (Figure 3.10), showing good separation of this from the AQP4-SMALPs by SEC.

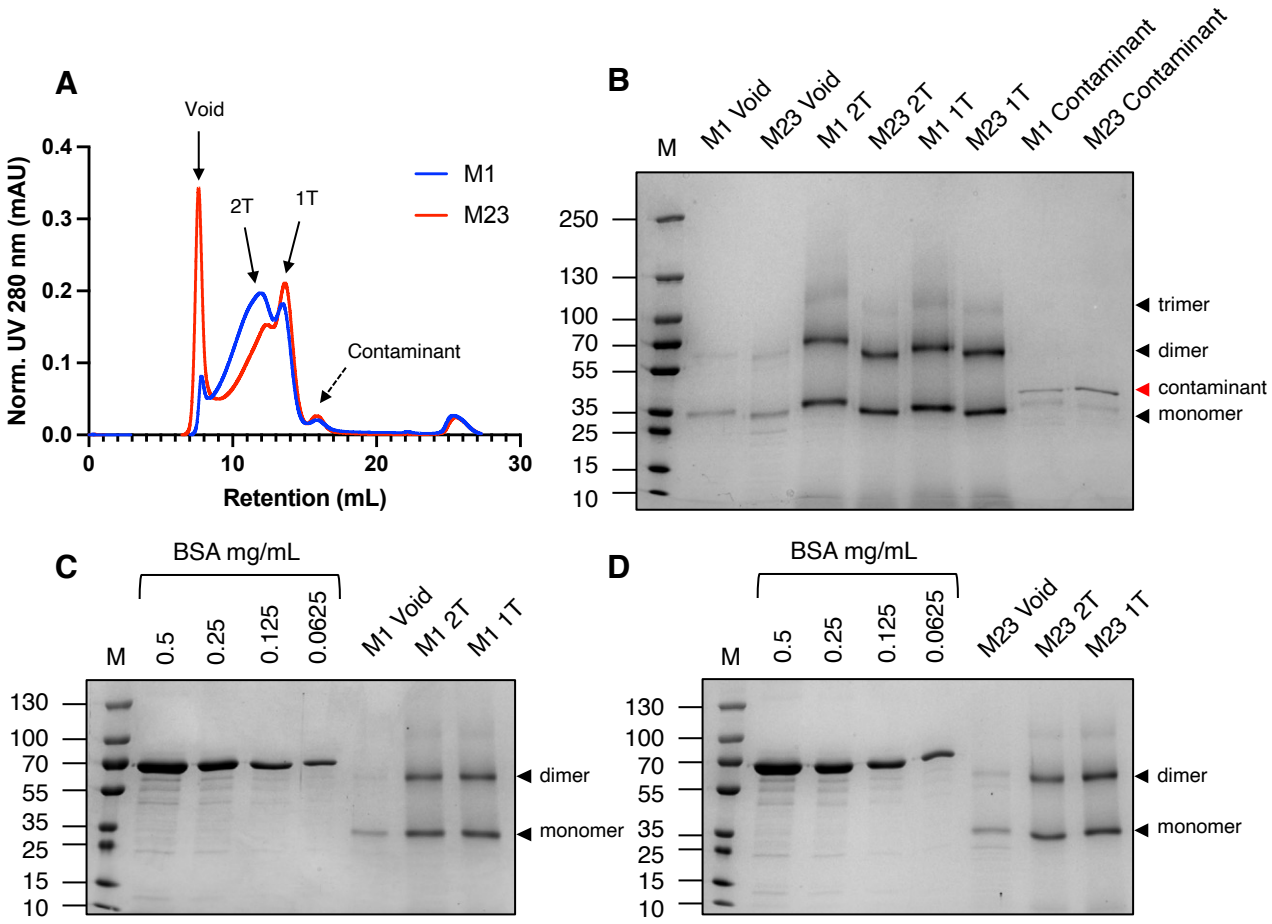

Figure 4.10. SDS-PAGE analysis of AQP4-SMALP SEC fractions after separation using the Superose 6 column.
A) Overlay of M1 (blue) and M23 (red) AQP4-SMALP SEC profiles from the new purification method shown in Figure 4.9A and B (Figure 4.9A and B solid black trace). Profiles show normalised mAU measured at UV 280 nm against the buffer retention volume (mL). Peaks and corresponding collected 600 µL fractions are labelled with arrows. 'Void' represents the SEC void peak, and the '2T' and '1T' peaks are predicted to represent 2- and 1-tetramer AQP4-SMALPs. A peak predicted to represent the IMAC purification contaminant is labelled with a dotted arrow. **B)** 4–16% gradient SDS-PAGE of fractions collected from SEC (**A**)**.** Lanes are labelled corresponding to the identified SEC peaks in **A**. **C, D)** SDS-PAGE for protein concentration estimation of M1 (**C**) and M23 (**D**) AQP4 in Void, 2T, and 1T fractions collected from SEC (**A**). Lanes are labelled corresponding to the identified SEC peaks in **A**. BSA was used as a standard in serial dilution. BSA concentrations are labelled for each lane. For gels **B**, **C** and **D**, positions of monomer, dimer and trimer bands of AQP4 are labelled with black arrows. A contaminant band is labelled with a red arrow. For all gels, MW markers are shown under 'M' with mass labels in kDa shown on the left of each gel. Gels were all stained with Coomassie blue.

AQP4 concentration was estimated for the void, 2T and 1T SEC fractions using densitometry analysis (Section 2.7.4.1), with a serial dilution of BSA to be used as a concentration standard curve. Table 4.1 shows concentration estimates using the SDS-PAGE shown in Figure 4.10C and D. Total protein quantity was determined using the volume of the collected SEC fraction. The AQP4 monomer concentrations were determined assuming a mass of 35.6 kDa and 33.1

kDa for the M1 and M23 isoforms, respectively. This was divided by four to determine the tetramer concentration, as this is the expected conformation in the 1T AQP4-SMALPs. The 1T AQP4-SMALP fraction contained the highest amount of AQP4 for both M1 and M23, with slightly less in the 2T fraction. The void contained much less AQP4 at a relatively even quantity for both isoforms.

Table 4.1. Protein concentration and quantity estimates after SEC.
Table shows estimated AQP4 concentration in collected SEC fractions (Figure 4.10). Concentration estimates were determined by densitometry analysis of gels shown in Figure 4.10C and D, using BSA as a protein concentration standard in serial dilution. This was used to quantity total protein based on collected SEC fraction volumes of 600 µL. AQP4 molar concentration was determined based on an assumption of 35.6 kDa for the M1 AQP4 monomer and 33.1 kDa for the M23 AQP4 monomer.

AQP4 isoform SEC fraction	Concentration (mg/mL)	Total protein quantity (µg)	AQP4 monomer concentration (µM)	AQP4 tetramer concentration (µM)
M1 Void (Void)	0.04	24	1.12	0.28
M1 2-tetramer (2T)	0.28	168	7.87	1.97
M1 1-tetramer (1T)	0.38	228	10.67	2.67
M23 Void (Void)	0.04	24	1.21	0.30
M23 2-tetramer (2T)	0.25	150	7.55	1.89
M23 1-tetramer (1T)	0.33	198	9.97	2.49

4.2.2. Analysis of SEC fractions by mass photometry

The fractions collected as described for Figure 4.10 were analysed by mass photometry (Section 2.8.2). Figure 4.11 shows a comparison of SEC fractions for each of the M1 and M23 AQP4 purifications. 2T and 1T SEC fractions for M1 and M23 were analysed at a final AQP4 tetramer concentration of ~17.5 nM. Tetramer concentration was used as this represented the expected conformation of AQP4 in 1-tetramer SMALPs. The void fraction and contaminant peak were analysed at a 20-fold final dilution. The concentration used for these fractions was determined as a dilution factor because the fraction contents were not certain and the relative protein quantity appeared much lower compared to the 2T and 1T fractions (Figure 4.10B). Figure 4.12 shows a comparison of M1 and M23 AQP4-SMALPs for the 2T and 1T SEC fractions. Samples for this comparison were analysed at a final AQP4 tetramer concentration of ~35 nM. For the reasons stated for Figure 4.11, tetramer concentration was used to determine final analysed concentration. For Figures 4.11 and 4.12, sample counts were

normalised for the overlayed histograms so that proportions of fraction components could be more accurately compared, regardless of the total number of recorded events.

For both the M1 and M23 AQP4 samples, the overlayed SEC fractions show a breakdown of species that match the appearance of peaks observed for IMAC purified AQP4-SMALPs. The relative proportions of each peak suggest that, as expected, 1- and 2-tetramer AQP4-SMALPs are most predominant in the 1T and 2T SEC fractions, respectively. Good separation of the contaminant can be seen, although this contaminant fraction appears to contain a small peak representing the 1-tetramer AQP4-SMALP. The mass prediction of the contaminant does not match that seen by SDS-PAGE. This could be because the contaminant forms a dimer, or exists within SMALP complexes, or due to the observed MW by SDS-PAGE being close to the lower detection (and prediction) limit for mass photometry (~30 kDa). No predominant peaks could be observed for the void fraction other than binding events at a low MW. This is likely due to it being a heterogenous mix of large particle sizes.

The 1T SEC fractions for both M1 and M23 AQP4 show a relatively homogeneous peak for the predicted 1-tetramer AQP4-SMALP. This SEC fraction also shows some evidence of 2-tetramer AQP4-SMALPs, as also observed by SMA-PAGE analysis (Figure 4.7). Particles predicted to be 1-, 2-, and 3-tetramer AQP4-SMALPs appear in the 2T SEC fraction. This fraction is much more heterogenous than the 1T fraction, but the 2-tetramer AQP4-SMALP appears to be the predominant peak for both M1 and M23 AQP4 samples. The mass estimate for the 1-tetramer AQP4-SMALP differs in the 1T and 2T SEC fractions, with the 2T SEC fraction having slightly higher estimates. This may be due to the 2T SEC fraction containing the larger particles of the 1-tetramer AQP4-SMALP distribution. M1 and M23 AQP4 samples show a different proportion of the 1-tetramer AQP4-SMALP in the 2T SEC fraction (higher proportion for M23 AQP4). This is similar to the relative proportions of the 1T and 2T SEC peaks observed for M1 and M23 AQP4 (Figure 4.10). Despite good separation of the contaminant and void, this analysis shows that there is some overlap of predicted 1- and 2-tetramer AQP4-SMALPs in the SEC fractionation contents. There is a very shallow peak above the mass of the predicted 3-tetramer peak, which could represent 4-tetramer AQP4-SMALPs. However, this is hard to distinguish above the background noise of binding events, thus, these counts have not been fitted with a Gaussian distribution.

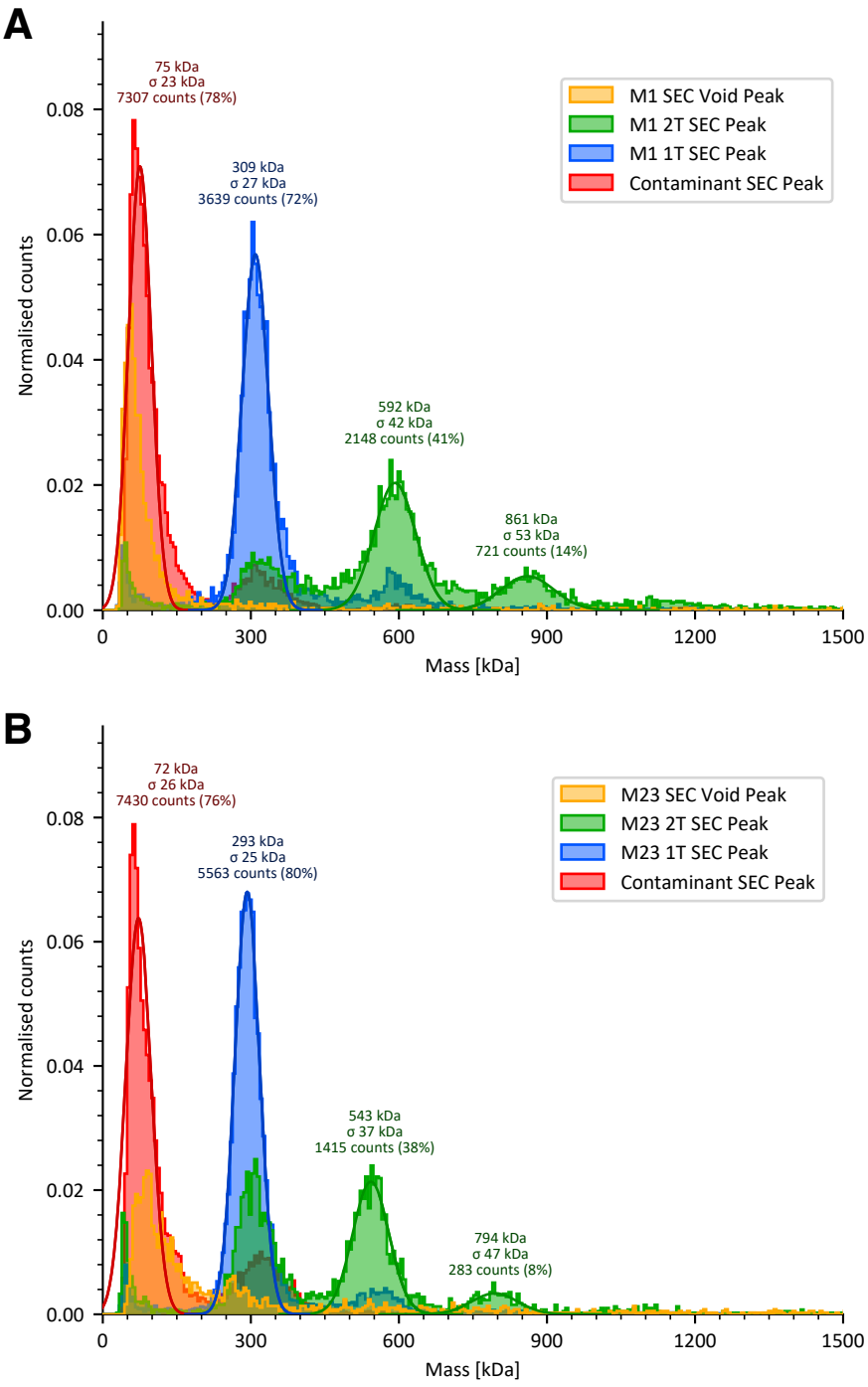

Figure 4.11. Mass photometry of fractions from SEC purified M1 and M23 AQP4-SMALPs. Identified M1 and M23 AQP4-SMALP SEC fractions (Figure 4.10) were analysed by mass photometry (n = 1 per sample). MS1000 was used for mass calibration. The figures show overlayed mass photometry histograms of SEC fractions collected for M1 (**A**) and M23 (**B**) AQP4-SMALPs, with normalised counts plotted against calibrated mass (kDa). Samples for **A** and **B** correspond to identified peaks from the SEC profiles in Figure 4.10A, where 'Void' represents the collected void fraction (yellow), '2T' represents the fraction predicted to contain 2-tetramer AQP4-SMALPs (green), '1T' represents the fraction predicted to contain 1-tetramer AQP4-SMALPs (blue), and 'contaminant' represents the fraction containing the IMAC purification contaminant (red). The histogram peaks in each sample are fitted with Gaussian distributions. Gaussian distributions are labelled with the mean (mass prediction), SD, and distribution counts (and percentage of total sample counts).

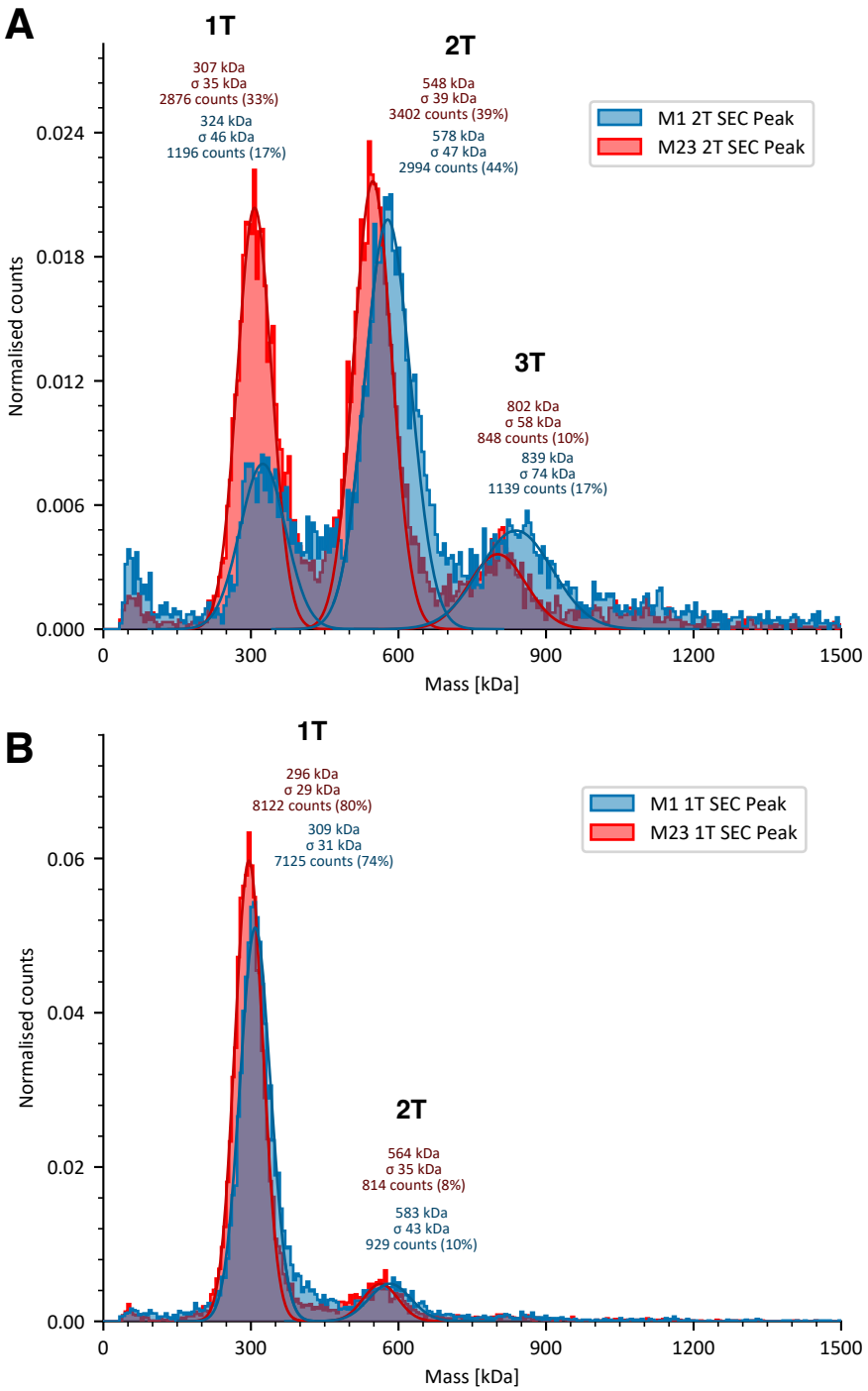

Figure 4.12. Comparison of SEC purified M1 and M23 AQP4-SMALPs using mass photometry. Identified M1 and M23 AQP4-SMALP SEC fractions (Figure 4.10) were analysed for comparison of M1 and M23 by mass photometry (n = 1 per sample). MS1000 was used for mass calibration. **A)** Overlayed mass photometry histograms of the '2T' SEC fraction for M1 (blue) and M23 (red) AQP4, predicted to contain 2-tetramer AQP4-SMALPs. **B)** Overlayed mass photometry histogram of the '1T' SEC fraction for M1 (blue) and M23 (red) AQP4, predicted to contain 1-tetramer AQP4-SMALPs. For **A** and **B**, histograms show normalised counts plotted against calibrated mass (kDa). The histogram peaks in each sample are fitted with Gaussian distributions. Gaussian distributions are labelled with the mean (mass prediction), SD, and distribution counts (and percentage of total sample counts). Peaks and corresponding mass labels are identified as 1T, 2T, and 3T, indicating peaks thought to represent 1-, 2-, and 3-termamer AQP4-SMALPs, respectively.

4.3. Flow-induced dispersion analysis (FIDA) of M1 and M23 AQP4-SMALPs

Having used SEC to separate AQP4-SMALPs of different sizes, the hydrodynamic radius (R_h) of the particles was measured using flow-induced dispersion analysis (FIDA). FIDA uses fluorescence (in this case the intrinsic fluorescence of protein tryptophan residues) to measure the particle dispersion under laminar flow through a capillary. Particle size influences its radial diffusion and thereby the dispersion, so that by measuring dispersion, R_h of the particle can be calculated (Pedersen, Østergaard and Jensen, 2019).

The 1T, 2T, and void SEC fractions for M1 and M23 AQP4-SMALPs were analysed by FIDA (Section 2.8.3). As indicated by SDS-PAGE, M1 and M23 AQP4 were present in the SEC void fractions (Figure 4.10B), so it was theorised that this fraction could contain large AQP4-SMALP particles. As FIDA offers a way to calculate R_h and polydispersity index (PDI), the void fractions were also investigated for uniformly sized SMALPs.

Figure 4.13 shows plots of the R_h mean ± SD determined from technical replicates for each of the AQP4-SMALP SEC fractions. Table 4.2 shows the R_h means ± SD plotted in Figure 4.13 and estimated PDI ± SD for each fraction. The SEC fraction containing the theorised 1-tetramer AQP4-SMALPs (1T) showed no significant difference between the M1 and M23 AQP4-SMALPs. The SEC fraction containing the 2-tetramer AQP4-SMALPs (2T) also showed a very similar R_h for M1 and M23 AQP4. The void fractions demonstrated a very large R_h compared to the other fractions, with M23 AQP4 having a larger calculated R_h than M1 AQP4 (~ 5 nm larger). A one-way ANOVA with Tukey's *post hoc* test found a significant difference between R_h means of the SEC 1T, 2T, and void fractions for M1 and M23 AQP4. A significant difference was found between M1 and M23 AQP4 in the void SEC fraction, but there was no significant difference between M1 and M23 AQP4 in the 1T and 2T fractions.

Generally, higher PDI values indicate higher heterogeneity of particle sizes in a sample, whereas values closer to 0 indicate homogeneity. According to Fidabio's quality control guidelines, PDI values > 0.05 indicate polydispersity in the sample (Fidabio, 2025). This suggests that 1T and 2T SEC fractions are homogenous, whereas the void fractions show higher variability in particle sizes (Table 4.2).

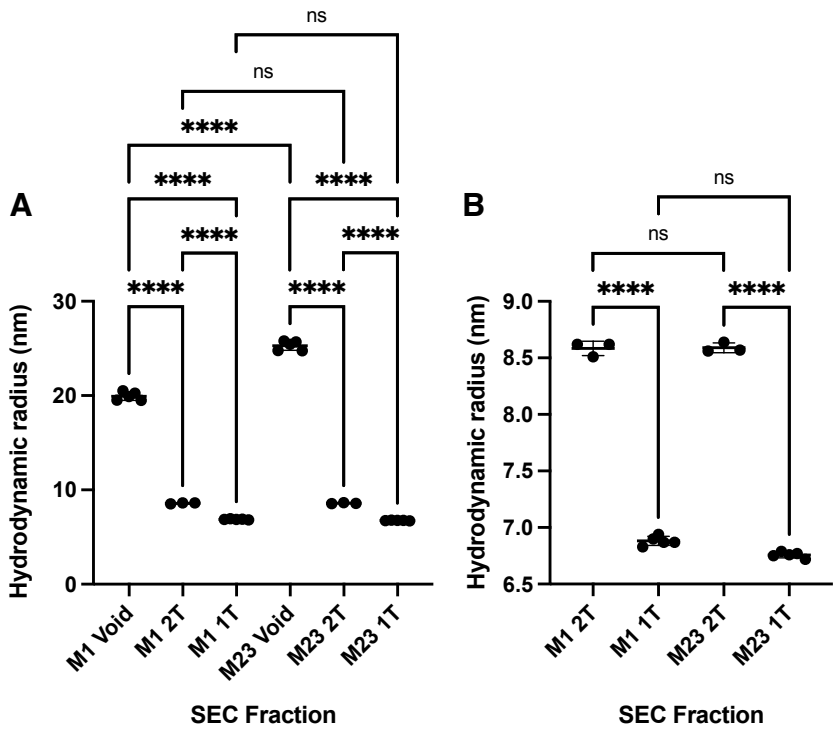

Figure 4.13. Flow-induced dispersion analysis (FIDA) of fractions from SEC purified M1 and M23 AQP4-SMALPs.
Identified M1 and M23 AQP4-SMALP SEC fractions (Figure 4.10) were analysed by FIDA**.** Plots show the mean hydrodynamic radius (R_h) ± SD determined for each sample (n ≥ 3, technical replicates). Samples correspond to identified peaks from the M1 and M23 SEC profiles in Figure 4.10A, where 'Void' represents the collected void fraction, '2T' represents the fraction predicted to contain 2-tetramer AQP4-SMALPs, and '1T' represents the fraction predicted to contain 1-tetramer AQP4-SMALPs. Statistical analysis was performed with a one-way ANOVA with Tukey's multiple comparisons *post hoc* test (ns – $p > 0.05$ (not significant), ****$p \leq 0.0001$). **A)** Plot showing all fractions. **B)** Plot showing 2T and 1T fractions only.

Table 4.2. Hydrodynamic radius (R_h) and polydispersity index (PDI) calculated from FIDA of fractions from SEC purified M1 and M23 AQP4-SMALPs.
Table shows mean R_h ± SD and mean PDI ± SD (n ≥ 3, technical replicates) of SEC fractons analysed by FIDA shown in Figure 4.13. Samples correspond to identified peaks from the M1 and M23 SEC profiles in Figure 4.10A, where 'Void' represents the collected void fraction, '2T' represents the fraction predicted to contain 2-tetramer AQP4-SMALPs, and '1T' represents the fraction predicted to contain 1-tetramer AQP4-SMALPs.

SEC Fraction	Mean R_h (nm) ± SD	Mean PDI ± SD
M1 Void	19.94 ± 0.44	0.0942 ± 0.0003
M1 2T	8.58 ± 0.06	0.0007 ± 0.0005
M1 1T	6.88 ± 0.04	0.0003 ± 0.0004
M23 Void	25.30 ± 0.50	0.0233 ± 0.0401
M23 2T	8.59 ± 0.04	0.0010 ± 0.0000
M23 1T	6.76 ± 0.06	0.0005 ± 0.0005

4.4. Thermal stability of M1 and M23 AQP4-SMALPs

With the AQP4-SMALP sizes separated by SEC, they were investigated for thermal stability to determine if AQP4-SMALPs of different sizes showed differences or similarity in thermal stability. MP-SMALPs have previously shown very good thermal stability when compared to alternatives such as detergent solubilisations of MPs (Jamshad, Charlton, *et al.*, 2015; Gulamhussein *et al.*, 2019), so thermal stability of the 1-tetramer AQP4-SMALPs was expected to be a high benchmark for comparison.

To measure thermal stability, an assay using CPM dye was used. CPM reacts with free thiols and fluoresces upon binding. The assay works on the principle of protein denaturation and unfolding with increasing temperature, causing the exposure of cysteine residues which bind to the CPM compound, resulting in fluorescence (Alexandrov *et al.*, 2008; Sampson *et al.*, 2021). The 1T, 2T and void SEC fractions for M1 and M23 AQP4 were subjected to the CPM dye thermal shift assay (Section 2.9.1). Protein samples were incubated with CPM dye and then subjected to increasing temperature from 20 °C to 100 °C with fluorescence measured over this temperature increase.

Figure 4.14A shows the resulting mean fluorescence profiles (n = 3, technical replicates) for each of the SEC fractions of M1 and M23 AQP4. Buffer blank and CPM only (no protein) samples were used for controls. Data was processed as described in Section 2.9.1.2. The mean fluorescence signal of the CPM control sample was used as a baseline subtraction to give a corrected fluorescence profile for the AQP4-SMALP samples (Figure 4.14B). The corrected fluorescence profiles of the AQP4-SMALP SEC samples were normalised and normalised profiles are shown in Figure 4.14C. Some of the samples (particularly M23 2T) showed a drop in fluorescence signal from the start of the profile. This was attributed to potential issues and variability of the assay. However, all samples showed a sharp increase in fluorescence and the beginning of a plateau approaching 100 °C.

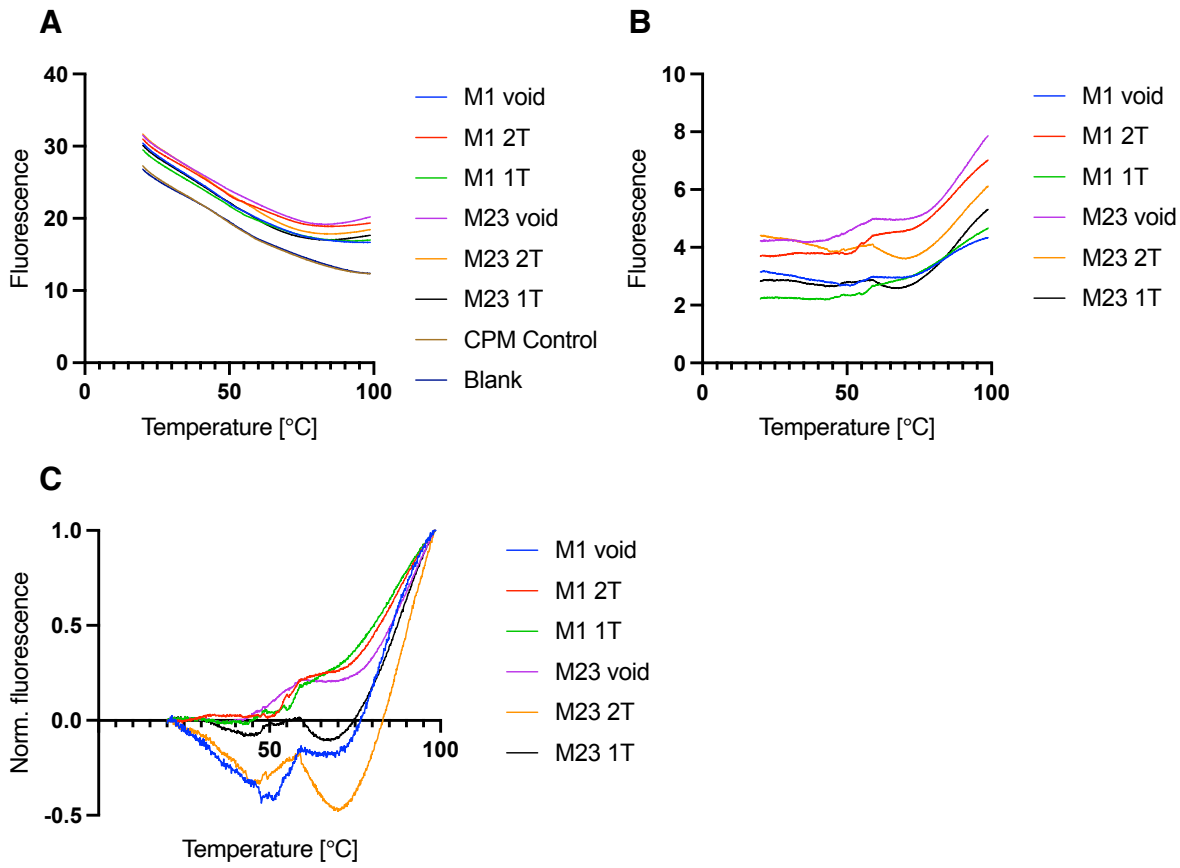

Figure 4.14. Thermal stability comparison of M1 and M23 AQP4-SMALP SEC fractions.
A CMP dye assay was used to measure protein thermal stability in identified M1 and M23 AQP4-SMALP SEC fractions (Figure 4.10) . Samples correspond to peaks from the SEC profiles in Figure 4.10A, where 'Void' represents the collected void fraction, '2T' represents the fraction predicted to contain 2-tetramer AQP4-SMALPs, and '1T' represents the fraction predicted to contain 1-tetramer AQP4-SMALPs. Samples were incubated with CPM dye and subjected to increasing temperature, and fluorescence signal measured to determine a melting curve. **A)** The mean fluorescence signal from each SEC fraction against temperature (°C), alongside CPM and blank controls (n = 3, technical replicates). **B)** Correction of the mean raw fluorescence values using the CPM control mean as baseline subtraction. **C)** Normalised baseline-corrected fluorescence signal.

To estimate the melting points (T_m), the first derivative of the normalised thermal profiles was calculated to determine the maximum rate of change (dF/dT_{max}). The resulting profiles are shown in Figure 4.15. Despite some fluorescence variability from the start of the assay, all samples appear to demonstrate a bell-shaped curve approaching 100 °C. A Lorentzian curve was fitted to each of the profiles, using the curve centre to estimate T_m. The curve was only fitted to x-values up to 97.5 °C to avoid the sharp increase of derivative values at the end of the melting curve (such as that seen for M1 1T and M23 2T). All samples show a very high T_m, suggesting they all contain very stable SMALPs. The largest difference in stability is between the M1 and M23 void fractions. However, without biological replicates, it is difficult to ascertain the significance of this. It is also important to note that the Lorentzian function does not give an optimal curve-fit to all of the samples, with the first derivatives of the M1 AQP4-SMALP 2T and 1T SEC fractions having a particularly poor fit (Figure 4.15.C and E). This lowers the validity of these T_m estimates.

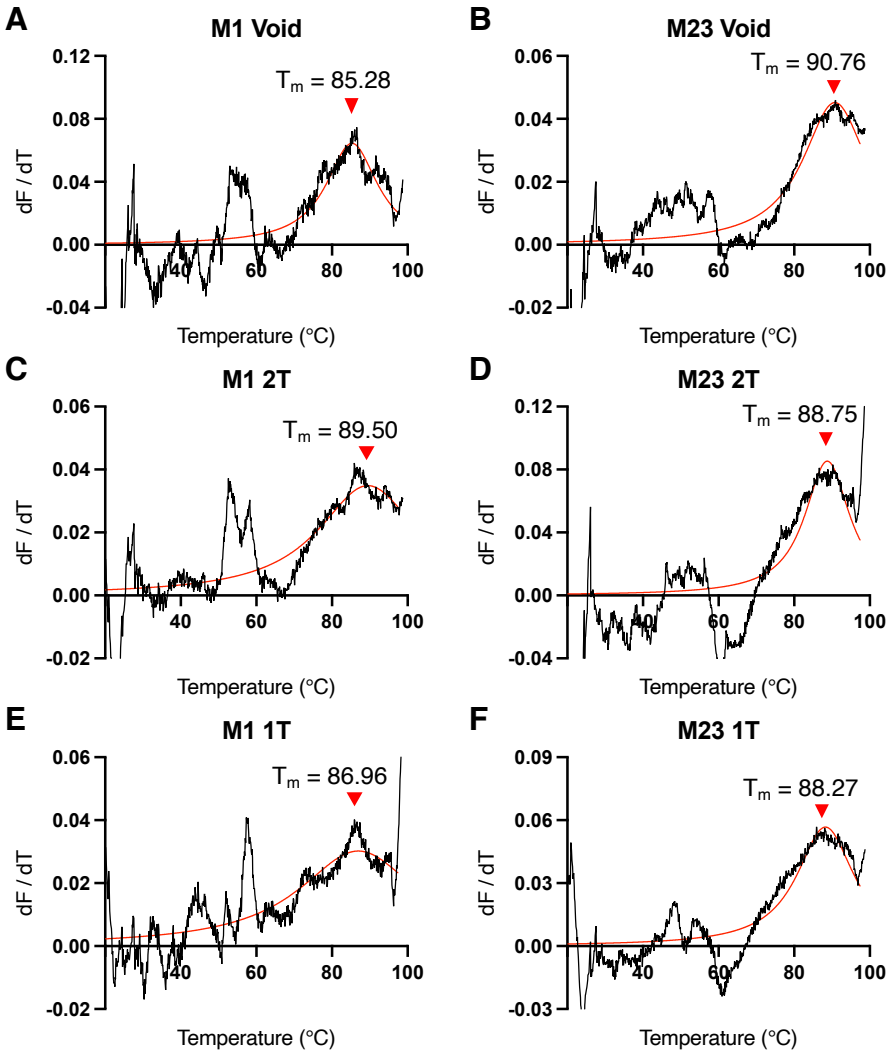

Figure 4.15. Estimation of the AQP4-SMALP melting points (T_m) from the protein thermal shift assay.

For each sample shown in Figure 4.14C, the first derivative of the melting curve was calculated (dF/dT). Figures show the dF/dT against temperature (°C). A) 1st derivative of the M1 SEC void. B) 1st derivative of the M23 SEC void. C) 1st derivative of M1 2T. D) 1st derivative of M23 2T. E) 1st derivative of M1 1T. F) 1st derivative M23 1T. The Lorentzian function was used to fit a curve to the 1st derivative profiles, using the curve centre to identify the dF/dT_{max} and estimate the melting point (T_m). T_m values are indicated for each profile, with arrows identifying the fitted Lorentzian curve centre.

4.5. Mass photometry identification of AQP4-SMALPs using a commercial anti-AQP4 Ab

With different AQP4-SMALP sizes identified, mass photometry was investigated as a method to identify AQP4 within the SMALPs using commercial anti-AQP4 Abs that are routinely used for techniques such as western blotting.

4.5.1. Characterisation of commercial Abs

Two Abs were being routinely used by our group for identification of AQP4 via techniques such as western blotting. These were both IgG rabbit monoclonal Abs (mAbs); one supplied by Abcam, and the other from Cell Signalling Technology. Firstly, these were compared by mass photometry (Section 2.8.2) to assess their homogeneity and predicted IgG mass (~150 kDa).

Figure 4.16 shows mass photometry histograms for these Abs, both analysed at a final concentration of 3 nM. Counts were normalised for the comparison to assess relative proportions of different peaks. Both present a peak at ~140 kDa, presumed to be the IgG Ab. Another peak is present in both samples at ~65 kDa. This was presumed to be BSA used in the storage buffers of these Abs. The Abcam Ab showed a very high proportion of BSA compared to the number of events detected for the IgG molecule. Therefore, the CST Ab was chosen for further assays.

Having chosen the CST Ab for assays probing AQP4, it was characterised at two concentrations alongside an anti-GFP Ab to be used as a negative control. The anti-GFP Ab is a polyclonal rabbit IgG Ab from Abcam, also routinely used by our group. As with previous mass photometry experiments, the concentrations used for these antibodies was determined by adjusting to a desired number of events detected by the mass photometer. If counts are too high and binding events are overlapping, this creates a noisy ratiometric image due to surface saturation, lowering the reliability of contrast measurements for single molecules. Often, for a sample otherwise showing a low amount of unbinding at low concentration, an increase in unbinding events, due to surface saturation, indicates measurement at too-high concentration (Kratochvíl *et al.*, 2024). This unbinding appears as positive contrast values (or negative kDa).

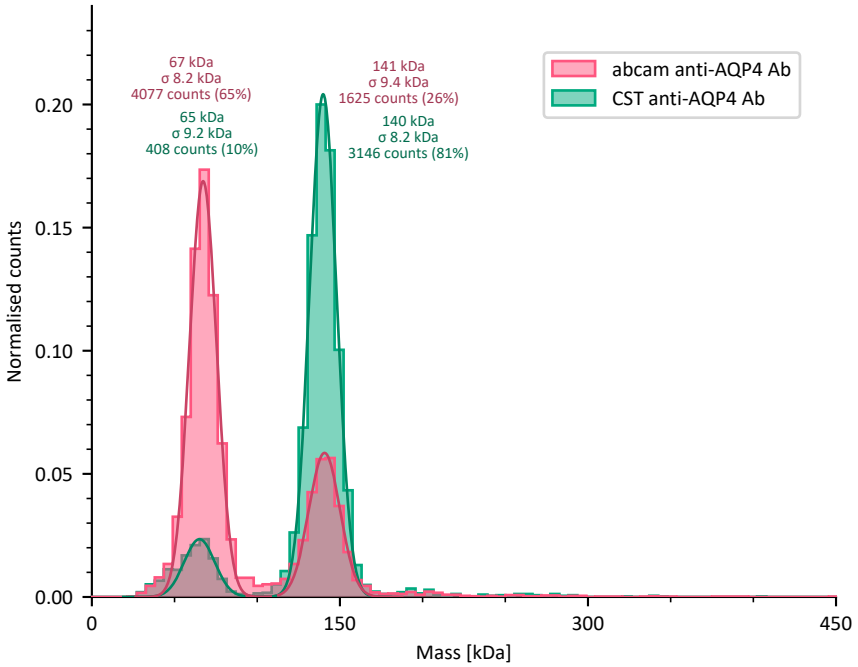

Figure 4.16. Characterising two commercial anti-AQP4 Abs with mass photometry.
The figure shows an overlayed mass photometry histogram of the CST (turquoise) and Abcam (pink) anti-AQP4 Abs. MS1000 was used for mass calibration. Both Abs were tested at a final concentration of 3 nM. Histograms show normalised counts plotted against calibrated mass (kDa). The histogram peaks in each sample are fitted with Gaussian distributions. Gaussian distributions are labelled with the mean (mass prediction), SD, and distribution counts (and percentage of total sample counts).

Figure 4.17. shows mass photometry histograms for these antibodies in vertical series, tested at two concentrations. The negative kDa region is shown to identify unbinding. The profiles appear very similar at very different final concentrations (anti-AQP4 Ab at 3 nM vs. anti-GFP at 33 nM). As the nM concentrations shown for the Abs were calculated based on the supplier information and an approximate MW of 150 kDa, this difference could be attributed to incorrect concentration estimates form the supplier. The far left peaks are not estimated for mass as these are presumed to be BSA or low MW noise.

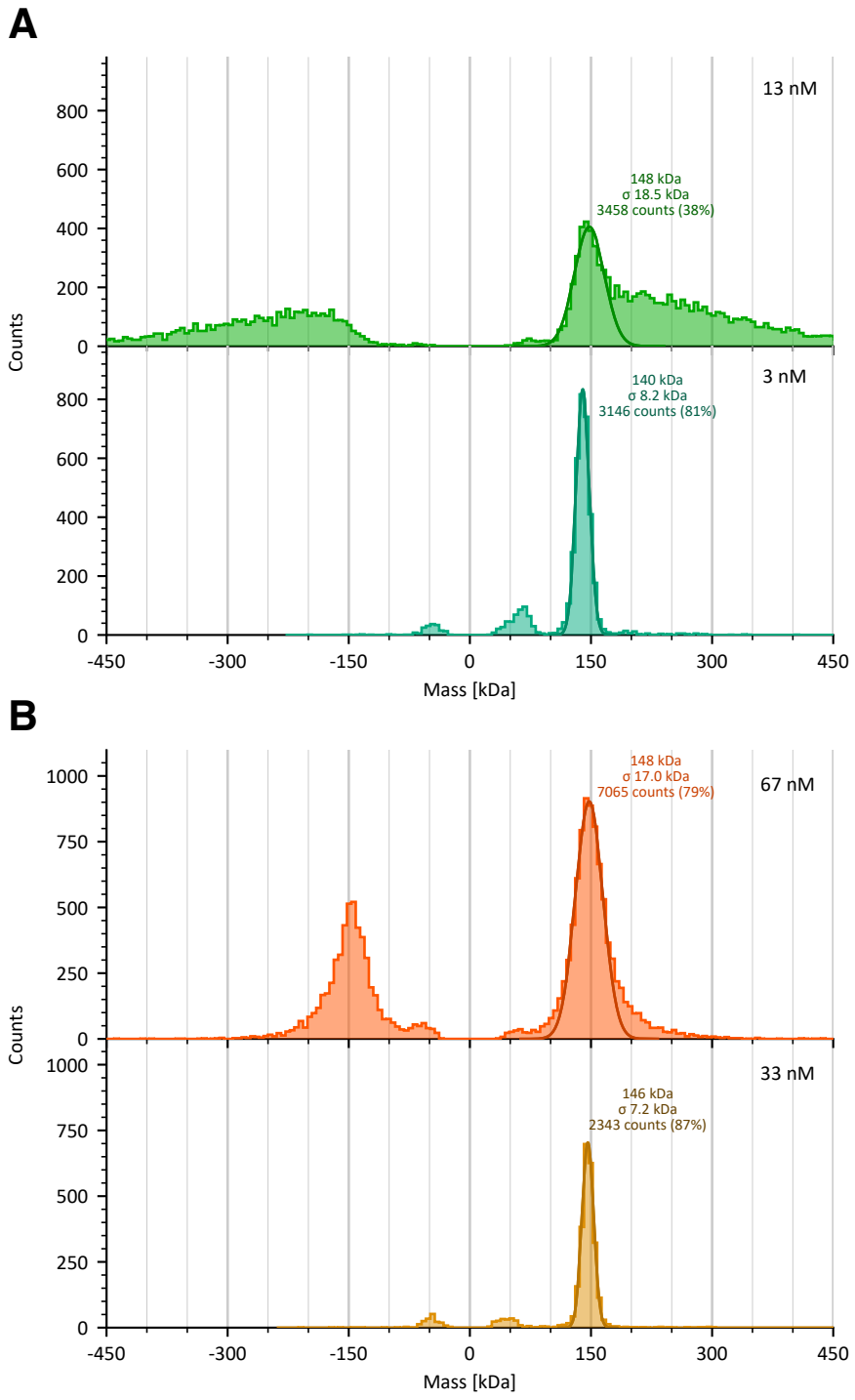

Figure 4.17. Mass photometry characterisation of an anti-AQP4 and anti-GFP Ab at different concentrations.
A) Mass photometry histograms of an anti-AQP4 Ab, analysed at two final concentrations – 13 nM and 3 nM (n = 1 per concentration). **B)** Mass photometry histograms of an anti-GFP Ab, analysed at two final concentrations – 67 nM and 33 nM (n = 1 per concentration). For both **A** and **B**, the negative x-axis is shown to identify molecule unbinding. The positive-mass histogram peaks in each sample are fitted with Gaussian distributions. Gaussian distributions are labelled with the mean, SD, and distribution counts (and percentage of total sample counts). MS1000 was used for mass calibration.

4.5.2. Anti-AQP4 Ab binding to AQP4-SMALPs at different concentrations

Having assessed the Abs individually, AQP4-SMALPs were incubated with the anti-AQP4 Ab to investigate binding. Given that the stoichiometry between this anti-AQP4 Ab and AQP4-SMALPs was unknown, assays were performed on the basis of being able to visualise either the Ab peak (Ab in excess), or the 1-tetramer AQP4-SMALP peak (AQP4 in excess). Stoichiometry would be difficult to determine due to the heterogeneity of the AQP4-SMALP samples, in particular with the 2T SEC fraction. Each anti-AQP4 IgG Ab has two antigen binding sites, and each 1-tetramer AQP4-SMALP most likely contained four AQP4 monomers. This means a range of binding stoichiometries were theoretically possible. The Ab was known to bind AQP4 monomers, as this Ab is used routinely by our group for observation of AQP4 monomers by western blot. However, it was also possible that these Abs would not be able to bind in close proximity due to steric hindrance. AQP4 tetramer concentration was used for assay optimisation and is specified here, as this is the theorised conformation in 1-tetramer AQP4-SMALPs. As there is no certainty around the contents of the '2T' SEC fraction, and considering that this fraction is very heterogeneous, AQP4 tetramer concentration was also used and specified for these reactions. Assay concentrations also had to be optimised so that there were not too many or too few detected events (counts).

The 1T and 2T SEC fractions for M1 and M23 AQP4-SMALPs were incubated (10 min, RT) at a concentration of 175 nM alone, with an anti-AQP4 Ab at 15 nM, or anti-AQP4 Ab at 65 nM. Reactions were droplet-diluted 5-fold into sample cassette wells and analysed by mass photometry (Section 2.8.2). The final concertation of AQP4 tetramers was 35 nM, analysed alone, with anti-AQP4 Ab at 3 nM, or anti-AQP4 at 13 nM. This allowed comparison to the concentrations of anti-AQP4 Ab visualised alone in Figure 4.17A.

Figure 4.18 shows the resulting mass photometry analysis for anti-AQP4 Ab incubations with the M1 (Figure 4.18A) and M23 (Figure 4.18B) AQP4-SMALPs in the 1T SEC fraction (Figure 4.10). For the reaction with 3 nM anti-AQP4 Ab, no Ab peak could be seen, suggesting it had all bound to AQP4. This was in contrast to when analysed alone, where a peak was clearly visible (Figure 4.17A). For both M1 and M23 AQP4, new peaks at ~440 kDa (M1, Figure 4.18A) and ~425 kDa (M23, Figure 4.18B) emerged, which most likely represented one anti-AQP4 Ab (~140 kDa, as observed alone), binding to the 1-tetramer AQP4-SMALP (~300 kDa for M1, ~285 kDa for M23). At 13 nM, the anti-AQP4 Ab peak became visible and the ~440 kDa (M1) and ~425 kDa (M23) peaks became more prominent. This profile did not present with an oversaturated ratiometric image (and unbinding), which is very different to that seen for the Ab alone at 13 nM (Figure 3.17A). This is likely explained by binding between the AQP4-SMALP

and Ab reducing the number of whole particle events, and would also suggest that multiple Abs were binding to individual AQP4-SMALPs. The peaks representing the 1-tetramer AQP4-SMALPs became almost indiscernible. Interestingly, peaks at ~585 kDa (M1) and ~565 kDa (M23), thought to represent the 2-tetramer AQP4-SMALPs, also became more prominent. It is possible that these represent two anti-AQP4 Abs binding to the 1-tetramer AQP4-SMALP, with this complex and the 2-tetramer SMALP contributing to this observed peak. No other peaks at a higher mass could be observed in these reactions. As before, the far left peaks are not estimated for mass as these are presumed to be BSA or low MW noise.

Figure 4.19 shows the resulting mass photometry analysis for anti-AQP4 Ab incubations with M1 (Figure 4.19A) and M23 (Figure 4.19B) AQP4-SMALPs in the 2T SEC fraction (Figure 4.10). For the reaction with 3 nM anti-AQP4 Ab, there was little change in the peak profile compared to the AQP4-SMALPs alone. As with the 1T SEC fractions, no Ab peak could be distinguished, suggesting it had all bound to AQP4. There was some reduction in the relative proportion of counts from the AQP4-SMALP peaks, which might be explained by Ab binding in multiple stoichiometries and creating a heterogenous mix of different particle sizes that cannot be individually distinguished. At 13 nM, the anti-AQP4 Ab peak became visible, and the AQP4-SMALP peaks reduced to a similar proportion of counts to a number of intermediate peaks appearing between the theorised 1-, 2-, and 3- tetramer AQP4-SMALP peaks. Appearance of peaks at 716 kDa (M1) and 682 kDa (M23) suggest binding of one anti-AQP4 Ab to the 2-tetramer AQP4-SMALPs. However, these are lower masses than expected for the given stoichiometry. Peaks at 1013 kDa (M1) and 985 kDa (M23) also appear, which could represent (as approximate values) two Abs binding to the theorised 2-tetramer AQP4-SMALP, or one Ab binding to the theorised 3-tetramer AQP4-SMALP. Interestingly, the 1-tetramer M1 AQP4-SMALP peak disappeared at this Ab concertation, whereas the 1-tetramer M23 AQP4-SMALP remained. As before, the far left peaks are not estimated for mass as these are presumed to be BSA or low MW noise.

This evidence suggests that there is a binding interaction between the anti-AQP4 Ab and the AQP4-SMALPs present in both the 1T and 2T SEC fractions. However, it is important to note that mass estimates of AQP4-SMALP peaks were not always consistent between the analysed reactions of the same sample. Some of the peak Gaussian fits are very broad, lowering the validity of estimated mass. This is likely a product of sample heterogeneity, particularly with the 2T AQP4-SMALP SEC fractions. This heterogeneity was further increased with the added anti-AQP4 Ab.

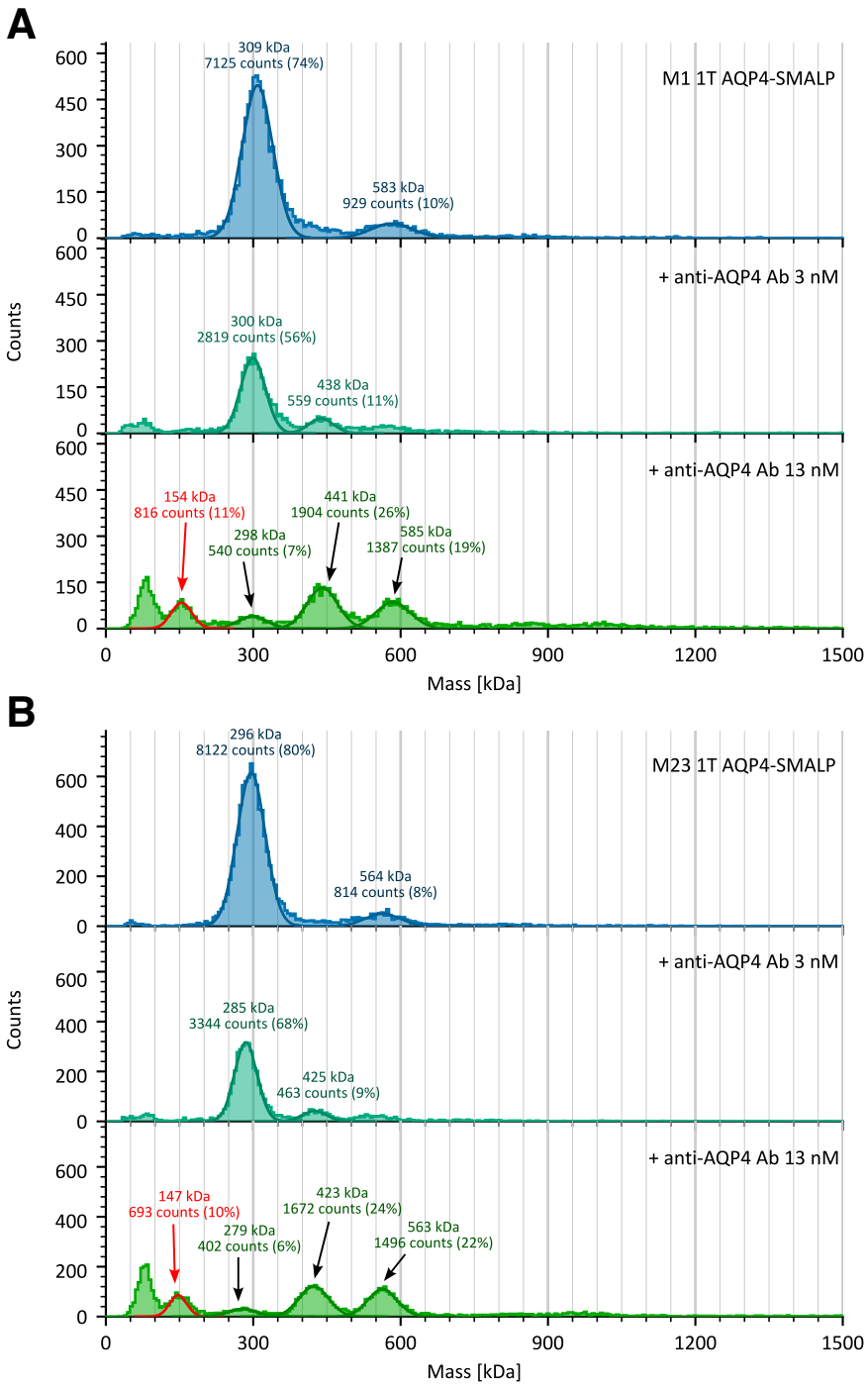

Figure 4.18. Mass photometry of 1-tetramer AQP4-SMALPs probed with an anti-AQP4 Ab at two different concentrations.
M1 and M23 1-tetramer (1T) AQP4-SMALPs were identified by SEC and corresponding fractions collected (Figure 4.10). AQP4-SMALPs were incubated (10 min, RT) at a concentration of 175 nM alone, with an anti-AQP4 Ab at 15 nM, or anti-AQP4 Ab at 65 nM. Reactions were droplet-diluted 5-fold into cassette wells (final concentrations: AQP4 tetramer, 35 nM; anti-AQP4 Ab, 3 nM or 13 nM) and analysed by mass photometry (n = 1 per reaction). MS1000 was used for mass calibration. Figures show histograms of the Ab reactions for M1 (**A**) and M23 (**B**) 1T AQP4-SMALPs, with counts plotted against calibrated mass (kDa). Reactions and final Ab concentrations are identified in the top-right of each histogram. The histogram peaks in each sample are fitted with Gaussian distributions. Gaussian distributions are labelled with the mean (mass prediction), SD, and distribution counts (and percentage of total sample counts). Ab peaks in the relevant samples are indicated with a red Gaussian distribution line and mass label.

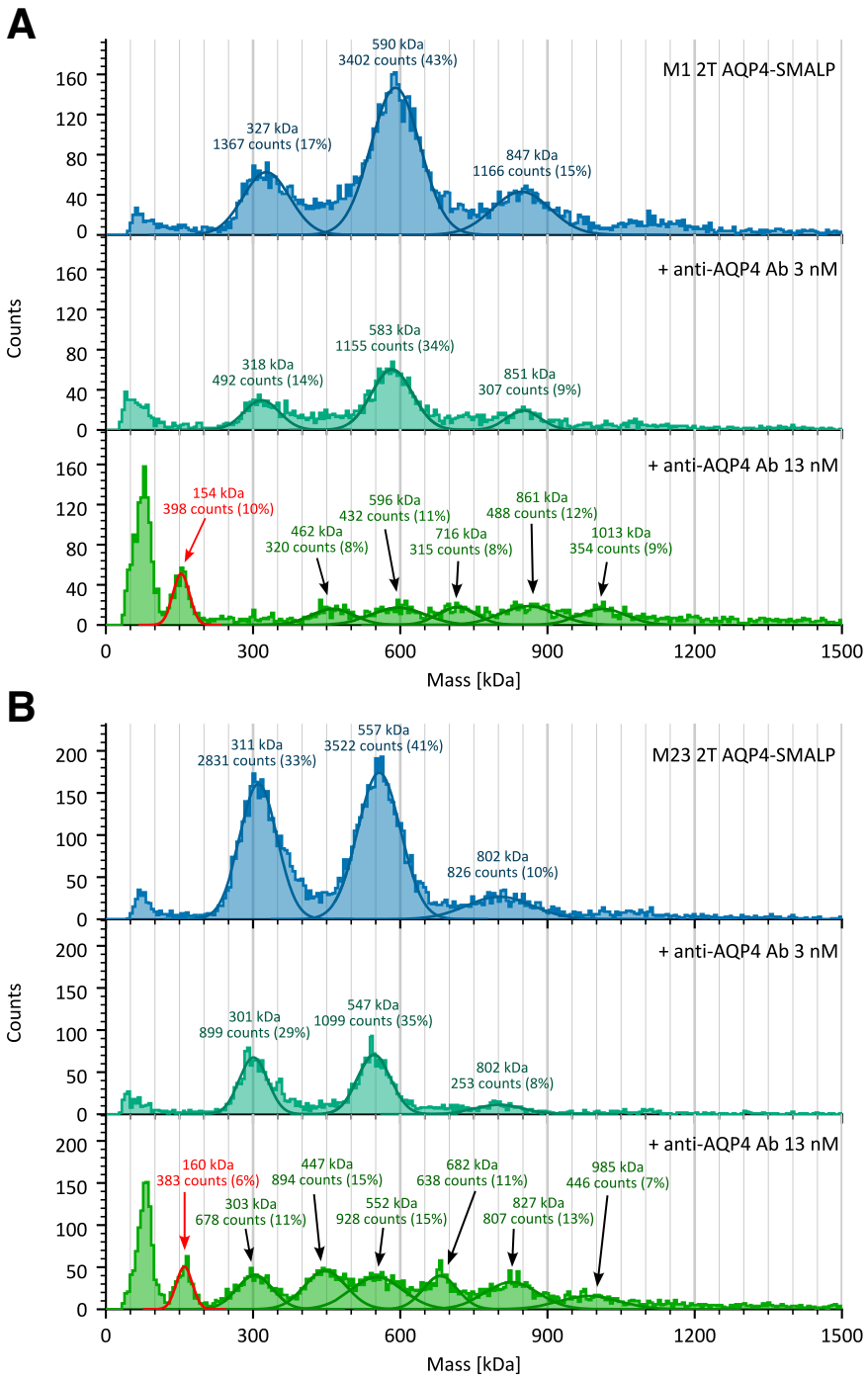

Figure 4.19. Mass photometry of 2-tetramer AQP4-SMALPs probed with an anti-AQP4 Ab at two different concentrations.
M1 and M23 2-tetramer (2T) AQP4-SMALPs were identified by SEC and corresponding fractions collected (Figure 4.10). AQP4-SMALPs were incubated (10 min, RT) at a concentration of 175 nM alone, with an anti-AQP4 Ab at 15 nM, or anti-AQP4 Ab at 65 nM. Reactions were droplet-diluted 5-fold into cassette wells (final concentrations: AQP4 tetramer, 35 nM; anti-AQP4 Ab, 3 nM or 13 nM) and analysed by mass photometry (n = 1 per reaction). MS1000 was used for mass calibration. Figures show histograms of the Ab reactions for M1 (**A**) and M23 (**B**) 2T AQP4-SMALPs, with counts plotted against calibrated mass (kDa). Reactions and final Ab concentrations are identified in the top-right of each histogram. The histogram peaks in each sample are fitted with Gaussian distributions. Gaussian distributions are labelled with the mean (mass prediction), SD, and distribution counts (and percentage of total sample counts). Ab peaks in the relevant samples are indicated with a red Gaussian distribution line and mass label.

4.5.2. Testing an anti-GFP Ab as a negative control

Having shown that there is an interaction between the AQP4-SMALPs and the anti-AQP4 Ab, the next step was to confirm that the observed interactions were facilitated by binding to AQP4, as opposed to non-specific binding to SMALPs. The characterised anti-GFP Ab (Figure 4.17B) was used in a similar assay as described for the anti-AQP4 Ab. As before, assay concentrations had to be optimised to prevent measurements that had too many or too few events (counts).

The 1T and 2T SEC fractions for M1 and M23 AQP4-SMALPs were incubated (10 min, RT) at a concentration of 175 nM alone, or with the anti-GFP Ab at 165 nM. Reactions were droplet-diluted 5-fold into sample cassette wells and analysed by mass photometry (Section 2.8.2). The final concertation of AQP4 tetramers was 35 nM, analysed alone, or with anti-GFP Ab at 33 nM. This allowed comparison to the 33 nM concentration of anti-GFP Ab visualised alone in Figure 4.17B.

Figure 4.18 shows the resulting mass photometry analysis for anti-GFP Ab incubations with the M1 (Figure 4.20A) and M23 (Figure 4.20B) AQP4-SMALPs in the 1T SEC fraction (Figure 4.10). Figure 4.19 shows the resulting mass photometry analysis for anti-GFP Ab incubations with M1 (Figure 4.21A) and M23 (Figure 4.21B) AQP4-SMALPs in the 2T SEC fraction (Figure 4.10). The mass photometry profiles for AQP4-SMALPs alone and AQP4-SMALPs incubated with 13 nM anti-AQP4 Ab are reproduced from Figures 4.18 and 4.19. These are added to the histogram vertical series for comparison to the anti-GFP Ab profile. A peak representing the anti-GFP Ab is visible in all incubations and no AQP4-SMALP peak shift can be identified. A change in the relative proportion of AQP4-SMALP counts can be seen with the anti-GFP Ab added, but this is explained by the presence of the anti-GFP Ab reducing the proportion of total binding events coming from AQP4-SMALPs. As before, the far left peaks are not estimated for mass as these are presumed to be BSA or low MW noise.

These data suggest that there is no binding interaction between the anti-GFP Ab and AQP4-SMALPs. Increasing the anti-GFP Ab to a final concentration of 67 nM resulted in an over-saturated ratiometric image, further supporting that no interaction was happening between the AQP4-SMALPs and the anti-GFP Ab. If binding was taking place, the total number of particles would likely have been reduced, resulting in fewer binding events, as seen with the anti-AQP4 Ab at high concentration.

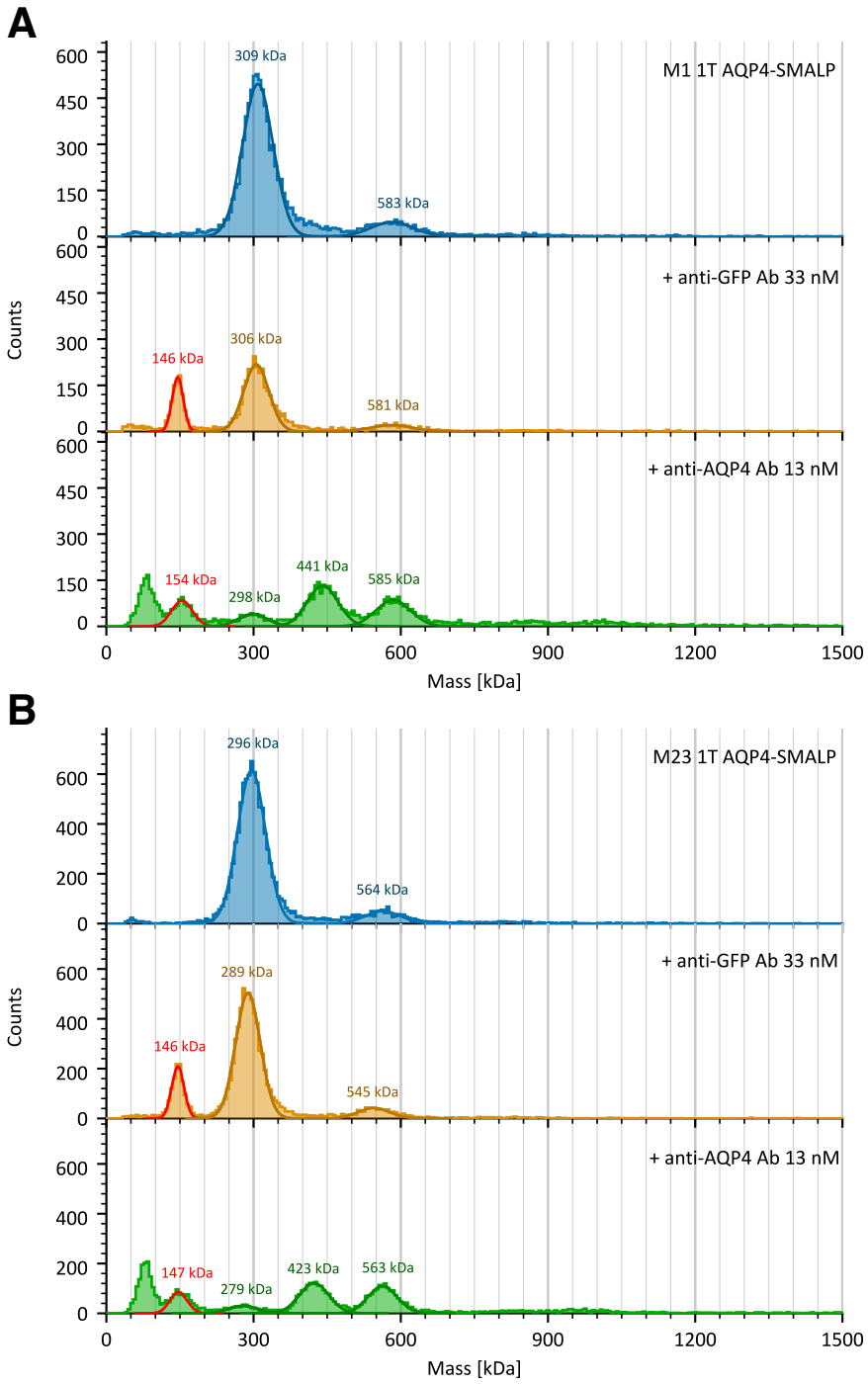

Figure 4.20. Mass photometry of 1-tetramer AQP4-SMALPs probed with an anti-AQP4 Ab and anti-GFP Ab negative control.
M1 and M23 1-tetramer (1T) AQP4-SMALPs were identified by SEC and corresponding fractions collected (Figure 4.10). AQP4-SMALPs were incubated (10 min, RT) at a concentration of 175 nM alone, with an anti-GFP Ab (165 nM), or anti-AQP4 Ab (65 nM). Reactions were droplet-diluted 5-fold into cassette wells (final concentrations: AQP4 tetramer, 35 nM; anti-GFP Ab, 33 nM; anti-AQP4 Ab, 13 nM) and analysed by mass photometry (n = 1 per reaction). MS1000 was used for mass calibration. Figures show histograms of the Ab reactions for M1 (**A**) and M23 (**B**) 1T AQP4-SMALPs, with counts plotted against calibrated mass (kDa). Reactions and final Ab concentrations are identified in the top-right of each histogram. The histogram peaks in each sample are fitted with Gaussian distributions and labelled with the mean (mass prediction). Ab peaks in the relevant samples are indicated with a red Gaussian distribution line and mass label. Blue and green profiles are reproduced from Figure 4.18 for comparison.

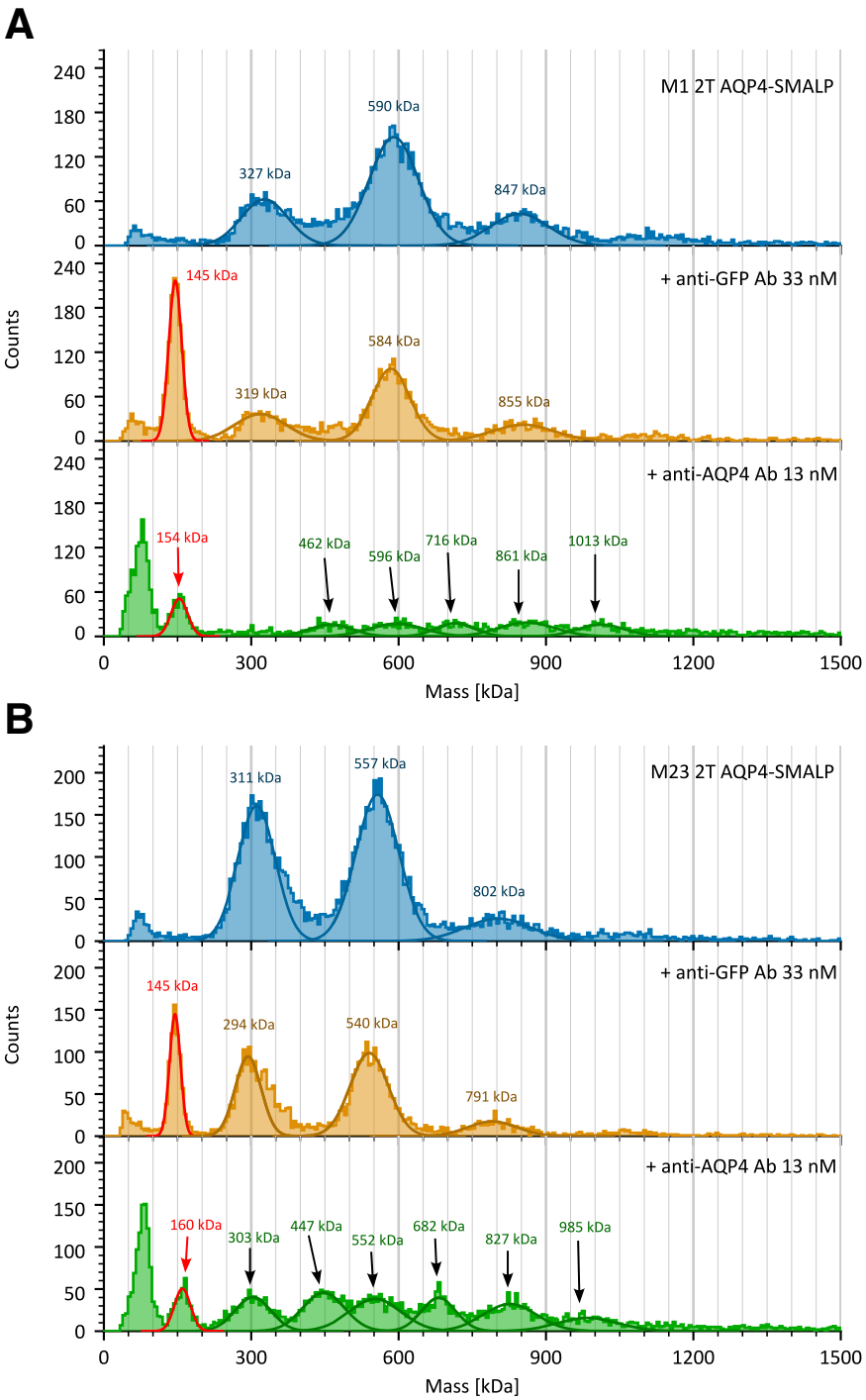

Figure 4.21. Mass photometry of 2-tetramer AQP4-SMALPs probed with an anti-AQP4 Ab and anti-GFP Ab negative control.
M1 and M23 2-tetramer (2T) AQP4-SMALPs were identified by SEC and corresponding fractions collected (Figure 4.10). AQP4-SMALPs were incubated (10 min, RT) at a concentration of 175 nM alone, with an anti-GFP Ab (165 nM), or anti-AQP4 Ab (65 nM). Reactions were droplet-diluted 5-fold into cassette wells (final concentrations: AQP4 tetramer, 35 nM; anti-GFP Ab, 33 nM; anti-AQP4 Ab, 13 nM) and analysed by mass photometry (n = 1 per reaction). MS1000 was used for mass calibration. Figures show histograms of the Ab reactions for M1 (**A**) and M23 (**B**) 2T AQP4-SMALPs, with counts plotted against calibrated mass (kDa). Reactions and final Ab concentrations are identified in the top-right of each histogram. The histogram peaks in each sample are fitted with Gaussian distributions and labelled with the mean (mass prediction). Ab peaks in the relevant samples are indicated with a red Gaussian distribution line and mass label. Blue and green profiles are reproduced from Figure 4.19 for comparison.

4.6. Comparing mass estimates for AQP4-SMALPs

Accurate mass measurement of MP-SMALPs can be challenging, due to the inherent heterogeneity of these particles (containing lipids, protein, and SMA). AQP4-SMALPs had now been characterised by mass photometry, SEC, and SMA-PAGE. These methods had all shown the presence of multiple SMALP sizes, and all offered a way to estimate mass relatively quickly and easily. Therefore, these techniques were assessed for their ability to precisely estimate the mass of these AQP4-SMALPs over multiple replicate measurements, and these estimates were compared for similarity between each method. Three AQP4-SMALP sizes had been consistently observed and identified by their theorised AQP4 tetrameric assembly; 1-tetramer (1T), 2-tetramer (2T), and 3-tetramer (3T). Mass estimates were calculated for each of these particles.

4.6.1. Mass estimation by mass photometry

Mass photometry works on the principle of molecule contrast being proportional to molecule mass. Therefore, a calibration curve can be made by measuring calibrant samples of known masses. Measured contrast is directly proportional to mass (kDa). Calibrations were routinely performed before each data acquisition session. In normal procedure, the user measures mass calibrants, fits Gaussian distributions to the histogram peaks, and assigns masses to the identified peaks. Mass standard curves and curve-fit accuracy values are then calculated automatically by Refeyn DMP software.

Two mass calibrants were used routinely during this project: MS1000 (Section 2.8.2) and NativeMark (Invitrogen). Figure 4.22A and C show example mass photometry measurements for these calibrants. The histograms show the measured contrast values before applied mass calibration. Figure 4.22B and D demonstrate the principle in which calibration curves are determined using these calibrants. The mass of each protein contributing to each peak in the mass photometry histogram is plotted against its measured contrast value.

Estimated masses from mass photometry (Section 2.8.2) of AQP4-SMALPs were compared across biological replicates (from different purifications) and technical replicates (of the same IMAC purification in one measurement session). AQP4-SMALP peaks were identified as ‘1T’, ‘2T’, and ‘3T’, representing theorised 1-, 2-, and 3-tetramers in SMALPs. Figure 4.23A shows an example mass photometry histogram for AQP4-SMALPs to demonstrate peak

identification. For each replicate, Gaussian distributions were fitted to the 1T, 2T, and 3T peaks. Gaussian means were taken as the mass estimate.

Figure 4.23B shows a plot of the mean ± SD estimated mass for each of the 1T, 2T, and 3T peaks for M1 and M23 AQP4-SMALPs. Means were calculated from biological replicates of three different expressions and purifications for M1 and M23 AQP4. For two of the repeats, masses were calibrated using NativeMark, and one repeat was calibrated using MS1000. MS1000 became available later in the project and gave a higher mass accuracy than NativeMark, as indicated by DMP software. Therefore, this was preferred for mass calibration of later experiments. Two repeats represent mass photometry of IMAC purified AQP4-SMALPs (including Figure 4.23A). One repeat represents mass photometry of IMAC and SEC purified AQP4-SMALPs. In this instance, the 1T peak from the 1T SEC fraction was used for estimation of 1T AQP4-SMALPs, and 2T and 3T peaks from the 2T SEC fraction were used for estimation of 2T and 3T AQP4-SMALPs. A one-way ANOVA with Tukey's *post hoc* test found a significant difference between mean mass estimates of the 1T, 2T, and 3T AQP4-SMALPs, for M1 and M23 AQP4. However, no significance was found between M1 and M23 AQP4 mass estimates when comparing each of the relative SMALP sizes (e.g. 1T M1 AQP4-SMALP vs. 1T M23 AQP4-SMALP).

Mass photometry was also assessed for its reliability and precision measuring AQP4-SMALPs in one measurement session. Figure 4.23C shows a plot of the mean ± SD estimated mass for each of the 1T, 2T, and 3T peaks for M1 and M23 AQP4-SMALPs, calculated from technical replicates of the IMAC purified samples shown in Figure 4.23A. A one-way ANOVA with Tukey's *post hoc* test found a significant difference between mean mass estimates of the 1T, 2T, and 3T AQP4-SMALPs, for M1 and M23 AQP4. For these technical replicates, significance was also found between M1 and M23 AQP4 mass estimates when comparing each of the relative SMALP sizes (e.g. 1T M1 AQP4-SMALP vs. 1T M23 AQP4-SMALP).

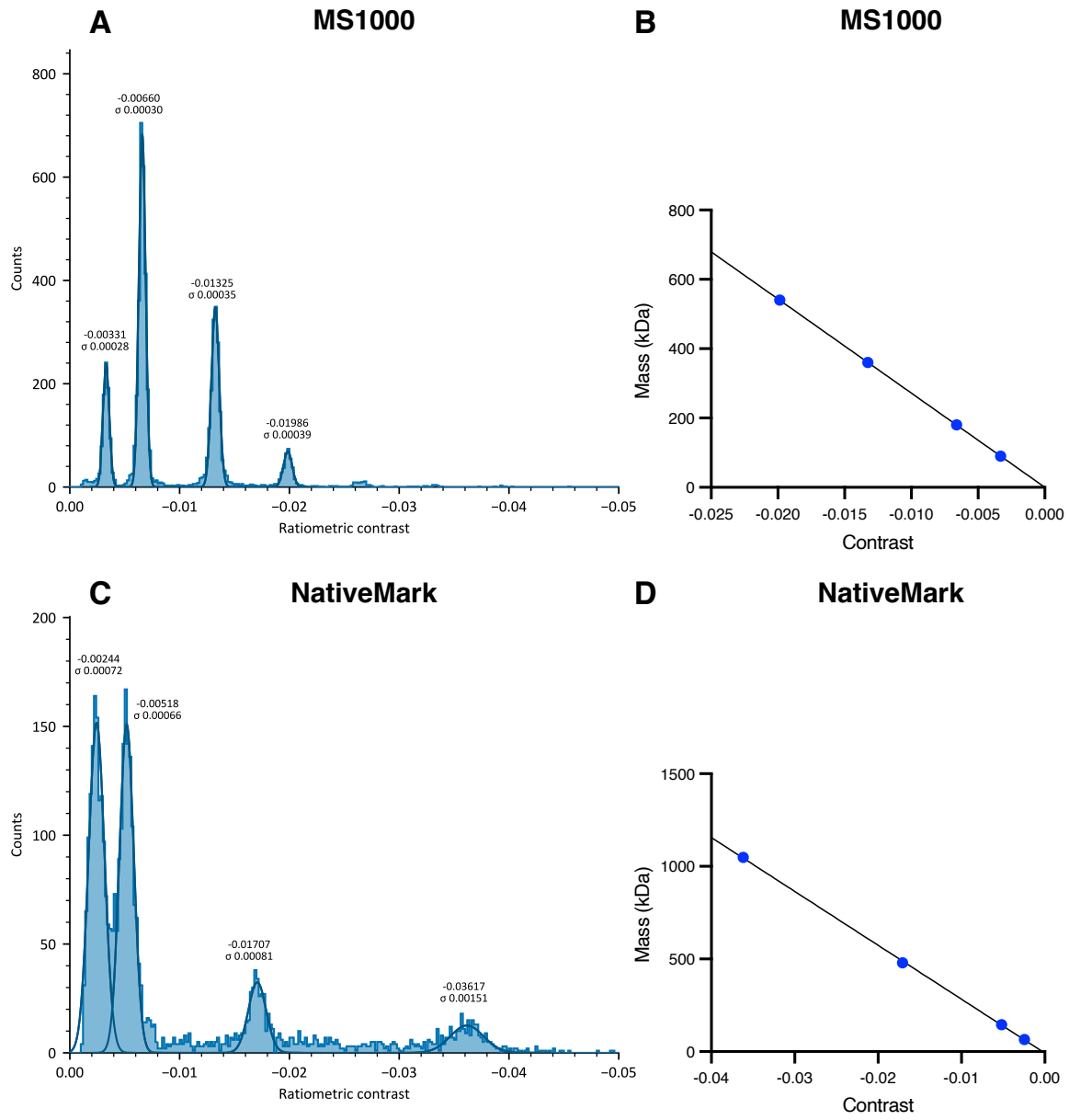

Figure 4.22. Principle of mass calibration for mass photometry.
A, C) Mass photometry histograms of MS1000 (**A**) and NativeMark (**C**) mass calibrants. Calibrant sample counts are plotted against ratiometric contrast. Peaks are fitted with Gaussian distributions and labelled with the distribution mean and SD. **B, D)** Known masses of MS1000 (**B**) and NativeMark (**D**) plotted against ratiometric contrast of corresponding identified peaks in **A** and **C**, respectively. A linear regression was calculated, and the line is shown on the graph to represent a standard curve. This figure serves as a demonstration of mass photometry mass calibration. In normal procedure, mass calibrants are measured, fitted with Gaussian distributions, and masses assigned to distribution peaks by the user. Standard curves for mass calibration of samples are then calculated automatically by Refeyn DMP software.

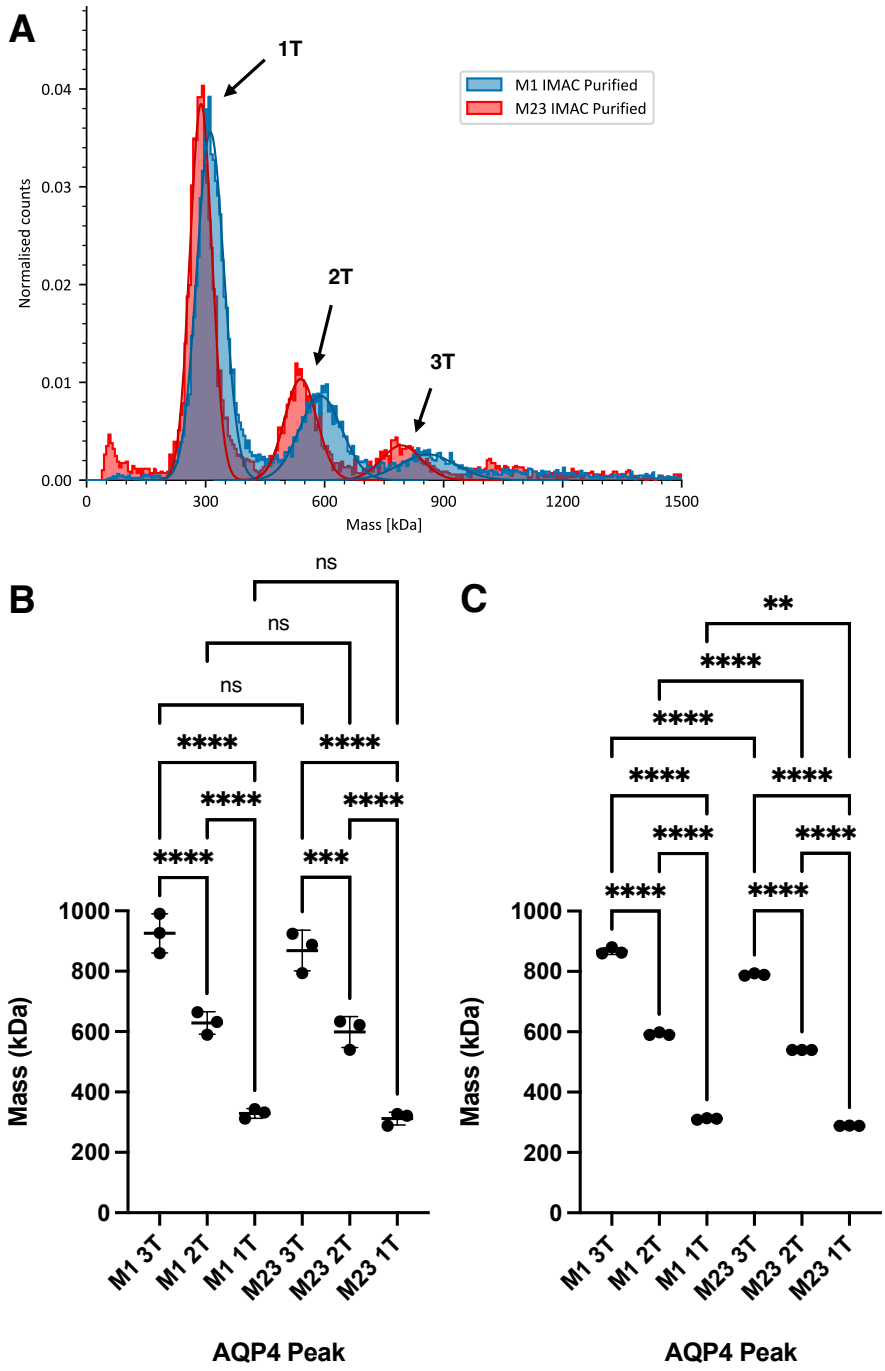

Figure 4.23. Estimation of AQP4-SMALP mass using mass photometry.
'1T', '2T', and '3T' peaks, representing theorised 1-, 2-, and 3-tetramer AQP4-SMALPs, were identified by mass photometry of purified AQP4-SMALPs. **A)** Mass photometry histogram demonstrating identification of AQP4-SMALP peaks for mass estimates, reproduced from Figure 4.4. The figure shows overlayed histograms of IMAC purified M1 (blue) and M23 (red) AQP4-SMALPs with normalised counts plotted against calibrated mass (kDa). The histogram peaks in each sample are fitted with Gaussian distributions (M1, blue; M23, red). Gaussian distributions are labelled according to peaks predicted to represent 1- (1T), 2- (2T), and 3- (3T) tetramer AQP4-SMALPs. Gaussian means were used as mass estimates for each peak in each sample. **B)** Mean mass estimates ± SD for each identified AQP4-SMALP peak from mass photometry biological replicates (n = 3), including the sample shown in **A**. NativeMark and MS1000 were used for mass calibration. **C)** Mean mass estimates ± SD for each identified AQP4-SMALP peak from technical replicates (n = 3) of the sample shown in **A**. MS1000 was used for mass calibration. Statistical analysis of each data set was performed with a one-way ANOVA with Tukey's multiple comparisons *post hoc* test (ns – $p > 0.05$ (not significant), **$p \leq 0.01$, ***$p \leq 0.001$, ****$p \leq 0.0001$).

4.6.2. Mass estimation by SEC

SEC can be used to estimate mass by running mass standards through the desired SEC column, identifying the proteins using the 280 nm trace, and using the protein retention volume to generate a mass standard curve. Retention values of samples of unknown masses can then be interpolated to estimate sample mass. Retention values for each protein were determined by finding the apex of the UV trace peak for that protein.

A mass standard curve was determined using the Sigma SEC Protein Standard Mix (15 – 600 kDa) through the Superose 6 column, as this was the favoured column for separation of AQP4-SMALPs. Figure 4.24A shows the SEC profile for the Sigma SEC standards, with the peaks labelled with the corresponding mass standard protein. Retention (mL) values for each of these peaks was plotted against the corresponding protein mass (Figure 4.24B), and a log transform of MW (kDa) was calculated in order to fit a linear standard curve (Figure 4.24C).

Estimated masses from SEC (Section 2.8.1) of AQP4-SMALPs were compared across biological replicates (from different purifications). AQP4-SMALP peaks were identified as '1T' and '2T', representing theorised 1- and 2-tetramers in SMALPs. Figure 4.25A shows an example SEC profile for AQP4-SMALPs to demonstrate peak identification. A peak representing the 3-tetramer (3T) AQP4-SMALP could not be identified from the AQP4-SMALP Superose 6 SEC profiles, and thus, a mass estimate for this SMALP was not calculated using SEC. The standard curve described in Figure 4.24 was used to calculate mass estimates for the 1T and 2T AQP4-SMALPs by interpolating peak retention volumes from the AQP4-SMALP Superose 6 SEC profiles.

Figure 4.25B shows a plot of the mean ± SD estimated mass for the 1T and 2T AQP4-SMALP SEC peaks for M1 and M23 AQP4. Means were calculated from three biological replicates of SEC from different M1 and M23 AQP4 purifications (including that shown in Figure 4.25A). A one-way ANOVA with Tukey's *post hoc* test found a significant difference between mean mass estimates of the 1T and 2T AQP4-SMALPs, for M1 and M23 AQP4. However, no significance was found between M1 and M23 AQP4 mass estimates when comparing each of the relative SMALP sizes (e.g. 1T M1 AQP4-SMALP vs. 1T M23 AQP4-SMALP).

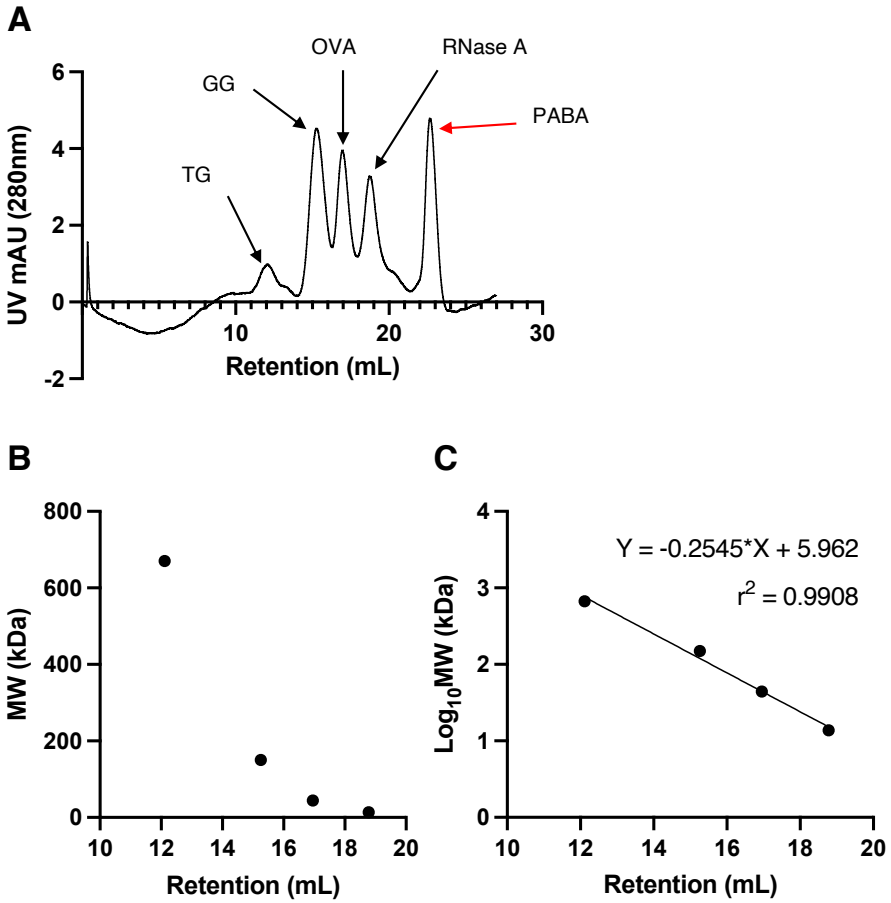

Figure 4.24. SEC mass standard curve using mass standards.
A) SEC profile of Sigma SEC Protein Standard Mix (15 – 600 kDa) separated using the Superose 6 column. Profiles show mAU measured at UV 280nm against the buffer retention volume (mL). Peaks are labelled to indicate the protein standards, where 'TG' is Thyroglobulin, 'GG' is γ-globulin, 'OVA' is Ovalbumin, 'RNAse A' is Ribonuclease A, and 'PABA' is para-aminobenzoic acid. PABA is used as a low molecular size marker. **B)** MW (kDa) of mass standards against their buffer retention volume (mL). **C)** Log_{10}MW (kDa) of mass standards against their buffer retention volume (mL). A linear regression was calculated, and the line is shown on the graph. The line equation and r^2 value are shown on the top right of the plot.

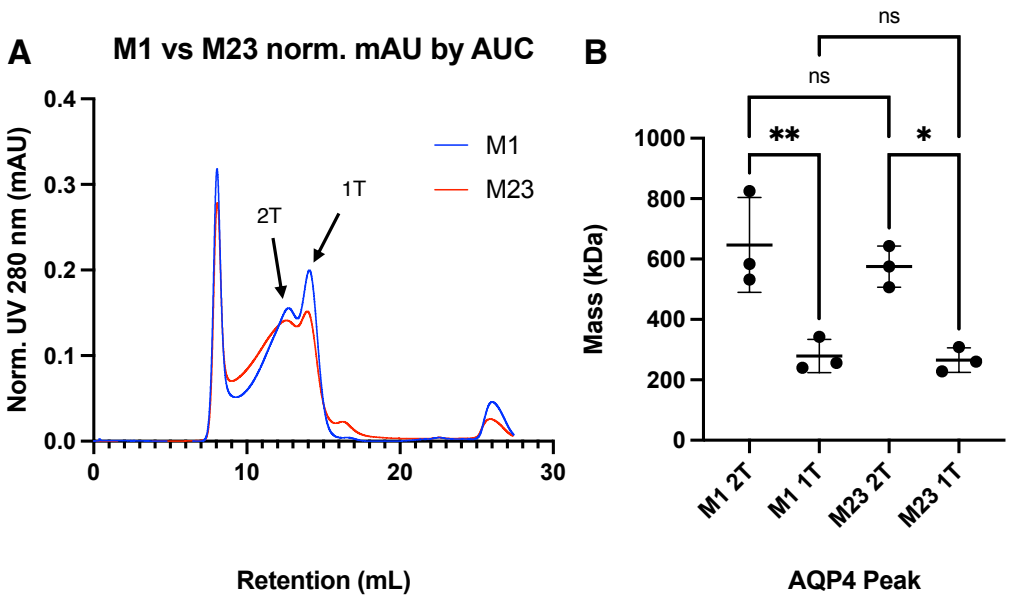

Figure 4.25. Estimation of AQP4-SMALP mass using SEC.
'1T' and '2T' peaks, representing theorised 1-, and 2-tetramer AQP4-SMALPs, were identified in SEC analysis of purified AQP4-SMALPs. Estimated masses were calculated for peak retention values using the standard curve shown in Figure 4.24. Calculated masses were compared across biological replicates from different purification samples. All samples were separated using the Superose 6 column. **A)** Overlay of M1 (blue) and M23 (red) AQP4-SMALP SEC profiles. Profiles show normalised mAU measured at UV 280 nm against the buffer retention volume (mL). Peaks predicted to represent 1- (1T) and 2- (2T) tetramer AQP4-SMALPs are labelled. This figure is one of three replicates and is used to demonstrate identification of peaks for mass estimates. **B)** Mean mass estimate ± SD for each identified AQP4-SMALP peak from SEC biological replicates (n = 3), including the sample shown in **A**. Statistical analysis was performed with a one-way ANOVA with Tukey's multiple comparisons *post hoc* test (ns – $p > 0.05$ (not significant), *$p \leq 0.05$, **$p \leq 0.01$).

4.6.3. Mass estimation by SMA-PAGE

SMA-PAGE can be used to estimate mass by separating mass standards alongside samples of unknown mass. The relative migration distance (R_f) can be calculated for each band representing each mass standard protein. R_f values can be plotted against mass to generate a standard curve. Unknown masses can be estimated by interpolating R_f values calculated for sample bands. R_f values were determined from gels by dividing band distance by dye-front distance.

Mass standard curves were determined for SMA-PAGE gels using Invitrogen NativeMark. BSA was routinely loaded adjacent on the same gel to identify the ~66 kDa band. Figure 4.26A shows an example SMA-PAGE separation of NativeMark alongside BSA, with the mass labelled for each protein standard representing each band. Masses corresponding to each band were plotted against the band R_f value (Figure 4.26B). A log transform of the MW (kDa) was calculated in order to fit a linear standard curve (Figure 4.26C). Figure 4.26 demonstrates an example mass standard curve for SMA-PAGE. A standard curve was calculated for each individual SMA-PAGE gel analysed for mass estimation of AQP4-SMALPs.

Estimated masses from SMA-PAGE (Section 2.7.5) of AQP4-SMALPs were compared across biological replicates (from different purifications). AQP4-SMALP bands were identified as '1T', '2T', and 3T representing theorised 1-, 2-, and 3-tetramers in SMALPs. Figure 4.27A shows an example SMA-PAGE gel of AQP4-SMALPs to demonstrate band identification. Standard curves were calculated as described (Figure 4.26) for each SMA-PAGE gel analysed. AQP4-SMALP mass estimates were calculated by interpolating AQP4-SMALP band R_f values into these standard curves.

Figure 4.27B shows a plot of the mean ± SD estimated mass for the 1T, 2T, and 3T AQP4-SMALP SMA-PAGE bands for M1 and M23 AQP4. Means were calculated from three biological replicates from different M1 and M23 AQP4 purifications. Two repeats represent SMA-PAGE of IMAC purified AQP4-SMALPs (including Figure 4.27A). One repeat represents SMA-PAGE of IMAC and SEC purified AQP4-SMALPs. In this instance, the 1T band from the 1T SEC fraction was used for estimation of 1T AQP4-SMALPs, and 2T and 3T bands from the 2T SEC fraction were used for estimation of 2T and 3T AQP4-SMALPs. A one-way ANOVA with Tukey's *post hoc* test found a significant difference between mean mass estimates of the 1T, 2T, and 3T AQP4-SMALPs, for M1 and M23 AQP4. However, no significance was found between M1 and M23 AQP4 mass estimates when comparing each of the relative SMALP sizes (e.g. 1T M1 AQP4-SMALP vs. 1T M23 AQP4-SMALP).

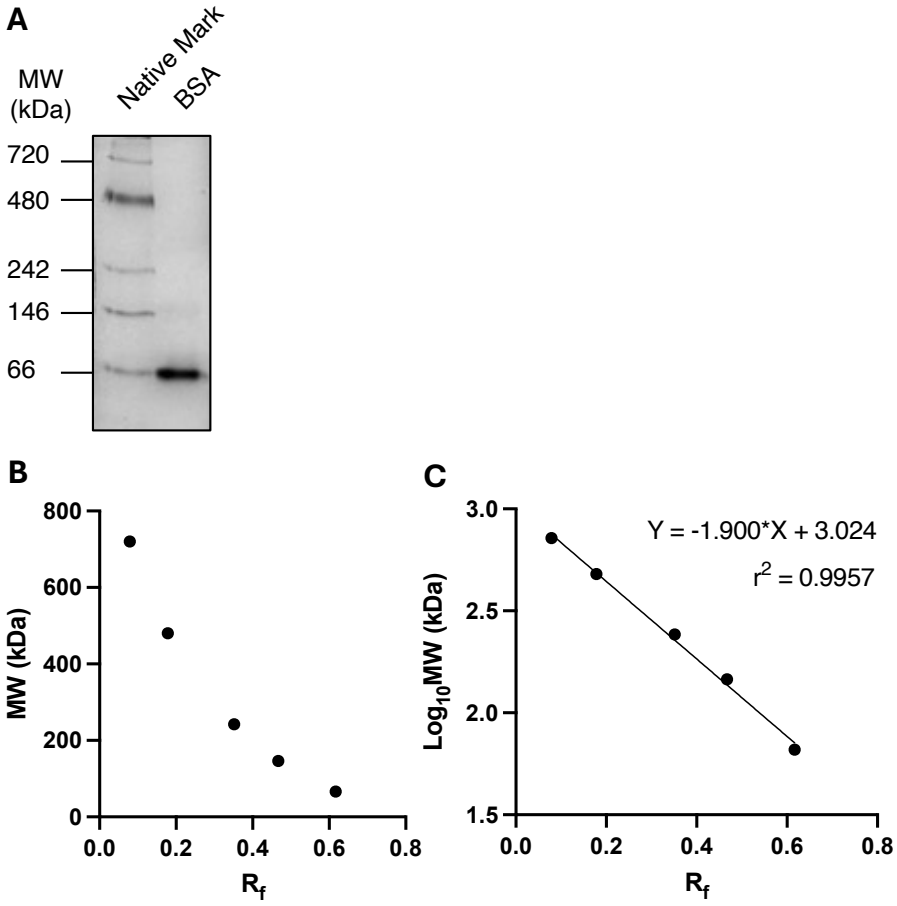

Figure 4.26. Example mass standard curve for SMA-PAGE.
A) 3–20% SMA-PAGE (native-PAGE) of NativeMark mass standards alongside BSA. MW (kDa) is labelled on the left of the gel. **B)** MW (kDa) of mass standards against their relative migration distance (R_f). **C)** Log_{10}MW (kDa) of mass standards against their relative migration distance (R_f). A linear regression was calculated, and the line is shown on the graph. The line equation and r^2 value are shown on the top right of the plot. Mass standard curves were determined for each SMA-PAGE gel. This figure serves as an example.

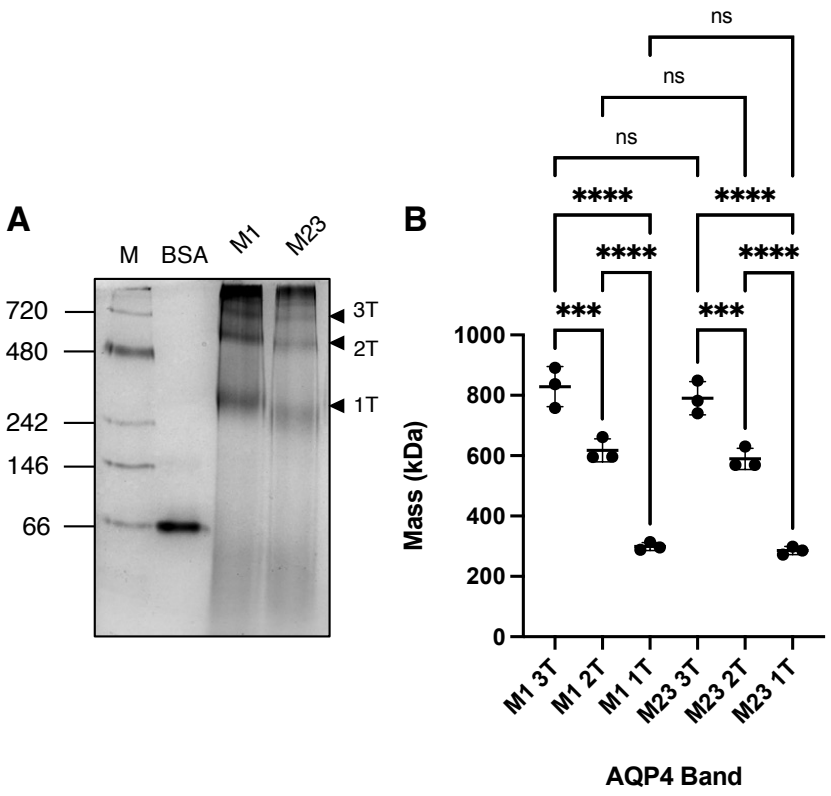

Figure 4.27. Estimation of AQP4-SMALP mass using SMA-PAGE.
'1T', '2T', and '3T' peaks, representing theorised 1-, 2-, and 3-tetramer AQP4-SMALPs, were identified in SMA-PAGE of purified AQP4-SMALPs. Estimated masses were calculated for AQP4-SMALP band R_f values using standard curves calculated for each gel, as demonstrated in Figure 4.26. Calculated masses were compared across biological replicates from different purification samples. **A)** 3–20% acrylamide gradient SMA-PAGE of Ni-NTA IMAC purified and concentrated M1 and M23 AQP4-SMALPs. Arrows indicate positions of predicted AQP4-SMALP bands. Positions are labelled with '1T', '2T', and '3T', representing theorised AQP4 tetrameric assembly of 1-, 2-, and 3-tetramers in SMALPs. NativeMark and BSA markers are shown under 'M' and 'BSA', respectively, with mass labels in kDa shown on the left. The gel was stained with Coomassie blue. This SMA-PAGE gel is one of three replicates and is used to demonstrate identification of bands for mass estimation. **B)** Mean mass estimate ± SD for each identified AQP4-SMALP band from SMA-PAGE biological replicates (n = 3), including the sample shown in **A**. Statistical analysis was performed with a one-way ANOVA with Tukey's multiple comparisons *post hoc* test (ns – $p > 0.05$ (not significant), ***$p \leq 0.001$, ****$p \leq 0.0001$).

4.6.4. Comparison of mass estimates

With mean mass estimates for AQP4-SMALPs now determined from biological repeats of each of mass photometry, SEC, and SMA-PAGE, the next step was to compare these estimates. Table 4.3 shows mean ± SD mass estimates of AQP4-SMALP sizes from mass photometry, SEC, and SMA-PAGE, for M1 and M23 AQP4. As demonstrated, all means were determined from biological replicates consisting of different AQP4-SMALP purifications. AQP4-SMALPs are identified by their theorised tetrameric assembly of AQP4 in SMALPs, with values shown corresponding to the method used for mass estimation – mass photometry (Figure 4.23), SEC (Figure 4.25), and SMA-PAGE (Figure 4.27). No 3-tetramer (3T) AQP4-SMALP peak was identified in SEC analysis of AQP4-SMALPs, and so this value was not estimated.

Although no significance was found between the means for M1 and M23 AQP4-SMALPs in any statistical analysis of the three methods, all methods demonstrated a mass difference between M1 and M23, with M23-AQP4 SMALPs always being estimated lower mass than M1 AQP4-SMALPs. It is important to note that mass photometry technical replicates (of the same purification samples) did find significance between M1 and M23 AQP4-SMALP estimated masses. In all cases, estimates became less reliable with increasing AQP4-SMALP mass (based on SD). Comparing across methods, SEC was the least reproducible method for mass estimation (based on SD).

Mass estimates between each method vary, but the pattern of size increase is similar for each one. When averaging all values for M1 AQP4-SMALPs, the 1T AQP4-SMALPs were estimated to be ~303 kDa, the 2T AQP4-SMALPs were estimated to be ~631 kDa, and the 3T AQP4-SMALPs were estimated to be ~877 kDa. When averaging all values for M23 AQP4-SMALPs, the 1T AQP4-SMALPs were estimated to be ~288 kDa, the 2T AQP4-SMALPs were estimated to be ~588 kDa, and the 3T AQP4-SMALPs were estimated to be ~830 kDa. Based on assumed masses of 35.6 kDa and 33.1 kDa for AQP4 monomers, AQP4 tetramer masses would be 142.4 kDa and 132.4 kDa for M1 and M23 AQP4, respectively. This gives a tetramer mass difference of 10 kDa, which is quite consistent with the estimated mass difference between 1-tetramer AQP4-SMALPs for M1 and M23 AQP4 when considering all estimation methods (~303 kDa and ~288 kDa).

AQP4-SMALP	Mass photometry mean mass (kDa) ± SD	SEC mean mass (kDa) ± SD	SMA-PAGE mean mass (kDa) ± SD
M1 AQP4 3-tetramer SMALP	925.7 ± 65.0	N/A	828.9 ± 66.7
M1 AQP4 2-tetramer SMALP	628.7 ± 37.1	646.9 ± 156.7	617.6 ± 37.9
M1 AQP4 1-tetramer SMALP	329.0 ± 15.7	279.3 ± 54.9	299.2 ± 13.1
M23 AQP4 3-tetramer SMALP	868.7 ± 67.1	N/A	790.5 ± 54.8
M23 AQP4 2-tetramer SMALP	598.7 ± 51.2	575.1 ± 68.2	589.6 ± 35.1
M23 AQP4 1-tetramer SMALP	312.0 ± 21.0	265.7 ± 40.6	285.5 ± 13.4

Table 4.3. AQP4-SMALP mass estimates from mass photometry, SEC, and SMA-PAGE.
Table shows mean mass ± SD (n = 3, biological replicates) for AQP4-SMALPs according to theorised tetrameric assembly of AQP4 tetramers within SMALPs. For each AQP4-SMALP, values are shown corresponding to the method used for mass estimation – mass photometry (Figure 4.23), SEC (Figure 4.25), and SMA-PAGE (Figure 4.27). No 3-tetramer (3T) AQP4-SMALP peak was identified in SEC analysis – values for these samples are shown as 'not applicable' (N/A).

4.7. Chapter Summary

This chapter has described how Ni-NTA IMAC purified M1 and M23 AQP4-SMALPs were characterised by mass photometry, SEC, and SMA-PAGE, to discover that multiple SMALP sizes exist for both AQP4 isoforms. Three SMALP sizes of increasing size were most prominently observed by mass photometry and SMA-PAGE. Considering the relationship between these SMALP sizes was observed as being individually linear for M1 and M23 AQP4, these SMALPs were theorised to contain different tetrameric forms of AQP4, and were identified as such – 1-tetramer (1T), 2-tetramer (2T), and 3-tetramer (3T) AQP4 SMALPs. SEC fractions were further characterised by FIDA to show a significant difference in hydrodynamic radius between the 1T and 2T SEC fractions. Thermal stability assays also indicated that these collected fractions demonstrated similar melting points. Ab binding assays were performed in solution and analysed by mass photometry to confirm the presence of AQP4 in these SMALP complexes. Mass estimates from mass photometry, SEC, and SMA-PAGE were then compared. When considering all mass estimation methods, the approximate difference in mass between the 1T AQP4-SMALP for M1 and M23 AQP4 was found to be consistent with the difference in tetramer mass between these isoforms.

5. NMO Ab binding to purified AQP4-SMALPs

Characterisation of purified AQP4-SMALPs in Chapter 4 demonstrated a series of particles likely corresponding to 1- (1T), 2- (2T), and 3- (3T) tetramers of AQP4 in SMALPs. These were clearly resolved by mass photometry and SMA-PAGE, but it is possible that higher-order AQP4 oligomers (above three tetramers) in SMALPs also exist. Some mass photometry profiles showed evidence of shallow peaks above the mass of the 3T AQP4-SMALP, and SMA-PAGE analysis of AQP4-SMALPs often showed unresolved protein at the top of gels. The SEC void peak also demonstrated the presence of AQP4 when analysed by SDS-PAGE. FIDA determined that the void fractions were relatively polydisperse (based on PDI), but contained particles of well-defined hydrodynamic radius, with M1 and M23 AQP4-SMALP void fractions giving significantly different radii (19.9 nm for M1, 25.3 nm for M23).

As discussed in Chapter 1, in the majority of cases, neuromyelitis optica spectrum disorders (NMOSDs) are characterised by pathogenic antibodies targeting AQP4 (NMO Abs) *(Paul et al.*, 2007; Jarius *et al.*, 2020). NMO Abs derived from NMOSD patient sera have been reported to bind to both M1 and M23 isoforms of AQP4 (Hinson *et al.*, 2007; Bennett *et al.*, 2009; Crane, Bennett and Verkman, 2009; Verkman *et al.*, 2011). However, multiple studies have observed a higher binding affinity of NMO Abs to M23 AQP4, thought to be facilitated by the formation of OAPs (Nicchia *et al.*, 2009; Mader *et al.*, 2010; Crane *et al.*, 2011; Pisani *et al.*, 2011, 2013; Soltys *et al.*, 2019).

This chapter describes how the purified AQP4-SMALPs characterised in the previous chapter were probed with NMO Abs to investigate binding interactions. As these AQP4-SMALPs were potentially encapsulating OAP fragments, it was theorised that the NMO Abs may show preferential binding to the larger SMALPs.

NMO Abs were kindly provided by Professor Sarosh R Irani's research group, Nuffield Department of Clinical Neurosciences, University of Oxford. These were prepared as recombinant Abs, as described by Damato *et al.*, 2022, and Sun *et al.*, 2025. Briefly, blood samples were taken from NMOSD patients. B cells were single-cell sorted and cultured. Culture supernatants were harvested and analysed for AQP4-IgGs using live cell-based assays. For wells with detectable AQP4-IgGs, RNA transcripts were preserved and reverse transcribed into cDNA. Genes for heavy- and light-chain Ig variable regions were amplified, and validated genes cloned into expression vectors. Human embryonic kidney (HEK) 293F cells were transfected with the expression vectors and cultured, the supernatant was

harvested, and IgGs were purified from the culture supernatant (Damato *et al.*, 2022; Sun *et al.*, 2025). The NMO Abs used here are identified as F3, D3, and F2. These identifiers refer to the well numbers in which cells were cultured and identified for production of AQP4 (NMO) IgGs.

5.1. Dot blots of purified AQP4-SMALPs

Dot blots were chosen to test for binding interactions between NMO Abs, as this is a relatively basic and high-throughput screening method for testing Ab binding to protein. If AQP4-SMALPs could successfully be immobilised on nitrocellulose (or similar) membranes, and show binding specificity for NMO Abs, this could provide a new and simple diagnostic method for NMOSD using patient sera.

5.1.1. Initial dot blot testing

Firstly, AQP4-SMALPs were tested against three NMO Abs to select for antibodies with favourable binding for further analysis. IMAC and SEC purified M1 and M23 AQP4-SMALPs were prepared as described (Section 2.6 and 2.8.1). The samples shown in Figure 5.1 were SEC purified using the Superdex 200 column, and correspond to the fractions described in Figure 4.6. 1 µL of each of the purified AQP4-SMALP samples was dot blotted onto nitrocellulose membranes. This was done in the same layout for five different blots to be probed with five different Abs: a commercial anti-AQP4 routinely used for western blotting in our laboratory (Figure 5.1A), an anti-His routinely used for western blotting (Figure 5.1B), NMO Ab F3 (Figure 5.1C), NMO Ab D3 (Figure 5.1D), and NMO Ab F2 (Figure 5.1E). Dot blot immunoassays were performed as described in Section 2.7.6.

Figure 5.1 shows the resulting dot blots. As expected, the commercial anti-AQP4 and anti-His Abs showed binding to all analysed AQP4-SMALP purification samples. By comparison, the NMO Abs only showed prominent intensity for the IMAC purified and SEC void AQP4-SMALP samples. This was observed for M1 and M23 AQP4. The intensity seen for the IMAC samples was likely due to the fact that it contained the contents of the SEC void, as it represents purified AQP4-SMALPs prior to SEC separation. Some intensity was also observed for the 2T AQP4-SMALP SEC fractions for NMO F3 and D3, but this intensity was very low compared to the IMAC and SEC void samples. The NMO F3 and D3 Abs presented comparably bold

intensities, whereas the intensity seen for the NMO F2 Ab appeared much lower. Therefore, the NMO F3 and D3 were chosen for further dot blotting.

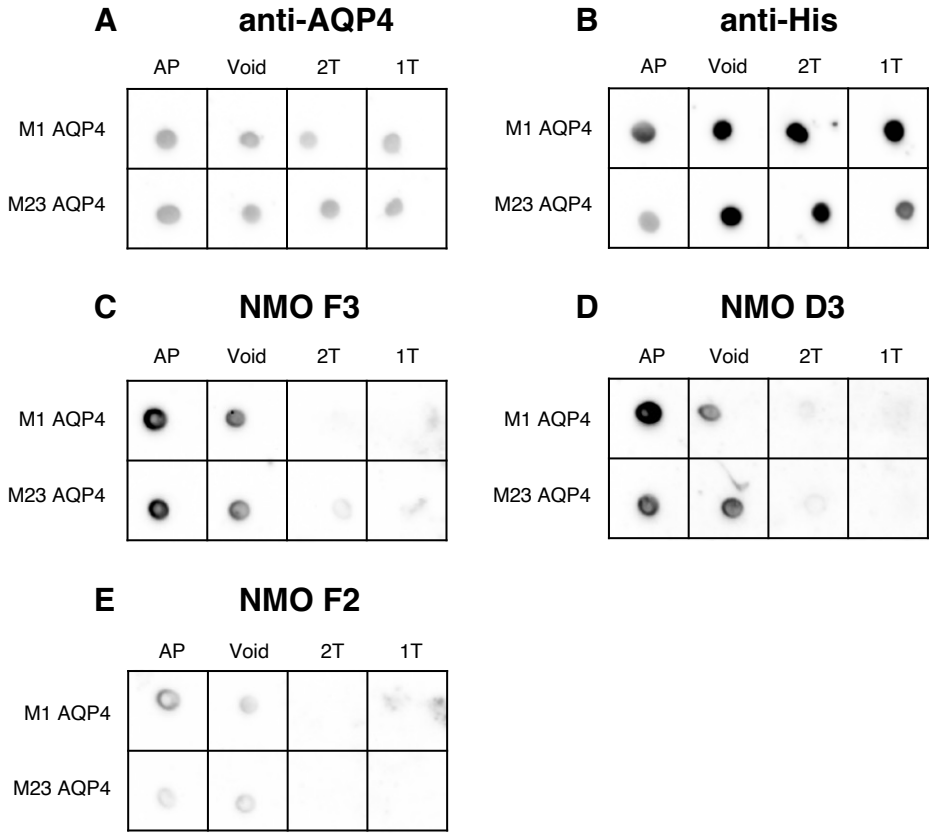

Figure 5.1. Dot blots of purified AQP4-SMALPs probed with commercial and NMO Abs. IMAC and SEC purified M1 and M23 AQP4-SMALPs were dot blotted onto nitrocellulose membranes for Ab probing. Dot blots were probed with the following Abs: **A)** Rabbit anti-AQP4 Ab (1:5,000), followed by an anti-rabbit-HRP Ab secondary (1:2,500). **B)** Mouse anti-His Ab (1:2,500), followed by an anti-mouse-HRP Ab secondary (1:2,500). **C)** NMO F3 Ab (1:1,000), followed by an anti-human-HRP Ab secondary (1:5,000). **D)** NMO D3 Ab (1:1,000), followed by an anti-human-HRP Ab secondary (1:5,000). **E)** NMO F2 Ab (1:1,000), followed by an anti-human-HRP Ab secondary (1:5,000). All blots were imaged using chemiluminescence. M1 and M23 AQP4-SMALP dots are labelled according to purification sample (Figure 4.6), where; 'AP' is IMAC purified only, 'Void' is the SEC void, '2T' is the SEC fraction predicted to contain 2-tetramer AQP4-SMALPs, and '1T' is the SEC fraction predicted to contain 1-tetramer AQP4-SMALPs.

Having shown that NMO Abs were binding to certain purified AQP4-SMALP samples, further dot blots were performed for purified AQP4, with and without denaturing conditions prior to blotting. Dot blots were performed as before (with the NMO F2 Ab excluded), but each purified AQP4-SMALP sample was also incubated (10 min, RT) with denaturing buffer (2% w/v SDS, 5% v/v βME, 50 mM Tris-HCl pH 6.8) prior to blotting, and blotted in the same layout as shown in Figure 5.1 alongside the non-denatured samples. IMAC purified M1 and M23 AQP4-

SMALPs were prepared as before. The SEC samples shown in Figure 5.2 were SEC purified using the Superose 6 column, and correspond to the fractions described in Figure 4.7. 1 µL of the non-denatured samples were blotted, with 2 µL of the denatured samples blotted after mixing 1:1 with 2× denaturing buffer. This was to give the same total protein for both non-denatured and denatured conditions for each individual purification sample. Dot blot immunoassays were performed as described in Section 2.7.6.

Figure 5.2 shows the resulting dot blots of the purified AQP4-SMALP samples with and without denaturation. The commercial anti-AQP4 and anti-His generally demonstrated a higher intensity for denatured samples. This may be a result of denaturation allowing the Abs better access to their binding epitopes. By comparison, the NMO Abs were unable to bind to the denatured AQP4-SMALPs, whereas they clearly demonstrated binding to the IMAC purified and SEC void fractions that were not denatured. This suggested that the NMO Abs were exclusively recognising a binding epitope created by the three-dimensional structure of AQP4.

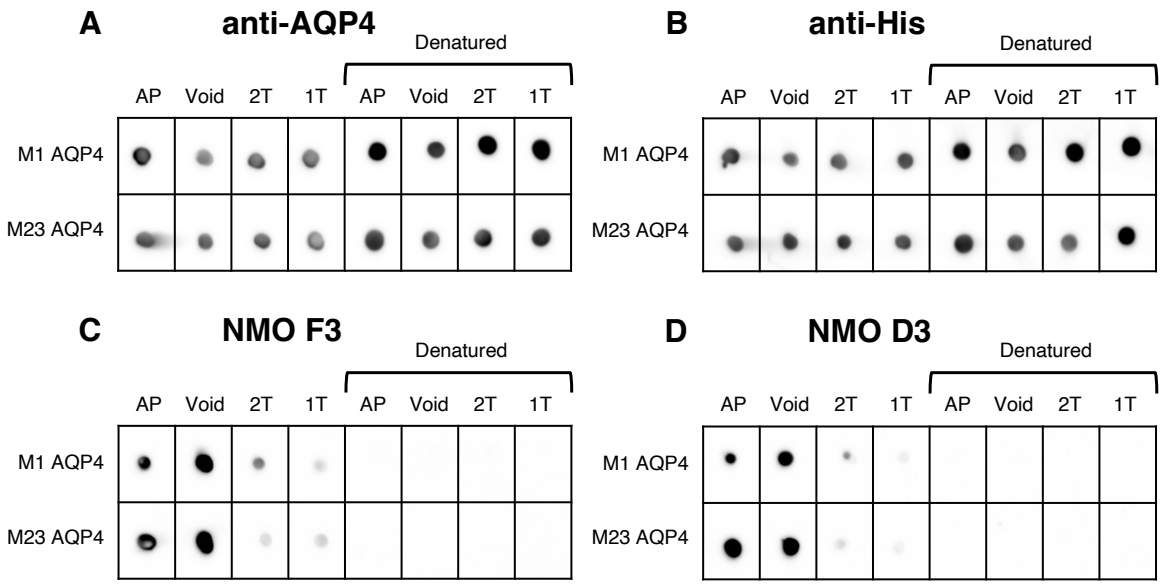

Figure 5.2. Dot blots to assess the effect of AQP4-SMALP denaturation on NMO Ab binding. IMAC and SEC purified M1 and M23 AQP4-SMALPs were incubated in non-denaturing or denaturing conditions, before dot blotting onto nitrocellulose membranes for Ab probing. Dot blots were probed with the following Abs: **A)** Rabbit anti-AQP4 Ab (1:5,000), followed by an anti-rabbit-HRP Ab secondary (1:2,500). **B)** Mouse anti-His Ab (1:2,500), followed by an anti-mouse-HRP Ab secondary (1:2,500). **C)** NMO F3 Ab (1:1,000), followed by an anti-human-HRP Ab secondary (1:5,000). **D)** NMO D3 Ab (1:1,000), followed by an anti-human-HRP Ab secondary (1:5,000). All blots were imaged using chemiluminescence. M1 and M23 AQP4-SMALP dots are labelled according to purification sample (Figure 4.7), where; 'AP' is IMAC purified only, 'Void' is the SEC void, '2T' is the SEC fraction predicted to contain 2-tetramer AQP4-SMALPs, and '1T' is the SEC fraction predicted to contain 1-tetramer AQP4-SMALPs. Denatured samples were incubated (10 min, RT) in denaturing buffer (2% w/v SDS, 5% v/v βME, 50 mM Tris-HCl pH 6.8) prior to blotting.

5.1.2. Generation of an MP-SMALP control for dot blotting

In order to confirm that NMO Ab binding was specific to AQP4, as opposed to non-specific binding to SMALP complexes or protein aggregation, it was important to generate another MP-SMALP control for dot blotting.

An adenosine A_{2A} receptor ($A_{2A}R$) *P. pastoris* clone was available in our library. This clone was optimised for expression and purification of $A_{2A}R$ by Dr Zharain Bawa (Bawa, 2014). This clone was cultured in bioreactors as described Section 2.4.5. For the induction phase, DMSO was added to a final concentration of 2% v/v and vessel temperature was lowered to 22 °C. Figure 5.3 shows the resulting bioreactor growth profile for the $A_{2A}R$ *P. pastoris* clone.

After harvesting cells from the bioreactor culture, they were stored at -80 °C and subsequently defrosted and broken using high pressure homogenisation, and the membrane fragment was

prepared as previously described (Sections 2.5.2 and 2.5.3). Resuspended $A_{2A}R$ membranes were separated by 4–16% SDS-PAGE at a concentration of 36 mg/mL and analysed by western blot (Section 2.7.3). $A_{2A}R$ expression in the membranes was probed using a mouse anti-His primary Ab (1:2,500, 16 h, 4 °C) to target the recombinant 6× His-tag, followed by a secondary anti-rabbit-HRP linked Ab (1:2,500, 1 h, RT), and visualisation by chemiluminescence. Figure 5.4A shows the resulting western blot.

Resuspended membranes of the $A_{2A}R$ *P. pastoris* clone were then solubilised at 45 mg/mL with 2.5% w/v SMA. Soluble fractions were separated by ultracentrifugation and $A_{2A}R$-SMALPs were purified by Ni-NTA IMAC (Section 2.6). Purified samples were concentrated to ~500 µL with 50 kDa MW cut-off and separated by SEC using the Superose 6 column. This column was chosen to match the favourable SEC column for AQP4-SMALP purifications. Figure 5.3B shows the resulting SEC profile for IMAC purified $A_{2A}R$-SMALPs. Peaks were identified by number in order of retention volume after the void peak. 600 µL samples were collected at the corresponding peak fractions. These collected SEC fractions were analysed by 3–20% gradient SMA-PAGE (Figure 5.4C). Positions of predicted $A_{2A}R$-SMALPs are labelled.

The $A_{2A}R$ IMAC purified only (AP), SEC void fraction (V), Peak 2 fraction (P2), and Peak 3 fraction (P3), were chosen as samples to be used in dot blot comparison with the four purified AQP4-SMALP samples (AP, Void, 2T, and 1T). As an $A_{2A}R$-SMALP band could not be identified by SMA-PAGE in the Peak 1 (P1) fraction (Figure 5.4C), and the Void and AP samples were desired as two of four comparisons to the AQP4-SMALPs, the P1 fraction was excluded from $A_{2A}R$-SMALP samples selected for dot blotting. The selected $A_{2A}R$ samples were analysed by 4–16% gradient SDS-PAGE (Figure 5.4D) for protein concentration estimation, using BSA as a standard in serial dilution, as described in Section 2.7.4.1. The intensity of the band present at ~40 kDa was used to estimate concentration of purified $A_{2A}R$. An $A_{2A}R$ band in the void fraction could not be identified, so the total intensity (above the background) of this lane was used to estimate protein concentration.

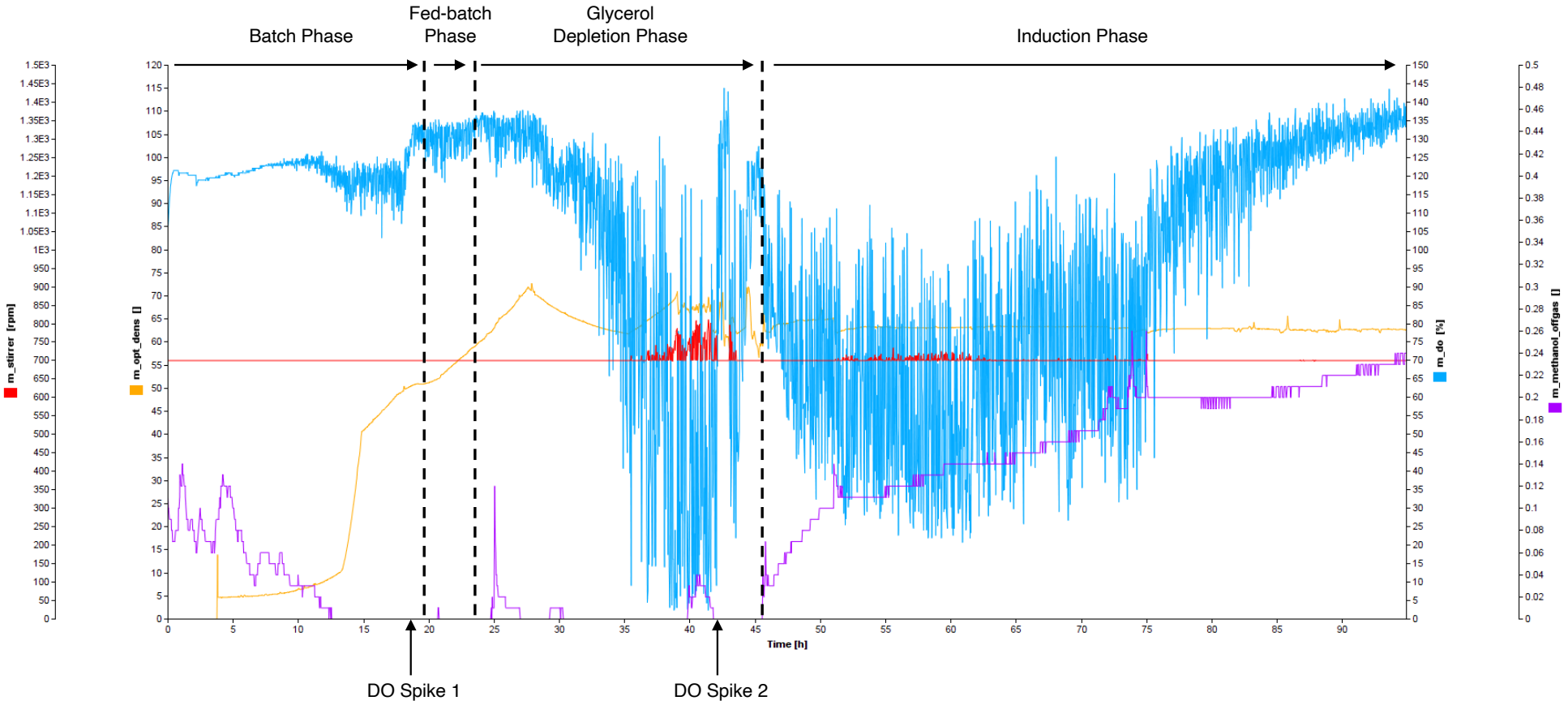

Figure 5.3. Bioreactor growth profile of the $A_{2A}R$ *P. pastoris* clone.
Blue: dissolved oxygen (%). Purple: MeOH off-gas (%). Yellow: Optical density of culture (AU). Red: Stirrer speed (rpm). Phases of culture feeding conditions are separated by dotted lines. Batch phase indicates the growth phase relying on the glycerol in the growth medium only. Fed-batch phase indicates the glycerol fed-batch stage with a feed rate of 14 mL L^{-1} h^{-1} of 50% v/v glycerol. Glycerol depletion phase indicates the growth and starvation phase (no feeding). Induction phase indicates MeOH induction with a feed rate of feed rate of 4.8 mL L^{-1} h^{-1} 50% v/v MeOH. At the start of induction, DMSO was added to a final concentration of 2% v/v and vessel temperature was lowered to 22 °C. Time points of DO spikes used to determine the start of the fed-batch and induction phases are indicated by DO spike arrows 1 and 2, respectively.

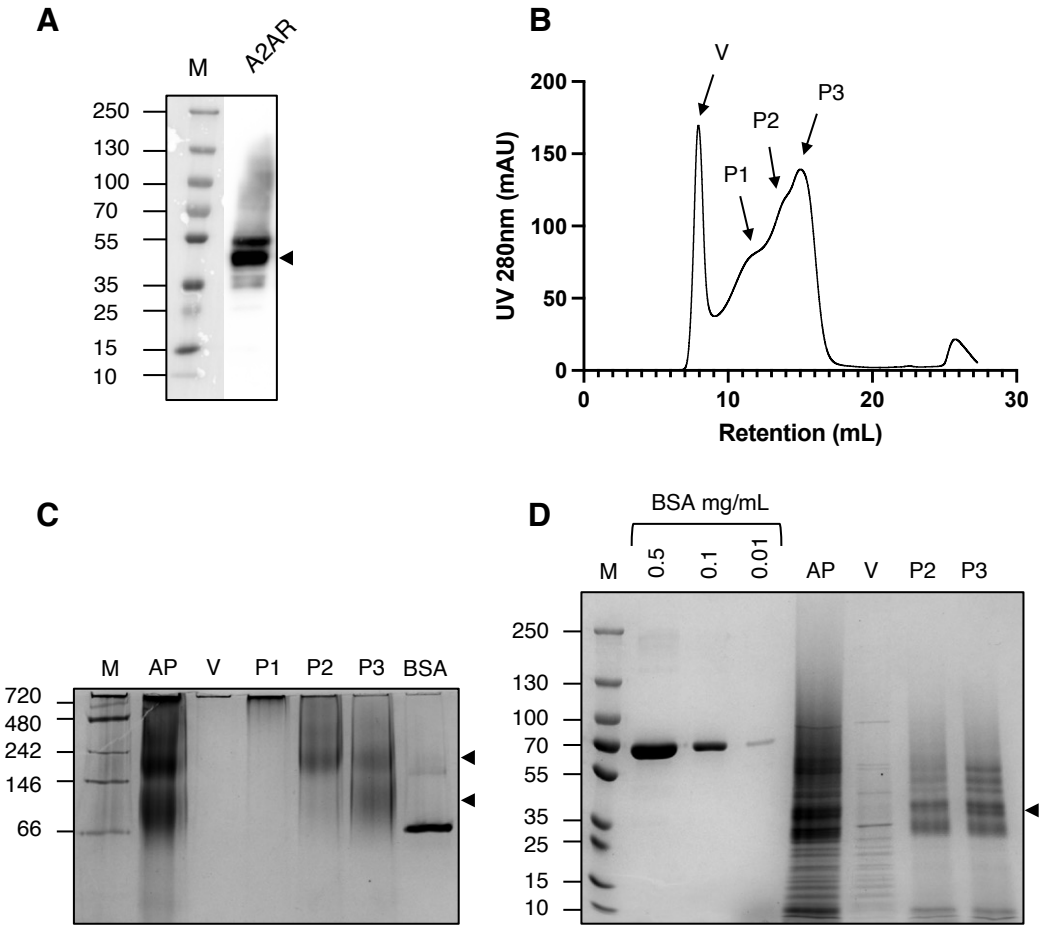

Figure 5.4 Purification of A_{2A}R-SMALPs from the A_{2A}R *P. pastoris* clone.
A) Western blot targeting expression of A_{2A}R in the membrane fragment. The A_{2A}R *P. pastoris* clone was grown and induced in bioreactors, followed by high pressure cell homogenisation. Membrane fragments were separated from cell lysates by ultracentrifugation. Resuspended membrane fragments were separated by 4–16% gradient SDS-PAGE at a concentration of 36 mg/mL, followed by western blotting. A_{2A}R was probed with a mouse anti-His Ab (1:2,500). An anti-mouse-HRP Ab was used as secondary (1:2,500) and the blot was imaged using chemiluminescence. The band predicted to represent A_{2A}R is labelled with an arrow. MW markers are shown under 'M' with mass labels in kDa shown on the left of the blot. **B)** SEC profile of IMAC purified A_{2A}R-SMALPs. Resuspended membranes of the A_{2A}R *P. pastoris* clone were solubilised at 45 mg/mL with 2.5% w/v SMA. Soluble fractions were separated by ultracentrifugation and A_{2A}R-SMALPs were purified by Ni-NTA IMAC. Purified samples were concentrated to ~500 µL and separated by SEC using the Superose 6 column. Profile shows mAU measured at UV 280 nm against the buffer retention volume (mL). Peaks are labelled corresponding to collected 600uL fractions: 'V', SEC void; 'P1', Peak 1; 'P2', Peak 2; 'P3', Peak 3. **C)** 3–20% gradient SMA-PAGE of A_{2A}R-SMALPs. 'AP' represents Ni-NTA IMAC purified and concentrated protein prior to SEC. The other samples are the void (V), and Peaks 1–3 (P1–3) fractions identified by SEC (**B**). Positions of bands predicted to represent A_{2A}R-SMALPs are labelled with arrows. NativeMark and BSA markers are shown under 'M' and 'BSA', respectively, with mass labels in kDa shown on the left of the gel. The gel was stained with Coomassie blue. **D)** SDS-PAGE for protein concentration estimation of A_{2A}R-SMALPs. 'AP' represents Ni-NTA IMAC purified and concentrated protein prior to SEC. The other samples are the void (V), and Peaks 2 and 3 (P2 and 3) fractions identified by SEC (**B**). The band predicted to represent A_{2A}R is labelled with an arrow. BSA was used as a standard in serial dilution. BSA concentrations are labelled for each lane. MW markers are shown under 'M' with mass labels in kDa shown on the left of the gel. The gel was stained with Coomassie blue.

5.1.3. Dot blotting of AQP4-SMALPs alongside the A_{2A}R-SMALP control

With A_{2A}R-SMALPs now purified as an MP-SMALP control, they were dot blotted alongside purified AQP4-SMALPs to be probed with the antibodies shown in Figure 5.2. Blotted concentrations for purified samples were normalised to 1 μM, based on estimated concentrations from SDS-PAGE alongside BSA standards (Section 2.7.4.1). Although AQP4 is presumed to be a tetramer in the 1T AQP4-SMALPs, conformations and oligomeric states in the void fractions and IMAC purified samples are unknown. Also, binding stoichiometries to NMO Abs is uncertain. For these reasons, concentration estimates for AQP4 were based on the monomer mass for M1 (35.6 kDa) and M23 (33.1 kDa) AQP4. A_{2A}R concentrations were estimated based on an estimated monomer mass of ~40 kDa, based on western blotting and SDS-PAGE analysis (Figure 5.4). As an A_{2A}R band could not be identified in its SEC void fraction, it was blotted at a mg/mL concentration equivalent to the A_{2A}R-SMALP Peak 3 SEC fraction.

For samples shown in Figure 5.5, IMAC purified samples were prepared as previously described (Section 2.6). AQP4-SMALPs were SEC purified using the Superose 6 column and correspond to the fractions described in Figure 4.7. A_{2A}R-SMALP samples were SEC purified using the Superose 6 column and correspond to samples shown in Figure 5.4. The purified MP-SMALPs were dot blotted as previously described (Section 2.7.6). 1 μL of each sample was dot blot blotted onto nitrocellulose membranes and this was done in the same layout for four different blots to be probed with four different Abs. Dot blot immunoassays were performed as described in Section 2.7.6. An SDS soak (2% w/v, 10 min) was used for blots to be probed with the commercial anti-AQP4 and anti-His Abs. Based on dot blot optimisation without SDS soak, the anti-His Ab had shown a lower intensity (binding affinity) for A_{2A}R than for AQP4, potentially due to a lower accessibility of the His-tag in A_{2A}R-SMALPs. The SDS soak and an increased anti-His Ab concentration (1:1250 instead of 1:2500) were used to improve binding to the A_{2A}R 6× His-tag.

Figure 5.5 shows the resulting dot blots. As expected, the commercial anti-AQP4 Ab only demonstrated binding to AQP4-SMALP samples, with the anti-His Ab binding to all purified samples for both AQP4- and A_{2A}R-SMALPs. A lower intensity was observed for the anti-His Ab binding to the A_{2A}R void, but this was expected, as an A_{2A}R band could not be identified by SDS-PAGE analysis of this fraction. For M1 and M23 AQP4, the NMO Abs presented the binding characteristics for AQP4-SMALPs as observed in Figures 5.1 and 5.2 (high intensity for the AP and Void samples). By comparison, a very low intensity was observed for the A_{2A}R-

SMALPs in the AP, SEC Void and SEC P2 samples, similar to that observed the 2T AQP4-SMALP SEC fractions. This was presumed to be non-specific binding of the NMO Abs.

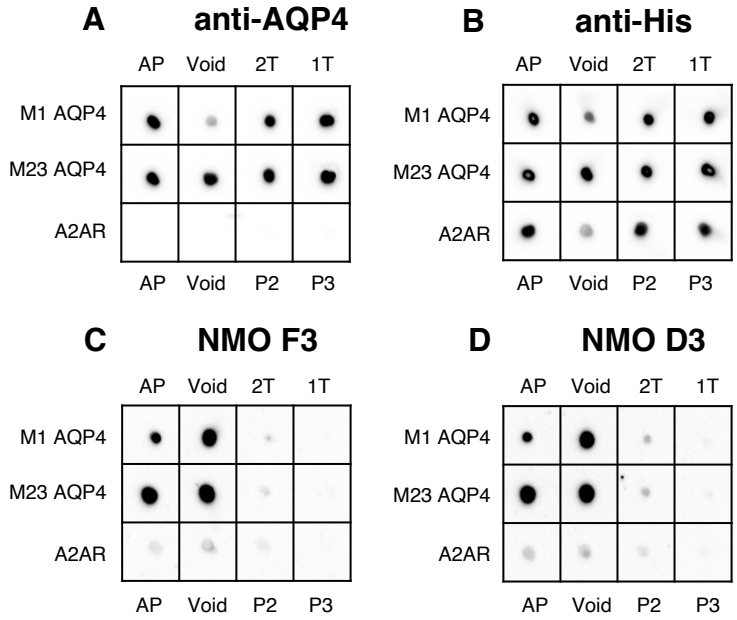

Figure 5.5. Dot blots of purified AQP4-SMALPs alongside purified A_{2A}R-SMALPs as an NMO Ab binding control.
IMAC and SEC purified AQP4-SMALPs (M1 and M23) and A_{2A}R-SMALPs were dot blotted onto nitrocellulose membranes for Ab probing. Protein concentration was normalised to 1 μM for blotting (based on monomer mass for AQP4 and A_{2A}R). Blots **A** and **B** were soaked in SDS (2% w/v, 10 min) prior to Ab incubations. Dot blots were probed with the following Abs: **A)** Rabbit anti-AQP4 Ab (1:5,000), followed by an anti-rabbit-HRP Ab secondary (1:2,500). **B)** Mouse anti-His Ab (1:1,250), followed by an anti-mouse-HRP Ab secondary (1:2,500). **C)** NMO F3 Ab (1:1,000), followed by an anti-human-HRP Ab secondary (1:5,000). **D)** NMO D3 Ab (1:1,000), followed by an anti-human-HRP Ab secondary (1:5,000). All blots were imaged using chemiluminescence. M1 and M23 AQP4-SMALP dots are labelled (top of blots) according to purification sample (Figure 4.7), where; 'AP' is IMAC purified only, 'Void' is the SEC void, '2T' is the SEC fraction predicted to contain 2-tetramer AQP4-SMALPs, and '1T' is the SEC fraction predicted to contain 1-tetramer AQP4-SMALPs. A_{2A}R-SMALP dots are labelled (bottom of blots) according to purification sample (Figure 5.4): 'V', SEC void; 'P1', Peak 1; 'P2', Peak 2; 'P3', Peak 3.

As some non-specific binding of the NMO Abs to A_{2A}R-SMALP purification samples was observed, the next step was to perform replicates of the dot blots so that the relative chemiluminescence intensities could be quantified. Due to limited resources of the NMO D3 Ab, these replicates were performed with the NMO F3 Ab.

Dot blots were performed as described, with replicates performed for probing with the NMO F3 Ab (n = 3, including Figure 5.5C). These were technical replicates using the same purification samples. For each blot replicate, a new primary Ab solution was made for NMO F3. Samples were blotted as described in Section 2.7.6 and as shown in Figure 5.5C. For each replicate blot, unprocessed images were used to find the integrated density of a fixed area over each sample dot. Integrated density values were normalised to the sum of integrated density measured for all samples on the blot. For two replicates, the NMO F3 Ab dilution used for primary Ab incubation was as described for Figure 5.5C (1:1,000). For one replicate, the NMO F3 Ab dilution used was 1:2,500. As the values for each blot were normalised, it was assumed that differences caused by varying Ab concentration would be negligible.

Figure 5.6 shows the resulting plot of quantified blots that were probed with the NMO F3 Ab, with mean normalised integrated density ± SD shown for each MP-SMALP sample. A one-way ANOVA with Tukey's *post hoc* test was performed for statistical analysis. The M1 AQP4 SEC void (M1 V), M23 AQP4-SMALP IMAC purified only (M23 AP), and M23 AQP4-SMALP SEC void (M23 V) showed the highest measured intensities. No significant difference was found between any of the A_{2A}R-SMALP samples, and no significance was found between any of the M1 / M23 AQP4-SMALP 2T / 1T SEC fractions and the A_{2A}R P3 / P4 SEC fractions. The other most relevant pairwise comparisons are shown on the plot. Most importantly, the M1 and M23 AQP4-SMALP V samples showed a significant difference to the A_{2A}R-SMALP V sample. Interestingly, no significant difference was found between M1 AQP4-SMALP AP and A_{2A}R-SMALP AP, whereas a significant difference was found between M23 AP and A_{2A}R AP. There was also a significant difference between M1 and M23 for the AP and V samples.

Although protein concentration of the samples loaded was normalised and comparable fractions compared between AQP4-SMALPs and A_{2A}R-SMALPs, it is important to note that the increased binding of NMO Abs to the AQP4-SMALP void fractions could result from non-specific interactions to aggregates. The conformations in the void fraction that allow for significantly higher affinity of NMO Abs are not clear. It is possible that this fraction contains aggregates of AQP4 or AQP4-SMALPs, with the NMO Abs having an affinity for non-specific interactions with aggregated AQP4.

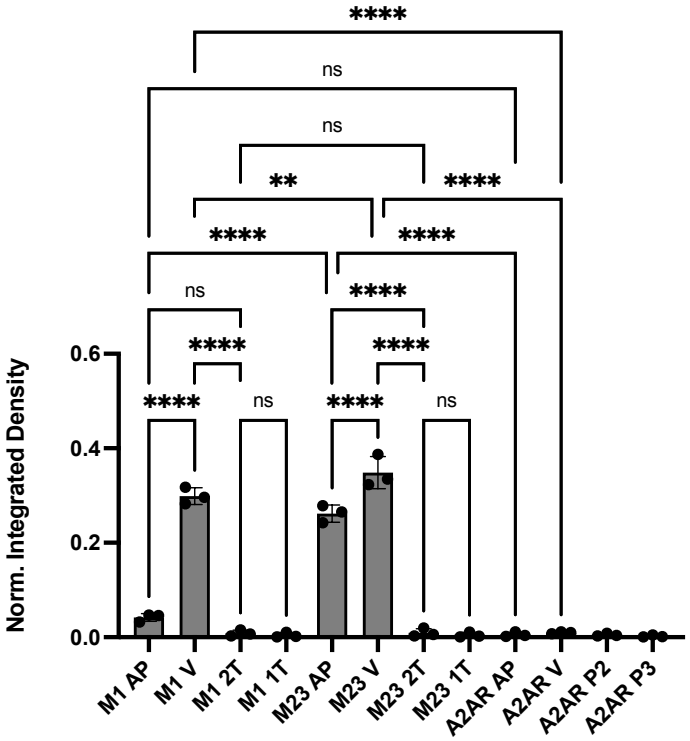

Figure 5.6. Quantification of dot blots probed with NMO F3.
IMAC and SEC purified AQP4-SMALPs (M1 and M23) and A_{2A}R-SMALPs were dot blotted onto nitrocellulose membranes for Ab probing. Protein concentration was normalised to 1 µM for blotting (based on monomer mass for AQP4 and A_{2A}R). Dot blots were probed with the NMO F3 Ab (1:1,000), followed by an anti-human-HRP Ab secondary (1:5,000). Blots were imaged using chemiluminescence and quantified by measuring the integrated density for each sample dot. The plot shows the mean normalised integrated density ± SD for each sample (n = 3, dot blot technical replicates using the same purification samples). AQP4-SMALP samples are identified by isoform (M1 or M23) and according to the purification sample (Figure 4.7), where; 'AP' is IMAC purified only, 'Void' is the SEC void, '2T' is the SEC fraction predicted to contain 2-tetramer AQP4-SMALPs, and '1T' is the SEC fraction predicted to contain 1-tetramer AQP4-SMALPs. A_{2A}R-SMALP samples are labelled according to purification sample (Figure 5.4): 'V', SEC void; 'P1', Peak 1; 'P2', Peak 2; 'P3', Peak 3. Statistical analysis was performed with a one-way ANOVA with Tukey's multiple comparisons *post hoc* test (ns – $p > 0.05$ (not significant), **$p \leq 0.01$, ****$p \leq 0.0001$).

5.2. Mass photometry analysis of AQP4-SMALPs and NMO Abs

Having characterised AQP4-SMALPs by mass photometry in Chapter 4, the logical next step was to probe 1T and 2T AQP4-SMALPs with NMO Abs in solution and analyse the reactions by mass photometry. There were no prominent peaks observed when the SEC void fractions were analysed (Figure 4.11), and thus, this fraction was not tested. As stated for the dot blot replicates, due to limited resources of the NMO D3 Ab, only the NMO F3 Ab was used for mass photometry analysis.

Firstly, the NMO F3 Ab was characterised alone at a final concentration of 7 nM (Figure 5.7). This presented a homogeneous peak at the expected mass for an IgG Ab (~150 kDa).

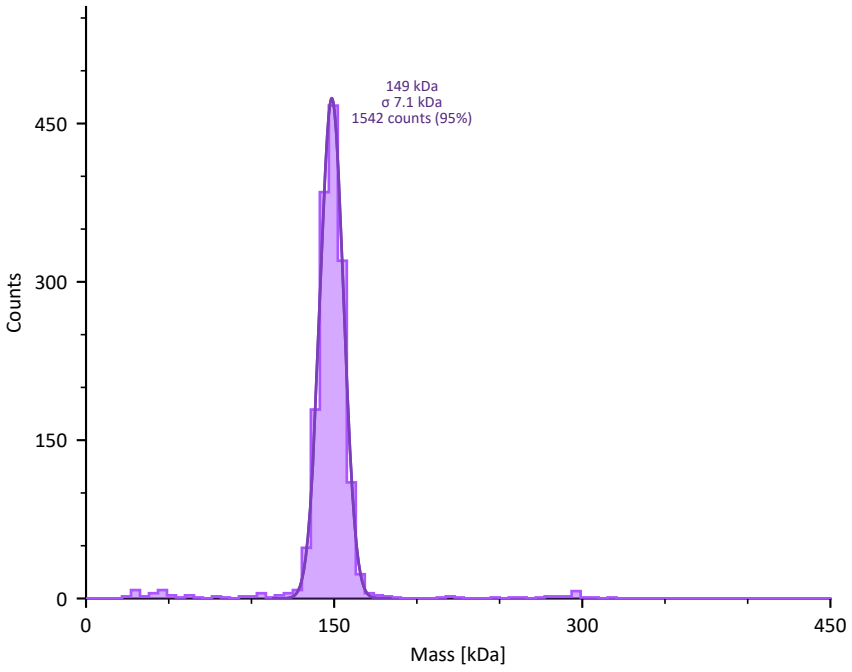

Figure 5.7. Mass photometry characterisation of the NMO F3 Ab.
Mass photometry histogram of the NMO F3 Ab, analysed at a final concentration of 7 nM (n = 1). MS1000 was used for mass calibration. The Ab histogram peak is fitted with a Gaussian distribution. Gaussian distributions are labelled with the mean, SD, and distribution counts (and percentage of total sample counts).

With NMO F3 Ab now characterised, the next step was to perform Ab binding assays for visualisation by mass photometry. As shown in Section 4.5, a commercial anti-AQP4 Ab was able to recognise AQP4 within SMALPs in solution, and binding could be visualised by mass photometry (Figure 4.18 and 4.19). Assays with the NMO F3 Ab were performed in a similar fashion in an attempt to observe a binding profile. As with the assays described in Section 4.5, assay concentrations had to be optimised to prevent measurements that had too many or too few events (counts). The 1T and 2T SEC fractions for M1 and M23 AQP4-SMALPs used in these assays correspond to the fractions collected from Superose 6 purification shown in Figure 4.10. For the reasons stated in Section 4.5.2, AQP4 tetramer concentration was used for assays and is stated here.

Firstly, the 1T SEC fractions for M1 and M23 AQP4-SMALPs were analysed alone at a final tetramer concentration of 35 nM. 1T AQP4-SMALPs were then incubated (10 min, RT) at a

concentration of 175 nM with the NMO F3 Ab at a concentration of 30 nM. Reactions were droplet-diluted 10-fold into sample cassette wells and analysed by mass photometry (Section 2.8.2). The final concentrations for the reaction sample were 17.5 nM for the AQP4 tetramers, and 3 nM for the NMO F3 Ab. Figure 5.8 shows the resulting mass photometry analysis for NMO F3 Ab incubations with the M1 (Figure 5.8A) and M23 (Figure 5.8B) AQP4-SMALPs in the 1T SEC fraction (Figure 4.10). Histograms for each AQP4 isoform are shown in vertical series for the AQP4-SMALPs alone, and AQP4-SMALPs incubated with the NMO Ab. As the final tetramer concentration for AQP4 was different for the analysis alone and analysis with the NMO Ab, counts were normalised for the displayed mass photometry histograms.

The 2T SEC fractions for M1 and M23 AQP4-SMALPs were also analysed alone at a final tetramer concentration of 35 nM. 2T AQP4-SMALPs were then incubated (10 min, RT) at a concentration of 140 nM with the NMO F3 Ab at a concentration of 28 nM. Reactions were droplet-diluted 4-fold into sample cassette wells and analysed by mass photometry (Section 2.8.2). The final concentrations for the reaction sample were 35 nM for the AQP4 tetramers, and 7 nM for the NMO F3 Ab. Figure 5.9 shows the resulting mass photometry analysis for NMO F3 Ab incubations with the M1 (Figure 5.9A) and M23 (Figure 5.8B) AQP4-SMALPs in the 2T SEC fraction (Figure 4.10). Histograms for each AQP4 isoform are shown in vertical series for the AQP4-SMALPs alone, and AQP4-SMALPs incubated with the NMO Ab. Although the final tetramer concentration for AQP4 was the same for the analysis alone and analysis with the NMO Ab, counts were normalised for the displayed mass photometry histograms to be consistent with the histograms displayed for 1T AQP4-SMALPs.

A peak representing the NMO F3 Ab is visible in all incubations (indicated with the red Gaussian line) and no AQP4-SMALP peak shift can be identified for the 1T and 2T SEC fraction contents. As with other mass photometry histograms analysed, the far left peaks are not estimated for mass as these are presumed to be low MW noise. Increasing the concentration of the NMO F3 Ab or the AQP4-SMALPs led to too high a density of binding events, making it impossible to produce trustworthy data at higher concentrations. These data suggest that either there is no binding interaction between the NMO F3 Ab and the 1T/2T AQP4-SMALPs, or that the binding affinity is too low to observe complex formation by mass photometry.

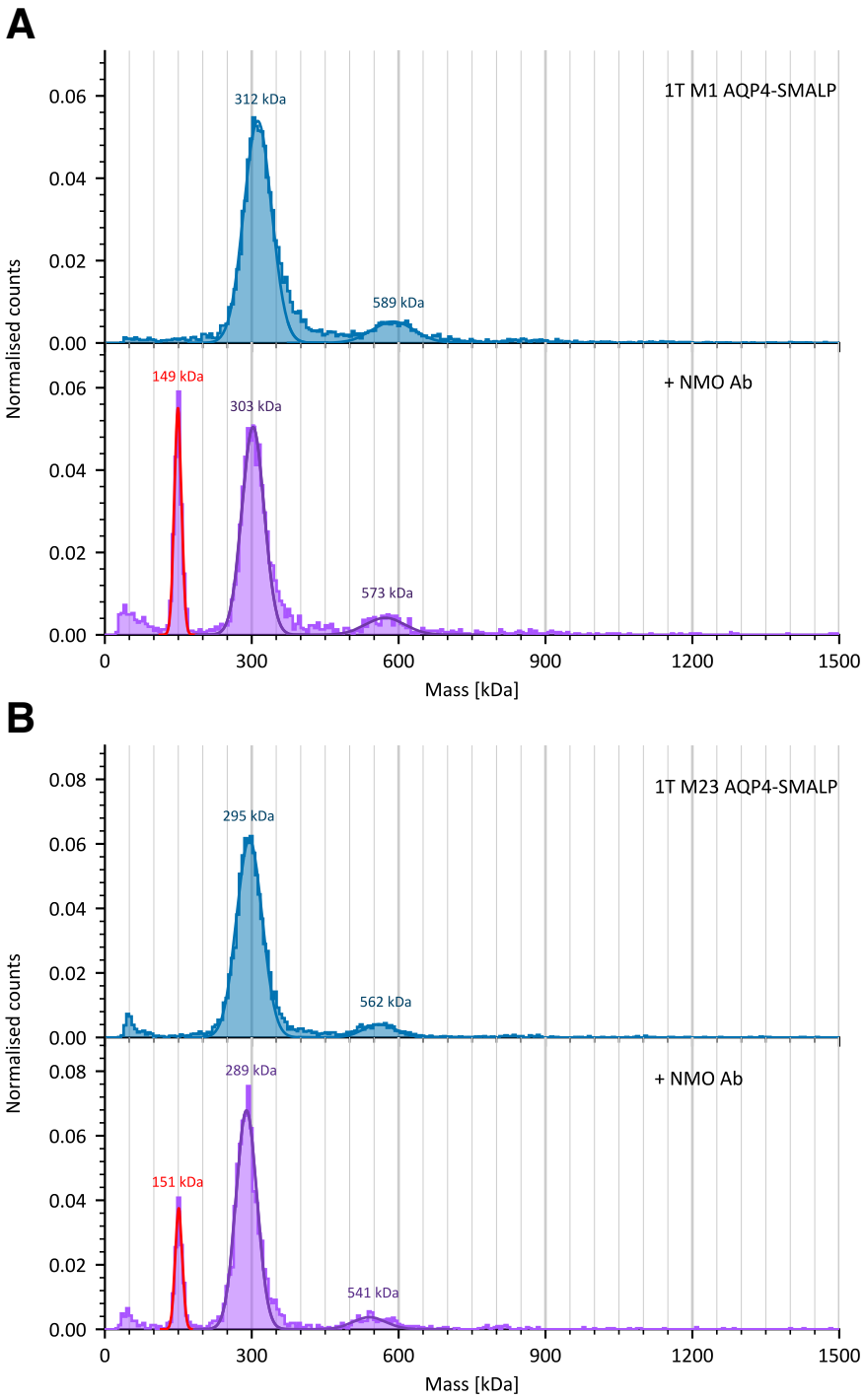

Figure 5.8. Mass photometry of 1-tetramer AQP4-SMALPs probed with the NMO F3 Ab.
M1 and M23 1-tetramer (1T) AQP4-SMALPs were identified by SEC and corresponding fractions collected (Figure 4.10). AQP4-SMALPs were first analysed alone at a final concentration of 35 nM (AQP4 tetramer concentration). AQP4-SMALPs were then incubated (10 min, RT) at a concentration of 175 nM with the NMO F3 Ab (30 nM), before 10-fold droplet-dilution of the reaction into cassette wells (final concentrations: AQP4 tetramer, 17.5 nM; NMO F3 Ab, 3 nM) for analysis by mass photometry (n = 1 per reaction). MS1000 was used for mass calibration. Figures show histograms of the Ab reactions for M1 (**A**) and M23 (**B**) 1T AQP4-SMALPs, with normalised counts plotted against calibrated mass (kDa). The histogram peaks in each sample are fitted with Gaussian distributions and labelled with the mean (mass prediction). Ab peaks in the relevant histograms are indicated with a red Gaussian distribution line and mass label.

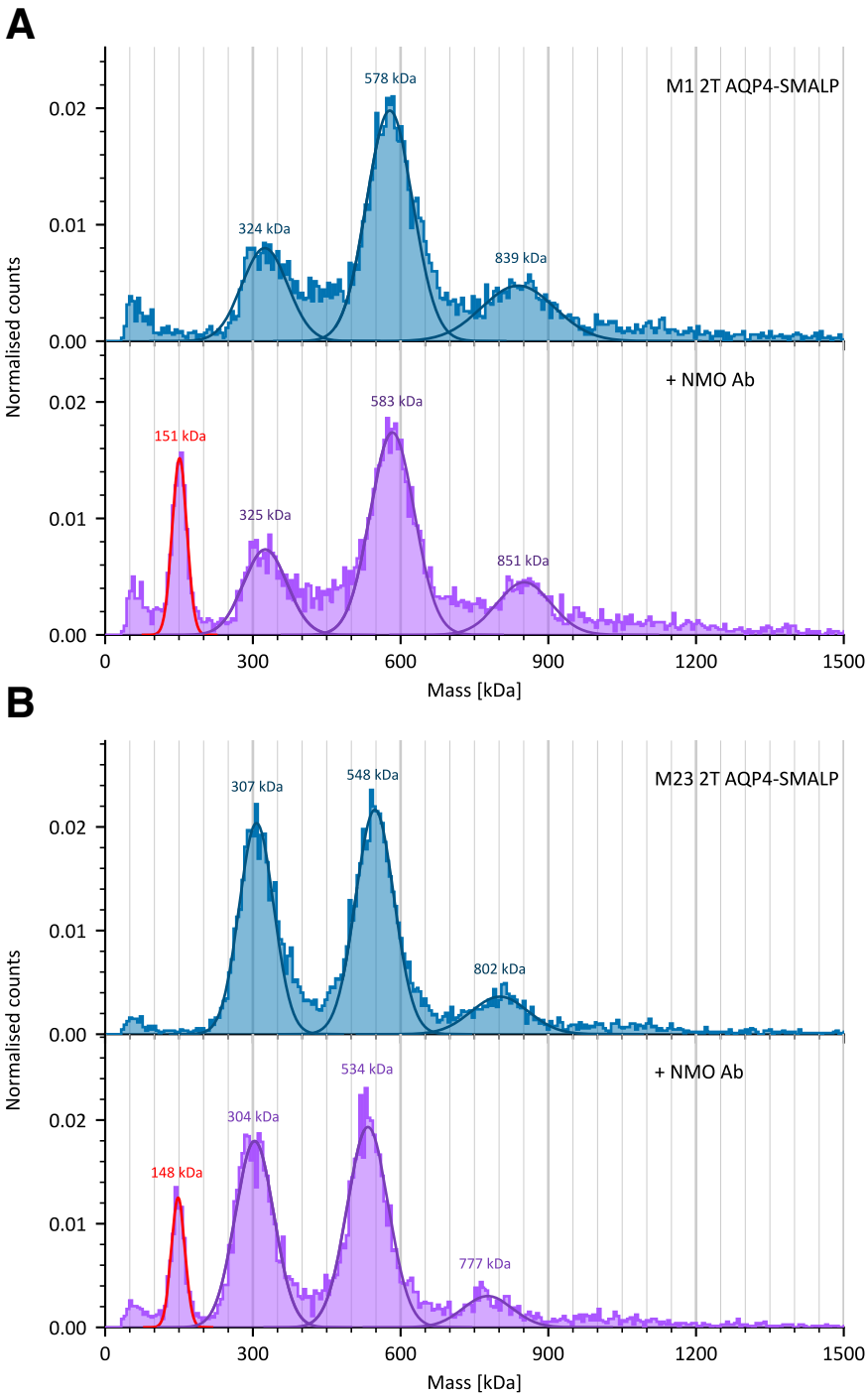

Figure 5.9. Mass photometry of 2-tetramer AQP4-SMALPs probed with the NMO F3 Ab.
M1 and M23 2-tetramer (2T) AQP4-SMALPs were identified by SEC and corresponding fractions collected (Figure 4.10). AQP4-SMALPs were first analysed alone at a final concentration of 35 nM (AQP4 tetramer concentration). AQP4-SMALPs were then incubated (10 min, RT) at a concentration of 140 nM with the NMO F3 Ab (28 nM), before 4-fold droplet-dilution of the reaction into cassette wells (final concentrations: AQP4 tetramer, 35 nM; NMO F3 Ab, 7 nM) for analysis by mass photometry (n = 1 per reaction). MS1000 was used for mass calibration. Figures show histograms of the Ab reactions for M1 (**A**) and M23 (**B**) 2T AQP4-SMALPs, with normalised counts plotted against calibrated mass (kDa). The histogram peaks in each sample are fitted with Gaussian distributions and labelled with the mean (mass prediction). Ab peaks in the relevant histograms are indicated with a red Gaussian distribution line and mass label.

5.3. Chapter Summary

This chapter has investigated binding of NMO Abs to purified AQP4-SMALPs. Dot blotting demonstrated that these NMO Abs preferentially bound to certain fractions of the purified AQP4-SMALP preparations. After establishing another purified MP-SMALP with an $A_{2A}R$ *P. pastoris* clone, dot blots were repeated using $A_{2A}R$-SMALPs as a non-specific binding control. Quantification of the dot bot chemiluminescence intensities demonstrated that NMO Abs showed a significant binding preference for M1 and M23 AQP4-SMALP SEC void fractions, and the IMAC-only purified M23 AQP4-SMALPs. Binding assays of the 1T and 2T AQP4-SMALP SEC fractions (containing 1T, 2T, and 3T AQP4-SMALPs) with the NMO F3 Ab did not present any clear AQP4-SMALP-IgG bound complexes when visualised with mass photometry. This lack of binding seen with mass photometry is consistent with that observed by dot blot analysis of these samples.

6. Investigating AQP4 OAP formation in *P. pastoris*

AQP4 is known to form OAPs (Yang, Brown and Verkman, 1996; Verbavatz *et al.*, 1997). M1 AQP4 is thought to be unable to form OAPs in the membrane, with M23 AQP4 being the facilitator for the formation of higher-order oligomers (Furman *et al.*, 2003; Crane, Bennett and Verkman, 2009). *S*-palmitoylation of cysteine residues at positions 13 and 17 is thought to play a key role in preventing M1 AQP4 from forming OAPs (Suzuki *et al.*, 2008; Carder *et al.*, 2024). M23 AQP4 lacks these N-terminal residues, and thus palmitoylation, allowing it to assemble into higher-order structures of multiple tetramer units. However, it is important to note that others have proposed that multiple other residues in the M1 AQP4 N-terminus (that M23 AQP4 lacks) are responsible for OAP prevention (Crane and Verkman, 2009), and that OAPs are regulated by multiple factors, including palmitoylation, relative expression of M1 and M23 isoforms, and phosphorylation state (Crane, Bennett and Verkman, 2009).

As seen in Chapter 4, M1 and M23 AQP4-SMALPs appear as multiple SMALP sizes after solubilisation and purification. This size increase was independently linear for both AQP4 isoforms, and the incremental size increase allowed for the mass of one additional tetramer. Therefore, these particles were theorised to contain an increasing number of tetramer units in increasing SMALP sizes, based on the ability of AQP4 to form OAPs.

In Chapter 5, NMO Abs appeared to bind to the M1 and M23 AQP4-SMALP SEC void fraction (Figure 5.5). Binding to the M23 AQP4-SMALP SEC void did appear to be stronger (Figure 5.6), but both M1 and M23 SEC void fractions demonstrated significantly increased NMO Ab binding compared to other purification fractions and A_{2A}R-SMALP controls. It is possible that this observed binding is due to large arrays of AQP4 tetramers being present in the SEC void. As previously stated, multiple studies have observed a higher binding affinity of NMO Abs to M23 AQP4, thought to be facilitated by the formation of OAPs (Nicchia *et al.*, 2009; Mader *et al.*, 2010; Crane *et al.*, 2011; Pisani *et al.*, 2011, 2013; Soltys *et al.*, 2019).

Piecing the evidence in Chapters 4 and 5 together, it appears that M1 AQP4 expressed in *P. pastoris* can form higher-order oligomers of AQP4 tetramers, which is in contrast to what is observed in mammalian expression systems (Furman *et al.*, 2003; Crane, Bennett and Verkman, 2009). The work presented in this chapter therefore sought to investigate whether M1 and M23 AQP4 can form OAPs in the membrane when expressed in *P. pastoris*. The palmitoylation state of AQP4 expressed in *P. pastoris* was then investigated, to determine whether the palmitoylation state of the M1 isoform could provide an explanation for the

presence of higher-order oligomers. The overall aim was to test the theory that SMA is encapsulating multiple tetramer units in SMALPs during membrane solubilisation.

6.1. BN-PAGE to visualise AQP4 OAPs

Firstly, blue native PAGE (BN-PAGE) was combined with immunoblotting to visualise AQP4 OAPs. AQP4 tetramers and OAPs have previously been visualised by BN-PAGE (Crane, Bennett and Verkman, 2009; Strand *et al.*, 2009; Rossi, Moritz, *et al.*, 2012; Kitchen *et al.*, 2016) and two-dimensional BN/SDS-PAGE (Sorbo *et al.*, 2008; Nicchia *et al.*, 2010; Rossi, Moritz, *et al.*, 2012; de Bellis *et al.*, 2021).

6.1.1. BN-PAGE of AQP4 expressed in *P. pastoris*

M1 and M23 AQP4 *P. pastoris* clones were grown and induced according to the small-scale growth and expression protocol, as described in Section 2.4.3. Non-induction control cultures were prepared for both AQP4 isoform clones, using BMGY media throughout the entire growth process (no MeOH added at any stage). Cells pellets were harvested, washed and resuspended in 5 mL cold dH_2O, and immediately broken by glass bead homogenisation for BN-PAGE (Section 2.7.7.1). Cell lysates were incubated with a native lysis buffer (containing Triton X-100) and separated by 10% acrylamide BN-PAGE (Section 2.7.7.3), followed by western blotting (Section 2.7.3). The blot shown in Figure 6.1 was initially probed with a rabbit anti-AQP4 Ab (1:5,000), followed by a secondary anti-rabbit-HRP Ab (1:2,500). However, this did not produce any signal – this was presumed to be on account of issues with preparation of the primary Ab. The blot was stripped (Section 2.7.3.2) and re-probed with a mouse anti-His Ab (1:2,500). An anti-mouse-HRP Ab was used as secondary (1:2,500) and the blot was imaged using chemiluminescence.

Figure 6.1 shows the resulting BN-PAGE western blot of M1 and M23 AQP4 *P. pastoris* clone lysates. The predicted tetramer band is marked with a red arrow. Both M1 and M23 AQP4 appear to show higher-order oligomers (marked with a black arrow), but these are not well resolved from the top of the gel.

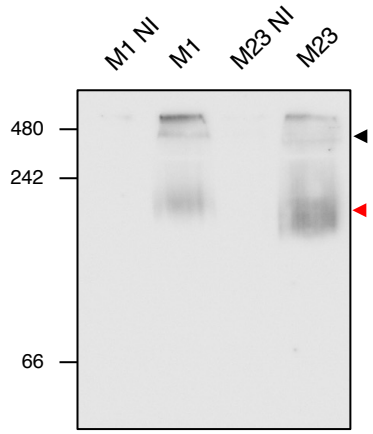

Figure 6.1. 10% acrylamide BN-PAGE of *P. pastoris* whole cell lysates from clones expressing M1 or M23 isoforms of AQP4.
P. pastoris cultures of clones expressing either the M1 or M23 isoform of AQP4 were grown, induced or not-induced (NI) for expression of AQP4, and broken by glass bead homogenisation. Cell lysates were incubated with a native lysis buffer (containing Triton X-100) and separated by 10% acrylamide BN-PAGE, followed by western blotting. AQP4 was probed with a mouse anti-His Ab (1:2,500). An anti-mouse-HRP Ab was used as secondary (1:2,500) and the blot was imaged using chemiluminescence. The red arrow indicates bands predicted to represent AQP4 tetramers. The black arrow indicates bands predicted to represent AQP4 higher-order oligomers. Approximate band positions of NativeMark and BSA are indicated on the left of the blot with corresponding mass (kDa).

M1 and M23 AQP4 *P. pastoris* clones were cultured and analysed by BN-PAGE again, but with some alterations for improvement of analysis: small-scale cultures were scaled up by 5× volume to provide a higher cell yield; cultures were grown in baffled flasks (as opposed to conical centrifuge tubes) with the aim of improving aeration, and thus, AQP4 expression; cell homogenisation was done at a higher concentration of resuspended cells to increase the lysate concentration; a low concentration gradient acrylamide gel was prepared so that higher-mass structures could be better resolved; and the anti-AQP4 Ab dilution was decreased to 1:2,500 to increase detection sensitivity (compared to 1:5,000 used previously). A freeze-thaw condition was also investigated for stability of higher-order oligomers after storage at -20 °C and defrosting.

M1 and M23 AQP4 *P. pastoris* clones were grown and induced according to the small-scale growth and expression protocol, as described in Section 2.4.3, but 250 mL baffled shake-flasks were used (instead of 50 mL conical tubes) and culture volume was increased to 25 mL (instead of 5 mL) for induction. Cells were harvested by centrifugation in 5 mL culture medium fractions and frozen (-80 °C). Cells were defrosted and broken by glass bead homogenisation for BN-PAGE, as described in Section 2.7.7.1, but cell pellets from 5 mL of culture were resuspended in 2.5 mL cold dH_2O (instead of 5 mL) for bead beating. Cell lysates were

incubated with a native lysis buffer (containing Triton X-100) and split into two conditions – lysates were either stored at 4 °C for 1 h (Figures 6.2A and C) or subjected to freeze-thaw conditions at -20 °C for 1 h, followed by defrosting (Figures 6.2B and D). Samples were then separated by 4–8% acrylamide BN-PAGE (Section 2.7.7.3), followed by western blotting (Section 2.7.3). AQP4 was probed with a rabbit anti-APQ4 Ab (1:2,500). An anti-rabbit-HRP Ab was used as secondary (1:2,500) and the blot was imaged using chemiluminescence (Figures 6.2A and B). The blot was then stripped (Section 2.7.3.2) and re-probed with a mouse anti-His Ab (1:2,500). An anti-mouse-HRP Ab was used as secondary (1:2,500) and the blot was imaged using chemiluminescence (Figures 6.2C and D). The non-freeze-thaw and freeze-thaw conditions were run on the same gel but were separated for blot chemiluminescence imaging due to higher intensity from the freeze-thaw samples.

Figure 6.2 shows the resulting 4–8% gradient BN-PAGE western blot of M1 and M23 AQP4 *P. pastoris* clone lysates. When probed with the anti-AQP4 Ab and anti-His Ab, both M1 and M23 showed a similar pattern of higher-order oligomers (black arrows) above the predicted tetramer band (red arrow). These higher-order oligomers appear to be maintained after freeze-thawing (Figure 6.2B). Interestingly, the anti-His Ab appeared to show a different pattern of intensity. A band just below the ~480 kDa marker appeared with this probe (Figure 6.2C) that is not easily visible when probing with the anti-AQP4 Ab. The freeze thaw samples probed with anti-His Ab also showed the strongest intensity at the top of the gel (Figure 6.2D). This could be attributed to positional differences of the binding epitopes for the anti-AQP4 and anti-His Abs on the AQP4 tetramer.

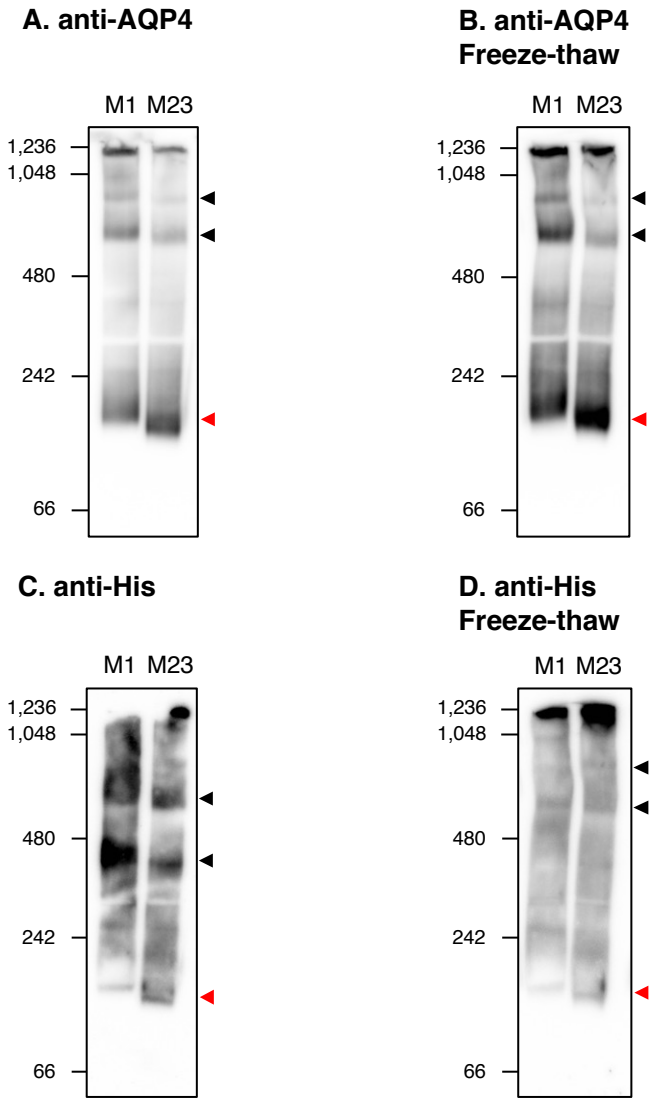

Figure 6.2. 4–8% acrylamide BN-PAGE of *P. pastoris* whole cell lysates from clones expressing M1 or M23 isoforms of AQP4.
P. pastoris cultures of clones expressing either the M1 or M23 isoform of AQP4 were grown, induced for expression of AQP4, and broken by glass bead homogenisation. Cell lysates were incubated with a native lysis buffer (containing Triton X-100) and spilt into two conditions: storage at 4 °C (1 h) or subjected to freeze-thaw conditions (-20 °C, 1 h, followed by defrosting). Samples were separated by 4–8% acrylamide BN-PAGE, followed by western blotting. **A, B)** AQP4 was probed with a rabbit anti-APQ4 Ab (1:2,500). An anti-rabbit-HRP Ab was used as secondary (1:2,500) and the blot was imaged using chemiluminescence. **C, D)** The blot was stripped and re-probed with a mouse anti-His Ab (1:2,500). An anti-mouse-HRP Ab was used as secondary (1:2,500) and the blot was imaged using chemiluminescence. **A** and **C** show lysates that were stored at 4 °C before BN-PAGE. **B** and **D** show lysates subjected to freeze-thaw before BN-PAGE. The red arrows indicate bands predicted to represent AQP4 tetramers. The black arrows indicate bands predicted to represent AQP4 higher-order oligomers. Approximate band positions of NativeMark and BSA are indicated on the left of the blots with corresponding mass (kDa).

6.1.2. BN-PAGE of AQP4 expressed in MDCK cells

Having shown that M1 AQP4 expressed in *P. pastoris* is able to form higher-order oligomers (OAPs), mammalian expression of AQP4 was used in order to confirm the typical absence of oligomeric formation by M1 AQP4, as observed by others (Crane and Verkman, 2009; Crane, Bennett and Verkman, 2009; Rossi, Moritz, *et al.*, 2012). Madin-Darby canine kidney (MDCK) cells were cultured and kindly provided by Drs Lucas Unger and Phil Kitchen of our research group. The MDCK cells were stably transfected with a construct of either the M1 or M23 isoform of AQP4, with a C-terminally fused GFP. These cells were lysed and analysed by the same BN-PAGE process used for the *P. pastoris* lysates. The dilution of the anti-AQP4 Ab was decreased to 1:1,000 from that used for the *P. pastoris* lysates (1:2,500) to further increase sensitivity of detection.

MDCK lysates were prepared using native lysis buffer (containing Triton X-100) as described in Section 2.7.7.2. As with the *P. pastoris* lysates, the MDCK lysates were split into two conditions. Lysates were either stored at 4 °C for 1 h (Figures 6.3A and C) or subjected to freeze-thaw conditions at -20 °C for 1 h, followed by defrosting (Figures 6.3B and D). Samples were then separated by 4–8% acrylamide BN-PAGE (Section 2.7.7.3), followed by western blotting (Section 2.7.3). AQP4 was probed with a rabbit anti-APQ4 Ab (1:1,000). An anti-rabbit-HRP Ab was used as secondary (1:2,500) and the blot was imaged using chemiluminescence (Figures 6.3A and B). The blot was then stripped (Section 2.7.3.2) and re-probed with a rabbit anti-GFP Ab (1:1,000). An anti-rabbit-HRP Ab was used as secondary (1:2,500) and the blot was imaged using chemiluminescence (Figures 6.3C and D). The non-freeze-thaw and freeze-thaw conditions were run on the same gel but were separated for blot chemiluminescence imaging due to higher intensity from the freeze-thaw samples.

Figure 6.3 shows the resulting 4–8% gradient BN-PAGE western blot of M1 and M23 AQP4 from MDCK cell lysates. When probed with the anti-AQP4 Ab and anti-GFP Ab, only M23 AQP4 showed the presence of higher-order oligomers (black arrows) above the predicted AQP4 tetramer band (red arrow). These higher-order oligomers appear to be maintained after freeze-thawing (Figures 6.3B and D), demonstrating their stability. The right panel of Figure 6.3A (6.3A.b) shows the top half of the blot (6.3A.a) imaged separately for improved signal detection of the AQP4 higher-order oligomers, as the signal from the M1 AQP4 tetramer masked the overall signal. As with the *P. pastoris* lysates, the non-freeze-thaw and freeze-thaw conditions were run on the same gel but were separated for chemiluminescence imaging due to the higher intensity of the freeze-thaw samples. Relative to the MW markers, the position of the AQP4 tetramer band from the MDCK construct was a higher mass than that

observed for the *P. pastoris* clone. This can be attributed to a MW increase from the GFP C-terminal fusion construct (~27 kDa per AQP4 monomer, ~108 kDa for the tetramer) used in the mammalian expression system.

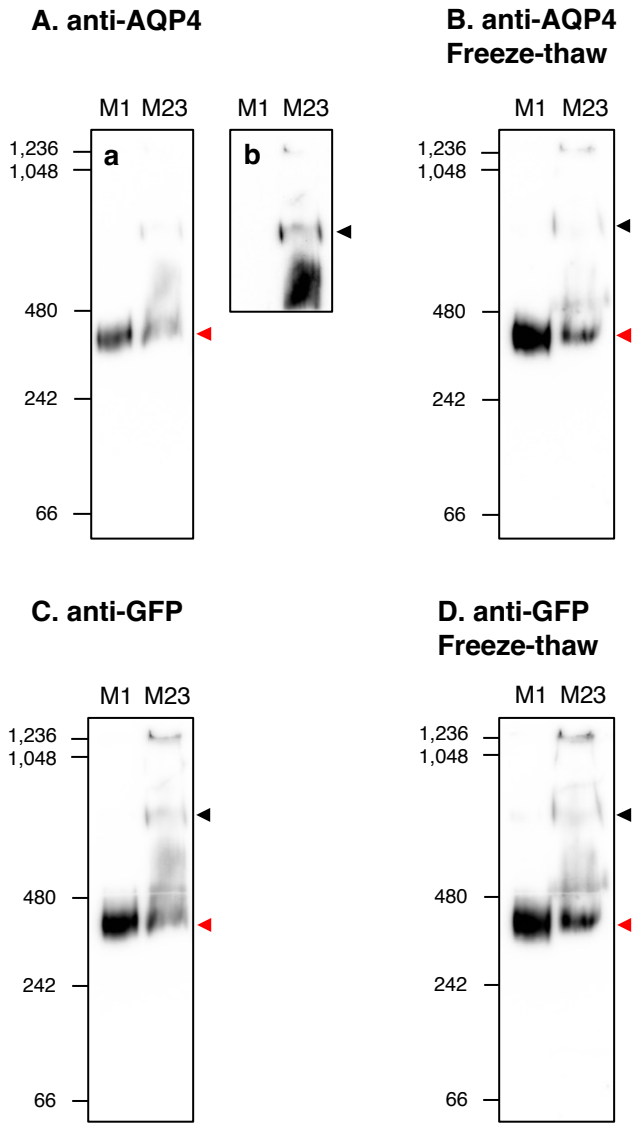

Figure 6.3. 4–8% acrylamide BN-PAGE of MDCK whole cell lysates from clones expressing M1 or M23 isoforms of AQP4-GFP.
MDCK cells stably transfected with either the M1 or M23 isoform of an AQP4-GFP construct were lysed using a native lysis buffer (containing Triton X-100). Cell lysates were spilt into two conditions: one half stored at 4 °C (1 h), and the other half subjected to freeze-thaw conditions (-20 °C, 1 h, followed by defrosting). Samples were separated by 4–8% acrylamide BN-PAGE, followed by western blotting. **A, B)** AQP4 was probed with a rabbit anti-APQ4 Ab (1:1,000). An anti-rabbit-HRP Ab was used as secondary (1:2,500) and the blot was imaged using chemiluminescence. Panel **A.b** shows the top half of **A.a** imaged separately for improved sensitivity of signal detection. **C, D)** The blot was stripped and re-probed with a rabbit anti-GFP Ab (1:1,000). An anti-rabbit-HRP Ab was used as secondary (1:2,500) and the blot was imaged using chemiluminescence. **A** and **C** show lysates that were stored at 4 °C before BN-PAGE. **B** and **D** show lysates subjected to freeze-thaw before BN-PAGE. The red arrows indicate bands predicted to represent AQP4 tetramers. The black arrows indicate bands predicted to represent AQP4 higher-order oligomers. Approximate band positions of NativeMark and BSA are indicated on the left of the blots with corresponding mass (kDa).

6.2. Investigating palmitoylation of AQP4 by *P. pastoris*

It had now been established that, unlike in mammalian expression systems, M1 AQP4 was forming higher-order oligomers when expressed in *P. pastoris*. As discussed, palmitoylation is thought to play a key role in regulating OAP formation for M1 AQP4. Suzuki *et al.* found that mutation of both Cys13 and Cys17 to alanine in the M1 isoform of rat AQP4 resulted in OAP formation. They were also able to experimentally determine that these cysteine residues were palmitoylated when expressed in CHO cells (Suzuki *et al.*, 2008). Recently, Carder *et al.* demonstrated that the palmitoylation state of M1 AQP4 expressed in Sf9 cells influences tetramer association in supported lipid bilayers. When M1 AQP4 was palmitoylated, it could associate into a dimer of tetramers, and when de-palmitoylated, could further associate into a trimer of tetramers (Carder *et al.*, 2024).

AQP4 expressed in *P. pastoris* was therefore investigated for the presence of palmitoylation, theorising that a lack of palmitoylation could be the cause of M1 AQP4 higher-order oligomers. Suzuki *et al.* used acyl-biotinyl exchange (ABE) chemistry to identify the presence of palmitoylation on M1 AQP4 (Suzuki *et al.*, 2008). ABE chemistry is a well-documented method for detecting protein palmitoylation (Drisdel *et al.*, 2006; Edmonds *et al.*, 2017; Leishman, Aljadeed and Anand, 2024), and has previously been used to identify palmitoylated proteins in yeast (Roth *et al.*, 2006; Lei *et al.*, 2021). Here, an ABE protocol adapted from Lei *et al.* was used to test whether recombinant hAQP4 was palmitoylated by *P. pastoris* (Lei *et al.*, 2021).

6.2.1. Principle of the ABE assay

Figure 6.4 demonstrates the principle of the adapted ABE assay used here to identify palmitoylated proteins. Firstly, proteins are extracted from cell lysates by chloroform-methanol (TCM-MeOH) precipitation. The extracted proteins are then subjected to three sequential reactions: *N*-ethylmaleimide (NEM) is added to permanently block free thiols (-SH), forming a C-S bond. Repeated TCM-MeOH precipitations are used to remove excess NEM, before the addition of hydroxylamine (HA) in the presence of pyridyldithiol-biotin (HPDP-biotin). For palmitoylated proteins, HA cleaves the thioester bond between cysteine and palmitate. HPDP-biotin then biotinylates proteins by forming disulfide bonds with the newly exposed thiols created by HA. Non-palmitoylated proteins are unaffected as they have been blocked with NEM, making them unable to bind to HPDP-biotin. Further repeated TCM-MeOH precipitations are used to remove excess biotin. Samples are then incubated with streptavidin agarose resin. Streptavidin binds to biotin with very high affinity, capturing the biotinylated (previously

palmitoylated) proteins. The resin is washed to remove unbound (non-palmitoylated) proteins. The bound proteins are then eluted by addition of Laemmli buffer, which breaks the HPDP-biotin disulfide bond and denatures streptavidin. The eluted proteins are then separated from the agarose resin by centrifugation. The target protein can then be probed via SDS-PAGE and western blotting to identify the presence of palmitoylation. For the assay, a condition without HA (-HA) is used as an assay negative control. Without HA, proteins cannot be biotinylated, and thus, a palmitoylated target protein should not be detected via western blot.

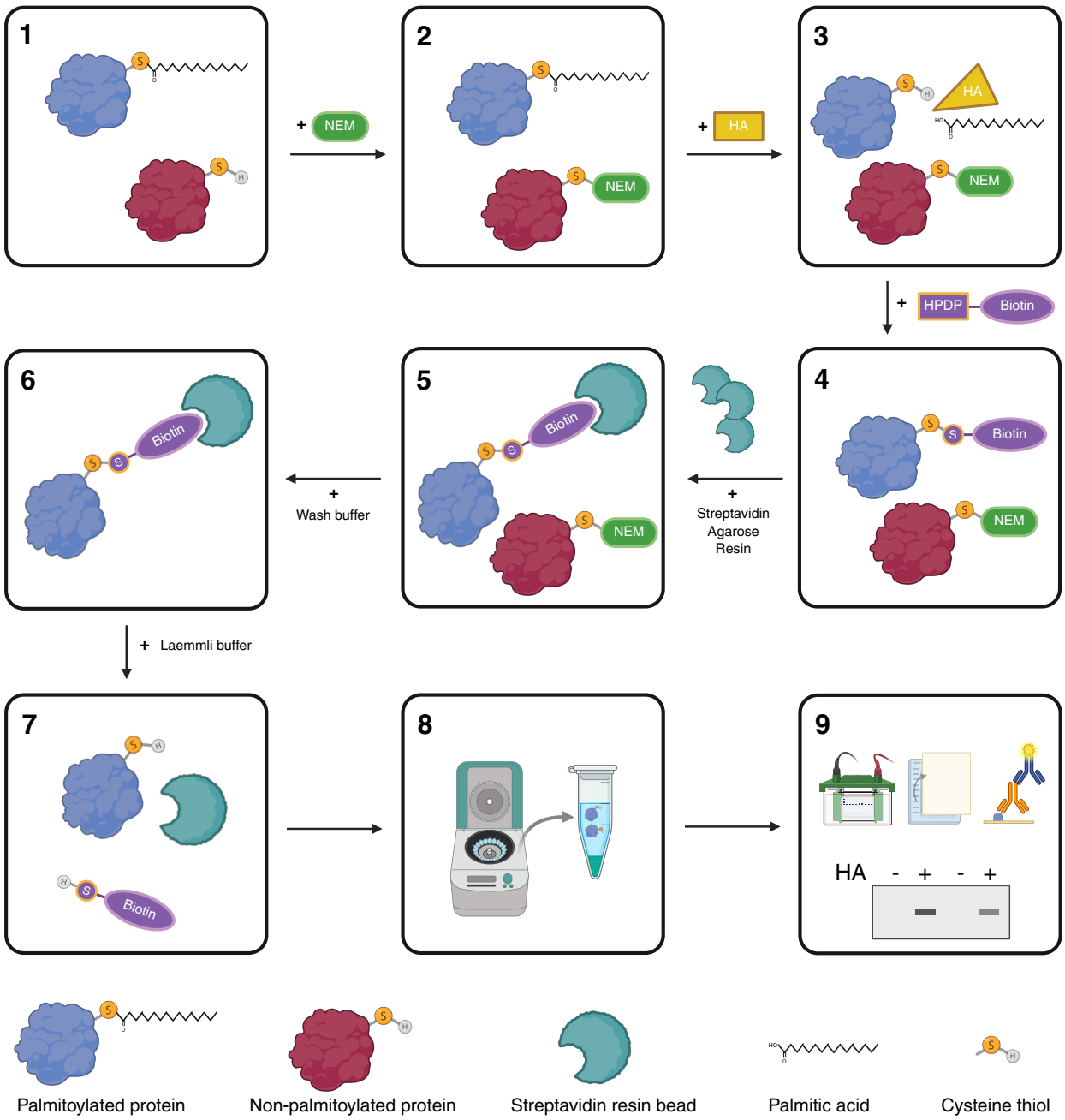

Figure 6.4. Schematic demonstrating the modified acyl-biotinyl exchange (ABE) assay to identify palmitoylated proteins.
1) Proteins are extracted from cell lysates by TCM-MeOH precipitation. Blue represents an *S*-palmitoylated protein, and red represents a non-palmitoylated protein with an exposed thiol. **2)** Addition of *N*-ethylmaleimide (NEM) permanently blocks free thiols. Repeated TCM-MeOH precipitation is used to remove excess NEM. **3)** Addition of hydroxylamine (HA) cleaves the thioester bond between cysteine and palmitate. **4)** Pyridyldithiol-biotin (HPDP-biotin) forms disulfide bonds with the newly exposed thiols. Repeated TCM-MeOH precipitation is used to remove excess biotin. **5)** Incubation with streptavidin agarose resin to bind biotinylated proteins. **6)** Washing the resin to remove unbound proteins. **7)** Elution of the previously-palmitoylated resin-bound proteins by addition of Laemmli buffer. **8)** Separation of the eluted sample from the agarose resin by centrifugation. **9)** The protein of interest is probed via SDS-PAGE and western blot. Figure created in BioRender.com.

6.2.2. Probing AQP4 for the presence of palmitoylation using the ABE assay

M1 and M23 AQP4 *P. pastoris* clones were grown and induced according to the small-scale growth and expression protocol, as described in Section 2.4.3, but 250 mL glass baffled shake-flasks were used (instead of 50 mL conical tubes) and culture volume was increased to 25 mL (instead of 5 mL) for induction. Cells were harvested by centrifugation in 5 mL culture medium fractions and frozen (-80 °C). Cells were defrosted and broken by glass bead homogenisation, as described in Section 2.9.3.1, with cell pellets from 5 mL of culture resuspended in 1 mL cold lysis buffer for bead beating. A Bradford assay using BSA as a standard in serial dilution was used to determine the lysate total protein concentration. M1 and M23 AQP4 *P. pastoris* lysates equivalent to 1 mg of total protein were probed for the presence of palmitoylation using the ABE assay (Section 2.9.3 and Figure 6.4). Briefly, lysates were incubated in lysis buffer containing Triton X-100 and NEM (30 min, 4 °C). Proteins were then extracted by TCM-MeOH precipitation and incubated with 10 mM NEM (16 h, 4 °C). Protein precipitations were repeated to remove excess NEM and precipitates were dissolved in 450 µL of buffer. 50 µL of the sample was retained as an assay input sample (Input). The remaining 400 µL was split equally into conditions with (+) and without (-) 0.7 M HA. Both buffer conditions contained 1 mM HPDP-biotin. Samples were incubated in these buffers (2 h, RT), followed by removal of excess HPDP-biotin by repeated TCM-MeOH precipitations. Precipitates were re-dissolved and incubated with streptavidin agarose resin (2 h, RT). The unbound fraction (FT) was collected after centrifugation to pellet the resin. The resin was then washed by five rounds of resuspension and centrifugation in fresh wash buffer. Bound protein (E) was eluted by incubation with Laemmli buffer (15 min, RT) and separated from the resin by centrifugation. Samples were separated by 4–16% gradient SDS-PAGE, followed by western blotting (Section 2.7.3). AQP4 in the samples was probed with a rabbit anti-AQP4 Ab (1:5,000), followed by a secondary anti-rabbit-HRP Ab (1:2,500), and visualised by chemiluminescence.

Figure 6.5 shows the resulting western blot of samples from the ABE assay. M1 and M23 AQP4 are clearly present in the assay input. M1 AQP4 showed a strong intensity in the +HA streptavidin elution (E). By comparison, M23 AQP4 showed a weak intensity in the +HA ‘E’ condition, comparable with its intensity in the -HA ‘E’ condition. M1 and M23 AQP4 were both visible at a low intensity in the -HA streptavidin elution (E). This could be due to incomplete blocking by NEM (causing biotinylation in places where palmitoylation was not previously present), non-specific of AQP4 binding to the streptavidin agarose resin, or insufficient washing to remove unbound AQP4 from the resin prior to sample elution. M1 and M23 AQP4 are also clearly present in the +HA unbound (FT) sample. It is worth noting that the unbound (FT) samples represent the intensity from 1 mL of total unbound sample collected, whereas

the elution (E) samples represent the intensity from 100 µL of resin elution. As such, the 'E' samples are 10× more concentrated relative to the FT samples.

These results show the detection of biotinylation of M1 AQP4. This means it must carry post-translational modifications through thioester bonds (that were cleaved by HA). Given the similar intensities of M23 AQP4 in the -HA and +HA conditions, M23 AQP4 is unlikely to have been biotinylated (or, at least, not as a result of previously having a thioester modification). These results suggest that M1 AQP4 is, to some extent, palmitoylated by *P. pastoris*, whereas M23 AQP4 is not.

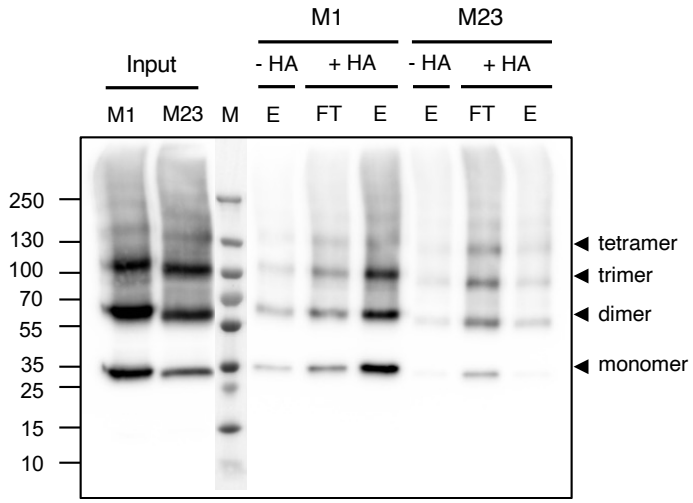

Figure 6.5. Western blot of M1 and M23 AQP4 *P. pastoris* clones subjected to the ABE assay to determine presence of palmitoylation.
P. pastoris cultures of clones expressing either the M1 or M23 isoform of AQP4 were grown, induced for expression of AQP4, and broken by glass bead homogenisation. Protein was extracted form whole cell lysates by TCM-MeOH precipitation and incubated with NEM. An assay input sample was taken (Input), and the remaining sample was incubated with HPDP-biotin in the presence (+) or absence (-) of HA. Samples were incubated with streptavidin agarose resin, the unbound flowthrough was collected (FT), the resin was washed, and bound proteins were eluted using Laemmli buffer (E). Assay samples were separated by 4–16% acrylamide SDS-PAGE, followed by western blotting. AQP4 in the samples was probed with a rabbit anti-APQ4 Ab (1:5,000). An anti-rabbit-HRP Ab was used as secondary (1:2,500) and the blot was imaged using chemiluminescence. Positions of monomer, dimer, trimer and tetramer bands of AQP4 are labelled with black arrows. MW markers are shown under 'M' with mass labels in kDa shown on the left of the blot.

6.2.3. Further optimisation of the ABE assay

Although the first ABE assay attempt showed good evidence for M1 AQP4 being palmitoylated by *P. pastoris*, there was some background signal of AQP4 present in the -HA condition (negative control). This suggested that there was an issue with the assay, or certain steps required further optimisation. As discussed, the presence of AQP4 in the -HA elution could be due to incomplete blocking by NEM (blockade of free thiols), non-specific binding of AQP4 to the streptavidin agarose resin, or insufficient washing of the streptavidin agarose resin to remove unbound AQP4 prior to sample elution. For the next ABE assay attempt, a few changes were made to mitigate these possibilities: NEM concentration was increased for NEM incubation to ensure complete blocking of free thiols, streptavidin binding was done at 4 °C to reduce possible non-specific binding, and SDS was added to the resin wash buffer to improve streptavidin agarose resin washing.

P. pastoris cultures from the previous preparation were used to generate lysates for M1 and M23 AQP4, as before (Section 6.2.2). The lysates were subjected to the ABE assay as described in Section 2.9.3 and 6.2.2, but with the following changes applied: NEM concentration was increased to 20 mM, from 10 mM previously, for the 16 h incubation; the streptavidin agarose resin incubation was done at 4 °C, instead of at RT, for the same amount of incubation time; and SDS was added (0.1% w/v) to the resin wash buffer. As before, samples were separated by 4–16% gradient SDS-PAGE, followed by western blotting (Section 2.7.3). AQP4 in the samples was probed with a rabbit anti-AQP4 Ab (1:5,000), followed by a secondary anti-rabbit-HRP Ab (1:2,500), and visualised by chemiluminescence (Figure 6.6A). A second SDS-PAGE and western blot of the samples was carried out for probing with a mouse anti-His Ab (1:2,500) and anti-mouse-HRP Ab secondary (1:2,500) (Figure 6.6B).

Figure 6.6 shows the resulting western blots for the optimised ABE assay of M1 and M23 AQP4 *P. pastoris* lysates. The anti-AQP4 Ab and anti-His Ab probe produced very similar blots. The results for these blots are consistent with that observed for Figure 6.5 – strong presence of M1 AQP4 in the +HA ‘E’ condition suggests that it palmitoylated by *P. pastoris* to some degree, whereas very low intensity of M23 AQP4 in this condition suggests that it is not palmitoylated. Compared to the previous ABE assay conditions (Figure 6.5), there is a reduction in AQP4 intensity in the -HA elution (E) samples, suggesting that the optimisation conditions did have an improvement on the assay performance. However, a faint AQP4 band in the -HA ‘E’ (and M23 +HA ‘E’) samples is still evident, suggesting that further optimisation could still be done to remove the background AQP4 signal. As before, it is worth noting that the ‘E’ samples (100 µL) are 10× more concentrated relative to the FT samples (1 mL).

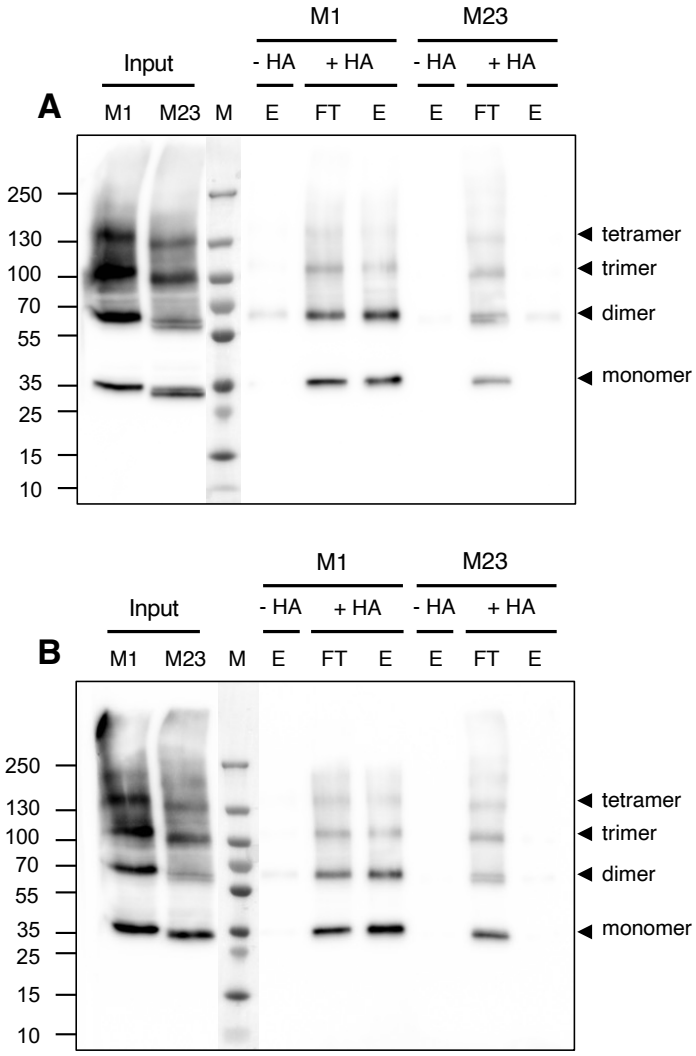

Figure 6.6. Optimisation of the ABE assay to determine presence of palmitoylation of AQP4 by *P. pastoris*.

P. pastoris cultures of clones expressing either the M1 or M23 isoform of AQP4 were grown, induced for expression of AQP4, and broken by glass bead homogenisation. Protein was extracted form whole cell lysates by TCM-MeOH precipitation and incubated with an increased concentration of NEM. An assay input sample was taken (Input), and the remaining sample was incubated with HPDP-biotin in the presence (+) or absence (-) of HA. Samples were incubated with streptavidin agarose resin at 4 °C, the unbound flowthrough was collected (FT), the resin was washed with the addition of SDS, and bound proteins were eluted using Laemmli buffer (E). Assay samples were separated by 4–16% acrylamide SDS-PAGE, followed by western blotting. **A)** Western blot of samples probed with a rabbit anti-APQ4 Ab (1:5,000). An anti-rabbit-HRP Ab was used as secondary (1:2,500) and the blot was imaged using chemiluminescence. **B)** Western blot of samples probed with a mouse anti-His Ab (1:2,500). An anti-mouse-HRP Ab was used as secondary (1:2,500) and the blot was imaged using chemiluminescence. For both blots, positions of monomer, dimer, trimer and tetramer bands of AQP4 are labelled with black arrows. MW markers are shown under 'M' with mass labels in kDa shown on the left of the blot.

Although the ABE assay optimisation improved the unexpected presence (background signal) of faint AQP4 bands in the -HA condition, a faint AQP4 band was still visible in this negative control (-HA) condition. As previously discussed, this background signal may be caused by an incomplete NEM blockade of free thiols, non-specific binding to the streptavidin agarose resin, or insufficient washing of unbound AQP4 from the agarose resin. This background signal is unlikely to invalidate the result, as M23 AQP4 showed a similarly low level of background signal (faint AQP4 band) in both -HA and +HA conditions, whereas M1 AQP4 showed a clear difference in band intensity between these conditions. This demonstrated that the faint background signal was present regardless of the HA condition, with a clear difference in band intensity between -HA and +HA depending on the AQP4 isoform. Despite this, quantifying and comparing the AQP4 band intensities from experimental replicates would give greater confidence that this observation is significant. To be able to disregard the background signal, it was important to demonstrate that there was no significant difference between -HA and +HA conditions for the M23 isoform, and no significant difference between M1 and M23 AQP4 in the -HA condition.

In total, three experimental replicates were performed for the ABE assay of M1 and M23 AQP4 *P. pastoris* clone lysates. The western blots of these replicates were all probed with the anti-AQP4 Ab, and includes the western blots shown in Figure 6.5 and Figure 6.6A. Although the assay conditions were slightly different before and after optimisation, these assays were still considered together as replicates for quantification. This was to determine whether a significant difference between M1 and M23 AQP4 could be found, regardless of the variation in intensity of the -HA condition between replicates. Each replicate used cells from the same batch preparation of M1 or M23 AQP4 *P. pastoris*, but new lysates were prepared for each assay.

The +HA and -HA elution (E) samples for M1 and M23 AQP4 in the three experimental replicate ABE assay western blots were quantified using densitometry (Section 2.7.4). The intensity for each sample was normalised to the intensity of the input sample of the relevant AQP4 isoform. Figure 6.7 shows a plot of the mean normalised intensity ± SD for each sample and HA condition. A two-way ANOVA with Tukey's *post hoc* test was performed for statistical analysis. No significant difference was found between the -HA and +HA condition for M23 AQP4. By contrast, a significant difference was found between -HA and +HA conditions for M1 AQP4, and a significant difference was found between M1 and M23 AQP4 in the +HA condition. This reinforces the idea that there may be some non-specific binding to the streptavidin agarose resin, but this does not affect the impact of the -HA negative control. M1

AQP4 shows a significant difference in intensity to M23 AQP4 in the +HA condition, suggesting that it is palmitoylated by *P. pastoris*, whilst the M23 isoform is not.

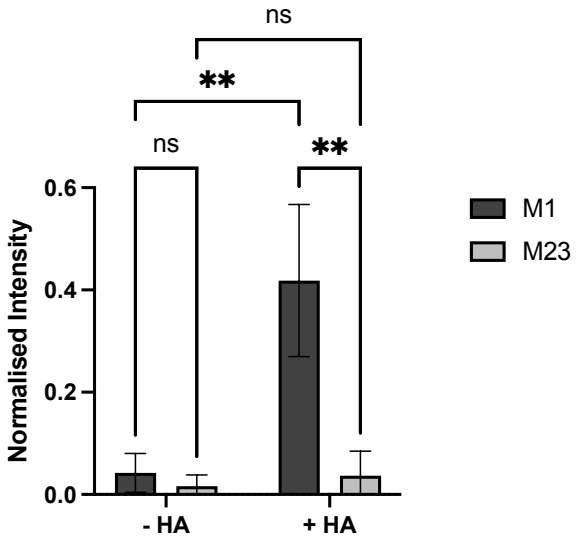

Figure 6.7. Quantification of ABE assay outputs for M1 and M23 AQP4.
Western blots of M1 and M23 AQP4 *P. pastoris* clones subjected to the ABE assay were quantified by densitometry analysis. The plot shows the mean ± SD (n = 3, experimental replicates) normalised intensities for M1 and M23 AQP4 in the streptavidin resin elution samples from the -HA (negative control) and +HA conditions of the ABE assay. Intensity was calculated as the sum of AQP4 monomer, dimer, trimer, and tetramer bands for each sample, where visible. Values were normalised to the corresponding input sample intensity. Statistical analysis was performed with a two-way ANOVA with Tukey's multiple comparisons *post hoc* test (ns – $p > 0.05$ (not significant), **$p \leq 0.01$).

6.3. Chapter Summary

The work in this chapter investigated the presence of OAP formation by AQP4 expressed in *P. pastoris*. BN-PAGE was used to identify the presence of higher-order AQP4 oligomers for both the M1 and M23 isoforms when expressed in *P. pastoris*. A comparative BN-PAGE analysis was performed on M1 and M23 AQP4 isoforms expressed in MDCK cells. This demonstrated that, as observed by others, M1 AQP4 does not typically form higher-order oligomers when expressed in mammalian cells, whereas M23 AQP4 does. Palmitoylation is thought to prevent M1 AQP4 from forming OAPs, and thus, it was theorised that a lack of palmitoylation by *P. pastoris* was the reason for the observed OAP formation. However, an ABE assay of the *P. pastoris* constructs found that M1 AQP4, and not M23 AQP4, carries post-translational modifications facilitated by thioester bonds, mostly likely representing some degree of *S*-palmitoylation by *P. pastoris*.

7. Discussion

The aim of this project was to determine whether AQP4 tetramers and higher-order oligomers or OAPs could be captured and characterised in SMALPs from the *P. pastoris* membrane. The idea was to create a recombinant expression model to further develop our understanding of AQP4 OAP formation, and in turn, create new research pathways to investigate these tetrameric arrays in the context of NMOSD.

Chapter 3 described how two clones of *P. pastoris* expressing recombinant constructs of either the M1 or M23 isoform of AQP4 were established for comparable expression and purification yield of AQP4. Bioreactors were utilised to increase production of membrane fragments for SMA solubilisation and purification.

Chapter 4 then utilised mass photometry, SEC, and SMA-PAGE to characterise purified AQP4-SMALPs, showing that multiple SMALP sizes exist for both AQP4 isoforms. These SMALPs of increasing size were theorised to contain different tetrameric assemblies of AQP4 – 1-tetramer (1T), 2-tetramer (2T), and 3-tetramer (3T) AQP4 SMALPs. Mass photometry Ab binding assays were used to confirm the presence of AQP4 in these SMALP complexes. Mass estimates from mass photometry, SEC, and SMA-PAGE were compared, finding the mass difference between the M1 and M23 1T AQP4-SMALP to be consistent with the tetramer mass difference of these isoforms.

Chapter 5 investigated binding of NMO Abs to purified AQP4-SMALPs via dot blotting and mass photometry. Binding could only be determined for the affinity purified and SEC void fraction of these AQP4-SMALPs.

Chapter 6 then investigated OAP formation by *P. pastoris* expressed AQP4, in an attempt to explain the presence of higher-order oligomers of M1 AQP4 in SMALPs. BN-PAGE identified higher-order oligomers for both the M1 and M23 AQP4 isoforms when expressed in *P. pastoris*, in contrast to M1 AQP4 expressed in MDCK cells. Lack of palmitoylation by *P. pastoris* was investigated as a possible explanation for these M1 AQP4 higher-order oligomers. However, an acyl-biotinyl exchange (ABE) assay determined that M1 AQP4 was very likely palmitoylated by *P. pastoris* to some degree.

7.1. Benefits of *P. pastoris* as an expression host for hAQP4

P. pastoris is an excellent expression system for the production of recombinant human proteins. As *P. pastoris* is a eukaryotic organism, it can allow protein folding and PTMs comparable to that of mammalian expression systems, and most importantly, comparable to the native expression in human cells (Daly and Hearn, 2005; Karbalaei, Rezaee and Farsiani, 2020). AQP4 has previously been successfully expressed in *P. pastoris* (Ho *et al.*, 2009; Öberg *et al.*, 2011; Kitchen *et al.*, 2020) and *P. pastoris* has a reputation for being a good expression host for production of recombinant human AQPs (Bill and Hedfalk, 2021; Al-Jubair *et al.*, 2022). Expression of hAPQ4 in *P. pastoris* was desirable for this project, as a key functional difference between the M1 and M23 AQP4 isoforms is a PTM. M1 AQP4 typically features *S*-palmitoylation of cysteine residues in the N-terminal region that the M23 isoform lacks. As already discussed, this palmitoylation is thought to play a key role in preventing M1 AQP4 from forming OAPs in cell membranes (Suzuki *et al.*, 2008; Carder *et al.*, 2024).

The first palmitoyl acyltransferases (PATs) of the zDHHC family, responsible for palmitoylation by *S*-acylation, were identified in *S. cerevisiae* yeast (Lobo *et al.*, 2002; Roth *et al.*, 2002). These enzymes are defined by a conserved DHHC domain found in many eukaryotic PATs (Mitchell *et al.*, 2006; Rana, Lee and Banerjee, 2018). However, the ability of, and extent to which, yeast expression systems palmitoylate recombinant proteins is unclear, and would likely need investigating on a case-by-case basis. *E. coli* (and prokaryotic systems generally) do not possess native PATs containing the DHHC domain for *S*-palmitoylation (Mitchell *et al.*, 2006; Sobocińska *et al.*, 2018). This has previously been cited as a reason to choose an alternative host for recombinant protein expression, due to palmitoylation being an important functional component (Chytła *et al.*, 2021).

This project has demonstrated that *P. pastoris* is able to palmitoylate the M1 (and not the M23) isoform of hAQP4. This is a demonstration of the advantages of using *P. pastoris* as a recombinant expression host to produce desirable PTMs. However, it is important to note that this project also demonstrated a difference in the behaviour of recombinant hAQP4 between yeast and mammalian expression systems, as observed with BN-PAGE analysis in Chapter 6. This could purely be due to differences between the eukaryotic systems, highlighting important considerations when using model expression systems.

7.2. Transformation of *P. pastoris* for improved expression of M23 AQP4

P. pastoris clones expressing the M1 or M23 isoform of AQP4 were already available at the start of this project. As shown in Chapter 3, the original M23 AQP4 clone showed comparably poor expression and purification yield compared to the established M1 AQP4 clone. Purification from the original M23 AQP4 clone also demonstrated that increasing the starting membrane material for solubilisation and purification is not a solution for poor yield, as it results in increased contamination relative to the yield of desired protein (Figure 3.2B). Therefore, a chemical transformation of GS115 *P. pastoris* with the M23 AQP4 pPICZ plasmid construct was performed to generate a new clone with improved expression.

An improved transformation efficiency (higher number of colonies) was found in the transformation condition with plasmid that had been further purified after linearisation (Figure 3.4). Presumably, the quality of linearised DNA was improved with the additional purification, by removing the buffer material and restriction enzyme from the maxi-prep and linearisation reaction steps. This may have improved the uptake of linearised plasmid DNA by competent cells. More work is required to establish the significance of this observation, but this result suggests that adding an additional DNA purification step would give a drastically improved chemical transformation protocol.

After transformation, colonies were selected at random to screen for high resistance to zeocin. The principle behind this step was to select for colonies with multiple integrated copies of the plasmid by homologous recombination, and thus, a higher resistance to zeocin. A high plasmid copy number has been reported to result in higher levels of expression of the recombinant protein. Growth with high selective pressure has been used previously to screen for clones with multiple plasmid copies (Scorer *et al.*, 1994; Athmaram *et al.*, 2012; Kumar, Mannil and Mutturi, 2020). This approach seemed to work in this case, as the two clones showing the strongest growth on high zeocin YPD agar (Figure 3.5), also presented with the highest M23 AQP4 expression (T1C3, T1C12; Figure 3.6). However, as others have found previously, the correlation between plasmid copy number and recombinant protein expression is not always linear (Aw and Polizzi, 2013). Therefore, it is important to consider that this approach may not be a universally applicable methodology.

7.3. SMA solubilisation and purification of AQP4-SMALPs from *P. pastoris* membranes

Having established the M1 and new M23 *P. pastoris* clone for comparable AQP4 expression, these clones were grown, induced for APQ4 expression, and the cells were disrupted for membrane fragment preparation. SMA was used for solubilisation of the membranes and the recombinant hAQP4 was affinity purified targeting the 6× His-tag. Purified AQP4-SMALPs were analysed by SDS-PAGE to reveal a characteristic multiple band pattern of AQP4 monomers, dimers, trimers, and tetramers (Figure 3.10). This demonstrated that both AQP4 isoforms could be solubilised and purified within SMALPs. Upon formation and stabilisation of MP-SMALPs, SMA interacts with the lipid bilayer surrounding membrane proteins, allowing it to encapsulate a native annulus of lipid (Gulati *et al.*, 2014). This allows SMALPs to preserve membrane protein complexes, such as that formed by homo-oligomers. This differs from detergents such as SDS, that disrupt non-covalent protein-protein interactions. Multiple studies have demonstrated the ability of SMA to encapsulate protein homo- and hetero-oligomers (Dörr *et al.*, 2014; Swainsbury *et al.*, 2014b; Postis *et al.*, 2015; Prabudiansyah *et al.*, 2015; Smirnova *et al.*, 2016). It is not surprising, therefore, that SMA would be able to encapsulate and preserve AQP4 tetramers within SMALPs.

Although no significant difference was found, M23 AQP4 did appear to solubilise less efficiently (44.7 ± 4.7%) with SMA than M1 AQP4 (50.6 ± 4.0%). This is unlikely to have a significant impact on purified M23 AQP4 yield, but it is interesting to speculate as to why it may have a lower solubilisation efficiency. If M23 AQP4 is preferentially forming large OAPs, as seen in mammalian expression systems (Furman *et al.*, 2003; Crane and Verkman, 2009; Crane, Bennett and Verkman, 2009), it may be more resistant to solubilisation into SMALPs, due to the difficulty of breaking down higher-order oligomers into tetramer units.

This laddering of AQP4 quaternary structures, as visualised by SDS-PAGE, demonstrates the apparent SDS resistance of AQP4 tetramers at high protein concentrations. This is something that has been observed by others before (Sørbø, Moe and Holen, 2007). In some cases here, a laddering of bands above the AQP4 tetramer mass was observed (Figure 3.10). This could represent APQ4 aggregation, or potentially, SDS resistant higher-order complexes.

SDS-PAGE analysis of IMAC purified AQP4-SMALPs presented a clear purification contaminant band at ~38 kDa (Figure 3.10). For a similar purification of $A_{2A}R$ from *P. pastoris*, Dr Idoia Company-Marín of our research group at Aston University observed a similar

contamination band via SDS-PAGE. Mass spectrometry analysis of this band identified it as fungal alcohol dehydrogenase 2 (ADH2) (Company-Marín, 2024). ADH contaminations are reportedly common during IMAC purification of proteins from *P. pastoris*, thought to be due to a high affinity of this native protein for Ni-NTA resins (Law *et al.*, 2001; Chen *et al.*, 2014). It is very likely, therefore, that the contaminant observed here is also an ADH isozyme. As seen in Chapter 4, this contaminant could be separated from IMAC purified AQP4-SMALPs by further purification using SEC (Figure 4.10). In this case, the contaminant did not cause an issue for generating homogenous samples for downstream analysis. However, if the target protein was of a similar size to the contaminant (~38 kDa), separation by SEC may not offer the same straightforward solution. This could be something to consider when choosing *P. pastoris* as an expression host and Ni-NTA IMAC purification to isolate recombinant proteins.

Degradation of M1 AQP4 and possible aggregation of M23 AQP4 was observed with extended time between IMAC purification and MW cut-off concentration (Figure 3.11). Some AQP4 was also visible in the centrifugal concentrator flowthrough for the newly purified AQP4-SMALPs, which may have been an early sign of degradation. Analysis of AQP4-SMALPs by SMA-PAGE ~1.5 months after IMAC purification and MW cut-off concentration showed some sign of AQP4-SMALP degradation (Figure 4.2), but not to the extent expected considering the degradation observed in Figure 3.11. Reducing time between IMAC purification, concentration, and SEC separation demonstrated different peak proportions in SEC profiles, with M1 AQP4 showing a significantly lower proportion in the void (Figure 4.9). After SEC, AQP4-SMALPs showed improved stability, and could be observed by mass photometry at the expected mass multiple days after SEC purification. AQP4-SMALPs were routinely kept for analysis for ~2 weeks after SEC purification. With all of these observations considered, it appears that degradation, particularly for M1 AQP4, was happening to a large extent between IMAC purification and 100 kDa MW cut-off concentration. It is possible that the centrifugal concentration process removed low MW proteases that were otherwise causing AQP4 degradation. Alternatively, AQP4 may be sensitive to high concentrations of imidazole required for IMAC resin elution. Further purification by SEC will have benefited both of these circumstances. M23 AQP4 may have shown better resistance to degradation because of greater propensity to form higher-order oligomers, explaining the aggregation observed in Figure 3.11. It is important to note that protease inhibitors were not used in buffers beyond cell lysis, which may have contributed to the observed degradation.

7.4. Biophysical characterisation of AQP4-SMALPs

The innate heterogeneity of MP-SMALPs makes characterisation of these particles difficult. Investigating the MP-SMALP complexes in a native and whole form can be challenging, especially when trying to address the overall particle mass. This project explored a combination of methods to characterise AQP4-SMALPs, including mass photometry, which allows for visualisation of unmodified single particles in solution (Young *et al.*, 2018). Mass photometry was an excellent way to easily assess sample heterogeneity and SEC fractionation, as demonstrated by Figures 4.3, 4.4, and 4.11.

When analysed by mass photometry, the APQ4-SMALPs presented as an array of different SMALP sizes that were independently linear for both M1 and M23 AQP4. As AQP4 is known to form OAPs (Yang, Brown and Verkman, 1996; Verbavatz *et al.*, 1997), it was theorised that these particles might represent single and multi-tetrameric assemblies of AQP4 within SMALPs (Figure 7.1). The peaks observed were therefore identified as 1- (1T), 2- (2T), and 3- (3T) tetramer complexes of AQP4 within SMALPs (Figure 4.5 and 7.1). These observed SMALP sizes by mass photometry were consistent with SEC and SMA-PAGE analysis (Figure 4.7). However, at this stage, it was also considered that these could be aggregates of the smallest SMALP, or different SMALP sizes only containing one tetramer.

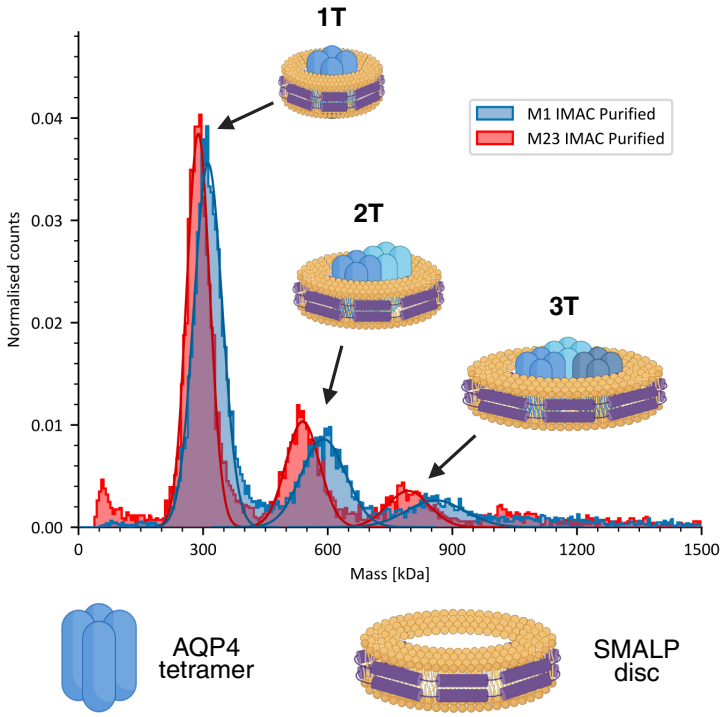

Figure 7.1. Proposed tetrameric assembly of AQP4 in SMALPs.
The figure shows a mass photometry histogram of IMAC purified M1 and M23 AQP4-SMALPs, reproduced from Figure 4.4, adapted to show proposed tetrameric assemblies of AQP4 in SMALPs. Histogram peaks are labelled with AQP4-SMALP complexes thought to contribute to the observed counts. These are identified as 1T, 2T, and 3T, representing 1-, 2-, and 3-tetramer AQP4-SMALPs, respectively. Figure created in BioRender.com.

The estimated mass of the M1 and M23 1T AQP4-SMALPs was ~303 and ~288 kDa (Section 4.6.4; based on all estimation methods), respectively. The predicted tetramer weights are ~142.4 and ~132.4 kDa, based on monomer weights of ~35.6 kDa and ~33.1 kDa for M1 and M23 AQP4, respectively. These monomer weights are determined from the full hAQP4 sequence of each isoform, plus the weight of the recombinant 6× His-tag (~0.8 kDa). The large estimated mass difference between the AQP4 tetramers and 1T AQP4-SMALPs is unlikely to be due to the 1T AQP4-SMALPs containing more than one AQP4 tetramer, as this would not allow enough remaining mass for lipids and SMA. Stroud *et al.* have suggested that five polymers of 3 kDa SMA 2:1 are required to encircle a 10 nm SMALP disc in one layer, stating the possibility of two SMA layers required to completely cover the disc edge. This would assume ~30 kDa of SMA for a 10 nm SMALP (Stroud, Hall and Dafforn, 2018). M1 AQP4-SMALPs corresponding to the 1T SEC fraction have been analysed by transmission electron microscopy (TEM) by Dr Philip Kitchen of our research group (Figure 7.2). 2D classes from cryogenic (cryo-) TEM appear to show single AQP4 tetramers within SMALP discs. Lipidomic analysis of AQP4-SMALPs (data also collected Dr Philip Kitchen) has shown that AQP4-SMALPs not only contain lipids but show a preference for certain lipids when compared to SMA solubilised and total *P. pastoris* membranes. Together, these data further support the assumption that the 1T AQP4-SMALPs observed here do indeed contain a single tetramer of AQP4 surround by an annulus of lipids.

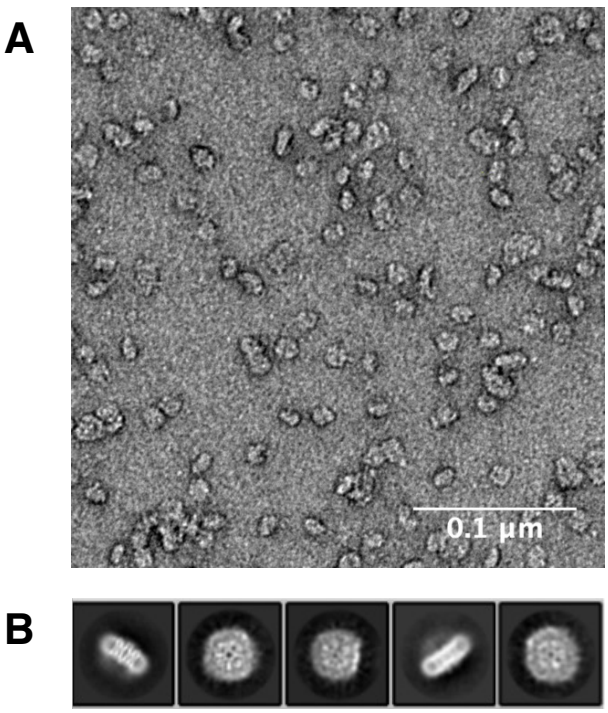

Figure 7.2. Transmission electron microscopy (TEM) of M1 AQP4-SMALPs.
M1 AQP4-SMALP samples corresponding to the 1T AQP4-SMALP SEC fraction. **A)** Negative-stain (NS) TEM of M1 AQP4-SMALPs. **B)** 2D classes from cryogenic (cryo-) TEM of M1 AQP4-SMALPs. Data collected by Dr Philip Kitchen, Aston University.

The existence of larger AQP4-SMALP sizes (identified as 2T and 3T), as demonstrated in Chapter 4, is not surprising. SMA has been shown to encapsulate protein complexes as large as ~1.2 MDa (specifically, trimeric photosystem I from *Thermosynechococcus elongatus*) in SMALPs (PSI-SMALPs) estimated to be ~1.5 MDa (Brady *et al.*, 2019, 2022) – though, this was performed with SMA 1440, as opposed to SMA 2000 used here. Initially, the possibility of AQP4-SMALP aggregates was considered. Negative stain (NS-) TEM has shown that lipid-only SMALP nanodiscs containing dipalmitoylphosphatidylcholine (DPPC) phospholipids can form large phospholipid stacks, although, this was interpreted as an artefact of the staining solution required for NS-TEM (J. J. Dominguez Pardo *et al.*, 2017). Instead, a number of factors were discovered that suggested these 2T and 3T AQP4-SMALPs were independent SMALP sizes containing two and three AQP4 tetramer units: the estimated mass increase between 1T-, 2T-, and 3T-AQP4-SMALPs did not align with exact sequential additions of the 1T-AQP4-SMALP mass (Figure 4.5 and Table 4.3); M1 and M23 AQP4-SMALPs demonstrated independently linear correlations of increasing particle size, as observed by mass photometry (Figure 4.5); the AQP4-SMALPs retained their size, as shown by mass photometry and SMA-PAGE, after separation by SEC (Figure 4.7 and 4.11); and finally, the 1T, 2T, and void SEC fractions all contained AQP4, as evidenced by SDS-PAGE analysis of

these SEC fractions (Figure 4.10). Together, this evidence strongly supports the interpretation that these AQP4-SMALPs are individual entities, all containing AQP4, as opposed to aggregates of the smallest AQP4-SMALP. Given the known ability of AQP4 to form higher-order oligomers, and the mass intervals between these AQP4-SMALP sizes, these SMALPs were proposed to contain a sequential increase in AQP4 tetramer units.

Olerinyova *et al.* have previously demonstrated how MP-SMALPs can be visualised using mass photometry. They used SMA to solubilise and purify (by affinity chromatography and SEC) the KcsA potassium channel tetramer (80 kDa) expressed in *E. coli*. Mass photometry analysis of different SEC fractions from purification of KcsA-SMALPs revealed a heterogenous mix of different SMALP sizes, particularly in the earlier retention volumes (Olerinyova *et al.*, 2021). They concluded that the ~250 kDa KcsA-SMALP observed was likely to contain a dimer of KcsA homo-tetramers, based on estimated protein-to-lipid ratios, with peaks at ~400 and ~600 kDa potentially representing higher-order KcsA oligomers. Clustering of KcsA homo-tetramers has previously been reported and is thought to play a role *in vivo* (Raja and Vales, 2009; Giudici *et al.*, 2013; Visscher *et al.*, 2017; Renart *et al.*, 2020). Olerinyova *et al.* also observed a mass photometry peak shoulder (to the ~250 kDa peak) of ~125 kDa, concluding that this was a small proportion of empty SMALPs. However, as this sample was representative of IMAC purified His-tagged KcsA, it could instead represent a species of single KcsA homo-tetramers in SMALPs. Contamination of empty SMALPs of this size after IMAC purification is not something that was observed in the work presented here.

Higher-order oligomers in SMALPs have also previously been observed by SMA-PAGE for Sav1866 (an ATP-binding cassette from *Staphylococcus aureus*). Analysis of SEC fractions from purification of Sav1866-SMALPs showed a single dominant band when analysed by SDS-PAGE, but multiple bands when analysed by SMA-PAGE, representing multiple different Sav1866-SMALP sizes (Pollock *et al.*, 2019, 2022). Pollock *et al.* also found that SMA-PAGE outperformed SEC in its ability to resolve Sav1866-SMALPs of different sizes. The same can be reported here, as SMA-PAGE was able to resolve the 3T AQP4-SMALPs, whereas a peak corresponding to this SMALP size was not visible in the AQP4-SMALP SEC UV traces. A contrasting observation was that Pollock *et al.* observed MP-SMALPs migrating via SMA-PAGE to a position representing the MW of the protein complex alone (when compared to protein standard markers). This contrasts with SMA-PAGE analysis of the 1T AQP4-SMALPs here, as they did not migrate to a position representing the weight of an AQP4 tetramer. Instead, they migrated to ~300 kDa. Considering the experimental procedure for SMA-PAGE performed here is very similar to that done by Pollock *et al.* (including the use of NativeMark as protein mass standard), this discrepancy could be attributed to differences in expression

host used for SMA solubilisation, as Pollock *et al.* used *E. coli* for MP production and membrane solubilisation (Pollock *et al.*, 2019). Considering the relatively close agreement of mass estimates between SMA-PAGE, mass photometry, and SEC for APQ4-SMALPs in this study, the observed SMA-PAGE migration distances (and subsequent mass estimates) were thought to be a correct interpretation.

The observations by Olerinyova *et al.* and Pollock *et al.* of multiple SMALP sizes after solubilisation and purification is very similar to that observed here for the AQP4-SMALPs. Their work presents other examples of how an MP known to form higher-order oligomers can create an array of SMALP sizes when solubilised from the expression host membrane. This suggests that AQP4 is not alone in its ability to form higher-order oligomers in SMALPs. Olerinyova *et al.* also analysed unoccupied (or empty) SMALPs consisting only of dimyristoylphosphatidylcholine (DMPC) phospholipids. This produced a mostly homogenous distribution of particle sizes with a mass of ~115 kDa (Olerinyova *et al.*, 2021). They also observed a wide distribution of larger lipid-only SMALP particles (500—2,000 kDa), but not in an ordered pattern of increasing particle size like that seen for KcsA- and AQP4- SMALPs. This further supports the idea that this array of different MP-SMALP sizes is driven by the native oligomeric interactions of these MPs, as opposed to SMA forcing this oligomeric assembly during encapsulation and MP-SMALP formation. However, it is not yet clear if, or how, SMA influences the association or dissociation of the MP higher-order oligomers during solubilisation.

7.5. Ab identification of AQP4 within SMALPs using mass photometry

In Chapter 4, mass photometry was used to identify AQP4 within SMALPs using a commercial anti-AQP4 Ab (Figures 4.18 – 4.21). This Ab was one used routinely by our research group for western blot probing of denatured AQP4, and thus, could probe for AQP4 epitopes on individual monomers. The commercial anti-AQP4 Ab appeared to bind to 1T AQP4-SMALPs with a 1:1 stoichiometry, based on the appearance of a peak at ~440 and ~425 kDa for M1 and M23 AQP4, respectively. With higher Ab concentrations, peaks previously observed at ~585 kDa (M1) and ~565 kDa (M23) for 2T AQP4-SMALPs became more prominent. It is possible that this instead represented a 2:1 stoichiometry of anti-AQP4 Abs binding to the 1T AQP4-SMALP. Incubation of the anti-AQP4 Ab with the 2T SEC fraction (containing 2T and 3T AQP4-SMALPs) revealed a heterogenous mix of particles. At high Ab concentration, there was an emergence of peaks that suggested a 1:1 stoichiometry of anti-AQP4 Ab binding to 2T and 3T AQP4-SMALPs. Whilst this confirmed the presence of AQP4 in these larger SMALPs,

the binding stoichiometries could not confirm the existence of tetramer oligomers. Incubation of the AQP4-SMALPs with an anti-GFP IgG Ab did not result in any visible binding (no observed histogram peak shift), confirming that the binding observed for the anti-AQP4 Ab was unlikely to be a result of non-specific IgG interactions with SMALPs.

A key problem with mass photometry was revealed with these Ab assay experiments. Mass estimates were not always consistent for the same sample before and after incubation with Ab. High sample heterogeneity, such as that seen for the Ab incubations with the 2T AQP4-SMALP SEC fraction, resulted in many histogram peaks with relatively low counts. This resulted in wider Gaussian distributions with higher SDs, and thus, lower confidence in mass estimates (Gaussian means). This clearly demonstrated the negative impact of sample heterogeneity on mass photometry measurements. Trialling higher concentrations of AQP4-SMALPs or Ab, in an attempt to improve resolution of the binding peaks, created an oversaturated image of binding events. Saturation of binding surfaces as a result of high sample concentration causes a noisy ratiometric image and overlapping signals, reducing the accuracy of mass estimation (Kratochvíl *et al.*, 2024).

Nevertheless, mass photometry demonstrated a simple way to identify target membrane proteins within SMALPs in solution using Ab binding assays. This provides an experimental proof-of-principle for further protein-protein interaction assays with MP-SMALPs using mass photometry.

7.6. Mass estimation of AQP4-SMALPs

As discussed, the innate heterogeneity of MP-SMALPs makes their biophysical characterisation difficult. Therefore, it is also difficult to estimate MP-SMALP mass, as measurements must consider weight contribution from proteins, lipids, and SMA. Accurate mass estimation of MP-SMALPs is potentially very useful, as it can provide information about the particle contents. For example, establishing the relative quantities of protein and lipid can give an indication of the importance of lipids associated with certain MPs. It can also give insight into MP oligomeric complexes encapsulated by the SMA. This relationship between protein and lipid is likely to vary for different MPs and also vary for different expression hosts used for solubilisation. This highlights the importance of a simple and accessible measurement strategy for multiple types of MP-SMALPs.

Three methods were explored for estimation of AQP4-SMALP mass in this project. Mass estimates from mass photometry, SEC, and SMA-PAGE were determined and compared with each other (Section 4.6 and Table 4.3). Mass measurement of particles by these methods relies on fundamentally different principles: mass photometry measures the light scattered by single particles, SEC separates particles by hydrodynamic size and, and SMA-PAGE separates particles by electrophoretic mobility through a polyacrylamide gel matrix. Although exact mass estimates varied, there was a general agreement between mass estimation methods for the different AQP4-SMALP sizes observed. In particular, mass photometry and SMA-PAGE estimates were quite similar for the 1T and 2T AQP4-SMALPs. Each method could also distinguish similar mass intervals between the different AQP4-SMALP sizes.

The estimated mass of the M1 and M23 1T AQP4-SMALPs was ~303 and ~288 kDa, respectively (Section 4.6.4; based on all estimation methods). Based on predicted tetramer weights of ~142 and ~132 kDa, this would give a combined lipid and SMA weight of ~161 and ~156 kDa for M1 and M23 1T AQP4-SMALPs, respectively. The estimated mass of the M1 and M23 2T AQP4-SMALPs was ~631 and ~588 kDa, respectively (Section 4.6.4; based on all estimation methods). Considering two AQP4 tetramers, this would give a combined lipid and SMA weight of ~347 and ~324 kDa for M1 and M23 2T AQP4-SMALPs, respectively. This would be equal to ~174 and ~162 kDa per M1 and M23 AQP4 tetramer unit, respectively. These values are quite close to that predicted for the 1T AQP4-SMALPs. Repeating the same calculation for 3T AQP4-SMALPs also gives similar values per tetramer unit (~150 and ~145 kDa for M1 and M23, respectively), certainly within the variability (SD) of mass estimates for these particles. Examples of previous mass estimates based on SV-AUC, native MS, and mass photometry of different MP-SMALPs show varying values for lipid and SMA contribution, highlighting that this relationship is likely dependant on the MP being solubilised (Hellwig *et al.*, 2018; Lee *et al.*, 2019; Olerinyova *et al.*, 2021; Cioccolo *et al.*, 2024).

Size estimates became more variable with increasing SMALP size, as demonstrated by the standard deviation. This could be attributed to greater variation in lipid and SMA mass contributions for larger and more complex AQP4-SMALPs. SEC demonstrated the least reproducible mass estimates. This might be explained by varied performance of the separation column for samples analysed multiple weeks or months apart, resulting in differences in sample retention volumes (and thus, mass estimates). The SEC-trace peak shift between different purification samples in Figure 4.9 may well be an example of this variable column performance, separating what should have been very similar AQP4-SMALP purification samples to slightly inconsistent retention volumes.

An important limitation to consider for all mass estimation methods was the use of soluble protein standards or calibrants to generate mass standard curves. These mass standards are not representative of SMALPs that contain a combination of protein, lipids, and SMA. The light scattering properties of MP-SMALP complexes may be very different from that of soluble proteins when analysed by mass photometry. As such, the standards used may introduce inherent mass error due to molecule density differences to the measured samples. Of course, a set of MP-SMALP mass standards is not an available alternative, and so soluble protein standards are a reasonable choice. Despite this, mass estimates of AQP4-SMALPs from three different methods gave consistent results, suggesting the estimated values may not be far from the real mass.

7.7. hAQP4 higher-order oligomers (OAP formation) in *P. pastoris*

Both M1 and M23 AQP4 demonstrated an array of SMALP sizes when solubilised from the *P. pastoris* membrane. These were proposed to contain an increasing number of tetramer units in increasing SMALP sizes, representing small higher-order oligomers. M1 AQP4 is thought to be unable to form OAPs in the membrane (Furman *et al.*, 2003; Crane, Bennett and Verkman, 2009), thus, the question remained as to why it was able to form higher-order oligomer SMALPs similar to M23 AQP4.

In Chapter 6, BN-PAGE was used to identify the presence of higher-order oligomers of AQP4 in *P. pastoris*, as this technique is well established for investigating the presence of AQP4 tetramers and OAPs (Crane, Bennett and Verkman, 2009; Strand *et al.*, 2009; Rossi, Moritz, *et al.*, 2012; Kitchen *et al.*, 2016). Both M1 and M23 AQP4 presented with higher-order oligomers in *P. pastoris* (Figure 6.2). This contrasted with MDCK cells, a mammalian expression host, in which only M23 AQP4 demonstrated this OAP forming ability (Figure 6.3). This provides an explanation for the observed similarity in SMALP particles for M1 and M23 AQP4, supporting the theory that 2T and 3T AQP4-SMALPs do in fact contain multiple tetramers.

Freeze-thaw samples analysed by BN-PAGE demonstrated retention of higher-order oligomers, perhaps a testament to OAP stability. However, as mentioned, samples had to be separated for chemiluminescence imaging due to higher intensity from the freeze-thaw samples. Slight denaturation of AQP4 after freeze-thawing of the samples may have further revealed epitopes for binding of western blot primary antibodies. There was also a difference in banding pattern for samples when probed with the commercial anti-AQP4 or anti-His Ab.

This could be attributed positional differences of the Ab binding epitopes on the AQP4 tetramer. The exact binding epitope of the commercial anti-AQP4 Ab is propriety, but the anti-His will bind to the C-terminal 6× His-tag. It is possible that binding epitopes for these Abs are more accessible with certain tetrameric assemblies. Interestingly, the freeze-thaw samples probed with the anti-His Ab showed predominant intensity at the top of the gel, suggesting the freeze-thaw process may have affected the accessibility of the C-terminal region of AQP4.

7.8. M1 AQP4 is palmitoylated by *P. pastoris*

Having shown that M1 AQP4 forms higher-order oligomers in *P. pastoris*, in contrast to mammalian constructs, potential reasons for tetramer association were investigated. Suzuki *et al.* proposed that palmitoylation of cysteine 13 and cysteine 17 (Cys13 and Cys17) prevented OAP formation of M1 AQP4. They were able to experimentally determine, using ABE chemistry, that these cysteine residues were palmitoylated when expressed in CHO cells (Suzuki *et al.*, 2008). Carder *et al.* recently used model membranes to demonstrate that, when palmitoylated, M1 AQP4 is able to form a dimer of tetramers, but when de-palmitoylated, could further associate into a trimer of tetramers (Carder *et al.*, 2024). The evidence presented by these studies suggests that palmitoylation plays a key role in OAP regulation. Therefore, the palmitoylation state of M1 AQP4 expressed in *P. pastoris* was investigated, theorising that a lack of palmitoylation may allow M1 AQP4 to associate into higher-order oligomers, as observed by BN-PAGE (Figure 6.2). The ability of *P. pastoris* to *S*-palmitoylate proteins is expected, based on previous research with *S. cerevisiae* and *P. pastoris* (Roth *et al.*, 2006; González Montoro *et al.*, 2011; Lei *et al.*, 2021). However, the ability of *P. pastoris* to palmitoylate recombinant proteins is not well defined and could potentially depend on the protein being expressed.

Using an ABE assay adapted from Lei *et al.* (Lei *et al.*, 2021), M1 AQP4 was found to be palmitoylated by *P. pastoris*, whereas M23 AQP4 was not (Figure 6.6. and 6.7), contrasting with the initial explanation for M1 AQP4 higher-order oligomers proposed here. It is unlikely that this palmitoylation exists on residues other than Cys13 and Cys17, as these are the only cysteines that the M23 isoform lacks (compared to the M1 isoform) and M23 AQP4 does not appear to be palmitoylated. Given the contradiction of *P. pastoris* expressed M1 AQP4 being palmitoylated, yet able to form OAPs (Figure 6.2), it is interesting to speculate possible reasons for this observation.

There was a high intensity of M1 AQP4 observed in the unbound fraction of the ABE assay (FT; Figure 6.5 and 6.6). Potentially, not all of M1 AQP4 was biotinylated by HPDP-biotin, or the capacity of the streptavidin resin may have been reached. However, given the presence of higher-order oligomers, it is possible that *P. pastoris* cannot efficiently palmitoylate M1 AQP4. The native palmitoylation machinery of *P. pastoris* may become saturated with the high quantity of AQP4 produced by over-expression, meaning that not all of the M1 AQP4 produced can be palmitoylated. It may be the case that only one of Cys13 or Cys17 is palmitoylated by *P. pastoris*, which may lower the efficiency of OAP prevention by palmitoylation. It is also important to remember that *S*-palmitoylation is a regulated and reversible PTM (Dietrich and Ungermann, 2004), so M1 AQP4 may be de-palmitoylated by *P. pastoris* in a response to certain culture conditions. Alternatively, conformational irregularities of some of the M1 AQP4 produced may not allow the yeast PATs to access the Cys13 and Cys17 residues in the N-terminus.

It is also possible that, compared to mammalian cells, differing environmental factors in *P. pastoris* cells allow for the formation of M1 AQP4 OAPs. For example, this could be differences in the lipid environment, or lack of molecular chaperones that assist in correct OAP formation or OAP prevention. Rossi *et al.* demonstrated that, in human brain and transfected CHO cells, M23 AQP4 was not able to form OAPs in the Golgi apparatus or ER, only doing so once it reached the cell membrane (Rossi, Baumgart, *et al.*, 2012). They speculated that various environmental differences between the cell membrane and the internal lipid bilayers may be the reason for the difference in observed OAP formation. If *P. pastoris* cannot replicate these environmental differences as in mammalian cells, this may allow M1 AQP4 to prematurely form OAPs in the Golgi and ER, which may lower the efficiency of OAP prevention strategies by mechanisms such as PAT enzyme palmitoylation, allowing for the formation of OAPs in the outer membrane.

7.9. NMO Ab binding to recombinant hAQP4

As SMA solubilisation and purification of AQP4 was potentially encapsulating OAP fragments from the *P. pastoris* membrane, Chapter 5 explored the potential for binding between purified AQP4-SMALPs and recombinant NMO Abs that had been derived from NMOSD patient blood samples. Most NMO Abs have a higher binding affinity for M23 AQP4, thought to be facilitated by the formation of OAPs (Nicchia *et al.*, 2009; Mader *et al.*, 2010; Crane *et al.*, 2011). Thus, it was proposed that NMO Ab binding could be observed for the larger SMALPs that potentially contained oligomers of AQP4 tetramers.

Dot blot assays found that NMO Ab bound preferentially to the SEC void fraction of both the M1 and M23 AQP4-SMALP purification, as well as to AQP4-SMALPs that had only been affinity purified. AQP4-SMALP samples only purified by IMAC represented samples prior to SEC separation, explaining the observed NMO Ab binding. Affinity for the M23 AQP4-SMALP void fraction was significantly greater than for the M1 AQP4-SMALP void fraction (Figure 5.6). This could be explained by a greater tendency for M23 AQP4 to form higher-order oligomers. Although AQP4 concentrations were normalised for dot blot analysis (in Figure 5.5), it is important to note that the M23 AQP4-SMALPs typically presented with a higher proportion in the SEC void than M1 AQP4-SMALPs (Figure 4.10). Binding intensities for the 1T and 2T SEC fraction, containing 1T, 2T, and 3T AQP4-SMALPs, were not significantly different from that observed for control A_{2A}R-SMALPs (Figure 5.5 and 5.6). This suggested that the intensity observed for AQP4-SMALPs was only representative of non-specific binding, rather than recognition of a binding epitope created by one or multiple AQP4 tetramers.

BN-PAGE analysis demonstrated that both M1 and M23 AQP4 were forming higher-order oligomers in *P. pastoris* (Figure 6.2). Therefore, given the apparent ability of SMA to accommodate large MP complexes, it is not unrealistic to think that the SEC void fraction of AQP4-SMALP purification contained large arrays of AQP4 in SMALPs. Multiple studies have demonstrated a higher binding affinity of NMO Abs for AQP4 OAPs (Nicchia *et al.*, 2009; Mader *et al.*, 2010; Crane *et al.*, 2011; Pisani *et al.*, 2011, 2013; Soltys *et al.*, 2019). It is thought that complex combinations of the AQP4 extracellular loops created by OAP formation provide favourable binding epitopes for NMO IgGs (Pisani *et al.*, 2011; Abe and Yasui, 2022; Gupta *et al.*, 2025). If the AQP4-SMALP SEC void fractions contained large arrays of AQP4 in SMALPs, the dot blot analysis shown here would be consistent with these observations by other studies. Mutational studies have shown that NMO Abs bind to epitopes displayed by AQP4 extracellular loops A, C, and E (Pisani *et al.*, 2011; Owens *et al.*, 2015). It has also been demonstrated that patient-derived NMO Abs do not recognise linear peptide forms of these epitopes, showing that 3D conformational structures are required for binding (Owens *et al.*, 2015). This aligns well with the dot blot analysis of denatured AQP4-SMALPs, in which no binding of NMO Abs to denatured AQP4 in the SEC void fraction was observed (Figure 5.2).

Mass photometry assays could not determine binding between NMO Abs and AQP4-SMALPs from the 2T and 1T SEC fractions. Compared to assays with the commercial anti-AQP4 Ab, a peak representing binding between AQP4-SMALPs and an IgG Ab could not be distinguished. This observation is consistent with the dot blot analysis of these SEC fractions. This lack of binding could be because the SMALP encapsulation of the theorised two (2T) and three (3T)

tetramers of AQP4 in SMALPs is not representative of OAP oligomerisation, instead being a forced assembly by SMA. However, considering NMO Abs were able to bind to soluble particles in the void fraction, and both M1 and M23 AQP4 demonstrated the ability to form higher-order oligomers when analysed by BN-PAGE, it is more likely that the affinity of NMO Abs to epitopes created by two and three tetramers is too low to be observed by mass photometry or dot blot analysis. As already discussed, samples cannot be analysed at high concentration by mass photometry. This means that low affinity interactions can be difficult to distinguish. If a binding interaction between AQP4-SMALPs and the NMO Abs was possible, it's possible that the interaction was missed. A clear peak for the NMO Ab was observed for mass photometry binding assays (Figures 5.8 and 5.9), but it's possible that the dissociation constant (K_d) for the NMO Abs is above the nanomolar range that mass photometry allows for.

A key diagnostic pathway for NMOSD is testing for the presence of serum AQP4-IgG Abs in patients (Wingerchuk *et al.*, 1999). This can be a difficult process, sometimes involving single B-cell sorting, NMO IgG cloning, expression, and purification, before testing for anti-AQP4 activity (Huang *et al.*, 2022). Dot blots, such as those shown here, could be the basis for a new diagnostic method. Purified recombinant hAQP4 could be produced to a high quantity and blotted onto membranes to be probed with patient sera. This would involve a long process of optimisation and checking for specificity but would potentially offer a rapid assessment for detection of anti-AQP4 IgGs in patients showing symptoms that are difficult to distinguish from multiple sclerosis.

7.10. Future work

In this project, 2.5% w/v SMA was used exclusively for comparable preparations of M1 and M23 AQP4. It would be interesting to attempt solubilisation of hAQP4 from *P. pastoris* membranes at different SMA concentrations. Lowering SMA concentration could favour the formation of larger AQP4-SMALPs, increasing the proportion, and potentially purification yield, of OAP relevant AQP4-SMALPs. For the same benefit, it would also be interesting to try other SMA copolymer types that favour larger SMALPs, such as SMA 1440 – used for the 1.5 MDa PSI-SMALP (Brady *et al.*, 2019, 2022). DIBMA is an another solubilisation copolymer, known to form larger lipid discs than SMA (Gulamhussein *et al.*, 2020). This is another alternative that could be trialled to capture larger AQP4 OAPs. Comparing AQP4 purifications using these copolymers with AQP4 purifications with traditional detergents, such as DDM, could offer insights into the importance of native lipids for AQP4 tetramers and OAPs.

Interrogating these AQP4-SMALPs with additional biophysical characterisation techniques could further support the observations of this study and potentially confirm the presence of multiple tetramers in the 2T and 3T AQP4-SMALPs. SAXS can provide information on particle size and shape, protein flexibility, morphological dispersity and even low-resolution structural data. Therefore, it could be used for analysis of AQP4-SMALPs to confirm the presence of different tetrameric assemblies, and give some indication as to whether these AQP4-SMALPs are truly discoidal structures. Cryo-EM of isolated 2T and 3T AQP4-SMALPs would also provide interesting comparisons with the data already collected (Figure 7.2). Analysing AQP4-SMALPs by DLS would offer another measure of particle dispersity and hydrodynamic size, thus, it would be interesting to compare this to the FIDA analysis of AQP4-SMALPs (Figure 4.13 and Table 4.2).

Additional mass estimation techniques could be explored to further support the consistency of estimates by mass photometry, SEC, and SMA-PAGE. Size-exclusion chromatography with multi-angle light scattering (SEC-MALS) allows direct measurement of MW during size separation. This has previously been used for MPs in SMALPs and MSP nano-discs (Hesketh *et al.*, 2020; Prabudiansyah, van der Valk and Aubin-Tam, 2021). SV-AUC and native-MS are other viable options that have been used previously for mass estimation of MP-SMALPs (Hellwig *et al.*, 2018; Lee *et al.*, 2019; Cioccolo *et al.*, 2024). It would also be interesting to compare the size of AQP4-SMALPs solubilised and purified from different host expression systems, to determine whether they influence mass contributions from associated lipids.

To further investigate palmitoylation of AQP4 by *P. pastoris*, mutation constructs of the M1 AQP4-pPICZ plasmid could be generated, in which Cys13 and Cys17 residues are mutated to alanine. These plasmid constructs could be used to generate new *P. pastoris* transformants for expression of M1 AQP4 Cys-mutants. The ABE assay could then be repeated to confirm palmitoylation of the expected residues. These cysteine residues could be mutated individually or together, and the effect on formation of higher-order oligomers by M1 AQP4 could be investigated by BN-PAGE. It would also be interesting to analyse the *P. pastoris* membrane fragments by BN-PAGE, rather than the whole lysates. Carder *et al.* were able to “re-palmitoylate” M1 AQP4 with 1-decyl-maleimide after cleaving palmitic acid with hydroxylamine (Carder *et al.*, 2024). A similar approach could be used here to ensure that all the M1 AQP4 expressed by *P. pastoris* is palmitoylated and observe the effect this has on formation of higher-order oligomers. If OAP formation by M1 AQP4 in *P. pastoris* can be prevented, SMA solubilisation and purification could be repeated to observe the impact on AQP4-SMALP sizes. This could confirm whether the array of AQP4-SMALP sizes is dependent on AQP4 oligomerisation or forced assembly by SMA encapsulation.

A very recent study used cryo-EM to structurally determine the binding of patient-derived NMO Ab Fab fragments to AQP4. This AQP4 had been recombinantly expressed in *P. pastoris*, solubilised with detergent, and reconstituted in to MSP nanodiscs (Gupta *et al.*, 2025). In cell-based assays, patient-derived NMO Ab Fab fragments have previously demonstrated similar binding affinities to AQP4 when compared with their divalent IgG counterparts (Crane *et al.*, 2011). It would be interesting to repeat mass photometry binding assays of AQP4-SMALPs with Fab fragments generated from the NMO Abs. It is possible that steric hinderance caused by the SMALPs may have hindered binding of the NMO IgGs. Removing the Fc region of the NMO IgGs might allow better access to the AQP4 epitopes in AQP4-SMALPs. It would also be interesting to use fluorescence microscopy or flow cytometry to investigate binding of NMO Abs to the cell membrane of *P. pastoris* AQP4 clones. This could provide insight into the oligomerisation of AQP4 tetramers in the yeast cell membrane.

7.11. Conclusion

This project used SMA to solubilise and purify M1 and M23 isoforms of AQP4 from *P. pastoris*. The resulting AQP4-SMALPs appeared to demonstrate different tetrameric assemblies of AQP4, potentially representing small OAP fragments. NMO Abs bound preferentially to purification fractions of M1 and M23 AQP4-SMALPs predicted to contain large arrays of AQP4. Although BN-PAGE analysis confirmed the presence of higher-order oligomers for both AQP4 isoforms, M1 AQP4 was found to be palmitoylated by *P. pastoris*, as observed in mammalian expression systems. A low degree of M1 AQP4 palmitoylation by *P. pastoris* may be an explanation for the observed tetrameric oligomerisation and requires further investigation.

Many questions remain about the exact physiological roles of AQP4 OAPs and the influence of NMO Ab binding on their dynamics (Nagelhus and Ottersen, 2013; Verkman *et al.*, 2013; Salman *et al.*, 2022), highlighting the need for further model systems for OAP investigation. This project has further demonstrated the suitability of *P. pastoris* as a heterologous expression system for hAQP4. There are a variety of options for future work to further support these findings and further utilise *P. pastoris* as a model system for investigating AQP4 in relation to OAPs and NMOSD.

References

Abe, Y. and Yasui, M. (2022) 'Aquaporin-4 in Neuromyelitis Optica Spectrum Disorders: A Target of Autoimmunity in the Central Nervous System', *Biomolecules*, 12(4), p. 591. Available at: https://doi.org/10.3390/biom12040591.

Agre, P., King, L.S., Yasui, M., Guggino, W.B., Ottersen, O.P., Fujiyoshi, Y., Engel, A. and Nielsen, S. (2002) 'Aquaporin water channels – from atomic structure to clinical medicine', *The Journal of Physiology*, 542(1), pp. 3–16. Available at: https://doi.org/10.1113/jphysiol.2002.020818.

Ahmad, M., Hirz, M., Pichler, H. and Schwab, H. (2014) 'Protein expression in Pichia pastoris: recent achievements and perspectives for heterologous protein production', *Applied Microbiology and Biotechnology*, 98(12), pp. 5301–5317. Available at: https://doi.org/10.1007/s00253-014-5732-5.

Akram, A., Hadasha, W., Kuyler, G.C., Smith, M.-P., Bailey-Dallaway, S., Preedy, A., Browne, C., Broadbent, L., Hill, A., Javaid, T., Nazar, H., Samra, N., Naveed, A., Tregunna, H., Joshi, H., Akhtar, N., Javed, A., Bowater, J., Ravenhill, J., Hajdu, P., Ali, Y., Tailor, Y., Mumtaz, S., Hamza, M., Gill, K., Gillett, J., Patton, F., Arshid, H., Zaheer, M., Qureshi, H., Edwards, I., Patel, S., Azadi, A., Pollock, N., Kitchen, P., Klumperman, B. and Rothnie, A.J. (2025) 'Solubilisation & purification of membrane proteins using benzylamine-modified SMA polymers', *Biophysical Chemistry*, 316, p. 107343. Available at: https://doi.org/10.1016/j.bpc.2024.107343.

Alexandrov, A.I., Mileni, M., Chien, E.Y.T., Hanson, M.A. and Stevens, R.C. (2008) 'Microscale fluorescent thermal stability assay for membrane proteins', *Structure (London, England: 1993)*, 16(3), pp. 351–359. Available at: https://doi.org/10.1016/j.str.2008.02.004.

Al-Jubair, T., Steffen, J.H., Missel, J.W., Kitchen, P., Salman, M.M., Bill, R.M., Gourdon, P. and Törnroth-Horsefield, S. (2022) 'High-yield overproduction and purification of human aquaporins from *Pichia pastoris*', *STAR Protocols*, 3(2), p. 101298. Available at: https://doi.org/10.1016/j.xpro.2022.101298.

Almén, M.S., Nordström, K.J., Fredriksson, R. and Schiöth, H.B. (2009) 'Mapping the human membrane proteome: a majority of the human membrane proteins can be classified according to function and evolutionary origin', *BMC Biology*, 7, p. 50. Available at: https://doi.org/10.1186/1741-7007-7-50.

Amiry-Moghaddam, M., Frydenlund, D.S. and Ottersen, O.P. (2004) 'Anchoring of aquaporin-4 in brain: Molecular mechanisms and implications for the physiology and pathophysiology of water transport', *Neuroscience*, 129(4), pp. 997–1008. Available at: https://doi.org/10.1016/j.neuroscience.2004.08.049.

Amiry-Moghaddam, M., Otsuka, T., Hurn, P.D., Traystman, R.J., Haug, F.-M., Froehner, S.C., Adams, M.E., Neely, J.D., Agre, P., Ottersen, O.P. and Bhardwaj, A. (2003) 'An alpha-syntrophin-dependent pool of AQP4 in astroglial end-feet confers bidirectional water flow between blood and brain', *Proceedings of the National Academy of Sciences of the United States of America*, 100(4), pp. 2106–2111. Available at: https://doi.org/10.1073/pnas.0437946100.

Ansell, T.B., Song, W., Coupland, C.E., Carrique, L., Corey, R.A., Duncan, A.L., Cassidy, C.K., Geurts, M.M.G., Rasmussen, T., Ward, A.B., Siebold, C., Stansfeld, P.J. and Sansom, M.S.P. (2023) 'LipIDens: simulation assisted interpretation of lipid densities in cryo-EM

structures of membrane proteins', *Nature Communications*, 14(1), p. 7774. Available at: https://doi.org/10.1038/s41467-023-43392-y.

Asor, R. and Kukura, P. (2022) 'Characterising biomolecular interactions and dynamics with mass photometry', *Current Opinion in Chemical Biology*, 68, p. 102132. Available at: https://doi.org/10.1016/j.cbpa.2022.102132.

Asor, R., Loewenthal, D., Wee, R. van, Benesch, J.L.P. and Kukura, P. (2025) 'Mass Photometry', *Annual Review of Biophysics*, 54(Volume 54, 2025), pp. 379–399. Available at: https://doi.org/10.1146/annurev-biophys-061824-111652.

Athmaram, T.N., Saraswat, S., Singh, A.K., Rao, M.K., Gopalan, N., Suryanarayana, V.V.S. and Rao, P.V.L. (2012) 'Influence of copy number on the expression levels of pandemic influenza hemagglutinin recombinant protein in methylotrophic yeast Pichia pastoris', *Virus Genes*, 45(3), pp. 440–451. Available at: https://doi.org/10.1007/s11262-012-0809-7.

Aw, R. and Polizzi, K.M. (2013) 'Can too many copies spoil the broth?', *Microbial Cell Factories*, 12(1), p. 128. Available at: https://doi.org/10.1186/1475-2859-12-128.

Ayub, H., Clare, M., Broadbent, L., Simms, J., Goddard, A.D., Rothnie, A.J. and Bill, R.M. (2022) 'Membrane Protein Production in the Yeast *Pichia pastoris*', in I. Mus-Veteau (ed.) *Heterologous Expression of Membrane Proteins: Methods and Protocols*. New York, NY: Springer US, pp. 187–199. Available at: https://doi.org/10.1007/978-1-0716-2368-8_10.

Azad, A.K., Raihan, T., Ahmed, J., Hakim, A., Emon, T.H. and Chowdhury, P.A. (2021) 'Human Aquaporins: Functional Diversity and Potential Roles in Infectious and Non-infectious Diseases', *Frontiers in Genetics*, 12, p. 654865. Available at: https://doi.org/10.3389/fgene.2021.654865.

Balakrishnan, S., Adolph, M., Tsai, M.-S., Akizuki, T., Gallagher, K., Cortez, D. and Chazin, W.J. (2024) 'Structure of RADX and mechanism for regulation of RAD51 nucleofilaments', *Proceedings of the National Academy of Sciences*, 121(12), p. e2316491121. Available at: https://doi.org/10.1073/pnas.2316491121.

Bartels, D.J., Mitchell, D.A., Dong, X. and Deschenes, R.J. (1999) 'Erf2, a Novel Gene Product That Affects the Localization and Palmitoylation of Ras2 in Saccharomyces cerevisiae', *Molecular and Cellular Biology*, 19(10), pp. 6775–6787. Available at: https://doi.org/10.1128/MCB.19.10.6775.

Bawa, Z. (2014) *Improving recombinant human adenosine A2A receptor production in yeast*. phd. Aston University. Available at: https://publications.aston.ac.uk/id/eprint/23176/ (Accessed: 4 September 2025).

Bayburt, T.H., Grinkova, Y.V. and Sligar, S.G. (2002) 'Self-Assembly of Discoidal Phospholipid Bilayer Nanoparticles with Membrane Scaffold Proteins', *Nano Letters*, 2(8), pp. 853–856. Available at: https://doi.org/10.1021/nl025623k.

de Bellis, M., Cibelli, A., Mola, M.G., Pisani, F., Barile, B., Mastrodonato, M., Banitalebi, S., Amiry-Moghaddam, M., Abbrescia, P., Frigeri, A., Svelto, M. and Nicchia, G.P. (2021) 'Orthogonal arrays of particle assembly are essential for normal aquaporin-4 expression level in the brain', *Glia*, 69(2), pp. 473–488. Available at: https://doi.org/10.1002/glia.23909.

Belmaati Cherkaoui, M., Vacca, O., Izabelle, C., Boulay, A.-C., Boulogne, C., Gillet, C., Barnier, J.-V., Rendon, A., Cohen-Salmon, M. and Vaillend, C. (2021) 'Dp71 contribution to

the molecular scaffold anchoring aquaporine-4 channels in brain macroglial cells', *Glia*, 69(4), pp. 954–970. Available at: https://doi.org/10.1002/glia.23941.

Bennett, J.L., Lam, C., Kalluri, S.R., Saikali, P., Bautista, K., Dupree, C., Glogowska, M., Case, D., Antel, J.P., Owens, G.P., Gilden, D., Nessler, S., Stadelmann, C. and Hemmer, B. (2009) 'Intrathecal pathogenic anti–aquaporin-4 antibodies in early neuromyelitis optica', *Annals of Neurology*, 66(5), pp. 617–629. Available at: https://doi.org/10.1002/ana.21802.

Berman, H.M., Westbrook, J., Feng, Z., Gilliland, G., Bhat, T.N., Weissig, H., Shindyalov, I.N. and Bourne, P.E. (2000) 'The Protein Data Bank', *Nucleic Acids Research*, 28(1), pp. 235–242. Available at: https://doi.org/10.1093/nar/28.1.235.

Betancur, M.O., Reis, V.C.B., Nicola, A.M., De Marco, J.L., de Moraes, L.M.P. and Torres, F.A.G. (2017) 'Multicopy plasmid integration in Komagataella phaffii mediated by a defective auxotrophic marker', *Microbial Cell Factories*, 16(1), p. 99. Available at: https://doi.org/10.1186/s12934-017-0715-8.

Bill, R.M. (2014) 'Playing catch-up with Escherichia coli: using yeast to increase success rates in recombinant protein production experiments', *Frontiers in Microbiology*, 5. Available at: https://doi.org/10.3389/fmicb.2014.00085.

Bill, R.M. and Hedfalk, K. (2021) 'Aquaporins – Expression, purification and characterization', *Biochimica et Biophysica Acta (BBA) - Biomembranes*, 1863(9), p. 183650. Available at: https://doi.org/10.1016/j.bbamem.2021.183650.

Bittrich, S., Rose, Y., Segura, J., Lowe, R., Westbrook, J.D., Duarte, J.M. and Burley, S.K. (2022) 'RCSB Protein Data Bank: improved annotation, search and visualization of membrane protein structures archived in the PDB', *Bioinformatics*, 38(5), pp. 1452–1454. Available at: https://doi.org/10.1093/bioinformatics/btab813.

Blaskovic, S., Blanc, M. and van der Goot, F.G. (2013) 'What does S-palmitoylation do to membrane proteins?', *The FEBS Journal*, 280(12), pp. 2766–2774. Available at: https://doi.org/10.1111/febs.12263.

Bobalova, J., Strouhalova, D. and Bobal, P. (2023) 'Common Post-translational Modifications (PTMs) of Proteins: Analysis by Up-to-Date Analytical Techniques with an Emphasis on Barley', *Journal of Agricultural and Food Chemistry*, 71(41), pp. 14825–14837. Available at: https://doi.org/10.1021/acs.jafc.3c00886.

Bowie, J.U. (2001) 'Stabilizing membrane proteins', *Current Opinion in Structural Biology*, 11(4), pp. 397–402. Available at: https://doi.org/10.1016/S0959-440X(00)00223-2.

Brady, N.G., Li, M., Ma, Y., Gumbart, J.C. and Bruce, B.D. (2019) 'Non-detergent isolation of a cyanobacterial photosystem I using styrene maleic acid alternating copolymers', *RSC Advances*, 9(54), pp. 31781–31796. Available at: https://doi.org/10.1039/C9RA04619D.

Brady, N.G., Qian, S. and Bruce, B.D. (2019) 'Analysis of styrene maleic acid alternating copolymer supramolecular assemblies in solution by small angle X-ray scattering', *European Polymer Journal*, 111, pp. 178–184. Available at: https://doi.org/10.1016/j.eurpolymj.2018.11.034.

Brady, N.G., Qian, S., Nguyen, J., O'Neill, H.M. and Bruce, B.D. (2022) 'Small angle neutron scattering and lipidomic analysis of a native, trimeric PSI-SMALP from a thermophilic cyanobacteria', *Biochimica et Biophysica Acta (BBA) - Bioenergetics*, 1863(7), p. 148596. Available at: https://doi.org/10.1016/j.bbabio.2022.148596.

Brady, N.G., Workman, C.E., Cawthon, B., Bruce, B.D. and Long, B.K. (2021) 'Protein Extraction Efficiency and Selectivity of Esterified Styrene–Maleic Acid Copolymers in Thylakoid Membranes', *Biomacromolecules*, 22(6), pp. 2544–2553. Available at: https://doi.org/10.1021/acs.biomac.1c00274.

van den Brink-van der Laan, E., Chupin, V., Killian, J.A. and de Kruijff, B. (2004) 'Stability of KcsA Tetramer Depends on Membrane Lateral Pressure', *Biochemistry*, 43(14), pp. 4240–4250. Available at: https://doi.org/10.1021/bi036129d.

Broadbent, L., Depping, P., Lodé, A., Vaitsopoulou, A., Hardy, D., Ayub, H., Mitchell-White, J., Kerr, I.D., Goddard, A.D., Bill, R.M. and Rothnie, A.J. (2022) 'Detergent-Free Membrane Protein Purification Using SMA Polymer', in I. Mus-Veteau (ed.) *Heterologous Expression of Membrane Proteins: Methods and Protocols*. New York, NY: Springer US, pp. 389–404. Available at: https://doi.org/10.1007/978-1-0716-2368-8_21.

Broecker, J., Eger, B.T. and Ernst, O.P. (2017) 'Crystallogenesis of Membrane Proteins Mediated by Polymer-Bounded Lipid Nanodiscs', *Structure*, 25(2), pp. 384–392. Available at: https://doi.org/10.1016/j.str.2016.12.004.

Brooks, C.L., Morrison, M. and Joanne Lemieux, M. (2013) 'Rapid expression screening of eukaryotic membrane proteins in Pichia pastoris', *Protein Science*, 22(4), pp. 425–433. Available at: https://doi.org/10.1002/pro.2223.

Burfeind, K.G., Murchison, C.F., Westaway, S.K., Simon, M.J., Erten-Lyons, D., Kaye, J.A., Quinn, J.F. and Iliff, J.J. (2017) 'The effects of noncoding aquaporin-4 single-nucleotide polymorphisms on cognition and functional progression of Alzheimer's disease', *Alzheimer's & Dementia : Translational Research & Clinical Interventions*, 3(3), pp. 348–359. Available at: https://doi.org/10.1016/j.trci.2017.05.001.

Byrne, B. (2015) '*Pichia pastoris* as an expression host for membrane protein structural biology', *Current Opinion in Structural Biology*, 32, pp. 9–17. Available at: https://doi.org/10.1016/j.sbi.2015.01.005.

Carder, J.D., Barile, B., Shisler, K.A., Pisani, F., Frigeri, A., Hipps, K.W., Nicchia, G.P. and Brozik, J.A. (2024) 'Thermodynamics and S-palmitoylation dependence of interactions between human aquaporin-4 M1 tetramers in model membranes', *The Journal of Physical Chemistry B*, 128(3), pp. 603–621. Available at: https://doi.org/10.1021/acs.jpcb.3c04529.

Cereghino, G.P.L., Cereghino, J.L., Ilgen, C. and Cregg, J.M. (2002) 'Production of recombinant proteins in fermenter cultures of the yeast *Pichia pastoris*', *Current Opinion in Biotechnology*, 13(4), pp. 329–332. Available at: https://doi.org/10.1016/S0958-1669(02)00330-0.

Chandra, A., Farrell, C., Wilson, H., Dervenoulas, G., De Natale, E.R., Politis, M., and Alzheimer's Disease Neuroimaging Initiative (2021) 'Aquaporin-4 polymorphisms predict amyloid burden and clinical outcome in the Alzheimer's disease spectrum', *Neurobiology of Aging*, 97, pp. 1–9. Available at: https://doi.org/10.1016/j.neurobiolaging.2020.06.007.

Chen, Y., Li, Y., Liu, P., Sun, Q. and Liu, Z. (2014) 'Optimized expression in Pichia pastoris eliminates common protein contaminants from subsequent His-tag purification', *Biotechnology Letters*, 36(4), pp. 711–718. Available at: https://doi.org/10.1007/s10529-013-1411-3.

Choy, B.C., Cater, R.J., Mancia, F. and Pryor, E.E. (2021) 'A 10-year meta-analysis of membrane protein structural biology: Detergents, membrane mimetics, and structure

determination techniques', *Biochimica et Biophysica Acta (BBA) - Biomembranes*, 1863(3), p. 183533. Available at: https://doi.org/10.1016/j.bbamem.2020.183533.

Chytła, A., Gajdzik-Nowak, W., Biernatowska, A., Sikorski, A.F. and Czogalla, A. (2021) 'High-Level Expression of Palmitoylated MPP1 Recombinant Protein in Mammalian Cells', *Membranes*, 11(9), p. 715. Available at: https://doi.org/10.3390/membranes11090715.

Ciappelloni, S., Bouchet, D., Dubourdieu, N., Boué-Grabot, E., Kellermayer, B., Manso, C., Marignier, R., Oliet, S.H.R., Tourdias, T. and Groc, L. (2019) 'Aquaporin-4 Surface Trafficking Regulates Astrocytic Process Motility and Synaptic Activity in Health and Autoimmune Disease', *Cell Reports*, 27(13), pp. 3860-3872.e4. Available at: https://doi.org/10.1016/j.celrep.2019.05.097.

Cioccolo, S., Barritt, J.D., Pollock, N., Hall, Z., Babuta, J., Sridhar, P., Just, A., Morgner, N., Dafforn, T., Gould, I. and Byrne, B. (2024) 'The mycobacterium lipid transporter MmpL3 is dimeric in detergent solution, SMALPs and reconstituted nanodiscs', *RSC Chemical Biology*, 5(9), pp. 901–913. Available at: https://doi.org/10.1039/D4CB00110A.

Company-Marín, I. (2024) *The Effect of Lipid Oxidation on the Activity of the Membrane Protein Adenosine 2A Receptor*. phd. Aston University. Available at: https://publications.aston.ac.uk/id/eprint/47170/ (Accessed: 4 September 2025).

Craig, A.F., Clark, E.E., Sahu, I.D., Zhang, R., Frantz, N.D., Al-Abdul-Wahid, M.S., Dabney-Smith, C., Konkolewicz, D. and Lorigan, G.A. (2016) 'Tuning the size of styrene-maleic acid copolymer-lipid nanoparticles (SMALPs) using RAFT polymerization for biophysical studies', *Biochimica et Biophysica Acta (BBA) - Biomembranes*, 1858(11), pp. 2931–2939. Available at: https://doi.org/10.1016/j.bbamem.2016.08.004.

Crane, J.M., Bennett, J.L. and Verkman, A.S. (2009) 'Live Cell Analysis of Aquaporin-4 M1/M23 Interactions and Regulated Orthogonal Array Assembly in Glial Cells', *Journal of Biological Chemistry*, 284(51), pp. 35850–35860. Available at: https://doi.org/10.1074/jbc.M109.071670.

Crane, J.M., Lam, C., Rossi, A., Gupta, T., Bennett, J.L. and Verkman, A.S. (2011) 'Binding Affinity and Specificity of Neuromyelitis Optica Autoantibodies to Aquaporin-4 M1/M23 Isoforms and Orthogonal Arrays', *Journal of Biological Chemistry*, 286(18), pp. 16516–16524. Available at: https://doi.org/10.1074/jbc.M111.227298.

Crane, J.M., Tajima, M. and Verkman, A.S. (2010) 'Live-cell imaging of aquaporin-4 diffusion and interactions in orthogonal arrays of particles', *Neuroscience*, 168(4), pp. 892–902. Available at: https://doi.org/10.1016/j.neuroscience.2009.08.034.

Crane, J.M. and Verkman, A.S. (2009) 'Determinants of aquaporin-4 assembly in orthogonal arrays revealed by live-cell single-molecule fluorescence imaging', *Journal of Cell Science*, 122(6), pp. 813–821. Available at: https://doi.org/10.1242/jcs.042341.

Cregg, J.M., Barringer, K.J., Hessler, A.Y. and Madden, K.R. (1985) 'Pichia pastoris as a host system for transformations.', *Molecular and Cellular Biology*, 5(12), pp. 3376–3385. Available at: https://doi.org/10.1128/mcb.5.12.3376.

Cui, Y. and Bastien, D.A. (2011) 'Water transport in human aquaporin-4: Molecular dynamics (MD) simulations', *Biochemical and Biophysical Research Communications*, 412(4), pp. 654–659. Available at: https://doi.org/10.1016/j.bbrc.2011.08.019.

Daly, R. and Hearn, M.T.W. (2005) ‘Expression of heterologous proteins in Pichia pastoris: a useful experimental tool in protein engineering and production’, *Journal of Molecular Recognition*, 18(2), pp. 119–138. Available at: https://doi.org/10.1002/jmr.687.

Damato, V., Theorell, J., Al-Diwani, A., Kienzler, A.-K., Makuch, M., Sun, B., Handel, A., Akdeniz, D., Berretta, A., Ramanathan, S., Fower, A., Whittam, D., Gibbons, E., McGlashan, N., Green, E., Huda, S., Woodhall, M., Palace, J., Sheerin, F., Waters, P., Leite, M.I., Jacob, A. and Irani, S.R. (2022) ‘Rituximab abrogates aquaporin-4–specific germinal center activity in patients with neuromyelitis optica spectrum disorders’, *Proceedings of the National Academy of Sciences*, 119(24), p. e2121804119. Available at: https://doi.org/10.1073/pnas.2121804119.

Darby, R.A.J., Cartwright, S.P., Dilworth, M.V. and Bill, R.M. (2012) ‘Which Yeast Species Shall I Choose? Saccharomyces cerevisiae Versus Pichia pastoris (Review)’, in R.M. Bill (ed.) *Recombinant Protein Production in Yeast: Methods and Protocols*. Totowa, NJ: Humana Press, pp. 11–23. Available at: https://doi.org/10.1007/978-1-61779-770-5_2.

Dawaliby, R., Trubbia, C., Delporte, C., Masureel, M., Van Antwerpen, P., Kobilka, B.K. and Govaerts, C. (2016) ‘Allosteric regulation of G protein–coupled receptor activity by phospholipids’, *Nature Chemical Biology*, 12(1), pp. 35–39. Available at: https://doi.org/10.1038/nchembio.1960.

Delandre, C., Penabaz, T.R., Passarelli, A.L., Chapes, S.K. and Clem, R.J. (2009) ‘Mutation of juxtamembrane cysteines in the tetraspanin CD81 affects palmitoylation and alters interaction with other proteins at the cell surface’, *Experimental Cell Research*, 315(11), pp. 1953–1963. Available at: https://doi.org/10.1016/j.yexcr.2009.03.013.

Denisov, I.G. and Sligar, S.G. (2016) ‘Nanodiscs for structural and functional studies of membrane proteins’, *Nature Structural & Molecular Biology*, 23(6), pp. 481–486. Available at: https://doi.org/10.1038/nsmb.3195.

Dietrich, L.E.P. and Ungermann, C. (2004) ‘On the mechanism of protein palmitoylation’, *EMBO reports*, 5(11), pp. 1053–1057. Available at: https://doi.org/10.1038/sj.embor.7400277.

Dominguez Pardo, Juan J., Dörr, J.M., Iyer, A., Cox, R.C., Scheidelaar, S., Koorengevel, M.C., Subramaniam, V. and Killian, J.A. (2017) ‘Solubilization of lipids and lipid phases by the styrene–maleic acid copolymer’, *European Biophysics Journal*, 46(1), pp. 91–101. Available at: https://doi.org/10.1007/s00249-016-1181-7.

Dominguez Pardo, J. J., Dörr, J.M., Renne, M.F., Ould-Braham, T., Koorengevel, M.C., van Steenbergen, M.J. and Killian, J.A. (2017) ‘Thermotropic properties of phosphatidylcholine nanodiscs bounded by styrene-maleic acid copolymers’, *Chemistry and Physics of Lipids*, 208, pp. 58–64. Available at: https://doi.org/10.1016/j.chemphyslip.2017.08.010.

Dörr, J.M., Koorengevel, M.C., Schäfer, M., Prokofyev, A.V., Scheidelaar, S., van der Cruijsen, E.A.W., Dafforn, T.R., Baldus, M. and Killian, J.A. (2014) ‘Detergent-free isolation, characterization, and functional reconstitution of a tetrameric K+ channel: The power of native nanodiscs’, *Proceedings of the National Academy of Sciences*, 111(52), pp. 18607–18612. Available at: https://doi.org/10.1073/pnas.1416205112.

Dörr, J.M., Scheidelaar, S., Koorengevel, M.C., Dominguez, J.J., Schäfer, M., van Walree, C.A. and Killian, J.A. (2016) ‘The styrene-maleic acid copolymer: a versatile tool in membrane research’, *European biophysics journal: EBJ*, 45(1), pp. 3–21. Available at: https://doi.org/10.1007/s00249-015-1093-y.

Drisdel, R.C., Alexander, J.K., Sayeed, A. and Green, W.N. (2006) 'Assays of protein palmitoylation', *Methods*, 40(2), pp. 127–134. Available at: https://doi.org/10.1016/j.ymeth.2006.04.015.

Edmonds, M.J., Geary, B., Doherty, M.K. and Morgan, A. (2017) 'Analysis of the brain palmitoyl-proteome using both acyl-biotin exchange and acyl-resin-assisted capture methods', *Scientific Reports*, 7(1), p. 3299. Available at: https://doi.org/10.1038/s41598-017-03562-7.

Fagerberg, L., Jonasson, K., Von Heijne, G., Uhlén, M. and Berglund, L. (2010) 'Prediction of the human membrane proteome', *PROTEOMICS*, 10(6), pp. 1141–1149. Available at: https://doi.org/10.1002/pmic.200900258.

Fidabio (2025) *PDI: Polydispersity Index*, *Fidabio*. Available at: https://www.fidabio.com/knowledge-subcategory/pdi-polydispersity-index (Accessed: 12 September 2025).

Foley, E.D.B., Kushwah, M.S., Young, G. and Kukura, P. (2021) 'Mass photometry enables label-free tracking and mass measurement of single proteins on lipid bilayers', *Nature Methods*, 18(10), pp. 1247–1252. Available at: https://doi.org/10.1038/s41592-021-01261-w.

Fu, D. and Lu, M. (2007) 'The structural basis of water permeation and proton exclusion in aquaporins (Review)', *Molecular Membrane Biology*, 24(5–6), pp. 366–374. Available at: https://doi.org/10.1080/09687680701446965.

Furman, C.S., Gorelick-Feldman, D.A., Davidson, K.G.V., Yasumura, T., Neely, J.D., Agre, P. and Rash, J.E. (2003) 'Aquaporin-4 square array assembly: Opposing actions of M1 and M23 isoforms', *Proceedings of the National Academy of Sciences of the United States of America*, 100(23), pp. 13609–13614. Available at: https://doi.org/10.1073/pnas.2235843100.

Ginsberg, N.S., Hsieh, C.-L., Kukura, P., Piliarik, M. and Sandoghdar, V. (2025) 'Interferometric scattering microscopy', *Nature Reviews Methods Primers*, 5(1), p. 23. Available at: https://doi.org/10.1038/s43586-025-00391-1.

Giudici, A.M., Molina, M.L., Ayala, J.L., Montoya, E., Renart, M.L., Fernández, A.M., Encinar, J.A., Ferrer-Montiel, A.V., Poveda, J.A. and González-Ros, J.M. (2013) 'Detergent-labile, supramolecular assemblies of KcsA: Relative abundance and interactions involved', *Biochimica et Biophysica Acta (BBA) - Biomembranes*, 1828(2), pp. 193–200. Available at: https://doi.org/10.1016/j.bbamem.2012.09.020.

Gomes, D., Agasse, A., Thiébaud, P., Delrot, S., Gerós, H. and Chaumont, F. (2009) 'Aquaporins are multifunctional water and solute transporters highly divergent in living organisms', *Biochimica et Biophysica Acta (BBA) - Biomembranes*, 1788(6), pp. 1213–1228. Available at: https://doi.org/10.1016/j.bbamem.2009.03.009.

González Montoro, A., Chumpen Ramirez, S., Quiroga, R. and Valdez Taubas, J. (2011) 'Specificity of Transmembrane Protein Palmitoylation in Yeast', *PLoS ONE*, 6(2), p. e16969. Available at: https://doi.org/10.1371/journal.pone.0016969.

Greaves, J. and Chamberlain, L.H. (2007) 'Palmitoylation-dependent protein sorting', *The Journal of Cell Biology*, 176(3), pp. 249–254. Available at: https://doi.org/10.1083/jcb.200610151.

Grethen, A., Oluwole, A.O., Danielczak, B., Vargas, C. and Keller, S. (2017) 'Thermodynamics of nanodisc formation mediated by styrene/maleic acid (2:1) copolymer', *Scientific reports*, 7(1), p. 11517. Available at: https://doi.org/10.1038/s41598-017-11616-z.

Grime, R.L., Logan, R.T., Nestorow, S.A., Sridhar, P., Edwards, P.C., Tate, C.G., Klumperman, B., Dafforn, T.R., Poyner, D.R., Reeves, P.J. and Wheatley, M. (2021) 'Differences in SMA-like polymer architecture dictate the conformational changes exhibited by the membrane protein rhodopsin encapsulated in lipid nano-particles', *Nanoscale*, 13(31), pp. 13519–13528. Available at: https://doi.org/10.1039/D1NR02419A.

Guan, X. and Fierke, C.A. (2011) 'Understanding protein palmitoylation: Biological significance and enzymology', *Science China Chemistry*, 54(12), pp. 1888–1897. Available at: https://doi.org/10.1007/s11426-011-4428-2.

Gulamhussein, A.A., Meah, D., Soja, D.D., Fenner, S., Saidani, Z., Akram, A., Lallie, S., Mathews, A., Painter, C., Liddar, M.K., Mohammed, Z., Chiu, L.K., Sumar, S.S., Healy, H., Hussain, N., Patel, J.H., Hall, S.C.L., Dafforn, T.R. and Rothnie, A.J. (2019) 'Examining the stability of membrane proteins within SMALPs', *European Polymer Journal*, 112, pp. 120–125. Available at: https://doi.org/10.1016/j.eurpolymj.2018.12.008.

Gulamhussein, A.A., Uddin, R., Tighe, B.J., Poyner, D.R. and Rothnie, A.J. (2020) 'A comparison of SMA (styrene maleic acid) and DIBMA (di-isobutylene maleic acid) for membrane protein purification', *Biochimica et Biophysica Acta (BBA) - Biomembranes*, 1862(7), p. 183281. Available at: https://doi.org/10.1016/j.bbamem.2020.183281.

Gulati, S., Jamshad, M., Knowles, T.J., Morrison, K.A., Downing, R., Cant, N., Collins, R., Koenderink, J.B., Ford, R.C., Overduin, M., Kerr, I.D., Dafforn, T.R. and Rothnie, A.J. (2014) 'Detergent-free purification of ABC (ATP-binding-cassette) transporters', *Biochemical Journal*, 461(2), pp. 269–278. Available at: https://doi.org/10.1042/BJ20131477.

Gupta, M., Khandelwal, N.K., Nelson, A., Hwang, P., Pourmal, S., Bennett, J.L. and Stroud, R.M. (2025) 'Structural basis of aquaporin-4 autoantibody binding in neuromyelitis optica', *Science Advances*, 11(8), p. eadq7560. Available at: https://doi.org/10.1126/sciadv.adq7560.

Hall, S.C.L., Tognoloni, C., Price, G.J., Klumperman, B., Edler, K.J., Dafforn, T.R. and Arnold, T. (2018) 'Influence of Poly(styrene-co-maleic acid) Copolymer Structure on the Properties and Self-Assembly of SMALP Nanodiscs', *Biomacromolecules*, 19(3), pp. 761–772. Available at: https://doi.org/10.1021/acs.biomac.7b01539.

Halsey, A.M., Conner, A.C., Bill, R.M., Logan, A. and Ahmed, Z. (2018) 'Aquaporins and Their Regulation after Spinal Cord Injury', *Cells*, 7(10), p. 174. Available at: https://doi.org/10.3390/cells7100174.

Hasegawa, H., Ma, T., Skach, W., Matthay, M.A. and Verkman, A.S. (1994) 'Molecular cloning of a mercurial-insensitive water channel expressed in selected water-transporting tissues', *The Journal of Biological Chemistry*, 269(8), pp. 5497–5500.

Hawkins, O.P., Jahromi, C.P.T., Gulamhussein, A.A., Nestorow, S., Bahra, T., Shelton, C., Owusu-Mensah, Q.K., Mohiddin, N., O'Rourke, H., Ajmal, M., Byrnes, K., Khan, M., Nahar, N.N., Lim, A., Harris, C., Healy, H., Hasan, S.W., Ahmed, A., Evans, L., Vaitsopoulou, A., Akram, A., Williams, C., Binding, J., Thandi, R.K., Joby, A., Guest, A., Tariq, M.Z., Rasool, F., Cavanagh, L., Kang, S., Asparuhov, B., Jestin, A., Dafforn, T.R., Simms, J., Bill, R.M., Goddard, A.D. and Rothnie, A.J. (2021) 'Membrane protein extraction and purification using partially-esterified SMA polymers', *Biochimica et Biophysica Acta (BBA) - Biomembranes*, 1863(12), p. 183758. Available at: https://doi.org/10.1016/j.bbamem.2021.183758.

Hellwig, N., Peetz, O., Ahdash, Z., Tascón, I., Booth, P.J., Mikusevic, V., Diskowski, M., Politis, A., Hellmich, Y., Hänelt, I., Reading, E. and Morgner, N. (2018) 'Native mass spectrometry goes more native: investigation of membrane protein complexes directly from SMALPs', *Chemical Communications (Cambridge, England)*, 54(97), pp. 13702–13705. Available at: https://doi.org/10.1039/c8cc06284f.

Hesketh, S.J., Klebl, D.P., Higgins, A.J., Thomsen, M., Pickles, I.B., Sobott, F., Sivaprasadarao, A., Postis, V.L.G. and Muench, S.P. (2020) 'Styrene maleic-acid lipid particles (SMALPs) into detergent or amphipols: An exchange protocol for membrane protein characterisation', *Biochimica et Biophysica Acta (BBA) - Biomembranes*, 1862(5), p. 183192. Available at: https://doi.org/10.1016/j.bbamem.2020.183192.

Hinson, S.R., Pittock, S.J., Lucchinetti, C.F., Roemer, S.F., Fryer, J.P., Kryzer, T.J. and Lennon, V.A. (2007) 'Pathogenic potential of IgG binding to water channel extracellular domain in neuromyelitis optica', *Neurology*, 69(24), pp. 2221–2231. Available at: https://doi.org/10.1212/01.WNL.0000289761.64862.ce.

Hinson, S.R., Romero, M.F., Popescu, B.F.Gh., Lucchinetti, C.F., Fryer, J.P., Wolburg, H., Fallier-Becker, P., Noell, S. and Lennon, V.A. (2012) 'Molecular outcomes of neuromyelitis optica (NMO)-IgG binding to aquaporin-4 in astrocytes', *Proceedings of the National Academy of Sciences*, 109(4), pp. 1245–1250. Available at: https://doi.org/10.1073/pnas.1109980108.

Hiroaki, Y., Tani, K., Kamegawa, A., Gyobu, N., Nishikawa, K., Suzuki, H., Walz, T., Sasaki, S., Mitsuoka, K., Kimura, K., Mizoguchi, A. and Fujiyoshi, Y. (2006) 'Implications of the Aquaporin-4 Structure on Array Formation and Cell Adhesion', *Journal of Molecular Biology*, 355(4), pp. 628–639. Available at: https://doi.org/10.1016/j.jmb.2005.10.081.

Ho, J.D., Yeh, R., Sandstrom, A., Chorny, I., Harries, W.E.C., Robbins, R.A., Miercke, L.J.W. and Stroud, R.M. (2009) 'Crystal structure of human aquaporin 4 at 1.8 Å and its mechanism of conductance', *Proceedings of the National Academy of Sciences*, 106(18), pp. 7437–7442. Available at: https://doi.org/10.1073/pnas.0902725106.

Hong, H., Choi, H.-K. and Yoon, T.-Y. (2022) 'Untangling the complexity of membrane protein folding', *Current opinion in structural biology*, 72, pp. 237–247. Available at: https://doi.org/10.1016/j.sbi.2021.11.013.

Huang, A., Jin, W., Fahad, A.S., Mussman, B.K., Nicchia, G.P., Madan, B., de Souza, M.O., Griffin, J.D., Bennett, J.L., Frigeri, A., Berkland, C.J. and DeKosky, B.J. (2022) 'Strategies to Screen Anti-AQP4 Antibodies from Yeast Surface Display Libraries', *Antibodies*, 11(2), p. 39. Available at: https://doi.org/10.3390/antib11020039.

Hub, J.S., Grubmüller, H. and de Groot, B.L. (2009) 'Dynamics and Energetics of Permeation Through Aquaporins. What Do We Learn from Molecular Dynamics Simulations?', in E. Beitz (ed.) *Aquaporins*. Berlin, Heidelberg: Springer, pp. 57–76. Available at: https://doi.org/10.1007/978-3-540-79885-9_3.

Iliff, J.J., Lee, H., Yu, M., Feng, T., Logan, J., Nedergaard, M. and Benveniste, H. (2013) 'Brain-wide pathway for waste clearance captured by contrast-enhanced MRI', *The Journal of Clinical Investigation*, 123(3), pp. 1299–1309. Available at: https://doi.org/10.1172/JCI67677.

Iliff, J.J., Wang, M., Liao, Y., Plogg, B.A., Peng, W., Gundersen, G.A., Benveniste, H., Vates, G.E., Deane, R., Goldman, S.A., Nagelhus, E.A. and Nedergaard, M. (2012) 'A Paravascular Pathway Facilitates CSF Flow Through the Brain Parenchyma and the Clearance of

Interstitial Solutes, Including Amyloid β', *Science translational medicine*, 4(147), p. 147ra111. Available at: https://doi.org/10.1126/scitranslmed.3003748.

Inan, M. and Meagher, M.M. (2001) 'Non-repressing carbon sources for alcohol oxidase (*AOX1*) promoter of *Pichia pastoris*', *Journal of Bioscience and Bioengineering*, 92(6), pp. 585–589. Available at: https://doi.org/10.1016/S1389-1723(01)80321-2.

Jamshad, M., Charlton, J., Lin, Y.-P., Routledge, S.J., Bawa, Z., Knowles, T.J., Overduin, M., Dekker, N., Dafforn, T.R., Bill, R.M., Poyner, D.R. and Wheatley, M. (2015) 'G-protein coupled receptor solubilization and purification for biophysical analysis and functional studies, in the total absence of detergent', *Bioscience Reports*, 35(2), p. e00188. Available at: https://doi.org/10.1042/BSR20140171.

Jamshad, M., Grimard, V., Idini, I., Knowles, T.J., Dowle, M.R., Schofield, N., Sridhar, P., Lin, Y.-P., Finka, R., Wheatley, M., Thomas, O.R., Palmer, R.E., Overduin, M., Govaerts, C., Ruysschaert, J.-M., Edler, K.J. and Dafforn, T.R. (2015) 'Structural analysis of a nanoparticle containing a lipid bilayer used for detergent-free extraction of membrane proteins', *Nano Research*, 8(3), pp. 774–789. Available at: https://doi.org/10.1007/s12274-014-0560-6.

Jarius, S., Aktas, O., Ayzenberg, I., Bellmann-Strobl, J., Berthele, A., Giglhuber, K., Häußler, V., Havla, J., Hellwig, K., Hümmert, M.W., Kleiter, I., Klotz, L., Krumbholz, M., Kümpfel, T., Paul, F., Ringelstein, M., Ruprecht, K., Senel, M., Stellmann, J.-P., Bergh, F.T., Tumani, H., Wildemann, B., Trebst, C., and Neuromyelitis Optica Study Group (NEMOS) (2023) 'Update on the diagnosis and treatment of neuromyelits optica spectrum disorders (NMOSD) – revised recommendations of the Neuromyelitis Optica Study Group (NEMOS). Part I: Diagnosis and differential diagnosis', *Journal of Neurology*, 270(7), pp. 3341–3368. Available at: https://doi.org/10.1007/s00415-023-11634-0.

Jarius, S., Paul, F., Weinshenker, B.G., Levy, M., Kim, H.J. and Wildemann, B. (2020) 'Neuromyelitis optica', *Nature Reviews Disease Primers*, 6(1), p. 85. Available at: https://doi.org/10.1038/s41572-020-0214-9.

Jin, B.-J., Rossi, A. and Verkman, A.S. (2011) 'Model of Aquaporin-4 Supramolecular Assembly in Orthogonal Arrays Based on Heterotetrameric Association of M1-M23 Isoforms', *Biophysical Journal*, 100(12), pp. 2936–2945. Available at: https://doi.org/10.1016/j.bpj.2011.05.012.

Johansson, I., Karlsson, M., Johanson, U., Larsson, C. and Kjellbom, P. (2000) 'The role of aquaporins in cellular and whole plant water balance', *Biochimica et Biophysica Acta (BBA) - Biomembranes*, 1465(1), pp. 324–342. Available at: https://doi.org/10.1016/S0005-2736(00)00147-4.

Joseph, M. and Nagaraj, R. (1995) 'Interaction of peptides corresponding to fatty acylation sites in proteins with model membranes', *The Journal of Biological Chemistry*, 270(28), pp. 16749–16755. Available at: https://doi.org/10.1074/jbc.270.28.16749.

Jung, J.S., Bhat, R.V., Preston, G.M., Guggino, W.B., Baraban, J.M. and Agre, P. (1994) 'Molecular characterization of an aquaporin cDNA from brain: candidate osmoreceptor and regulator of water balance', *Proceedings of the National Academy of Sciences of the United States of America*, 91(26), pp. 13052–13056. Available at: https://doi.org/10.1073/pnas.91.26.13052.

Jung, J.S., Preston, G.M., Smith, B.L., Guggino, W.B. and Agre, P. (1994) 'Molecular structure of the water channel through aquaporin CHIP. The hourglass model.', *Journal of*

Biological Chemistry, 269(20), pp. 14648–14654. Available at: https://doi.org/10.1016/S0021-9258(17)36674-7.

Kaldenhoff, R., Kai, L. and Uehlein, N. (2014) 'Aquaporins and membrane diffusion of CO2 in living organisms', *Biochimica et Biophysica Acta (BBA) - General Subjects*, 1840(5), pp. 1592–1595. Available at: https://doi.org/10.1016/j.bbagen.2013.09.037.

Karbalaei, M., Rezaee, S.A. and Farsiani, H. (2020) 'Pichia pastoris: A highly successful expression system for optimal synthesis of heterologous proteins', *Journal of Cellular Physiology*, 235(9), pp. 5867–5881. Available at: https://doi.org/10.1002/jcp.29583.

Kesidis, A., Depping, P., Lodé, A., Vaitsopoulou, A., Bill, R.M., Goddard, A.D. and Rothnie, A.J. (2020) 'Expression of eukaryotic membrane proteins in eukaryotic and prokaryotic hosts', *Methods (San Diego, Calif.)*, 180, pp. 3–18. Available at: https://doi.org/10.1016/j.ymeth.2020.06.006.

Kitchen, P., Conner, M.T., Bill, R.M. and Conner, A.C. (2016) 'Structural Determinants of Oligomerization of the Aquaporin-4 Channel', *Journal of Biological Chemistry*, 291(13), pp. 6858–6871. Available at: https://doi.org/10.1074/jbc.M115.694729.

Kitchen, P., Salman, M.M., Halsey, A.M., Clarke-Bland, C., MacDonald, J.A., Ishida, H., Vogel, H.J., Almutiri, S., Logan, A., Kreida, S., Al-Jubair, T., Missel, J.W., Gourdon, P., Törnroth-Horsefield, S., Conner, M.T., Ahmed, Z., Conner, A.C. and Bill, R.M. (2020) 'Targeting Aquaporin-4 Subcellular Localization to Treat Central Nervous System Edema', *Cell*, 181(4), pp. 784-799.e19. Available at: https://doi.org/10.1016/j.cell.2020.03.037.

Kitchen, P., Salman, M.M., Pickel, S.U., Jennings, J., Törnroth-Horsefield, S., Conner, M.T., Bill, R.M. and Conner, A.C. (2019) 'Water channel pore size determines exclusion properties but not solute selectivity', *Scientific Reports*, 9(1), p. 20369. Available at: https://doi.org/10.1038/s41598-019-56814-z.

Knowles, T.J., Finka, R., Smith, C., Lin, Y.-P., Dafforn, T. and Overduin, M. (2009) 'Membrane Proteins Solubilized Intact in Lipid Containing Nanoparticles Bounded by Styrene Maleic Acid Copolymer', *Journal of the American Chemical Society*, 131(22), pp. 7484–7485. Available at: https://doi.org/10.1021/ja810046q.

Kopf, A.H., Koorengevel, M.C., van Walree, C.A., Dafforn, T.R. and Killian, J.A. (2019) 'A simple and convenient method for the hydrolysis of styrene-maleic anhydride copolymers to styrene-maleic acid copolymers', *Chemistry and Physics of Lipids*, 218, pp. 85–90. Available at: https://doi.org/10.1016/j.chemphyslip.2018.11.011.

Kratochvíl, J., Wee, R. van, Loewenthal, D., Thiele, J.C., Bardzil, J., Iqbal, K., Thorpe, S. and Kukura, P. (2024) 'Best practice mass photometry: A guide to optimal single molecule mass measurement'. bioRxiv, p. 2024.12.03.624087. Available at: https://doi.org/10.1101/2024.12.03.624087.

Kreida, S. and Törnroth-Horsefield, S. (2015) 'Structural insights into aquaporin selectivity and regulation', *Current Opinion in Structural Biology*, 33, pp. 126–134. Available at: https://doi.org/10.1016/j.sbi.2015.08.004.

Kress, B.T., Iliff, J.J., Xia, M., Wang, M., Wei, H., Zeppenfeld, D., Xie, L., Kang, H., Xu, Q., Liew, J., Plog, B.A., Ding, F., Deane, R. and Nedergaard, M. (2014) 'Impairment of paravascular clearance pathways in the aging brain', *Annals of neurology*, 76(6), pp. 845–861. Available at: https://doi.org/10.1002/ana.24271.

Krogh, A., Larsson, B., von Heijne, G. and Sonnhammer, E.L.L. (2001) 'Predicting transmembrane protein topology with a hidden markov model: application to complete genomes', *Journal of Molecular Biology*, 305(3), pp. 567–580. Available at: https://doi.org/10.1006/jmbi.2000.4315.

Kruse, E., Uehlein, N. and Kaldenhoff, R. (2006) 'The aquaporins', *Genome Biology*, 7(2), p. 206. Available at: https://doi.org/10.1186/gb-2006-7-2-206.

Kumar, S., Mannil, A. and Mutturi, S. (2020) 'Modified chemical method for efficient transformation and diagnosis in *Pichia pastoris*', *Protein Expression and Purification*, 174, p. 105685. Available at: https://doi.org/10.1016/j.pep.2020.105685.

Kümpfel, T., Giglhuber, K., Aktas, O., Ayzenberg, I., Bellmann-Strobl, J., Häußler, V., Havla, J., Hellwig, K., Hümmert, M.W., Jarius, S., Kleiter, I., Klotz, L., Krumbholz, M., Paul, F., Ringelstein, M., Ruprecht, K., Senel, M., Stellmann, J.-P., Bergh, F.T., Trebst, C., Tumani, H., Warnke, C., Wildemann, B., Berthele, A., Albrecht, P., Angstwurm, K., Asseyer, S., Gomes, A.B.A.G.R., Bayas, A., Behnke, S., Bittner, S., Buetow, F., Buttmann, M., Duchow, A., Engels, D., Etgen, T., Fischer, K., Frank, B., Gahlen, A., Gass, A., Gehring, J., Geis, C., Gold, R., Göreci, Y., Graf, J., Groppa, S., Grothe, M., Gutbrod, J., Guthke, K., Haarmann, A., Hastermann, M., Hemmer, B., Herfurth, M., Herwerth, M., Hoffmann, F., Hoffmann, O., Hümmert, M.W., Husseini, L., Junghans, J., Kaste, M., Kern, P., Kern, K., Kermer, P., Kleinschnitz, C., Köhler, W., Körbel, K., Kowarik, M., Kraemer, M., Kretschmer, J., Kurka, N., Ladopoulus, T., Lauenstein, A.-S., Laurent, S., Lee, D.-H., Lehrieder, D., Leypoldt, F., Liebetrau, M., Linker, R., Lindenblatt, G., Lohmann, L., Lüssi, F., Luedemann, P., Maiworm, M., Marziniak, M., Mayer, C., Meister, S., Mering, M., Metz, I., Meuth, S., Naumann, J., Neuhaus, O., Neziraj, T., Niederschweiberer, M., Niehaus, S., Otto, C., Pache, F., Pakeerathan, T., Passoke, S., Pawlitzki, M., Pellkofer, H., Pompsch, M., Pröbstel, A.-K., Pul, R., Rauer, S., Retzlaff, N., Riedlinger, A., Rommer, P., Rothhammer, V., Rostásy, K., Rust, R., Ruschil, C., Schwab, M., Seipelt, M., Schindler, P., Schwake, C., Schwarz, P., Sommer, C., Stefanou, A., Sprenger, T., Steinbrecher, A., Stephanik, H., Stoppe, M., Stürner, K., Süße, M., Tarampanis, A., Tauber, S., Tkachenko, D., Walter, A., Wandinger, K.-P., Walz, A., Weber, M., Weise, J., Wickel, J., Wiendl, H., Winkelmann, A., Yalachkov, Y., Zettl, U., Ziemann, U., Zipp, F., and The Neuromyelitis Optica Study Group (NEMOS) (2024) 'Update on the diagnosis and treatment of neuromyelitis optica spectrum disorders (NMOSD) – revised recommendations of the Neuromyelitis Optica Study Group (NEMOS). Part II: Attack therapy and long-term management', *Journal of Neurology*, 271(1), pp. 141–176. Available at: https://doi.org/10.1007/s00415-023-11910-z.

Landis, D.M.D. and Reese, T.S. (1974) 'ARRAYS OF PARTICLES IN FREEZE-FRACTURED ASTROCYTIC MEMBRANES', *Journal of Cell Biology*, 60(1), pp. 316–320. Available at: https://doi.org/10.1083/jcb.60.1.316.

Law, R.H.P., Robinson, H.C., Rowley, M.J. and Mackay, I.R. (2001) 'The ubiquitous 38 kDa contaminant in glutamic acid decarboxylase preparation from the cytosol of Pichia pastoris after immobilised metal ion affinity chromatography is an alcohol dehydrogenase', *Biotechnology Letters*, 23(9), pp. 697–703. Available at: https://doi.org/10.1023/A:1010368921034.

Lee, A.G. (2003) 'Lipid–protein interactions in biological membranes: a structural perspective', *Biochimica et Biophysica Acta (BBA) - Biomembranes*, 1612(1), pp. 1–40. Available at: https://doi.org/10.1016/S0005-2736(03)00056-7.

Lee, H.J., Lee, H.S., Youn, T., Byrne, B. and Chae, P.S. (2022) 'Impact of novel detergents on membrane protein studies', *Chem*, 8(4), pp. 980–1013. Available at: https://doi.org/10.1016/j.chempr.2022.02.007.

Lee, S.C., Collins, R., Lin, Y., Jamshad, M., Broughton, C., Harris, S.A., Hanson, B.S., Tognoloni, C., Parslow, R.A., Terry, A.E., Rodger, A., Smith, C.J., Edler, K.J., Ford, R., Roper, D.I. and Dafforn, T.R. (2019) 'Nano-encapsulated Escherichia coli Divisome Anchor ZipA, and in Complex with FtsZ', *Scientific Reports*, 9(1), p. 18712. Available at: https://doi.org/10.1038/s41598-019-54999-x.

Lee, S.C., Knowles, T.J., Postis, V.L.G., Jamshad, M., Parslow, R.A., Lin, Y., Goldman, A., Sridhar, P., Overduin, M., Muench, S.P. and Dafforn, T.R. (2016) 'A method for detergent-free isolation of membrane proteins in their local lipid environment', *Nature Protocols*, 11(7), pp. 1149–1162. Available at: https://doi.org/10.1038/nprot.2016.070.

Lei, Y., Zhu, J., Li, H., Kong, E. and Lu, K. (2021) 'Protocol to quantify palmitoylation of cysteines in budding yeast', *STAR Protocols*, 3(1), p. 101035. Available at: https://doi.org/10.1016/j.xpro.2021.101035.

Leishman, S., Aljadeed, N.M. and Anand, P.K. (2024) 'Protocol for a semi-quantitative approach to identify protein S-palmitoylation in cultured cells by acyl biotin exchange assay', *STAR Protocols*, 5(2), p. 103054. Available at: https://doi.org/10.1016/j.xpro.2024.103054.

Lennon, V.A., Kryzer, T.J., Pittock, S.J., Verkman, A.S. and Hinson, S.R. (2005) 'IgG marker of optic-spinal multiple sclerosis binds to the aquaporin-4 water channel', *Journal of Experimental Medicine*, 202(4), pp. 473–477. Available at: https://doi.org/10.1084/jem.20050304.

Lennon, V.A., Wingerchuk, D.M., Kryzer, T.J., Pittock, S.J., Lucchinetti, C.F., Fujihara, K., Nakashima, I. and Weinshenker, B.G. (2004) 'A serum autoantibody marker of neuromyelitis optica: distinction from multiple sclerosis', *The Lancet*, 364(9451), pp. 2106–2112. Available at: https://doi.org/10.1016/S0140-6736(04)17551-X.

Levental, I., Lingwood, D., Grzybek, M., Coskun, Ü. and Simons, K. (2010) 'Palmitoylation regulates raft affinity for the majority of integral raft proteins', *Proceedings of the National Academy of Sciences*, 107(51), pp. 22050–22054. Available at: https://doi.org/10.1073/pnas.1016184107.

Li, D., Li, J., Zhuang, Y., Zhang, L., Xiong, Y., Shi, P. and Tian, C. (2015) 'Nano-size uni-lamellar lipodisq improved in situ auto-phosphorylation analysis of E. coli tyrosine kinase using 19F nuclear magnetic resonance', *Protein & Cell*, 6(3), pp. 229–233. Available at: https://doi.org/10.1007/s13238-014-0129-x.

Li, Z. and Buck, M. (2021) 'Beyond history and "on a roll": The list of the most well-studied human protein structures and overall trends in the protein data bank', *Protein Science : A Publication of the Protein Society*, 30(4), pp. 745–760. Available at: https://doi.org/10.1002/pro.4038.

Lobo, S., Greentree, W.K., Linder, M.E. and Deschenes, R.J. (2002) 'Identification of a Ras palmitoyltransferase in Saccharomyces cerevisiae', *The Journal of Biological Chemistry*, 277(43), pp. 41268–41273. Available at: https://doi.org/10.1074/jbc.M206573200.

Logez, C., Damian, M., Legros, C., Dupré, C., Guéry, M., Mary, S., Wagner, R., M'Kadmi, C., Nosjean, O., Fould, B., Marie, J., Fehrentz, J.-A., Martinez, J., Ferry, G., Boutin, J.A. and Banères, J.-L. (2016) 'Detergent-free Isolation of Functional G Protein-Coupled Receptors into Nanometric Lipid Particles', *Biochemistry*, 55(1), pp. 38–48. Available at: https://doi.org/10.1021/acs.biochem.5b01040.

Long, A.R., O'Brien, C.C., Malhotra, K., Schwall, C.T., Albert, A.D., Watts, A. and Alder, N.N. (2013) 'A detergent-free strategy for the reconstitution of active enzyme complexes from native biological membranes into nanoscale discs', *BMC Biotechnology*, 13(1), p. 41. Available at: https://doi.org/10.1186/1472-6750-13-41.

Long, S.B., Campbell, E.B. and Mackinnon, R. (2005) 'Crystal structure of a mammalian voltage-dependent Shaker family K+ channel', *Science (New York, N.Y.)*, 309(5736), pp. 897–903. Available at: https://doi.org/10.1126/science.1116269.

Lu, M., Lee, M.D., Smith, B.L., Jung, J.S., Agre, P., Verdijk, M.A., Merkx, G., Rijss, J.P. and Deen, P.M. (1996) 'The human AQP4 gene: definition of the locus encoding two water channel polypeptides in brain', *Proceedings of the National Academy of Sciences of the United States of America*, 93(20), pp. 10908–10912. Available at: https://doi.org/10.1073/pnas.93.20.10908.

Lueking, A., Holz, C., Gotthold, C., Lehrach, H. and Cahill, D. (2000) 'A System for Dual Protein Expression in *Pichia pastoris* and *Escherichia coli*', *Protein Expression and Purification*, 20(3), pp. 372–378. Available at: https://doi.org/10.1006/prep.2000.1317.

Mader, S. and Brimberg, L. (2019) 'Aquaporin-4 Water Channel in the Brain and Its Implication for Health and Disease', *Cells*, 8(2), p. 90. Available at: https://doi.org/10.3390/cells8020090.

Mader, S., Lutterotti, A., Pauli, F.D., Kuenz, B., Schanda, K., Aboul-Enein, F., Khalil, M., Storch, M.K., Jarius, S., Kristoferitsch, W., Berger, T. and Reindl, M. (2010) 'Patterns of Antibody Binding to Aquaporin-4 Isoforms in Neuromyelitis Optica', *PLOS ONE*, 5(5), p. e10455. Available at: https://doi.org/10.1371/journal.pone.0010455.

Mitchell, D.A., Vasudevan, A., Linder, M.E. and Deschenes, R.J. (2006) 'Protein palmitoylation by a family of DHHC protein S-acyltransferases', *Journal of Lipid Research*, 47(6), pp. 1118–1127. Available at: https://doi.org/10.1194/jlr.R600007-JLR200.

Moëlo, C. (2025a) *Aquaporins Orthogonal Arrays of Particles.* Available at: https://app.biorender.com/profile/template/details/t-653973792853e40ea83c1efb-aquaporins-orthogonal-arrays-of-particles.

Moëlo, C. (2025b) *Aquaporins Protein Structure.* Available at: https://app.biorender.com/profile/template/details/t-64dc7715ca282432f872c179-aquaporins-protein-structure.

Morrison, K.A., Akram, A., Mathews, A., Khan, Z.A., Patel, J.H., Zhou, C., Hardy, D.J., Moore-Kelly, C., Patel, R., Odiba, V., Knowles, T.J., Javed, M.-H., Chmel, N.P., Dafforn, T.R. and Rothnie, A.J. (2016) 'Membrane protein extraction and purification using styrene–maleic acid (SMA) copolymer: effect of variations in polymer structure', *Biochemical Journal*, 473(23), pp. 4349–4360. Available at: https://doi.org/10.1042/BCJ20160723.

Murata, K., Mitsuoka, K., Hirai, T., Walz, T., Agre, P., Heymann, J.B., Engel, A. and Fujiyoshi, Y. (2000) 'Structural determinants of water permeation through aquaporin-1', *Nature*, 407(6804), pp. 599–605. Available at: https://doi.org/10.1038/35036519.

Nagelhus, E.A. and Ottersen, O.P. (2013) 'Physiological Roles of Aquaporin-4 in Brain', *Physiological Reviews*, 93(4), pp. 1543–1562. Available at: https://doi.org/10.1152/physrev.00011.2013.

Nedergaard, M. and Goldman, S.A. (2020) ‘Glymphatic failure as a final common pathway to dementia’, *Science*, 370(6512), pp. 50–56. Available at: https://doi.org/10.1126/science.abb8739.

Neely, J.D., Christensen, B.M., Nielsen, S. and Agre, P. (1999) ‘Heterotetrameric Composition of Aquaporin-4 Water Channels’, *Biochemistry*, 38(34), pp. 11156–11163. Available at: https://doi.org/10.1021/bi990941s.

Newport, T.D., Sansom, M.S.P. and Stansfeld, P.J. (2019) ‘The MemProtMD database: a resource for membrane-embedded protein structures and their lipid interactions’, *Nucleic Acids Research*, 47(D1), pp. D390–D397. Available at: https://doi.org/10.1093/nar/gky1047.

Nicchia, G.P., Mastrototaro, M., Rossi, A., Pisani, F., Tortorella, C., Ruggieri, M., Lia, A., Trojano, M., Frigeri, A. and Svelto, M. (2009) ‘Aquaporin-4 orthogonal arrays of particles are the target for neuromyelitis optica autoantibodies’, *Glia*, 57(13), pp. 1363–1373. Available at: https://doi.org/10.1002/glia.20855.

Nicchia, G.P., Nico, B., Camassa, L.M.A., Mola, M.G., Loh, N., Dermietzel, R., Spray, D.C., Svelto, M. and Frigeri, A. (2004) ‘The role of aquaporin-4 in the blood–brain barrier development and integrity: Studies in animal and cell culture models’, *Neuroscience*, 129(4), pp. 935–944. Available at: https://doi.org/10.1016/j.neuroscience.2004.07.055.

Nicchia, G.P., Rossi, A., Mola, M.G., Pisani, F., Stigliano, C., Basco, D., Mastrototaro, M., Svelto, M. and Frigeri, A. (2010) ‘Higher order structure of aquaporin-4’, *Neuroscience*, 168(4), pp. 903–914. Available at: https://doi.org/10.1016/j.neuroscience.2010.02.008.

Nishiyama, S., Misu, T., Nuriya, M., Takano, R., Takahashi, T., Nakashima, I., Yasui, M., Itoyama, Y., Aoki, M. and Fujihara, K. (2016) ‘Complement-dependent and -independent aquaporin 4-antibody-mediated cytotoxicity in human astrocytes: Pathogenetic implications in neuromyelitis optica’, *Biochemistry and Biophysics Reports*, 7, pp. 45–51. Available at: https://doi.org/10.1016/j.bbrep.2016.05.012.

Öberg, F., Sjöhamn, J., Conner, M.T., Bill, R.M. and Hedfalk, K. (2011) ‘Improving recombinant eukaryotic membrane protein yields in Pichia pastoris: The importance of codon optimization and clone selection’, *Molecular Membrane Biology*, 28(6), pp. 398–411. Available at: https://doi.org/10.3109/09687688.2011.602219.

Olerinyova, A., Sonn-Segev, A., Gault, J., Eichmann, C., Schimpf, J., Kopf, A.H., Rudden, L.S.P., Ashkinadze, D., Bomba, R., Frey, L., Greenwald, J., Degiacomi, M.T., Steinhilper, R., Killian, J.A., Friedrich, T., Riek, R., Struwe, W.B. and Kukura, P. (2021) ‘Mass Photometry of Membrane Proteins’, *Chem*, 7(1), pp. 224–236. Available at: https://doi.org/10.1016/j.chempr.2020.11.011.

Oluwole, A.O., Danielczak, B., Meister, A., Babalola, J.O., Vargas, C. and Keller, S. (2017) ‘Solubilization of Membrane Proteins into Functional Lipid-Bilayer Nanodiscs Using a Diisobutylene/Maleic Acid Copolymer’, *Angewandte Chemie International Edition*, 56(7), pp. 1919–1924. Available at: https://doi.org/10.1002/anie.201610778.

Orwick, M.C., Judge, P.J., Procek, J., Lindholm, L., Graziadei, A., Engel, A., Gröbner, G. and Watts, A. (2012) ‘Detergent-Free Formation and Physicochemical Characterization of Nanosized Lipid–Polymer Complexes: Lipodisq’, *Angewandte Chemie International Edition*, 51(19), pp. 4653–4657. Available at: https://doi.org/10.1002/anie.201201355.

Orwick-Rydmark, M., Lovett, J.E., Graziadei, A., Lindholm, L., Hicks, M.R. and Watts, A. (2012) ‘Detergent-Free Incorporation of a Seven-Transmembrane Receptor Protein into

Nanosized Bilayer Lipodisq Particles for Functional and Biophysical Studies', *Nano Letters*, 12(9), pp. 4687–4692. Available at: https://doi.org/10.1021/nl3020395.

Overington, J.P., Al-Lazikani, B. and Hopkins, A.L. (2006) 'How many drug targets are there?', *Nature Reviews Drug Discovery*, 5(12), pp. 993–996. Available at: https://doi.org/10.1038/nrd2199.

Owens, G.P., Ritchie, A., Rossi, A., Schaller, K., Wemlinger, S., Schumann, H., Shearer, A., Verkman, A.S. and Bennett, J.L. (2015) 'Mutagenesis of the Aquaporin 4 Extracellular Domains Defines Restricted Binding Patterns of Pathogenic Neuromyelitis Optica IgG', *Journal of Biological Chemistry*, 290(19), pp. 12123–12134. Available at: https://doi.org/10.1074/jbc.M115.647149.

Ozu, M., Galizia, L., Acuña, C. and Amodeo, G. (2018) 'Aquaporins: More Than Functional Monomers in a Tetrameric Arrangement', *Cells*, 7(11), p. 209. Available at: https://doi.org/10.3390/cells7110209.

Palace, J., Leite, M.I., Nairne, A. and Vincent, A. (2010) 'Interferon Beta Treatment in Neuromyelitis Optica: Increase in Relapses and Aquaporin 4 Antibody Titers', *Archives of Neurology*, 67(8), pp. 1016–1017. Available at: https://doi.org/10.1001/archneurol.2010.188.

Papadopoulos, M.C. and Verkman, A.S. (2012) 'Aquaporin 4 and neuromyelitis optica', *Lancet neurology*, 11(6), pp. 535–544. Available at: https://doi.org/10.1016/S1474-4422(12)70133-3.

Papadopoulos, M.C. and Verkman, A.S. (2013) 'Aquaporin water channels in the nervous system', *Nature Reviews Neuroscience*, 14(4), pp. 265–277. Available at: https://doi.org/10.1038/nrn3468.

Paul, F., Jarius, S., Aktas, O., Bluthner, M., Bauer, O., Appelhans, H., Franciotta, D., Bergamaschi, R., Littleton, E., Palace, J., Seelig, H.-P., Hohlfeld, R., Vincent, A. and Zipp, F. (2007) 'Antibody to Aquaporin 4 in the Diagnosis of Neuromyelitis Optica', *PLOS Medicine*, 4(4), p. e133. Available at: https://doi.org/10.1371/journal.pmed.0040133.

Pedersen, M.E., Østergaard, J. and Jensen, H. (2019) 'Flow-Induced Dispersion Analysis (FIDA) for Protein Quantification and Characterization', in T.M. Phillips (ed.) *Clinical Applications of Capillary Electrophoresis: Methods and Protocols*. New York, NY: Springer, pp. 109–123. Available at: https://doi.org/10.1007/978-1-4939-9213-3_8.

Peng, W., Achariyar, T.M., Li, B., Liao, Y., Mestre, H., Hitomi, E., Regan, S., Kasper, T., Peng, S., Ding, F., Benveniste, H., Nedergaard, M. and Deane, R. (2016) 'Suppression of glymphatic fluid transport in a mouse model of Alzheimer's disease', *Neurobiology of Disease*, 93, pp. 215–225. Available at: https://doi.org/10.1016/j.nbd.2016.05.015.

Phuan, P.-W., Ratelade, J., Rossi, A., Tradtrantip, L. and Verkman, A.S. (2012) 'Complement-dependent Cytotoxicity in Neuromyelitis Optica Requires Aquaporin-4 Protein Assembly in Orthogonal Arrays', *The Journal of Biological Chemistry*, 287(17), pp. 13829–13839. Available at: https://doi.org/10.1074/jbc.M112.344325.

Pisani, F., Mastrototaro, M., Rossi, A., Nicchia, G.P., Tortorella, C., Ruggieri, M., Trojano, M., Frigeri, A. and Svelto, M. (2011) 'Identification of Two Major Conformational Aquaporin-4 Epitopes for Neuromyelitis Optica Autoantibody Binding', *Journal of Biological Chemistry*, 286(11), pp. 9216–9224. Available at: https://doi.org/10.1074/jbc.M110.123000.

Pisani, F., Simone, L., Mola, M.G., De Bellis, M., Frigeri, A., Nicchia, G.P. and Svelto, M. (2021) 'Regulation of aquaporin-4 expression in the central nervous system investigated using M23-AQP4 null mouse', *Glia*, 69(9), pp. 2235–2251. Available at: https://doi.org/10.1002/glia.24032.

Pisani, F., Sparaneo, A., Tortorella, C., Ruggieri, M., Trojano, M., Mola, M.G., Nicchia, G.P., Frigeri, A. and Svelto, M. (2013) 'Aquaporin-4 Autoantibodies in Neuromyelitis Optica: AQP4 Isoform-Dependent Sensitivity and Specificity', *PLOS ONE*, 8(11), p. e79185. Available at: https://doi.org/10.1371/journal.pone.0079185.

Pollock, N.L., Lee, S.C., Patel, J.H., Gulamhussein, A.A. and Rothnie, A.J. (2018) 'Structure and function of membrane proteins encapsulated in a polymer-bound lipid bilayer', *Biochimica et Biophysica Acta (BBA) - Biomembranes*, 1860(4), pp. 809–817. Available at: https://doi.org/10.1016/j.bbamem.2017.08.012.

Pollock, N.L., Lloyd, J., Montinaro, C., Rai, M. and Dafforn, T.R. (2022) 'Conformational trapping of an ABC transporter in polymer lipid nanoparticles', *Biochemical Journal*, 479(2), pp. 145–159. Available at: https://doi.org/10.1042/BCJ20210312.

Pollock, N.L., Rai, M., Simon, K.S., Hesketh, S.J., Teo, A.C.K., Parmar, M., Sridhar, P., Collins, R., Lee, S.C., Stroud, Z.N., Bakker, S.E., Muench, S.P., Barton, C.H., Hurlbut, G., Roper, D.I., Smith, C.J.I., Knowles, T.J., Spickett, C.M., East, J.M., Postis, V.L.G. and Dafforn, T.R. (2019) 'SMA-PAGE: A new method to examine complexes of membrane proteins using SMALP nano-encapsulation and native gel electrophoresis', *Biochimica et Biophysica Acta (BBA) - Biomembranes*, 1861(8), pp. 1437–1445. Available at: https://doi.org/10.1016/j.bbamem.2019.05.011.

Popot, J.-L. (2010) 'Amphipols, nanodiscs, and fluorinated surfactants: three nonconventional approaches to studying membrane proteins in aqueous solutions', *Annual Review of Biochemistry*, 79, pp. 737–775. Available at: https://doi.org/10.1146/annurev.biochem.052208.114057.

Postis, V., Rawson, S., Mitchell, J.K., Lee, S.C., Parslow, R.A., Dafforn, T.R., Baldwin, S.A. and Muench, S.P. (2015) 'The use of SMALPs as a novel membrane protein scaffold for structure study by negative stain electron microscopy', *Biochimica et Biophysica Acta (BBA) - Biomembranes*, 1848(2), pp. 496–501. Available at: https://doi.org/10.1016/j.bbamem.2014.10.018.

Prabudiansyah, I., Kusters, I., Caforio, A. and Driessen, A.J.M. (2015) 'Characterization of the annular lipid shell of the Sec translocon', *Biochimica et Biophysica Acta (BBA) - Biomembranes*, 1848(10, Part A), pp. 2050–2056. Available at: https://doi.org/10.1016/j.bbamem.2015.06.024.

Prabudiansyah, I., van der Valk, R. and Aubin-Tam, M.-E. (2021) 'Reconstitution and functional characterization of the FtsH protease in lipid nanodiscs', *Biochimica et Biophysica Acta (BBA) - Biomembranes*, 1863(2), p. 183526. Available at: https://doi.org/10.1016/j.bbamem.2020.183526.

Preston, G.M., Carroll, T.P., Guggino, W.B. and Agre, P. (1992) 'Appearance of Water Channels in Xenopus Oocytes Expressing Red Cell CHIP28 Protein', *Science*, 256(5055), pp. 385–387. Available at: https://doi.org/10.1126/science.256.5055.385.

Qiu, W., Fu, Z., Xu, G.G., Grassucci, R.A., Zhang, Y., Frank, J., Hendrickson, W.A. and Guo, Y. (2018) 'Structure and activity of lipid bilayer within a membrane-protein transporter',

Proceedings of the National Academy of Sciences, 115(51), pp. 12985–12990. Available at: https://doi.org/10.1073/pnas.1812526115.

Raja, M. and Vales, E. (2009) 'Effects of sodium chloride on membrane fusion and on the formation of aggregates of potassium channel KcsA in Escherichia coli membrane', *Biophysical Chemistry*, 142(1–3), pp. 46–54. Available at: https://doi.org/10.1016/j.bpc.2009.03.005.

Ramazi, S. and Zahiri, J. (2021) 'Post-translational modifications in proteins: resources, tools and prediction methods', *Database: The Journal of Biological Databases and Curation*, 2021, p. baab012. Available at: https://doi.org/10.1093/database/baab012.

Rana, M.S., Lee, C.-J. and Banerjee, A. (2018) 'The molecular mechanism of DHHC protein acyltransferases', *Biochemical Society Transactions*, 47(1), pp. 157–167. Available at: https://doi.org/10.1042/BST20180429.

Rash, J.E., Davidson, K.G.V., Yasumura, T. and Furman, C.S. (2004) 'Freeze-fracture and immunogold analysis of aquaporin-4 (AQP4) square arrays, with models of AQP4 lattice assembly', *Neuroscience*, 129(4), pp. 915–934. Available at: https://doi.org/10.1016/j.neuroscience.2004.06.076.

Rash, J.E., Yasumura, T., Hudson, C.S., Agre, P. and Nielsen, S. (1998) 'Direct immunogold labeling of aquaporin-4 in square arrays of astrocyte and ependymocyte plasma membranes in rat brain and spinal cord', *Proceedings of the National Academy of Sciences of the United States of America*, 95(20), pp. 11981–11986. Available at: https://doi.org/10.1073/pnas.95.20.11981.

Rasmussen, M.K., Mestre, H. and Nedergaard, M. (2018) 'The glymphatic pathway in neurological disorders', *The Lancet Neurology*, 17(11), pp. 1016–1024. Available at: https://doi.org/10.1016/S1474-4422(18)30318-1.

Rehan, S., Paavilainen, V.O. and Jaakola, V.-P. (2017) 'Functional reconstitution of human equilibrative nucleoside transporter-1 into styrene maleic acid co-polymer lipid particles', *Biochimica et Biophysica Acta (BBA) - Biomembranes*, 1859(5), pp. 1059–1065. Available at: https://doi.org/10.1016/j.bbamem.2017.02.017.

Renart, M.L., Giudici, A.M., Díaz-García, C., Molina, M.L., Morales, A., González-Ros, J.M. and Poveda, J.A. (2020) 'Modulation of Function, Structure and Clustering of K+ Channels by Lipids: Lessons Learnt from KcsA', *International Journal of Molecular Sciences*, 21(7), p. 2554. Available at: https://doi.org/10.3390/ijms21072554.

Roche, J.V. and Törnroth-Horsefield, S. (2017) 'Aquaporin Protein-Protein Interactions', *International Journal of Molecular Sciences*, 18(11), p. 2255. Available at: https://doi.org/10.3390/ijms18112255.

Rossi, A., Baumgart, F., van Hoek, A.N. and Verkman, A.S. (2012) 'Post-Golgi Supramolecular Assembly of Aquaporin-4 in Orthogonal Arrays', *Traffic*, 13(1), pp. 43–53. Available at: https://doi.org/10.1111/j.1600-0854.2011.01299.x.

Rossi, A., Moritz, T.J., Ratelade, J. and Verkman, A.S. (2012) 'Super-resolution imaging of aquaporin-4 orthogonal arrays of particles in cell membranes', *Journal of Cell Science*, 125(18), pp. 4405–4412. Available at: https://doi.org/10.1242/jcs.109603.

Rossi, A., Pisani, F., Nicchia, G.P., Svelto, M. and Frigeri, A. (2010) 'Evidences for a Leaky Scanning Mechanism for the Synthesis of the Shorter M23 Protein Isoform of Aquaporin-4:

IMPLICATION IN ORTHOGONAL ARRAY FORMATION AND NEUROMYELITIS OPTICA ANTIBODY INTERACTION', *Journal of Biological Chemistry*, 285(7), pp. 4562–4569. Available at: https://doi.org/10.1074/jbc.M109.069245.

Rossi, A., Ratelade, J., Papadopoulos, M.C., Bennett, J.L. and Verkman, A.S. (2012) 'Neuromyelitis optica IgG does not alter aquaporin-4 water permeability, plasma membrane M1/M23 isoform content, or supramolecular assembly', *Glia*, 60(12), pp. 2027–2039. Available at: https://doi.org/10.1002/glia.22417.

Roth, A.F., Feng, Y., Chen, L. and Davis, N.G. (2002) 'The yeast DHHC cysteine-rich domain protein Akr1p is a palmitoyl transferase', *Journal of Cell Biology*, 159(1), pp. 23–28. Available at: https://doi.org/10.1083/jcb.200206120.

Roth, A.F., Wan, J., Bailey, A.O., Sun, B., Kuchar, J.A., Green, W.N., Phinney, B.S., Yates, J.R. and Davis, N.G. (2006) 'Global Analysis of Protein Palmitoylation in Yeast', *Cell*, 125(5), pp. 1003–1013. Available at: https://doi.org/10.1016/j.cell.2006.03.042.

Rothnie, A.J. (2016) 'Detergent-Free Membrane Protein Purification', in I. Mus-Veteau (ed.) *Heterologous Expression of Membrane Proteins: Methods and Protocols*. New York, NY: Springer, pp. 261–267. Available at: https://doi.org/10.1007/978-1-4939-3637-3_16.

Sabater, L., Giralt, A., Boronat, A., Hankiewicz, K., Blanco, Y., Llufriu, S., Alberch, J., Graus, F. and Saiz, A. (2009) 'Cytotoxic effect of neuromyelitis optica antibody (NMO-IgG) to astrocytes: An *in vitro* study', *Journal of Neuroimmunology*, 215(1), pp. 31–35. Available at: https://doi.org/10.1016/j.jneuroim.2009.07.014.

Salman, M.M., Kitchen, P., Halsey, A., Wang, M.X., Törnroth-Horsefield, S., Conner, A.C., Badaut, J., Iliff, J.J. and Bill, R.M. (2022) 'Emerging roles for dynamic aquaporin-4 subcellular relocalization in CNS water homeostasis', *Brain*, 145(1), pp. 64–75. Available at: https://doi.org/10.1093/brain/awab311.

Sampson, C.D.D., Fàbregas Bellavista, C., Stewart, M.J. and Mulligan, C. (2021) 'Thermostability-based binding assays reveal complex interplay of cation, substrate and lipid binding in the bacterial DASS transporter, VcINDY', *Biochemical Journal*, 478(21), pp. 3847–3867. Available at: https://doi.org/10.1042/BCJ20210061.

Scheidelaar, S., Koorengevel, M.C., Pardo, J.D., Meeldijk, J.D., Breukink, E. and Killian, J.A. (2015) 'Molecular Model for the Solubilization of Membranes into Nanodisks by Styrene Maleic Acid Copolymers', *Biophysical Journal*, 108(2), pp. 279–290. Available at: https://doi.org/10.1016/j.bpj.2014.11.3464.

Scheidelaar, S., Koorengevel, M.C., van Walree, C.A., Dominguez, J.J., Dörr, J.M. and Killian, J.A. (2016) 'Effect of Polymer Composition and pH on Membrane Solubilization by Styrene-Maleic Acid Copolymers', *Biophysical Journal*, 111(9), pp. 1974–1986. Available at: https://doi.org/10.1016/j.bpj.2016.09.025.

Scorer, C.A., Clare, J.J., McCombie, W.R., Romanos, M.A. and Sreekrishna, K. (1994) 'Rapid Selection Using G418 of High Copy Number Transformants of Pichia pastoris for High–level Foreign Gene Expression', *Bio/Technology*, 12(2), pp. 181–184. Available at: https://doi.org/10.1038/nbt0294-181.

Seddon, A.M., Curnow, P. and Booth, P.J. (2004) 'Membrane proteins, lipids and detergents: not just a soap opera', *Biochimica et Biophysica Acta (BBA) - Biomembranes*, 1666(1), pp. 105–117. Available at: https://doi.org/10.1016/j.bbamem.2004.04.011.

Shang, J., Ding, M. and Zhou, X. (2025) ‘Recent advances in S-palmitoylation and its emerging roles in human diseases’, *Journal of Hematology & Oncology*, 18, p. 83. Available at: https://doi.org/10.1186/s13045-025-01738-7.

Silberstein, C., Bouley, R., Huang, Y., Fang, P., Pastor-Soler, N., Brown, D. and Van Hoek, A.N. (2004) ‘Membrane organization and function of M1 and M23 isoforms of aquaporin-4 in epithelial cells’, *American Journal of Physiology-Renal Physiology*, 287(3), pp. F501–F511. Available at: https://doi.org/10.1152/ajprenal.00439.2003.

Simone, L., Pisani, F., Mola, M.G., De Bellis, M., Merla, G., Micale, L., Frigeri, A., Vescovi, A.L., Svelto, M. and Nicchia, G.P. (2019) ‘AQP4 Aggregation State Is a Determinant for Glioma Cell Fate’, *Cancer Research*, 79(9), pp. 2182–2194. Available at: https://doi.org/10.1158/0008-5472.CAN-18-2015.

Smirnova, I.A., Sjöstrand, D., Li, F., Björck, M., Schäfer, J., Östbye, H., Högbom, M., von Ballmoos, C., Lander, G.C., Ädelroth, P. and Brzezinski, P. (2016) ‘Isolation of yeast complex IV in native lipid nanodiscs’, *Biochimica et Biophysica Acta (BBA) - Biomembranes*, 1858(12), pp. 2984–2992. Available at: https://doi.org/10.1016/j.bbamem.2016.09.004.

Smith, A.J., Jin, B.-J., Ratelade, J. and Verkman, A.S. (2014) ‘Aggregation state determines the localization and function of M1– and M23–aquaporin-4 in astrocytes’, *Journal of Cell Biology*, 204(4), pp. 559–573. Available at: https://doi.org/10.1083/jcb.201308118.

Smotrys, J.E. and Linder, M.E. (2004) ‘Palmitoylation of Intracellular Signaling Proteins: Regulation and Function’, *Annual Review of Biochemistry*, 73(Volume 73, 2004), pp. 559–587. Available at: https://doi.org/10.1146/annurev.biochem.73.011303.073954.

Sobocińska, J., Roszczenko-Jasińska, P., Ciesielska, A. and Kwiatkowska, K. (2018) ‘Protein Palmitoylation and Its Role in Bacterial and Viral Infections’, *Frontiers in Immunology*, 8. Available at: https://doi.org/10.3389/fimmu.2017.02003.

Soltermann, F., Foley, E.D.B., Pagnoni, V., Galpin, M., Benesch, J.L.P., Kukura, P. and Struwe, W.B. (2020) ‘Quantifying Protein–Protein Interactions by Molecular Counting with Mass Photometry’, *Angewandte Chemie (International Ed. in English)*, 59(27), pp. 10774–10779. Available at: https://doi.org/10.1002/anie.202001578.

Soltys, J., Liu, Y., Ritchie, A., Wemlinger, S., Schaller, K., Schumann, H., Owens, G.P. and Bennett, J.L. (2019) ‘Membrane assembly of aquaporin-4 autoantibodies regulates classical complement activation in neuromyelitis optica’, *The Journal of Clinical Investigation*, 129(5), pp. 2000–2013. Available at: https://doi.org/10.1172/JCI122942.

Sonn-Segev, A., Belacic, K., Bodrug, T., Young, G., VanderLinden, R.T., Schulman, B.A., Schimpf, J., Friedrich, T., Dip, P.V., Schwartz, T.U., Bauer, B., Peters, J.-M., Struwe, W.B., Benesch, J.L.P., Brown, N.G., Haselbach, D. and Kukura, P. (2020) ‘Quantifying the heterogeneity of macromolecular machines by mass photometry’, *Nature Communications*, 11(1), p. 1772. Available at: https://doi.org/10.1038/s41467-020-15642-w.

Sørbø, J.G., Moe, S.E. and Holen, T. (2007) ‘Early upregulation in nasal epithelium and strong expression in olfactory bulb glomeruli suggest a role for Aquaporin-4 in olfaction’, *FEBS Letters*, 581(25), pp. 4884–4890. Available at: https://doi.org/10.1016/j.febslet.2007.09.018.

Sorbo, J.G., Moe, S.E., Ottersen, O.P. and Holen, T. (2008) ‘The Molecular Composition of Square Arrays’, *Biochemistry*, 47(8), pp. 2631–2637. Available at: https://doi.org/10.1021/bi702146k.

Stetsenko, A. and Guskov, A. (2017) 'An Overview of the Top Ten Detergents Used for Membrane Protein Crystallization', *Crystals*, 7(7), p. 197. Available at: https://doi.org/10.3390/cryst7070197.

Strand, L., Moe, S.E., Solbu, T.T., Vaadal, M. and Holen, T. (2009) 'Roles of Aquaporin-4 Isoforms and Amino Acids in Square Array Assembly', *Biochemistry*, 48(25), pp. 5785–5793. Available at: https://doi.org/10.1021/bi802231q.

Stroud, Z., Hall, S.C.L. and Dafforn, T.R. (2018) 'Purification of membrane proteins free from conventional detergents: SMA, new polymers, new opportunities and new insights', *Methods*, 147, pp. 106–117. Available at: https://doi.org/10.1016/j.ymeth.2018.03.011.

Sui, H., Han, B.-G., Lee, J.K., Walian, P. and Jap, B.K. (2001) 'Structural basis of water-specific transport through the AQP1 water channel', *Nature*, 414(6866), pp. 872–878. Available at: https://doi.org/10.1038/414872a.

Sun, B., Fernandes, D., Soltys, J., Kienzler, A.-K., Paneva, S., Harrison, R., Ramanathan, S., Harrison, A.L., Makuch, M., Fichtner, M.L., Donat, R.F., Akdeniz, D., Bayuangga, H., Im, M.G., Williams, R., Vasconcelos, A., Thomsen, S., Fower, A., Sun, R., Fox, H., Mgbachi, V., Davies, A., Tseng, M., Handel, A., Kelly, M., Zhao, M., Bancroft, J., Bashford-Rogers, R., Pluvinage, J.V., Dandekar, R., Alvarenga, B.D., Dustin, L.B., Rinaldi, S., Owens, R., Anthony, D., Bennett, D.L., Waters, P., Davis, S.J., Wilson, M.R., O'Connor, K.C., Carvalho, A.L. and Irani, S.R. (2025) 'Permissive central tolerance plus defective peripheral checkpoints license pathogenic memory B cells in CASPR2-antibody encephalitis', *Science Advances*, 11(16), p. eadr9986. Available at: https://doi.org/10.1126/sciadv.adr9986.

Sun, C., Benlekbir, S., Venkatakrishnan, P., Wang, Y., Hong, S., Hosler, J., Tajkhorshid, E., Rubinstein, J.L. and Gennis, R.B. (2018) 'Structure of the alternative complex III in a supercomplex with cytochrome oxidase', *Nature*, 557(7703), pp. 123–126. Available at: https://doi.org/10.1038/s41586-018-0061-y.

Suzuki, H., Nishikawa, K., Hiroaki, Y. and Fujiyoshi, Y. (2008) 'Formation of aquaporin-4 arrays is inhibited by palmitoylation of N-terminal cysteine residues', *Biochimica et Biophysica Acta (BBA) - Biomembranes*, 1778(4), pp. 1181–1189. Available at: https://doi.org/10.1016/j.bbamem.2007.12.007.

Swainsbury, D.J.K., Scheidelaar, S., van Grondelle, R., Killian, J.A. and Jones, M.R. (2014a) 'Bacterial Reaction Centers Purified with Styrene Maleic Acid Copolymer Retain Native Membrane Functional Properties and Display Enhanced Stability', *Angewandte Chemie*, 126(44), pp. 11997–12001. Available at: https://doi.org/10.1002/ange.201406412.

Swainsbury, D.J.K., Scheidelaar, S., van Grondelle, R., Killian, J.A. and Jones, M.R. (2014b) 'Bacterial Reaction Centers Purified with Styrene Maleic Acid Copolymer Retain Native Membrane Functional Properties and Display Enhanced Stability', *Angewandte Chemie International Edition*, 53(44), pp. 11803–11807. Available at: https://doi.org/10.1002/anie.201406412.

Tabaczar, S., Czogalla, A., Podkalicka, J., Biernatowska, A. and Sikorski, A.F. (2017) 'Protein palmitoylation: Palmitoyltransferases and their specificity', *Experimental Biology and Medicine*, 242(11), pp. 1150–1157. Available at: https://doi.org/10.1177/1535370217707732.

Tajima, M., Crane, J.M. and Verkman, A.S. (2010) 'Aquaporin-4 (AQP4) Associations and Array Dynamics Probed by Photobleaching and Single-molecule Analysis of Green Fluorescent Protein-AQP4 Chimeras', *Journal of Biological Chemistry*, 285(11), pp. 8163–8170. Available at: https://doi.org/10.1074/jbc.M109.093948.

Tanghe, A., Van Dijck, P. and Thevelein, J.M. (2006) 'Why do microorganisms have aquaporins?', *Trends in Microbiology*, 14(2), pp. 78–85. Available at: https://doi.org/10.1016/j.tim.2005.12.001.

Tani, K., Mitsuma, T., Hiroaki, Y., Kamegawa, A., Nishikawa, K., Tanimura, Y. and Fujiyoshi, Y. (2009) 'Mechanism of Aquaporin-4's Fast and Highly Selective Water Conduction and Proton Exclusion', *Journal of Molecular Biology*, 389(4), pp. 694–706. Available at: https://doi.org/10.1016/j.jmb.2009.04.049.

Tascón, I., Sousa, J.S., Corey, R.A., Mills, D.J., Griwatz, D., Aumüller, N., Mikusevic, V., Stansfeld, P.J., Vonck, J. and Hänelt, I. (2020) 'Structural basis of proton-coupled potassium transport in the KUP family', *Nature Communications*, 11(1), p. 626. Available at: https://doi.org/10.1038/s41467-020-14441-7.

Teo, A.C.K., Lee, S.C., Pollock, N.L., Stroud, Z., Hall, S., Thakker, A., Pitt, A.R., Dafforn, T.R., Spickett, C.M. and Roper, D.I. (2019) 'Analysis of SMALP co-extracted phospholipids shows distinct membrane environments for three classes of bacterial membrane protein', *Scientific Reports*, 9(1), p. 1813. Available at: https://doi.org/10.1038/s41598-018-37962-0.

Tuller, F., Holzer, H., Schanda, K., Aboulenein-Djamshidian, F., Höftberger, R., Khalil, M., Seifert-Held, T., Leutmezer, F., Berger, T. and Reindl, M. (2016) 'Characterization of the binding pattern of human aquaporin-4 autoantibodies in patients with neuromyelitis optica spectrum disorders', *Journal of Neuroinflammation*, 13(1), p. 176. Available at: https://doi.org/10.1186/s12974-016-0642-3.

Unger, L., Ronco-Campaña, A., Kitchen, P., Bill, R.M. and Rothnie, A.J. (2021) 'Biological insights from SMA-extracted proteins', *Biochemical Society Transactions*, 49(3), pp. 1349–1359. Available at: https://doi.org/10.1042/BST20201067.

Urner, L.H. (2022) 'Advances in membrane mimetics and mass spectrometry for understanding membrane structure and function', *Current Opinion in Chemical Biology*, 69, p. 102157. Available at: https://doi.org/10.1016/j.cbpa.2022.102157.

Van Itallie, C.M., Gambling, T.M., Carson, J.L. and Anderson, J.M. (2005) 'Palmitoylation of claudins is required for efficient tight-junction localization', *Journal of Cell Science*, 118(Pt 7), pp. 1427–1436. Available at: https://doi.org/10.1242/jcs.01735.

Verbavatz, J.-M., Ma, T., Gobin, R. and Verkman, A.S. (1997) 'Absence of orthogonal arrays in kidney, brain and muscle from transgenic knockout mice lacking water channel aquaporin-4', *Journal of Cell Science*, 110(22), pp. 2855–2860. Available at: https://doi.org/10.1242/jcs.110.22.2855.

Verkman, A.S. (2005) 'More than just water channels: unexpected cellular roles of aquaporins', *Journal of Cell Science*, 118(15), pp. 3225–3232. Available at: https://doi.org/10.1242/jcs.02519.

Verkman, A.S. (2012) 'Aquaporins in Clinical Medicine', *Annual Review of Medicine*, 63(Volume 63, 2012), pp. 303–316. Available at: https://doi.org/10.1146/annurev-med-043010-193843.

Verkman, A.S. (2013) 'Aquaporins', *Current biology : CB*, 23(2), pp. R52–R55. Available at: https://doi.org/10.1016/j.cub.2012.11.025.

Verkman, A.S., Binder, D.K., Bloch, O., Auguste, K. and Papadopoulos, M.C. (2006) 'Three distinct roles of aquaporin-4 in brain function revealed by knockout mice', *Biochimica et*

Biophysica Acta (BBA) - Biomembranes, 1758(8), pp. 1085–1093. Available at: https://doi.org/10.1016/j.bbamem.2006.02.018.

Verkman, A.S. and Mitra, A.K. (2000) 'Structure and function of aquaporin water channels', *American Journal of Physiology. Renal Physiology*, 278(1), pp. F13-28. Available at: https://doi.org/10.1152/ajprenal.2000.278.1.F13.

Verkman, A.S., Phuan, P., Asavapanumas, N. and Tradtrantip, L. (2013) 'Biology of AQP4 and Anti-AQP4 Antibody: Therapeutic Implications for NMO', *Brain Pathology*, 23(6), pp. 684–695. Available at: https://doi.org/10.1111/bpa.12085.

Verkman, A.S., Ratelade, J., Rossi, A., Zhang, H. and Tradtrantip, L. (2011) 'Aquaporin-4: orthogonal array assembly, CNS functions, and role in neuromyelitis optica', *Acta Pharmacologica Sinica*, 32(6), pp. 702–710. Available at: https://doi.org/10.1038/aps.2011.27.

Verkman, A.S., Smith, A.J., Phuan, P., Tradtrantip, L. and Anderson, M.O. (2017) 'The aquaporin-4 water channel as a potential drug target in neurological disorders', *Expert Opinion on Therapeutic Targets*, 21(12), pp. 1161–1170. Available at: https://doi.org/10.1080/14728222.2017.1398236.

Visscher, K.M., Medeiros-Silva, J., Mance, D., Rodrigues, J.P.G.L.M., Daniëls, M., Bonvin, A.M.J.J., Baldus, M. and Weingarth, M. (2017) 'Supramolecular Organization and Functional Implications of K+ Channel Clusters in Membranes', *Angewandte Chemie (International Ed. in English)*, 56(43), pp. 13222–13227. Available at: https://doi.org/10.1002/anie.201705723.

Wagner, K., Unger, L., Salman, M.M., Kitchen, P., Bill, R.M. and Yool, A.J. (2022) 'Signaling Mechanisms and Pharmacological Modulators Governing Diverse Aquaporin Functions in Human Health and Disease', *International Journal of Molecular Sciences*, 23(3), p. 1388. Available at: https://doi.org/10.3390/ijms23031388.

Wingerchuk, D.M., Banwell, B., Bennett, J.L., Cabre, P., Carroll, W., Chitnis, T., de Seze, J., Fujihara, K., Greenberg, B., Jacob, A., Jarius, S., Lana-Peixoto, M., Levy, M., Simon, J.H., Tenembaum, S., Traboulsee, A.L., Waters, P., Wellik, K.E. and Weinshenker, B.G. (2015) 'International consensus diagnostic criteria for neuromyelitis optica spectrum disorders', *Neurology*, 85(2), pp. 177–189. Available at: https://doi.org/10.1212/WNL.0000000000001729.

Wingerchuk, D.M., Hogancamp, W.F., O'Brien, P.C. and Weinshenker, B.G. (1999) 'The clinical course of neuromyelitis optica (Devic's syndrome)', *Neurology*, 53(5), pp. 1107–1107. Available at: https://doi.org/10.1212/WNL.53.5.1107.

Wolburg, H. (1995) 'Orthogonal arrays of intramembranous particles: a review with special reference to astrocytes', *Journal Fur Hirnforschung*, 36(2), pp. 239–258.

Wu, D. and Piszczek, G. (2020) 'Measuring the affinity of protein-protein interactions on a single-molecule level by mass photometry', *Analytical Biochemistry*, 592, p. 113575. Available at: https://doi.org/10.1016/j.ab.2020.113575.

Xue, M., Cheng, L., Faustino, I., Guo, W. and Marrink, S.J. (2018) 'Molecular Mechanism of Lipid Nanodisk Formation by Styrene-Maleic Acid Copolymers', *Biophysical Journal*, 115(3), pp. 494–502. Available at: https://doi.org/10.1016/j.bpj.2018.06.018.

Yang, B., Brown, D. and Verkman, A.S. (1996) 'The Mercurial Insensitive Water Channel (AQP-4) Forms Orthogonal Arrays in Stably Transfected Chinese Hamster Ovary Cells',

Journal of Biological Chemistry, 271(9), pp. 4577–4580. Available at: https://doi.org/10.1074/jbc.271.9.4577.

Yang, B., Ma, T. and Verkman, A.S. (1995) 'cDNA Cloning, Gene Organization, and Chromosomal Localization of a Human Mercurial Insensitive Water Channel: EVIDENCE FOR DISTINCT TRANSCRIPTIONAL UNITS', *Journal of Biological Chemistry*, 270(39), pp. 22907–22913. Available at: https://doi.org/10.1074/jbc.270.39.22907.

Yang, J., Cao, C., Liu, J., Liu, Y., Lu, J., Yu, H., Li, X., Wu, J., Yu, Z., Li, H. and Chen, G. (2024) 'Dystrophin 71 deficiency causes impaired aquaporin-4 polarization contributing to glymphatic dysfunction and brain edema in cerebral ischemia', *Neurobiology of Disease*, 199, p. 106586. Available at: https://doi.org/10.1016/j.nbd.2024.106586.

Yang, X., Kovalenko, O.V., Tang, W., Claas, C., Stipp, C.S. and Hemler, M.E. (2004) 'Palmitoylation supports assembly and function of integrin–tetraspanin complexes', *Journal of Cell Biology*, 167(6), pp. 1231–1240. Available at: https://doi.org/10.1083/jcb.200404100.

Yin, H. and Flynn, A.D. (2016) 'Drugging Membrane Protein Interactions', *Annual review of biomedical engineering*, 18, pp. 51–76. Available at: https://doi.org/10.1146/annurev-bioeng-092115-025322.

Yoder, N. and Gouaux, E. (2020) 'The His-Gly motif of acid-sensing ion channels resides in a reentrant "loop" implicated in gating and ion selectivity', *eLife*. Edited by L. Csanády, K.J. Swartz, L. Csanády, Y. Jiang, and S.A. Pless, 9, p. e56527. Available at: https://doi.org/10.7554/eLife.56527.

Young, G., Hundt, N., Cole, D., Fineberg, A., Andrecka, J., Tyler, A., Olerinyova, A., Ansari, A., Marklund, E.G., Collier, M.P., Chandler, S.A., Tkachenko, O., Allen, J., Crispin, M., Billington, N., Takagi, Y., Sellers, J.R., Eichmann, C., Selenko, P., Frey, L., Riek, R., Galpin, M.R., Struwe, W.B., Benesch, J.L.P. and Kukura, P. (2018) 'Quantitative mass imaging of single biological macromolecules', *Science*, 360(6387), pp. 423–427. Available at: https://doi.org/10.1126/science.aar5839.

Young, J.W., Pfitzner, E., Wee, R. van, Kirschbaum, C., Kukura, P. and Robinson, C.V. (2024) 'Characterization of membrane protein interactions by peptidisc-mediated mass photometry', *iScience*, 27(2). Available at: https://doi.org/10.1016/j.isci.2024.108785.

Yu, J., Yool, A.J., Schulten, K. and Tajkhorshid, E. (2006) 'Mechanism of Gating and Ion Conductivity of a Possible Tetrameric Pore in Aquaporin-1', *Structure*, 14(9), pp. 1411–1423. Available at: https://doi.org/10.1016/j.str.2006.07.006.

Yu, J., Zhu, H., Lape, R., Greiner, T., Du, J., Lü, W., Sivilotti, L. and Gouaux, E. (2021) 'Mechanism of gating and partial agonist action in the glycine receptor', *Cell*, 184(4), pp. 957-968.e21. Available at: https://doi.org/10.1016/j.cell.2021.01.026.

Zeppenfeld, D.M., Simon, M., Haswell, J.D., D'Abreo, D., Murchison, C., Quinn, J.F., Grafe, M.R., Woltjer, R.L., Kaye, J. and Iliff, J.J. (2017) 'Association of Perivascular Localization of Aquaporin-4 With Cognition and Alzheimer Disease in Aging Brains', *JAMA Neurology*, 74(1), pp. 91–99. Available at: https://doi.org/10.1001/jamaneurol.2016.4370.

Zeuthen, T. and Klaerke, D.A. (1999) 'Transport of Water and Glycerol in Aquaporin 3 Is Gated by H+', *Journal of Biological Chemistry*, 274(31), pp. 21631–21636. Available at: https://doi.org/10.1074/jbc.274.31.21631.

Zha, J., Liu, D., Ren, J., Liu, Z. and Wu, X. (2023) ‘Advances in Metabolic Engineering of Pichia pastoris Strains as Powerful Cell Factories’, *Journal of Fungi*, 9(10), p. 1027. Available at: https://doi.org/10.3390/jof9101027.

Zhou, H.-X. and Cross, T.A. (2013) ‘Influences of Membrane Mimetic Environments on Membrane Protein Structures’, *Annual review of biophysics*, 42, pp. 361–392. Available at: https://doi.org/10.1146/annurev-biophys-083012-130326.

Zhu, D.-D., Yang, G., Huang, Y.-L., Zhang, T., Sui, A.-R., Li, N., Su, W.-H., Sun, H.-L., Gao, J.-J., Ntim, M., Guan, R.-X., Jin, L.-L., Yu, J., Huang, Z.-Y., Ma, T.-H. and Li, S. (2022) ‘AQP4-A25Q Point Mutation in Mice Depolymerizes Orthogonal Arrays of Particles and Decreases Polarized Expression of AQP4 Protein in Astrocytic Endfeet at the Blood–Brain Barrier’, *Journal of Neuroscience*, 42(43), pp. 8169–8183. Available at: https://doi.org/10.1523/JNEUROSCI.0401-22.2022.

Zoghbi, M.E., Cooper, R.S. and Altenberg, G.A. (2016) ‘The Lipid Bilayer Modulates the Structure and Function of an ATP-binding Cassette Exporter’, *Journal of Biological Chemistry*, 291(9), pp. 4453–4461. Available at: https://doi.org/10.1074/jbc.M115.698498.

Zoonens, M. and Popot, J.-L. (2014) ‘Amphipols for Each Season’, *The Journal of Membrane Biology*, 247(9), pp. 759–796. Available at: https://doi.org/10.1007/s00232-014-9666-8.

Appendix

```
sp|P55087-1|AQP4_HUMAN      MSDRPTARRWGKCGPLCTRENIMVAFKGVWTQAFWKAVTAEFLAMLIFVLLSLGSTINWG        60
M1-hAQP4-pPICZ              MSDRPTARRWGKCGPLCTRENIMVAFKGVWTQAFWKAVTAEFLAMLIFVLLSLGSTINWG        60
sp|P55087-2|AQP4_HUMAN      ----------------------MVAFKGVWTQAFWKAVTAEFLAMLIFVLLSLGSTINWG        38
M23-hAQP4-pPICZ             ----------------------MVAFKGVWTQAFWKAVTAEFLAMLIFVLLSLGSTINWG        38
                                                   ************************************

sp|P55087-1|AQP4_HUMAN      GTEKPLPVDMVLISLCFGLSIATMVQCFGHISGGHINPAVTVAMVCTRKISIAKSVFYIA        120
M1-hAQP4-pPICZ              GTEKPLPVDMVLISLCFGLSIATMVQCFGHISGGHINPAVTVAMVCTRKISIAKSVFYIA        120
sp|P55087-2|AQP4_HUMAN      GTEKPLPVDMVLISLCFGLSIATMVQCFGHISGGHINPAVTVAMVCTRKISIAKSVFYIA        98
M23-hAQP4-pPICZ             GTEKPLPVDMVLISLCFGLSIATMVQCFGHISGGHINPAVTVAMVCTRKISIAKSVFYIA        98
                            ************************************************************

sp|P55087-1|AQP4_HUMAN      AQCLGAIIGAGILYLVTPPSVVGGLGVTMVHGNLTAGHGLLVELIITFQLVFTIFASCDS        180
M1-hAQP4-pPICZ              AQCLGAIIGAGILYLVTPPSVVGGLGVTMVHGNLTAGHGLLVELIITFQLVFTIFASCDS        180
sp|P55087-2|AQP4_HUMAN      AQCLGAIIGAGILYLVTPPSVVGGLGVTMVHGNLTAGHGLLVELIITFQLVFTIFASCDS        158
M23-hAQP4-pPICZ             AQCLGAIIGAGILYLVTPPSVVGGLGVTMVHGNLTAGHGLLVELIITFQLVFTIFASCDS        158
                            ************************************************************

sp|P55087-1|AQP4_HUMAN      KRTDVTGSIALAIGFSVAIGHLFAINYTGASMNPARSFGPAVIMGNWENHWIYWVGPIIG        240
M1-hAQP4-pPICZ              KRTDVTGSIALAIGFSVAIGHLFAINYTGASMNPARSFGPAVIMGNWENHWIYWVGPIIG        240
sp|P55087-2|AQP4_HUMAN      KRTDVTGSIALAIGFSVAIGHLFAINYTGASMNPARSFGPAVIMGNWENHWIYWVGPIIG        218
M23-hAQP4-pPICZ             KRTDVTGSIALAIGFSVAIGHLFAINYTGASMNPARSFGPAVIMGNWENHWIYWVGPIIG        218
                            ************************************************************

sp|P55087-1|AQP4_HUMAN      AVLAGGLYEYVFCPDVEFKRRFKEAFSKAAQQTKGSYMEVEDNRSQVETDDLILKPGVVH        300
M1-hAQP4-pPICZ              AVLAGGLYEYVFCPDVEFKRRFKEAFSKAAQQTKGSYMEVEDNRSQVETDDLILKPGVVH        300
sp|P55087-2|AQP4_HUMAN      AVLAGGLYEYVFCPDVEFKRRFKEAFSKAAQQTKGSYMEVEDNRSQVETDDLILKPGVVH        278
M23-hAQP4-pPICZ             AVLAGGLYEYVFCPDVEFKRRFKEAFSKAAQQTKGSYMEVEDNRSQVETDDLILKPGVVH        278
                            ************************************************************

sp|P55087-1|AQP4_HUMAN      VIDVDRGEEKKGKDQSGEVLSSV------   323
M1-hAQP4-pPICZ              VIDVDRGEEKKGKDQSGEVLSSVHHHHHH   329
sp|P55087-2|AQP4_HUMAN      VIDVDRGEEKKGKDQSGEVLSSV------   301
M23-hAQP4-pPICZ             VIDVDRGEEKKGKDQSGEVLSSVHHHHHH   307
                            **********************
```

Figure A.1. hAQP4 M1 and M23 isoform amino acid sequences.
Clustal Omega (1.2.4) multiple sequence alignment of hAQP4 M1 and M23 isoform amino acid sequences, against the hAQP4 amino acid sequences sequenced from the pPICZ plasmid constructs (Figure 2.1).